NNT : 2024ENTP0005

THÈSE DE DOCTORAT DE L'ENTPE

Membre de l'Université de Lyon

École Doctorale N° 162
Mécanique, Énergétique, Génie Civil et Acoustique

Spécialité : MÉCANIQUE

CAMILA ELIZABETH DA SILVEIRA ZANIN

Exploiting nonlinear dynamics in mass-in-mass chains for metamaterial design

Exploitation de la dynamique non-linéaire dans des chaînes « mass-in-mass » pour la conception de métamatériaux

---

Jury composé de :

MICHON, GUILHEM	Professeur, ISAE-SUPAERO	-	Président et Rapporteur
BERGER, SÉBASTIEN	Professeur, INSA Centre-Val de Loire	-	Rapporteur
TURE SAVADKOOHI, ALIREZA	Directeur de Recherche, ENTPE	-	Directeur de thèse
BAGUET, SÉBASTIEN	Maître de conférences, INSA Lyon	-	Co-directeur de thèse
DUFOUR, RÉGIS	Professeur, INSA Lyon	-	Encadrant

Acknowledgments

This PhD dissertation represents the culmination of the doctoral research conducted between December 2020 and March 2023, the outcome of a collaboration among the Laboratoire de Tribologie et Dynamique des Systèmes (LTDS), UMR CNRS 5513, the Laboratoire de Mécanique des Contacts et des Structures (LaMCoS), UMR CNRS 5259, and the Computational Optimal Design of Engineering Systems laboratory (CODES), supported by the LABEX CeLyA, France (ANR-10-LABX-0060) of Université de Lyon, within the program "Investissements d'Avenir" operated by the French National Research Agency (ANR). Thus, I would like to express my sincere gratitude to the aforementioned laboratories for hosting me and to LABEX CeLyA for funding this research.
My sincere thanks to the jury members for accepting to review this PhD work. Your time and expertise are highly appreciated.
I would like to thank my PhD supervisors, Alireza Ture Savadkoohi, Sébastien Baguet and Régis Dufour, for their continuous support and guidance throughout my academic journey.
I express my sincere gratitude to Samy Missoum for warmly welcoming me to the University of Arizona and introducing me to the intriguing field of optimization research.
My gratitude also goes to Emmanuel Gourdon for the enriching discussions in the field of acoustics. Furthermore, a big thanks to Emanuele De Bono for his support in the experimental aspect of this thesis.
I express my sincere appreciation and gratitude to all my friends and colleagues at the laboratories LTDS, LaMCoS and CODES, for their support and for sharing moments of joy. Particularly, I cite Jean, Aurélie, and Matthieu, with whom I shared the office space and exciting scientific discoveries. I must also mention my friends from the "Terre" team, Sofia and Antoine, whose engaging discussions made my lunches much more interesting.
I would like to express my gratitude to my friends in France, who have become my family here: Jennifer, Laura, Nicolas, Milena, Guilherme, Taiane, Lucas, Nerissa, Matheus S., Asaph, Igor, Matheus G., and the entire "Triplex do Guarujá" group. The carefree moments we shared during these years of thesis made this journey much more pleasant. A big thanks also goes to my friends in Brazil who are always with me, no matter the distance: Barbara, Ingrid, Gabriela B., Gabriela O., and Marina.
A special thanks to my partner, Gabriel, who shared our home and the experience of pursuing a PhD throughout these years. His support and love have not only made these challenging years bearable but also transformed them into a beautiful chapter of our lives.
I express my gratitude to my family, who, despite the distance, always cheers for me. A special mention goes to my brother, Carlos Henrique, for always being an example and a great friend.
Finally, I want to express my profound gratitude to the most important individuals in my life. The biggest thanks to my parents, Eliane and Ademar, for always believing in me. Thank you for being a constant source of inspiration. I would not have made it this far without you.

Abstract: This thesis focuses on the interactions of nonlinear mass-in-mass cells and on modeling their behaviors, serving as a preliminary step towards the creation of new types of nonlinear metamaterials with designed behaviors. During this investigation, a specific piecewise nonlinearity is explored, initially in a single mass-in-mass cell and, subsequently, in a chain of coupled cells. For the latter, certain approximations are applied to transition from the discrete to the continuous domain and to study the behavior of the chain in the vicinity of one of its arbitrary modes. Both fast and slow dynamics are unveiled for the single cell and the chain, providing design tools to tune parameters of the piecewise nonlinearity. Moreover, a stochastic optimization study is conducted to design a mass-in-mass meta-cell. Given the mechanical complexity of implementing the explored nonlinearity in this thesis, an experimental study is performed on a programmable electroacoustic loudspeaker.

Résumé long en français

Les phénomènes de bruits et de vibrations peuvent être avantageusement exploités, par exemple, pour récupérer leur énergie afin d'alimenter des capteurs déportés, pour surveiller l'intégrité des structures ou pour augmenter la précision de mesure d'accélération ou de masse infime de dispositifs médicaux. Exploiter ces phénomènes nécessite avant tout de maîtriser leurs effets afin d'induire des réponses spécifiques. Pour ce faire, des stratégies telles que le couplage d'absorbeurs au système principal ou la conception de matériaux aux comportements sur mesure peuvent être employées pour atténuer les oscillations et réguler les comportements vibratoires des structures.
Le contrôle passif des vibrations explore la localisation de l'énergie dans des composants structurels spécifiques ou sa transformation pour être absorbée par des oscillateurs couplés, ne nécessitant aucune source d'alimentation externe pour son activation. Ce système de contrôle voit ses forces de contrôle dépendre de la réponse de la structure principale, constituant ainsi un élément essentiel pour garantir le comportement souhaitable des systèmes tout au long de leur durée de vie opérationnelle.
Le couplage d'un oscillateur essentiellement non linéaire à un oscillateur primaire est abordé dans cette thèse dans un premier temps. Cet oscillateur non linéaire agit comme un puits d'énergie non linéaire, également appelé « Nonlinear Energy Sink » (NES). Dans de tels systèmes, il est possible d'induire un transfert irréversible d'énergie vibratoire de l'oscillateur primaire vers le non linéaire en raison de la capture de résonance dans le manifold de 1:1 résonance du système. Les NES présentent des performances élevées dans le contrôle de bandes larges en raison de leur capacité à osciller à n'importe quelle fréquence lorsque correctement conçus, leur permettant éventuellement d'entrer en résonance avec n'importe quel système.
Finalement, cette recherche se concentre sur les interactions entre les cellules « mass-in-mass » non linéaires et la modélisation de leurs comportements, et se veut ainsi une étape préliminaire vers la création de nouveaux types de métamatériaux non linéaires à comportement prédéfini. Cela englobe des développements analytiques et numériques, ainsi que des études d'optimisation visant à ajuster de manière précise les paramètres de conception de la non linéarité explorée dans cette étude.
Ce manuscrit comporte cinq chapitres rapportant les avancées scientifiques faites durant trois ans de travail.

Le **Chapitre 1** situe les travaux dans le contexte de la littérature scientifique et offre une revue approfondie des systèmes de contrôle, en explorant les systèmes de contrôle passifs et différents types de métamatériaux. De plus, il expose la méthodologie générale employée dans ce manuscrit pour la conception des systèmes de contrôle des vibrations. Cela comprend tout d'abord le développement d'un modèle du système étudié, suivi de l'exploitation des non-linéarités dont les paramètres doivent être conçus. Ensuite, le modèle du système est réduit, et les outils de dynamique non linéaire sont utilisés pour clarifier ses différentes caractéristiques dynamiques. Cette étape peut être suivie d'une procédure d'optimisation, impliquant l'imposition de métriques spécifiques et l'ajustement fin de la non-linéarité pour obtenir les résultats souhaités. Enfin, la procédure est suivie par des vérifications numériques et/ou expérimentales.

Le **Chapitre 2** explore les dynamiques d'une méta-cellule « mass-in-mass » non-linéaire, constituée d'un oscillateur qui encapsule un autre oscillateur doté d'une force de rappel originale car non linéaire par morceaux : cubique dans un intervalle de déflexion et linéaire ailleurs. La forme complexifiée des équations du système est traitée par la méthode des échelles multiples afin d'identifier ses dynamiques rapides et lentes, conduisant à la détermination de la variété invariante

lente ainsi que des points singuliers et d'équilibre du système. Le système considéré peut être utilisé pour le contrôle passif de la masse extérieure en agissant comme un NES, avec une non linéarité par morceaux, ou être considéré comme une seule méta-cellule avec des caractéristiques spatiales dans une chaîne de méta-cellules.

Le **Chapitre 3** aborde l'étude d'une chaîne de méta-cellules couplées introduites dans le Chapitre 2. Dans un premier temps, le système discret est exposé, suivi de la transition vers le domaine continu. Les caractéristiques modales du système continu sont évaluées, et le système est étudié autour de l'un de ses modes arbitraires. En recourant à la méthode des échelles multiples en temps, les équations du système complexifié sont analysées pour mettre en évidence les dynamiques rapides et lentes. Finalement, les réponses dynamiques du système original sont comparées à celles obtenues à partir des prédictions analytiques du système projeté.

Le **Chapitre 4** recourt à un algorithme d'optimisation stochastique pour concevoir la méta-cellule « mass-in-mass » non-linéaire, sujet abordé dans le Chapitre 2. Cette approche stochastique devient nécessaire en raison de la sensibilité des systèmes non linéaires, tels que celui-ci, aux perturbations dans les paramètres de conception et aux conditions initiales, induisant un comportement discontinu. En d'autres termes, même de légères modifications de ces facteurs peuvent déclencher une transition d'un état d'efficacité « élevée » à « basse ». L'efficacité de la méta-cellule du Chapitre 2 après optimisation est comparée à celle d'une méta-cellule avec une non linéarité cubique optimisée, ainsi qu'à celle d'un oscillateur à un degré de liberté.

Le **Chapitre 5** explore les possibilités de conception mécanique de la non linéarité étudiée dans cette thèse, puis se focalise sur l'étude d'un haut-parleur électroacoustique programmable. Une technique d'inversion de modèle permettant de programmer numériquement l'impédance du haut-parleur pour obtenir un comportement non-linéaire souhaité est présentée. Une non linéarité de type Duffing est programmée, et le haut-parleur électroacoustique est couplé à un mode acoustique d'un tube fermé. Cette étude met en évidence la faisabilité de programmer le comportement d'un haut-parleur électroacoustique.

Le **Chapitre 6** conclut le manuscrit et dresse les perspectives pour de nouveaux développements de cette recherche.

Cette thèse de doctorat représente une avancée significative dans le domaine de la conception des métamatériaux en exploitant les dynamiques non linéaires. En étudiant des méta-cellules « mass-in-mass » et des méta-chaînes avec une non-linéarité spécifique, cette recherche ouvre de nouvelles voies pour la création de métamatériaux aux comportements sur mesure.
La dynamique d'une méta-cellule « mass-in-mass » non linéaire est étudiée, conduisant à la détection de la variété invariante lente et des points caractéristiques dynamiques du système. La non-linéarité par morceaux exploitée résulte en une variété invariante lente avec quatre extrema locaux, distincts de ceux observés dans les systèmes avec des non-linéarités cubiques pures et linéaires par morceaux, par exemple. Les développements analytiques offrent des outils de conception pour ajuster la non-linéarité par morceaux de la masse interne, ce qui permet au système d'exprimer des réponses périodiques ou non périodiques en fonction des caractéristiques de la force externe donnée ou pour atteindre des objectifs spécifiques, tels que le contrôle ou la récupération d'énergie.
L'étude d'une chaîne constituée de méta-cellules couplées est abordée. Les caractéristiques modales du système sont évaluées, et le système est étudié dans le voisinage de l'un de ses modes arbitraires. Les comparaisons entre les réponses dynamiques du système original et celles du système projeté sur un mode arbitraire révèlent des divergences, qui peuvent être attribuées à la négligence des interactions intermodales. Néanmoins, les résultats analytiques basés sur l'approximation à un seul

mode fournissent des outils de conception préliminaires pour ajuster les paramètres de la non-linéarité afin d'obtenir des réponses qualitativement conçues du système. Pour réduire les divergences entre les réponses dynamiques du système d'origine et celles du système projeté, la chaîne devrait être étudiée autour d'au moins deux modes et ainsi tenir compte des résonances internes.
De plus, l'application de techniques d'optimisation stochastique pour concevoir des méta-cellules non linéaires démontre le potentiel d'optimisation des performances de ces systèmes. Les résultats mettent en évidence la supériorité de la non-linéarité par morceaux dans la réduction de l'énergie vibratoire, ouvrant la voie à des conceptions de métamatériaux plus efficaces.
En outre, l'étude expérimentale utilisant un haut-parleur électro-acoustique programmable couplé à un mode acoustique d'un tube met en évidence la mise en uvre pratique des comportements non linéaires. Une technique d'inversion de modèle est appliquée pour programmer numériquement l'impédance du haut-parleur, dans le but d'obtenir un comportement ciblé de type Duffing. La non-linéarité programmée du haut-parleur électroacoustique conduit à deux types de réponses distincts observés dans les expériences : périodiques et non périodiques. Les résultats expérimentaux démontrent la faisabilité de la programmation du comportement d'un haut-parleur électroacoustique.
Dans l'ensemble, cette thèse jette les bases pour la recherche future dans le domaine de la conception des métamatériaux. En fournissant une compréhension approfondie des dynamiques non linéaires et en proposant des stratégies de conception pratiques, elle ouvre la voie au développement de métamatériaux innovants aux comportements sur mesure.

Contents

Introduction **9**

1 Literature review and global methodology **11**
1.1 Vibration control . . . 11
1.2 Passive control solutions . . . 12
1.2.1 Tuned mass damper . . . 12
1.2.2 Nonlinear absorbers . . . 12
1.3 Metamaterials . . . 14
1.3.1 Electromagnetic metamaterials . . . 15
1.3.2 Acoustic metamaterials . . . 16
1.3.3 Mechanical metamaterials . . . 17
1.3.4 Nonlinear metamaterials . . . 18
1.3.5 Linear mass-in-mass systems . . . 20
1.3.6 Nonlinear mass-in-mass systems . . . 21
1.4 Global methodology . . . 22
1.5 Conclusions of the chapter . . . 22

2 Study of a nonlinear mass-in-mass meta-cell **25**
2.1 The system and governing equations . . . 25
2.2 Multiple scales method, complex variables of Manevitch and Galerkin method . . . 27
2.3 Detection of different dynamics of the system . . . 30
2.3.1 Fast dynamics: ε^0 order of system equations . . . 30
2.3.2 Stability analysis of the SIM . . . 32
2.3.3 Slow dynamics: ε^1 order of system equations . . . 33
2.3.4 Backbone curves of the system . . . 35
2.3.5 Parametric study of singular points . . . 36
2.4 Numerical results versus analytical predictions . . . 40
2.4.1 Free response . . . 40
2.4.2 Forced responses . . . 41
2.4.3 Backbone curves . . . 53
2.5 Conclusions of the chapter . . . 54

3 Chain of nonlinear meta-cells **57**
3.1 Model of the discrete chain . . . 57
3.2 Passage from discrete to continuous domain . . . 58
3.3 Evaluation of modal characteristics . . . 59
3.4 Study of the system in the vicinity of one of its arbitrary modes . . . 61
3.5 Detection of different dynamics of the projected system . . . 62
3.5.1 Fast dynamics: ε^0 order of system equations . . . 62
3.5.2 Slow dynamics: ε^1 order of system equations . . . 63
3.6 Numerical results versus analytical predictions . . . 64
3.6.1 Post-treatment of data . . . 64
3.6.2 Numerical examples . . . 66
3.7 Conclusions of the chapter . . . 81

4 Stochastic optimization **83**
4.1 Introduction to the optimization study . . . 83
4.2 Potential discontinuous behavior of the system . . . 84
4.2.1 Sources of incertitudes . . . 84
4.2.2 Efficiency metric . . . 84
4.2.3 Potential discontinuous behavior . . . 84
4.3 Formulation of the optimization problem . . . 88
4.4 Optimization algorithm . . . 89
4.4.1 Design of experiments . . . 89
4.4.2 Clustering . . . 90
4.4.3 Support vector machine . . . 90
4.4.4 Kriging meta-model . . . 91
4.4.5 Computation of the expected value using two Kriging . . . 92
4.4.6 Adaptive sampling . . . 93
4.4.7 Algorithm . . . 94
4.5 Results . . . 95
4.5.1 Optimization problem considering unforced systems . . . 96
4.5.2 Optimization problem considering forced systems . . . 100
4.6 Conclusions of the chapter . . . 102

5 Experiments using a programmable electroacoustic loudspeaker **105**
5.1 Introduction to the experimental study . . . 105
5.2 Experimental setup . . . 106
5.2.1 Acoustical mode of the tube . . . 107
5.2.2 Loudspeaker and global system . . . 109
5.3 Digital programming . . . 109
5.3.1 Model-inversion . . . 109
5.3.2 Parameters identification . . . 110
5.3.3 Nonlinear targeted dynamics . . . 111
5.4 Experimental results . . . 113
5.5 Conclusions of the chapter . . . 115

6 Conclusion and perspectives **117**
6.1 Results . . . 117
6.2 Perspectives . . . 119
6.2.1 Perspectives for analytical approaches . . . 119
6.2.2 Perspectives for optimization study . . . 119
6.2.3 Perspectives for experimental study . . . 119

Bibliography **121**

A Time averaging **135**

B Space averaging **137**

C Time averaging II **139**

Introduction

In addition to the many benefits arising from noise and vibrations, such as energy harvesting, structural health monitoring, and medical device applications, there is a need to design their effects for reducing large oscillations and induce specific responses in mechanical and structural systems. Solutions include strategies such as coupling absorbers to the primary system or designing materials with tailored behaviors for attenuating oscillations and controlling vibration behaviors. This PhD research aims to localize vibro-acoustic energies in coupled nonlinear mass-in-mass meta-cells and develop design tools for achieving desired dynamic behaviors in both individual meta-cells and chains of these units. This involves analytical and numerical developments, along with optimization studies to fine-tune parameters for designing such systems. The thesis is globally structured as follows:

Chapter 1 provides an overall review of control systems, with emphasis on passive control systems, and different types of metamaterials. Additionally, it presents the general methodology employed in this manuscript to design systems for vibration control.

Chapter 2 delves into the dynamics of a single nonlinear mass-in-mass meta-cell, consisting of an outer mass that houses an inner mass with a piecewise restoring force term that is globally non-smooth. This term exhibits pure cubic behavior in a given clearance and then linear terms elsewhere, constituting a new type of nonlinearity for such mass-in-mass cells. The complexified form of system equations is treated by the multiple scales method to find its fast and slow dynamics, leading to the determination of the slow invariant manifold and the system's singular and equilibrium points. The considered system can be employed for the control process of the outer mass, acting as a nonlinear energy sink (NES) with piecewise nonlinearity, or be regarded as a single meta-cell with spacial characteristics in a chain of nonlinear mass-in-mass meta-cells.

Chapter 3 presents the study of a chain of coupled meta-cells introduced in Chapter 2. Initially, the discrete system is outlined, followed by the transition to the continuous domain. The modal characteristics of the continuous system are evaluated and the system is studied in the vicinity of one of its arbitrary modes. Employing the multiple time scale method, the complexified system equations are analysed to unveil both fast and slow dynamics. Ultimately, the dynamic responses of the original system are compared with those obtained from analytical predictions of the projected system.

Chapter 4 employs a stochastic optimization algorithm to design the mass-in-mass meta-cell, which was previously studied in Chapter 2. This stochastic approach becomes necessary because nonlinear systems, such the studied one, are highly sensitive to perturbations in design parameters and also to initial conditions, resulting in behavior that is almost discontinuous, and even minor alterations in these factors can trigger a transition from a state of "high" to "low" efficiency. The efficiency of the meta-cell with the nonlinearity considered in Chapter 2 after optimization is compared to that with an optimized pure cubic nonlinearity, as well as to that of a single degree-of-freedom oscillator.

Chapter 5 presents possibilities for mechanically designing the nonlinearity explored in this thesis and the study of a programmable electroacoustic loudspeaker. A model-inversion technique is introduced for digitally programming the impedance of the loudspeaker to achieve a desired nonlinear behavior. A Duffing-type nonlinearity is implemented, and the electroacoustic loudspeaker

is coupled to an acoustical mode of a closed tube. This study demonstrates the feasibility of programming the behavior of an electroacoustic loudspeaker.

Finally, **Chapter 6** provides the conclusions of the thesis accompanied by the perspectives for future research.

CHAPTER 1

Literature review and global methodology

This chapter provides an overall review of control systems, with emphasis on passive control systems, and different types of metamaterials. Additionally, it presents the global methodology employed in this manuscript to design systems for vibration control.

1.1 Vibration control

Structures are subjected to time-dependent forces that can generate significant vibration amplitudes. Design tools are essential to ensure these systems exhibit desirable behavior throughout their operational lifespan, thus ensuring the comfort and safety of the users. One of the most critical factors in designing these structures is controlling the vibrations, which can be achieved by adjusting various aspects of the system, such as its stiffness, weight, damping, or shape, or by using active or passive counterforces [Housner et al., 1997]. This section introduces different types of control systems.

Passive control The passive control process involves localizing the energy within specific structural components or transforming it to be absorbed by coupled oscillators [Mead, 1998]. This control system does not require any external power source for its activation. In this case, the control forces depend on the response of the primary structure.

Active control Active control systems comprise sensors and actuators that can change how the primary structure responds to external forces. These systems require external sources to power control actuators, which apply forces to the structure in prescribed manners. These forces can either add or dissipate energy from the structural system. In active feedback control systems, the actuators receive signals which are functions of the primary structure's response detected by physical sensors [Housner et al., 1997, Chu et al., 2005].

Hybrid control The hybrid control system exploits the combined properties of active and passive control systems [Chu et al., 2005]. For instance, the vibration control of cables can be achieved by combining a distributed passive solution using shape-wrapped memory alloy wires with an open-loop actuator [Faravelli et al., 2009].

Semi-active control Semi-active control systems belong to the category of active vibration control systems. These systems require less external energy than standard active control systems to change system parameters, such as damping and stiffness [Liu et al., 2005a, Liu et al., 2008].

Semi-passive control Semi-passive systems belong to a category of passive vibration control systems, showcasing adaptability properties of certain multi-physics materials and systems, generally electromechanical ones, such as shunted piezoelectric ceramics, which serve as sensors and actuators in structural vibration control systems, establishing a robust connection between

mechanical and electrical fields [Moheimani and Fleming, 2006]. The adaptability properties of these systems provide useful tools for control, where the electromechanical parameters are modified according to the vibratory behavior of the primary structure. Furthermore, these systems require a minimal amount of energy to adapt their properties in response to the vibrations [Guyomar and Badel, 2006, Guyomar et al., 2007].

1.2 Passive control solutions

This section reviews passive control systems, with particular emphasis on a specific system known as nonlinear energy sink (NES).

1.2.1 Tuned mass damper

The vibration characteristics of many structures can be studied considering a linear oscillator with a single degree-of-freedom (dof). A way to prevent the resonance phenomenon, where the undamped system's response becomes infinite due to the forcing frequency being equal to the natural frequency, is to attach a mass-spring unit to the primary structure with a restoring forcing function such as $f(\alpha) = \lambda\alpha$. Through a proper design, the frequency of the unit can be tuned to match that of the primary system, effectively reducing the motion of the structure to zero. In this case, the original system changes from 1-dof to 2-dof, resulting in the emergence of two new natural frequencies. However, the response of the 2-dof system is infinite at the new frequencies. If a finite amount of damping is introduced into the system, it will no longer exhibit infinite responses at resonance and zero motion at the frequency of the original system.
The viscous spring-mass unit used to reduce the motions of a vibrating primary structure, when attached to it, is known as Tuned Mass Damper (TMD). Frahm [Frahm, 1909] first discussed this concept with an undamped oscillator. Then, damping was added to improve the robustness of the control in [Ormondroyd and Den Hartog, 1928]. In order to enhance the efficiency of the TMD in vibration control, Den Hartog proposed in [Den Hartog, 1934] a method for tuning the absorber's parameters. In [Brock, 1946], the study was completed using a perturbation method to obtain the optimal damping ratio. The exact analytic expressions can be found in [Asami and Nishihara, 2003].
Such linear devices are very efficient around the tuned frequency. However, they lose their efficiencies elsewhere. That is why this type of absorber is not suitable when the frequency of the exciting force varies over a range of frequencies. This limitation can be overcome by exploiting the nonlinear capacities of coupled oscillators [Roberson, 1952].

1.2.2 Nonlinear absorbers

Roberson first quantified the effectiveness of a nonlinear absorber in [Roberson, 1952], where the concept of "suppression bandwidth" was introduced and a cubic part was added to the linear restoring forcing function of the vibration absorber, showing that the range of operational frequency increases with respect to the linear absorber. The considered system is depicted in Fig. 1.1, where $F(\alpha) = \lambda\alpha \pm \nu\alpha^3$ stands for the scaled nonlinear cubic restoring forcing function of the absorber. The algebraic sign of the cubic part of the function F can have a positive or negative algebraic sign, indicating a hard or soft stiffness, respectively.
This work was followed by [Pipes, 1953], where a nonlinear spring with hyperbolic sine characteristics was considered, [Arnold, 1955] with a Duffing type absorber whose behavior was described by dimensionless response diagrams, and [Henry and Tobias, 1959, Henry and Tobias, 1961], where it was considered a general model of 2-dof nonlinear oscillators focusing on exploiting

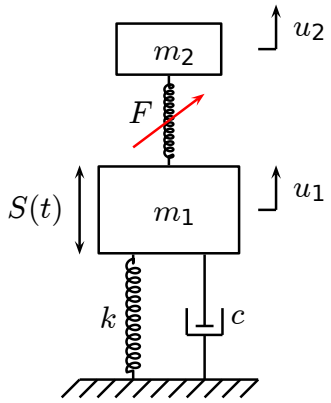

Figure 1.1: Model of primary oscillator (mass m_1, stiffness k, damping c) equipped with nonlinear oscillator (mass m_2, nonlinear coupling force F), u_1 and u_2 being the two dofs, see [Roberson, 1952].

nonlinear characteristics of coupled oscillators.
Different types of nonlinear passive absorbers have been developed since then: pendulum type [Sevin, 1961, Struble and J. H. Heinbockel, 1963], auto-parametric [Haxton and A. D. S. Barr, 1972], magnetic field-based dampers [Yamakawa et al., 1977, Kojima and Saito, 1983], softening controllers via arrays of Belleville washers mounted back to back [Hunt and Nissen, 1982, Nissen et al., 1985], bow-type or shallow arch spring [Rice and McCraith, 1987], impact dampers [Ema and Marui, 1996, Ema and Marui, 2000], and the focus of this section: nonlinear energy sinks [Gendelman et al., 2001, Vakakis and Gendelman, 2001, Vakakis, 2001].

Nonlinear Energy Sink The term "nonlinear energy sink" (NES) was used for the first time in [Gendelman et al., 2001, Vakakis and Gendelman, 2001]. The principle is based on coupling an essentially nonlinear oscillator (the NES) to a primary oscillator. In such systems, it is possible to induce an irreversible transfer of vibrational energy from the primary oscillator to the nonlinear one. This phenomenon is known as energy pumping or targeted energy transfer (TET). It was studied in [Gendelman et al., 2001, Vakakis and Gendelman, 2001] using two analytical techniques: the first one is based on the perturbation analysis of the system dynamics in the neighborhood of the 1:1 resonance, while the second one uses the assumption of 1:1 internal resonance in the fast dynamics, complexification and averaging of the equations of motion. From that, it was shown that the energy pumping is due to resonance capture in the 1:1 resonance manifold of the system.
In these first studies on energy pumping, the masses of the oscillators have been assumed equal, representing an obstacle for real applications. Gendelman [Gendelman et al., 2005] studied the dynamics of a linear oscillator coupled to a NES of substantially lower mass and demonstrated that efficient energy pumping might be obtained for a system with mass asymmetry.
The high performance of NES in controlling broad bands is due to its ability to oscillate at any frequency when designed accordingly, which permits it to potentially enter into resonance with any system. Meanwhile, different types of systems have been studied for control process based on NES technology, including nonlinear systems, such as piecewise linear [Lamarque et al., 2012] and Bouc-Wen type systems [Lamarque et al., 2013], primary linear structures with multiple dofs [Vakakis et al., 2003, Vakakis et al., 2004], chains of semi-infinite [Manevitch et al., 2003] and infinite linear oscillators [Rothos and Vakakis, 2009], and continuous systems such as thin plates [Georgiades and Vakakis, 2009] and elastic strings [Luongo and Zulli, 2015].

It was demonstrated that a system with NES can exhibit quasi-periodic rather than periodic response in the vicinity of a main (1:1) resonance [Gendelman et al., 2006, Gendelman and Starosvetsky, 2007]. In [Gendelman and Starosvetsky, 2007], it was shown that the combination of essential nonlinearity and strong mass asymmetry in periodically forced systems gives rise to another possibility of quasi-periodic response. This regime, referred to as a strongly modulated response (SMR), is generated by repeated bifurcations of the system around an unstable branch of an invariant manifold, and it was studied in detail in the articles [Starosvetsky and Gendelman, 2008, Gendelman, 2008].
NESs have been applied in many domains, such as in mechanics and acoustics. For instance, Lee et al. [Lee et al., 2007] studied the control of aeroelastic instabilities of a 2-dof rigid wing model by a NES. A similar problem was treated in [Luongo and Zulli, 2014] thanks to a method mixing multiple scale and harmonic balance methods. Leroux et al. [Leroux et al., 2023] investigated the control of a beam with elastic boundary conditions under galloping instabilities via multiple scale method. The application of NES to noise control was explored in [Cochelin et al., 2006a, Bellet et al., 2010]. Both studies tested the use of a thin viscoelastic membrane as a NES and examined the energy transfer from an acoustic system to the membrane. Roncen et al. [Roncen et al., 2023] recently investigated a pneumatic NES called AirNES. This system uses a circular membrane to delimit two air chambers connected via a pipeline, where the membrane provides the nonlinear elastic force, while the flow of air at high velocity within the channel creates nonlinear damping.

Examples of non-cubic NES The NES in its early developments was composed of a pure cubic restoring forcing function, which induces relatively simple analytical development and whose feasibility is quite easy. The first works relating to non-cubic NES are listed in [Gendelman, 2004], where the case of any polynomial nonlinearity is treated analytically. The analysis methods of targeted energy transfer in 2-dof oscillators were extended for the case of the NES with non-polynomial potentials in [Gendelman, 2008]. Two types of NES were considered as examples: with softening and piecewise-linear restoring forcing terms. In [Georgiadis et al., 2005], the energy pumping capacities of systems with non-smooth nonlinearities were demonstrated. The NES studied in this reference presented a piecewise-linear restoring force, which can easily be implemented as it requires conventional linear springs. The analysis of piecewise nonlinear NES was further developed in [Lamarque et al., 2011].
Vibro-impact NES (VI NES) involves sharp changes in the slope of restoring forces, corresponding to inelastic impacts through which energy is dissipated. Seismic-induced vibration control using VI NESs was studied in [Nucera et al., 2007], where a 2-dof linear system was considered the primary structure. In [Gendelman, 2012], the invariant manifold approach was extended to describe the transient responses in systems with VI NESs. In [Gourc et al., 2015], the dynamic response of a harmonically forced system with a VI NES was investigated theoretically and experimentally. In [Gendelman and Alloni, 2015], it was shown that in addition to the dynamic behaviors similar to those of forced systems with other types of NES, a primary linear system with VI NES also exhibits chaotic strongly modulated response (CSMR). This is due to the special structure of the slow invariant manifold (SIM), which presents only one stable and one unstable branches.
The bistable NES (BNES), characterized by a negative linear stiffnesses and a nonlinear (cubic) stiffness, are introduced in [Manevitch et al., 2014, Romeo et al., 2015]. In [Mattei et al., 2016a], it is shown that beyond a certain load level, bistability leads to quasi-periodic or chaotic oscillations, enabling a more effective reduction of energy in the primary system. Additionally, [Bergeot and Berger, 2023] indicates that a BNES can be more efficient than a NES with cubic stiffness.
It should be mentioned other atypical types of NES, such as the one in [Ture Savadkoohi et al., 2016a] that combines geometric (cubic potential) and material (hysteresis behavior of Bouc-Wen type) nonlinearities, the "rotational NES" designed as a rotating

eccentric mass [Gendelman et al., 2012], and the NES consisting of a buckled thin beam with a small mass at its center and, thus, presenting two equilibrium positions [Mattei et al., 2016b].
This section provided a brief overview of different absorbers. In the next section, we explore the concept of metamaterials, which may be based on unit cells or particles composed of previously discussed devices: linear (e.g. TMD) or nonlinear (e.g. NES) absorbers.

1.3 Metamaterials

In nature, the physical properties of conventional materials, so-called right-handed, depend on their compositions and are always positive. Whereas metamaterials, namely manufactured structures composed of micro-scale unit cells arranged randomly or periodically, exhibit unusual properties at the macro scale due to the particular arrangement and design of their constituents. The physical properties of metamaterials are described by effective parameters, which can be positive, negative, near-zero, or approaching-infinity, as shown in Fig. 1.2 [Lee et al., 2017] for acoustic metamaterials classified according to the sign of mass density and bulk modulus.

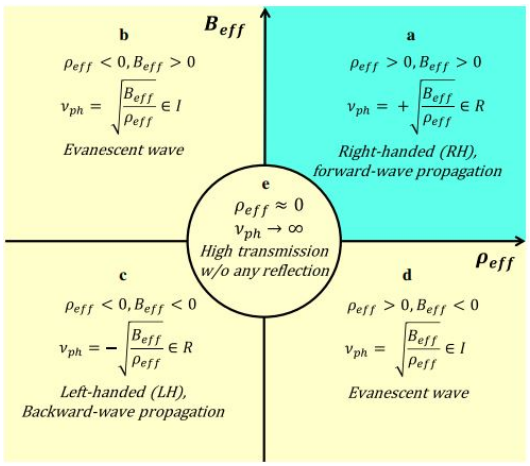

Figure 1.2: Effective mass density ρ_{eff} and bulk modulus B_{eff} diagram for acoustic metamaterials [Lee et al., 2017]. v_{ph} denotes the phase velocity. R and I indicate purely real and imaginary parts of phase velocity, respectively. Normal materials in nature belong to **(a)** with double positive parameters. Metamaterials can be classified as negative mass density **b**, double negative parameters **(c)**, negative bulk modulus **(d)** and near-zero mass density **(e)**.

Various types of metamaterials with applications in different fields can be found in the literature. This section aims to provide an overview of the developments and applications of metamaterials. To this end, we will explore electromagnetic, acoustic, mechanical, and nonlinear metamaterials in the following text. Linear and nonlinear mass-in-mass metamaterials are particularly significant to this study and will be discussed separately.

1.3.1 Electromagnetic metamaterials

The concept of metamaterials was probably first introduced in 1968 by Veselago in [Veselago, 1968], where it was theoretically shown that possible materials with negative electric permittivity and negative magnetic permeability could be combined to produce a left-handed material, in which electromagnetic waves propagate with group and phase velocities that are antiparallel, namely a phenomenon associated with a negative index of refraction. However, it was

only three decades later that this type of metamaterial was validated experimentally, having a range of frequencies over which the refractive index was negative for one direction of propagation [Smith et al., 2000].
In [Shelby et al., 2001], it was introduced a 2D metamaterial with an isotropic, negative refractive index, using split-ring resonators and wire elements to create negative magnetic permeability [Pendry et al., 1999] and negative electric permittivity [Pendry et al., 1996], respectively.
The concept of negative refractive index was used to propose a perfect lens in [Pendry, 2000], bringing light to a focus in the microwave band without the constraints imposed by wavelength. In Fig. 1.3, the light diverging from a point source is bent to a negative angle in the negative refractive index medium before reaching a focus for a second time when released from the medium. Further, Pendry et al. [Pendry et al., 2006] also conceived the invisibility cloaking capability of metamaterials by redirecting electromagnetic fields.

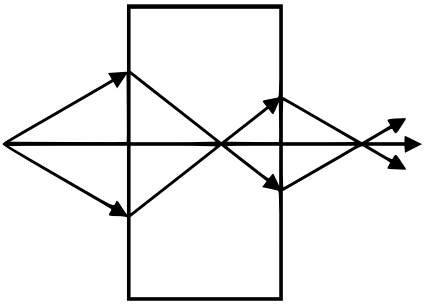

Figure 1.3: Refraction of light trough a negative refractive index medium [Pendry, 2000].

In [Magnus et al., 2008], contrary to ordinary magnetic metamaterials based on resonant elements, it was presented the first experimental study of a non-resonant metamaterial based on an array of superconducting plates designed to operate at zero frequency.
Electromagnetic metamaterials can have applications in different areas, from communication to human health. In [Boyvat and Hafner, 2012], a metamaterial was designed to shape the magnetic field's flow, and it was demonstrated that the shielding performance might be improved by designing anisotropic, inhomogeneous metamaterials. A practical design of metamaterial-enhanced magnetic induction was proposed in [Guo et al., 2017] using a spherical coil array, and it was found that this metamaterial can significantly extend the wireless communication range. In [Ali et al., 2017], a hybridized magnetic metamaterial hat was developed to enhance the uniformity of radio frequency rotational symmetry around its axis and, thus, to improve the signal-to-noise ratio for rat brain imaging. A potential application for this metamaterial could be to enhance the resolution of magnetic resonance imaging for the human brain.
As we can see, electromagnetic metamaterials can have numerous applications and an important role in the quality of human lives. Besides that, they compose the first class of metamaterials, paving the way for the development of other types.

1.3.2 Acoustic metamaterials

The mathematical analogy between acoustic and electromagnetic waves inspired the development of acoustic metamaterials. To this end, researchers have used microstructures to achieve the negative effective mass [Liu et al., 2005b], and it was found that if the acoustic metamaterial is treated as an equivalent elastic solid, then its effective mass density would be frequency-dependent and become negative in certain frequency ranges, namely band gaps [Brillouin, 1946]. A system with negative effective mass was experimentally studied in [Yao et al., 2008], and low transmissions were observed in the negative mass range, as predicted by the theory.

Hu et al. [Hu et al., 2017] investigated a modified acoustic metamaterial with local resonators (inner masses) connected by linear springs. It was demonstrated that this system could present three band gaps, whereas the conventional metamaterial (a mass-in-mass array) presented only one band gap.
In [Fang et al., 2006a], it was reported a class of ultrasonic metamaterials consisting of an array of subwavelength Helmholtz resonators with designed acoustic inductance and capacitance. It was shown that these materials present an effective dynamic modulus with negative values near the resonance frequency. The analogy between a Helmholtz resonator and an inductor-capacitor circuit is represented in Fig. 1.4.

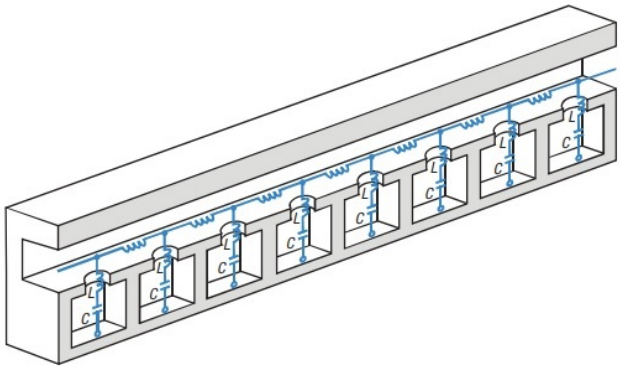

Figure 1.4: Array of subwavelength Helmholtz resonators with designed acoustic inductance and capacitance [Fang et al., 2006b].

An acoustic metamaterial with local resonators was studied in [Huang and Sun, 2011], and it was shown that it can exhibit an unusual frequency-dependent effective stiffness, which becomes negative for waves with frequencies in the band gap. Wave propagation in the metamaterial was numerically simulated when it was placed between two elastic environments: when the spectrum of the sent wave packet was out of the band gap, it propagated through the metamaterial, whereas a large portion of the wave packet was reflected by the metamaterial when the wave spectrum covered the band gap.
Jing et al. [Jing et al., 2012] considered a 2D membrane-based acoustic metamaterial with a near-zero refractive index. The effective density near zero around the membrane resonance frequency resulted in its near-zero refractive index. It was demonstrated that, around the resonance frequency, only waves of normal incidence could penetrate through the metamaterial, while the rest were reflected. Thus, the proposed metamaterial acts as an angular filter.
In [Zhu et al., 2013], a dispersive acoustic metamaterial with graded refractive was experimentally demonstrated for the first time. From dispersion and wave velocity control by designed gradient subwavelength structures, this metamaterial traps broadband acoustic waves and spatially separates different frequency components, which is called the acoustic rainbow trapping effect.
It is important to mention that the adaptation of organisms led to the development of efficient materials and structures, serving as inspiration for the development of bio-inspired metamaterials [Bosia et al., 2022]. For instance, [Huang et al., 2021] uses this concept to create a lightweight membrane inspired by a spider web topology and presenting a significant sound attenuation. Acoustic metamaterials have also been proposed based on a mammalian cochlear prototype, which acts as a local resonant system with negative dynamic effective mass characteristics [Ma et al., 2014]. Furthermore, locally resonant metamaterials, composed of square and honeycomb-shaped unit cells, were designed and proved effective in sound wave absorption [Ebrahimi-Nejad and Kheybari, 2018].

1.3.3 Mechanical metamaterials

The field of mechanical metamaterials was initially focused on achieving unique mechanical properties such as a negative Poisson's ratio [Ren et al., 2018, Lakes, 1987]. However, recent advancements in the field of engineering and materials science have led to the development of new classes of metamaterials, including nonlinear ones [Bertoldi et al., 2017]. In this section, we discuss various types of mechanical metamaterials. However, a specific section is reserved for the nonlinear category.

Contrary to materials with positive Poisson's, the metamaterials presenting negative Poisson's ratio, also called auxetics, expand in the transverse direction when stretched or contract when compressed [Ren et al., 2018]. Research into auxetics began in the late 1980s when Lakes first presented an auxetic polyurethane foam [Lakes, 1987]. Since then, plenty of auxetic materials have been fabricated, such as a microporous form of ultra-high molecular weight polyethylene [Alderson and Evans, 1992] and expanded microporous polytetrafluoroethylene [Caddock and Evans, 1989]. One of the most popular applications is auxetic textile structures, once they can present enhanced drapeability and energy absorption [Alderson et al., 2012].

In [Nicolaou and Motter, 2012], it was explored concepts to design metamaterials exhibiting negative compressibility transitions, during which a material contracts when tensioned (or expands when compressed), contrary to ordinary materials behavior. This type of metamaterial could be useful for the design of actuators, force amplifiers, micromechanical controls, and protective devices.

Another characteristic of ordinary materials is the loss of mechanical performance as density decreases. In [Zheng et al., 2014], it was presented a class of ultralight metamaterials that exhibits high stiffness properties with a nearly linear scaling relationship between Young's modulus and density, regardless of the constituent material. This performance derives from a network of nearly isotropic microscale unit cells with high structural connectivity and nanoscale features.

Mechanical metamaterials with vanishing shear modulus, also called pentamodes, avoid the coupling of compression and shear waves by making the bulk modulus much larger than the shear modulus, similar to isotropic fluids. Such metamaterials were first studied by Milton and Cherkaev in 1995 [Milton and Cherkaev, 1995], but their feasibility was demonstrated only in 2012 by Kadik et al. [Kadic et al., 2012]. An exciting application was presented in [Buckmann et al., 2014], where an elasto-mechanical unfeelability cloak made of pentamode metamaterials was designed and fabricated.

Unlike most solids that expand when heated, the ones exhibiting negative thermal expansions contract upon heating [Takenaka, 2012]. In [Wang et al., 2016], it was experimentally studied composite lattices with tunable negative thermal expansion in three directions and over a large temperature range. This is induced by the interaction of components with distinct thermal expansion coefficients.

Chen et al. [Chen et al., 2016] designed an adaptive gradient-index metamaterial for flexural wave sensing, fabricated by bonding a periodic array of shunted negative capacitance piezoelectric patches to an aluminum beam. It was demonstrated that the proposed system could overcome the detection limit of flexural wave signals by amplifying its broadband by more than two orders of magnitude.

In [Zhong et al., 2018], a metamaterial I-girder was designed by integrating a mass-spring-damper subsystem to act as a multifrequency vibration absorber. The results showed that the metamaterial I-girder could absorb elastic waves caused by traffic loads and earthquakes on composite cable-stayed bridges.

The following section delves into a different type of mechanical metamaterials known as nonlinear metamaterials.

1.3.4 Nonlinear metamaterials

Gao et al. [Gao et al., 2018] presented a nonlinear metamaterial model with an effective negative mass. Each element was composed of a shell with a nonlinear spring-mass attached on both sides, and the elements were connected by linear springs. It was numerically proved that the structure including the nonlinearity broadens wave attenuation frequency regions compared with the corresponding linear counterparts.
In [Khajehtourian and Hussein, 2014], wave propagation in a 1D narrow bar with alternating spring-mass resonators was investigated. Deformation in the bar was large and elastic, leading to the model being nonlinear, and local resonator dynamics evaluated the system behavior. They approximated a dispersion relation for this model and predicted the bandwidth parameters analytically. Then the effect of nonlinearity on the band gap parameters was studied.
Medina et al. [Medina et al., 2020] explored the complex energy landscape of a flexible and porous metamaterial characterized by multiple bifurcations. The bifurcation diagrams were used to design a metamaterial whose responses can be reprogrammed, moving it from one stable branch to another. Furthermore, it was shown that targeted imperfections can be used to enhance such programmability.
Geometric nonlinearities can be introduced in a system by exploiting mechanical instabilities, such as elastic buckling. Bertoldi et al. [Bertoldi et al., 2010] explored these instabilities in a square lattice of circular holes in an elastomeric matrix. It was shown that the pattern transformation (see Fig. 1.5) leads to unidirectional negative Poisson's ratio behavior when the system is under compression.
Babaee et al. [Babaee et al., 2013] exploited buckling to design a new class of 3D auxetic materials consisting of an array of patterned elastomeric spherical shells. When subjected to deformation, the proposed system undergoes a substantial isotropic volume reduction. More recently, a numerical and experimental study was presented on the isolation performance of two metamaterials: a classic auxetic and an enhanced one with resonant inclusions [Pyskir et al., 2021]. As a result, the resonant design exhibits a huge improvement in the bandgaps.

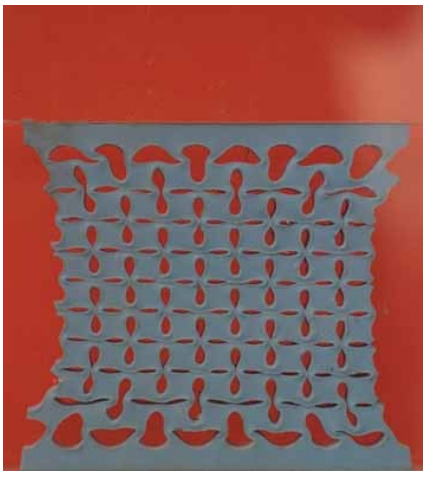

Figure 1.5: Square lattice of circular holes in an elastomeric matrix subjected to uniaxial compression [Bertoldi et al., 2010].

In [Florijn et al., 2014], a metamaterial was introduced whose response to uniaxial compression could be programmed by lateral confinement. The proposed metamaterial was composed of a quasi-2D elastic slab of material patterned by a regular array of large and small holes and, depending on the amplitude of the lateral confinement, the pattern switch was either smooth or discontinuous and; thus, the force-displacement curves could be tuned.

A tunable and switchable acoustic metamaterials class was introduced in [Wang et al., 2014]. The studied system was composed of resonating units dispersed into an elastic matrix and connected to it through elastic beams, whose buckling was exploited to control the propagation of elastic waves. Since the stiffness of the beams varies significantly under external load, the resonant frequency of the units changes, providing a wide range of tunability for the band gap.
Another class of flexible mechanical metamaterials is the one based on origami, i.e., the ancient art of folding paper. Two folded metamaterials based on the Miura-ori fold pattern [Miura, 1993] are described in [Schenk and Guest, 2013]. First, a folded shell structure is introduced, where the fold pattern provides a negative Poisson's ratio for in-plane deformations and a positive ratio for out-of-plane bending. Second, a 3D cellular metamaterial that can fold and unfold uniformly is obtained by stacking individual folded layers, as the one presented in Fig. 1.6.

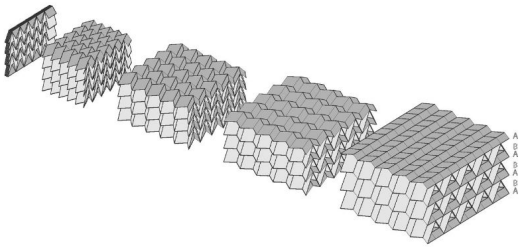

Figure 1.6: 3D cellular metamaterial designed by stacking folded layers. [Schenk and Guest, 2013].

Another method of assembling origami was presented in [Filipov et al., 2015], which consists in coupling rigidly foldable origami tubes in a way that substantially increases the system stiffness and enables the deployment through only one flexible deformation mode. Origami-based mechanical metamaterials present a potential simplicity of manufacture. They can be useful in impact absorption as well as deployable structures, with applications ranging from automotive safety (e.g., airbags [Lang, 2009]) to space exploration (e.g., a foldable telescope lens [Gardner et al., 2006]).
The manuscript focuses on a specific class of nonlinear metamaterials, namely nonlinear mass-in-mass metamaterials, which is discussed in a separate section. But first, we explore the linear mass-in-mass metamaterials.

1.3.5 Linear mass-in-mass systems

A mass-in-mass unit can be represented by a single mass with an effective mass (see Fig. 1.7), defined to have the equivalent dynamic behavior of the outer mass m_1 and must be frequency dependent. In [Huang et al., 2009], wave propagation was studied in a 1D lattice of linear mass-in-mass units to understand the physical meaning of negative effective mass and the corresponding band gaps. According to Newton's second law of motion, acceleration would be in the opposite direction to the applied force if the mass becomes negative. In other words, negative effective mass yields spatial decay of wave amplitude. These effects have been seen to occur close to the local resonance frequency. Furthermore, it was also discussed the continuum representation of the mass-in-mass system using the classical elastic solid and the multi-displacement continuum model.
In [Huang and Sun, 2010], it was studied a mass-in-mass lattice system where each cell consists of three separate masses connected by linear springs. It was demonstrated the existence of several band gaps that can be shifted by changing the resonance frequencies of the resonators.
The wave attenuation in the band gap of a mass-in-mass chain was studied from the energy transfer point of view in [Huang and Sun, 2009]. It was found that most of the work done by the external force on the system is stored by the internal mass when the forcing frequency is close to the local resonance frequency. However, the energy is temporarily stored in the internal mass since it is taken

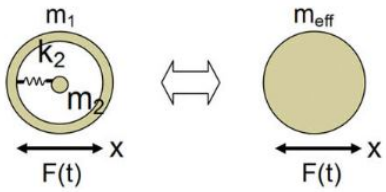

Figure 1.7: A mass-in-mass unit and its effective mass model [Huang et al., 2009].

out by the external force in the form of negative work in a cyclic manner.
The efficiency of such systems has also been validated experimentally. In [Yao et al., 2008], the negative effective mass of a mass-in-mass system was proved, and low transmission of elastic waves in the band gap was observed. In [Mikoshiba et al., 2013], it was studied a 1D array of unit cells with internal resonators that also act as generators and verified experimentally the existence of the band gap close to the local resonance frequency. In [Manimala et al., 2014], the notion of negative effective mass was illustrated by studying a mass-in-mass structure built using coil springs and a steel mass encased in a polycarbonate shell. In Fig. 1.8, we can see the mass-in-mass system and the experimental and theoretical effective masses plotted with respect to the excitation frequency.

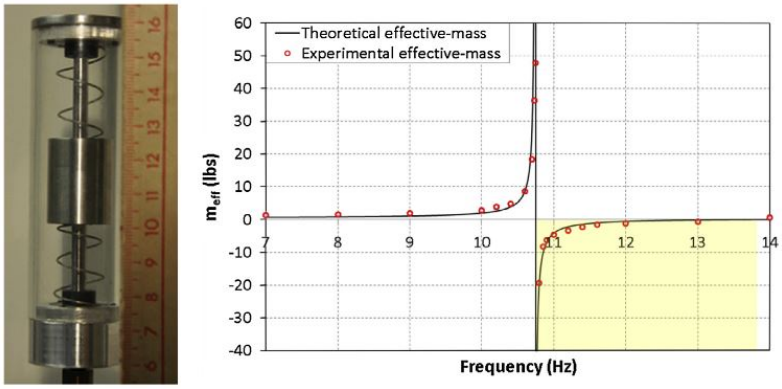

Figure 1.8: Mass-in-mass unit and comparison of theoretical and experimental effective mass [Manimala et al., 2014].

As one application, Zhou et al. [Zhou et al., 2023] proposed to modify conventional underground basements to protect high-rise buildings during earthquake excitations. This was proposed based on the concept of a floating floor structure, in which the floor is isolated from the supporting beam. Thus, the basement was modified to form a locally resonant meta-basement, as shown in Fig. 1.9, that can be treated as a mass-in-mass system. Finally, the results show that the proposed meta-basement can reduce high-rise buildings' seismic responses.
In order to enhance the effectiveness of systems that locate vibratory energies, nonlinearities have been incorporated. The following section delves into the topic of nonlinear mass-in-mass systems.

1.3.6 Nonlinear mass-in-mass systems

The energy exchange between different modes of a system, a mechanism known as inter-modal tunneling and studied in [Kopidakis et al., 2001, Aubry et al., 2001], was investigated in a 1D mass-in-mass chain by Lazarov and Jensen [Lazarov and Jensen, 2007]. In this study, the band gaps were investigated in the system with linear and nonlinear oscillators: for the first one, the gap was lo-

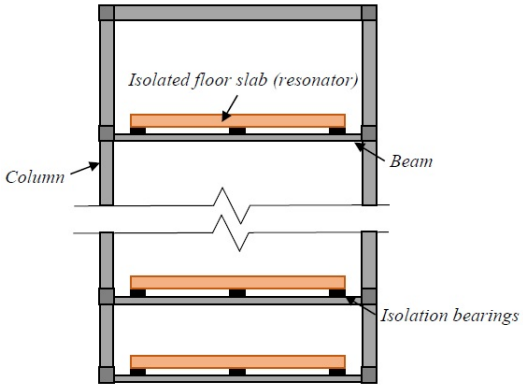

Figure 1.9: Meta-basement system [Zhou et al., 2023].

cated in the resonant frequency of the oscillator; for the chain with Duffing type nonlinearity, it was shown that the position of the band gap could be shifted by changing the degree of nonlinearity or the wave amplitude.
In [Cveticanin and Zukovic, 2017], the dynamics of a mass-in-mass unit with Duffing type nonlinearity was analytically and numerically studied. The effective mass ratio was introduced, showing that the frequencies corresponding to the negative effective mass ratio were located in the band gap. Nevertheless, the amplitude of motion differs slightly from zero. Finally, it was concluded that the nonlinear mass-in-mass unit presents a wider frequency gap than the linear one.
Besides the inter-modal energy tunneling, another energy transfer mechanism was studied theoretically and numerically in [Silva et al., 2019]. This mechanism arises due to a nonlinear interaction between propagating and evanescent waves triggered by auto-parametric resonance, manifesting itself through the appearance of a subharmonic transmission attenuation zone.
In [Zega et al., 2020], the existence of the subharmonic attenuation zone was experimentally proved by designing a mass-in-mass unit cell with a predominantly quadratic nonlinear coupling term. The experimental set-up used in this study is shown in Fig. 1.10.

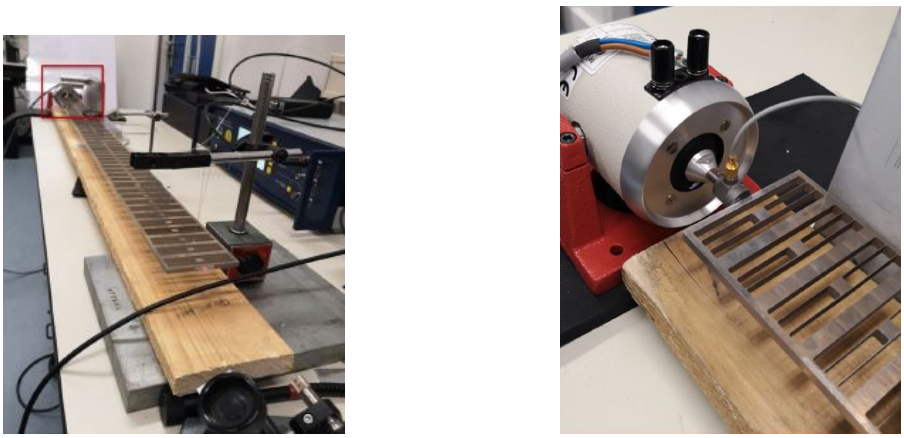

(a) (b)

Figure 1.10: Experimental set-up used in [Zega et al., 2020]: (a) Overview; b) Close-up view of the structure attached to the shaker.

1.4 Global methodology

Suppose we aim to create a new (meta)system or a system with controlled behavior. In this case, the global methodology employed in this manuscript is as follows: First, we develop a system model and then we exploit nonlinearities whose parameters should be designed. For instance, we may utilize a cubic nonlinearity, defined as $F(\alpha) = k\alpha^3$, with k as the design parameter. Subsequently, the system model is reduced, and the nonlinear dynamics tools are used to clarify its different dynamical characteristics. This step can be followed by an optimization procedure, which involves imposing specific metrics and fine-tuning the nonlinearity to achieve desired outcomes. The procedure is followed by numerical and/or experimental verifications for validating the designed nonlinearity. Finally, the result is a refined system with significantly improved behavior or a new system with designed behaviors. A schematic representation of the employed methodology is depicted in Fig. 1.11.

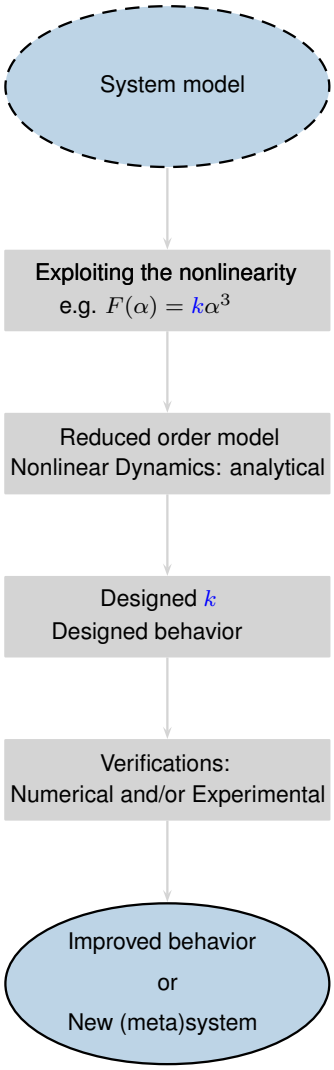

Figure 1.11: Global methodology for designing (meta)systems.

1.5 Conclusions of the chapter

This introductory chapter presents a literature review focusing mainly on technological solutions for controlling structural vibrations. One of the systems under investigation is the nonlinear passive vibration absorber known as NES, which has been extensively studied and found to be versatile in its applications. It is also explored the concept and various forms of metamaterials, which can be composed of unit cells or particles containing vibration absorbers, such as the ones discussed in the first part of the chapter. Additionally, it is provided a comprehensive overview of the general methodology used in this manuscript to design new systems.
The main objective of this thesis is to qualitatively grasp the behavior of coupled nonlinear mass-in-mass cells, arranged in the form of a chain, around one of its arbitrary modes. To better understand the unconventional nonlinearity exploited in this thesis, the next chapter investigates the energy exchanges between particles of a unit of the cell before extending the analysis to the chain of oscillators.

CHAPTER 2

Study of a nonlinear mass-in-mass meta-cell

In this chapter, the dynamics of a nonlinear mass-in-mass meta-cell, a two-degrees-of-freedom system, is investigated. The meta-cell comprises an outer mass that houses an inner mass with a piecewise restoring force term that is globally non-smooth, containing pure cubic behavior in a given clearance and then linear behavior elsewhere, constituting a new type of nonlinearity for such mass-in-mass cells. The complexified form of system equations is treated by the multiple time scale method to find its fast and slow dynamics, leading to the determination of the slow invariant manifold and the system's singular and equilibrium points. The outcomes of this chapter have already been communicated in [da Silveira Zanin et al., 2022].

2.1 The system and governing equations

The studied system is shown in Fig. 2.1. It consists of an outer rigid mass m_1 and an inner rigid mass m_2. The outer mass is grounded by a linear spring with constant stiffness k_1 and linear damping with a constant coefficient c_1. Both masses are coupled via a damping coefficient c_2 and a nonlinear restoring force $F(\alpha)$, where α represents the relative displacement of the two masses. Besides that, the primary system (m_1) is forced by an external sinusoidal excitation $S(t) = P\sin(\Omega t)$.

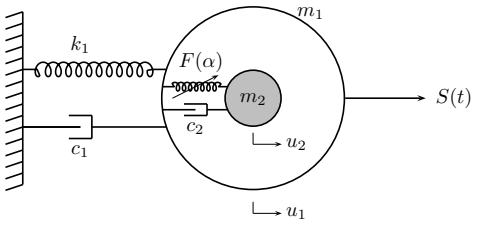

Figure 2.1: Model of the mass-in-mass meta-cell. The inner mass m_2 with nonlinear restoring force function $F(\alpha)$ is housed by the outer mass m_1.

Let u_1 and u_2 represent the generalized displacements of masses m_1 and m_2, respectively, as dependent variables, and let t be the independent time variable. The dynamic behavior in the time domain is governed by the following set of two equations:

$$\begin{cases} m_1 u_1'' + k_1 u_1 + c_1 u_1' + F(u_1 - u_2) + c_2(u_1' - u_2') = P\sin(\Omega t) \\ m_2 u_2'' + F(u_2 - u_1) + c_2(u_2' - u_1') = 0 \end{cases} \tag{2.1}$$

where $(.)'$ stands for the derivative of a variable with respect to t.
Let us suppose that $F(\alpha)$ is odd, reading as:

$$F(\alpha) = -F(-\alpha) = \begin{cases} k_{NL}\alpha^3 & \text{if} \quad -\delta \leq \alpha \leq \delta \\ k_L(\alpha - \delta) + k_{NL}\delta^3 & \text{if} \quad \alpha > \delta \\ k_L(\alpha + \delta) - k_{NL}\delta^3 & \text{if} \quad \alpha < -\delta \end{cases} \tag{2.2}$$

In details, the function $F(\alpha)$ is cubic in the clearance of 2δ and it becomes linear elsewhere. The schematic representation of $F(\alpha)$ is illustrated in Fig. 2.2.

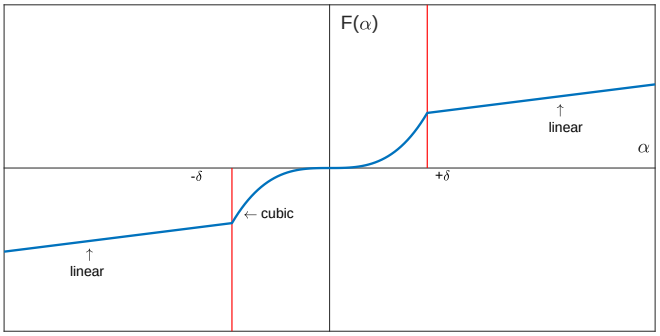

Figure 2.2: Schematic representation of the restoring force function $F(\alpha)$ (see Eq. (2.2)).

A dimensionless time τ is introduced as:

$$\tau = \omega t = \sqrt{\frac{k_1}{m_1}}t \tag{2.3}$$

The differential operator is redefined as follows:

$$\frac{\mathrm{d}.}{\mathrm{d}t} = \frac{\mathrm{d}.}{\mathrm{d}\tau}\frac{\mathrm{d}\tau}{\mathrm{d}t} = \sqrt{\frac{k_1}{m_1}}\frac{\mathrm{d}.}{\mathrm{d}\tau} \quad , \quad \frac{\mathrm{d}^2.}{\mathrm{d}t^2} = \frac{k_1}{m_1}\frac{\mathrm{d}^2.}{\mathrm{d}\tau^2} \tag{2.4}$$

After introduction of the dimensionless time τ, Eq. (2.1) can be rewritten as follows:

$$\begin{cases} k_1\ddot{u}_1 + k_1u_1 + c_1\sqrt{\frac{k_1}{m_1}}\dot{u}_1 + F(u_1 - u_2) + c_2\sqrt{\frac{k_1}{m_1}}(\dot{u}_1 - \dot{u}_2) = P\sin\left(\frac{\Omega}{\omega}\tau\right) \\ \frac{m_2}{m_1}k_1\ddot{u}_2 + F(u_2 - u_1) + c_2\sqrt{\frac{k_1}{m_1}}(\dot{u}_2 - \dot{u}_1) = 0 \end{cases} \tag{2.5}$$

where $\dot{(\ )}$ stands for the derivative of a variable with respect to τ.
Assuming that the outer mass, m_1, is much bigger than the inner one, m_2, i.e., $0 < \varepsilon = \frac{m_2}{m_1} \ll 1$, the following parameters are introduced:

$$\begin{aligned} &\varepsilon\zeta_1 = \frac{c_1}{\sqrt{k_1m_1}} \quad , \quad \varepsilon\zeta_2 = \frac{c_2}{\sqrt{k_1m_1}} \quad , \quad \varepsilon\gamma = \frac{P}{k_1} \quad , \quad \vartheta = \frac{\Omega}{\omega} \\ &\varepsilon f(u_1 - u_2) = \frac{F(u_1 - u_2)}{k_1} \quad , \quad \varepsilon K_{NL} = \frac{k_{NL}}{k_1} \quad , \quad \varepsilon K_L = \frac{k_L}{k_1} \end{aligned} \tag{2.6}$$

Consequently, Eq. (2.5) adopts the following dimensionless form:

$$\begin{cases} \ddot{u}_1 + u_1 + \varepsilon\zeta_1\dot{u}_1 + \varepsilon f(u_1 - u_2) + \varepsilon\zeta_2(\dot{u}_1 - \dot{u}_2) = \varepsilon\gamma\sin(\vartheta\tau) \\ \varepsilon\ddot{u}_2 + \varepsilon f(u_2 - u_1) + \varepsilon\zeta_2(\dot{u}_2 - \dot{u}_1) = 0 \end{cases} \tag{2.7}$$

New variables w and v corresponding to the center of mass of the two particles and the relative displacement, respectively, are introduced as

$$\begin{bmatrix} w \\ v \end{bmatrix} = \begin{bmatrix} 1 & \varepsilon \\ 1 & -1 \end{bmatrix} \begin{bmatrix} u_1 \\ u_2 \end{bmatrix} \tag{2.8}$$

Here, the passage to relative displacements is relevant since the nonlinearity is present in the inter-oscillator coupling. Thus, Eq. (2.7) is rewritten as follows:

$$\begin{cases} \ddot{u}_1 + u_1 + \varepsilon\zeta_1\dot{u}_1 + \varepsilon f(v) + \varepsilon\zeta_2(\dot{v}) = \varepsilon\gamma\sin(\vartheta\tau) \\ \varepsilon\ddot{u}_2 + \varepsilon f(-v) + \varepsilon\zeta_2(-\dot{v}) = 0 \end{cases} \tag{2.9}$$

Adding and subtracting the two equations from (2.9), a new system of equations is obtained:

$$\begin{cases} \ddot{u}_1 + \varepsilon\ddot{u}_2 + u_1 + \varepsilon\zeta_1\dot{u}_1 = \varepsilon\gamma\sin(\vartheta\tau) \\ \ddot{u}_1 - \ddot{u}_2 + u_1 + \varepsilon\zeta_1\dot{u}_1 + f(v)(\varepsilon+1) + \zeta_2\dot{v}(\varepsilon+1) = \varepsilon\gamma\sin(\vartheta\tau) \end{cases} \tag{2.10}$$

where w and v can be injected, reading to:

$$\begin{cases} \ddot{w} + u_1 + \varepsilon\zeta_1\dot{u}_1 = \varepsilon\gamma\sin(\vartheta\tau) \\ \ddot{v} + u_1 + \varepsilon\zeta_1\dot{u}_1 + f(v)(\varepsilon+1) + \zeta_2\dot{v}(\varepsilon+1) = \varepsilon\gamma\sin(\vartheta\tau) \end{cases} \tag{2.11}$$

From (2.8), we obtain

$$\begin{cases} u_1 = \dfrac{w+\varepsilon v}{1+\varepsilon} \\ u_2 = \dfrac{w-v}{1+\varepsilon} \end{cases} \tag{2.12}$$

Finally, a dimensionless equation written in function of w and v is obtained from Eqs. (2.12) and (2.11) as follows:

$$\begin{cases} \ddot{w} + \dfrac{w+\varepsilon v}{1+\varepsilon} + \varepsilon\zeta_1\dfrac{\dot{w}+\varepsilon\dot{v}}{1+\varepsilon} = \varepsilon\gamma\sin(\vartheta\tau) \\ \ddot{v} + \dfrac{w+\varepsilon v}{1+\varepsilon} + \varepsilon\zeta_1\dfrac{\dot{w}+\varepsilon\dot{v}}{1+\varepsilon} + f(v)(\varepsilon+1) + \zeta_2\dot{v}(\varepsilon+1) = \varepsilon\gamma\sin(\vartheta\tau) \end{cases} \tag{2.13}$$

In the next section, the different methods employed to study the dynamic behavior of the system are presented.

2.2 Multiple scales method, complex variables of Manevitch and Galerkin method

The dynamic behavior of the system is studied by applying the multiple time scales method [Nayfeh and Mook, 1995], where time scales τ_j are defined as follows:

$$\tau_j = \varepsilon^j\tau, j \in \mathbb{N} \tag{2.14}$$

This definition involves the mass ratio ε, which is a small parameter, allowing the introduction of orders of magnitude between time scales. Thus, the time is decomposed in fast (τ_0) and slow scales ($\tau_j = \varepsilon^j\tau, j = 1, 2, ...$). The differential operator is redefined as follows:

$$\begin{aligned} \frac{\mathrm{d}.}{\mathrm{d}\tau} &= \frac{\mathrm{d}\tau_0}{\mathrm{d}\tau}\frac{\partial.}{\partial\tau_0} + \frac{\mathrm{d}\tau_1}{\mathrm{d}t}\frac{\partial.}{\partial\tau_1} + \frac{\mathrm{d}\tau_2}{\mathrm{d}t}\frac{\partial.}{\partial\tau_2} + ... = \frac{\partial.}{\partial\tau_0} + \varepsilon\frac{\partial.}{\partial\tau_1} + \varepsilon^2\frac{\partial.}{\partial\tau_2} + ... \\ \frac{\mathrm{d}^2.}{\mathrm{d}\tau^2} &= \frac{\partial^2.}{\partial\tau_0^2} + 2\varepsilon\frac{\partial.}{\partial\tau_0}\frac{\partial.}{\partial\tau_1} + \varepsilon^2\left(\frac{\partial^2.}{\partial\tau_1^2} + 2\frac{\partial.}{\partial\tau_0}\frac{\partial.}{\partial\tau_2}\right) + ... \end{aligned} \tag{2.15}$$

It should be mentioned that there are other methods to detect dynamics of such coupled nonlinear systems, such as the harmonic balance method [Karkar et al., 2014, Xie et al., 2017, Guo et al., 2022] which seeks immediately for periodic regimes of the system.
For further developments, the multiple scales method will be combined with a change of complex variables. As presented by Manevitch in [Manevitch, 2001], a change of complex variables makes it possible to reduce the order of the differential equations from 2 to 1. The complex variables of Manevitch are applied according to the following relationship:

$$\begin{cases} \varphi_1 e^{i\vartheta\tau} = \dot{w} + i\vartheta w \ , & \varphi_1^* e^{-i\vartheta\tau} = \dot{w} - i\vartheta w \\ \varphi_2 e^{i\vartheta\tau} = \dot{v} + i\vartheta v \ , & \varphi_2^* e^{-i\vartheta\tau} = \dot{v} - i\vartheta v \end{cases} \tag{2.16}$$

with $i^2 = -1$.
From that, w, v and their derivatives can be written as follows:

$$\begin{cases} w = \dfrac{\varphi_1 e^{i\vartheta\tau} - \varphi_1^* e^{-i\vartheta\tau}}{2i\vartheta}, \dot{w} = \dfrac{\varphi_1 e^{i\vartheta\tau} + \varphi_1^* e^{-i\vartheta\tau}}{2}, \\ \ddot{w} = \dfrac{1}{2}(\dot{\varphi}_1 e^{i\vartheta\tau} + \dot{\varphi}_1^* e^{-i\vartheta\tau}) + \dfrac{i\vartheta}{2}(\varphi_1 e^{i\vartheta\tau} - \varphi_1^* e^{-i\vartheta\tau}) \\ \\ v = \dfrac{\varphi_2 e^{i\vartheta\tau} - \varphi_2^* e^{-i\vartheta\tau}}{2i\vartheta}, \dot{v} = \dfrac{\varphi_2 e^{i\vartheta\tau} + \varphi_2^* e^{-i\vartheta\tau}}{2}, \\ \ddot{v} = \dfrac{1}{2}(\dot{\varphi}_2 e^{i\vartheta\tau} + \dot{\varphi}_2^* e^{-i\vartheta\tau}) + \dfrac{i\vartheta}{2}(\varphi_2 e^{i\vartheta\tau} - \varphi_2^* e^{-i\vartheta\tau}) \end{cases} \tag{2.17}$$

The change of variables in Eq. (2.13) reads:

$$\begin{cases} \dfrac{1}{2}(\dot{\varphi}_1 e^{i\vartheta\tau} + \dot{\varphi}_1^* e^{-i\vartheta\tau}) + \dfrac{i\vartheta}{2}(\varphi_1 e^{i\vartheta\tau} - \varphi_1^* e^{-i\vartheta\tau}) + \dfrac{1}{1+\varepsilon}\left(\dfrac{\varphi_1 e^{i\vartheta\tau} - \varphi_1^* e^{-i\vartheta\tau}}{2i\vartheta}\right) + \\ \dfrac{\varepsilon}{1+\varepsilon}\left(\dfrac{\varphi_2 e^{i\vartheta\tau} - \varphi_2^* e^{-i\vartheta\tau}}{2i\vartheta}\right) + \dfrac{\varepsilon\zeta_1}{1+\varepsilon}\left(\dfrac{\varphi_1 e^{i\vartheta\tau} + \varphi_1^* e^{-i\vartheta\tau}}{2} + \varepsilon\left(\dfrac{\varphi_2 e^{i\vartheta\tau} + \varphi_2^* e^{-i\vartheta\tau}}{2}\right)\right) \\ = \varepsilon\gamma\sin(\vartheta\tau) \\ \\ \dfrac{1}{2}(\dot{\varphi}_2 e^{i\vartheta\tau} + \dot{\varphi}_2^* e^{-i\vartheta\tau}) + \dfrac{i\vartheta}{2}(\varphi_2 e^{i\vartheta\tau} - \varphi_2^* e^{-i\vartheta\tau}) + \dfrac{1}{1+\varepsilon}\left(\dfrac{\varphi_1 e^{i\vartheta\tau} - \varphi_1^* e^{-i\vartheta\tau}}{2i\vartheta}\right) + \\ \dfrac{\varepsilon}{1+\varepsilon}\left(\dfrac{\varphi_2 e^{i\vartheta\tau} - \varphi_2^* e^{-i\vartheta\tau}}{2i\vartheta}\right) + \dfrac{\varepsilon\zeta_1}{1+\varepsilon}\left(\dfrac{\varphi_1 e^{i\vartheta\tau} + \varphi_1^* e^{-i\vartheta\tau}}{2} + \varepsilon\left(\dfrac{\varphi_2 e^{i\vartheta\tau} + \varphi_2^* e^{-i\vartheta\tau}}{2}\right)\right) + \\ f(\varphi_2, \varphi_2^*)(\varepsilon+1) + \zeta_2\left(\dfrac{\varphi_2 e^{i\vartheta\tau} + \varphi_2^* e^{-i\vartheta\tau}}{2}\right)(\varepsilon+1) = \varepsilon\gamma\sin(\vartheta\tau) \end{cases} \tag{2.18}$$

Applying the complex variables of Manevitch enables to separate the vibration of the system into fast ($e^{i\vartheta\tau}$) and slow (φ_1, φ_2) variations, corresponding to the time scales τ_0 and $\tau_j = \varepsilon^j\tau, j = 1, 2, ...$, respectively. In other words, the amplitudes of these complex variables describe the envelope of physical variables, i.e., w and v in the dimensionless form of equations, with a spectral content mainly described by the harmonic ϑ. One example can be seen in Fig. 2.3. In this figure, the time history response of w is represented by the blue curve, obtained through numerical time integration of Eq. (2.13), while the amplitude of φ_1 is depicted in red, representing the envelope of the response. The numerical time integrations in this thesis are performed using the *MATLAB* function *ode45*, which is based on an explicit Runge-Kutta formula of 4th and 5th orders.
In order to keep only the resonant terms corresponding to the harmonic ϑ, a Galerkin method is applied based on the truncated Fourier series via keeping the first harmonic. For a generic function

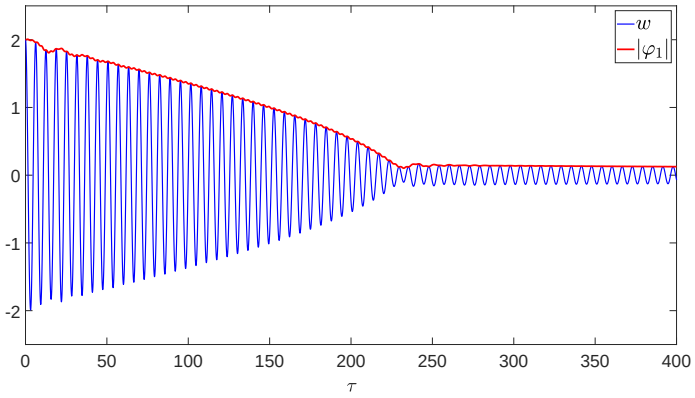

Figure 2.3: Correlation between the variable w and the amplitude $|\varphi_1|$ of its corresponding complex variable (in red).

$s(\varphi_1, \varphi_2, \varphi_1^*, \varphi_2^*)$, this task is carried out via:

$$S(\varphi_1, \varphi_2, \varphi_1^*, \varphi_2^*) = \frac{\vartheta}{2\pi} \int_0^{\frac{2\pi}{\vartheta}} s(\varphi_1, \varphi_2, \varphi_1^*, \varphi_2^*) e^{-i\vartheta\tau} d\tau \tag{2.19}$$

When using this technique, it will be assumed that $\varphi_1, \varphi_2, \varphi_1^*, \varphi_2^*$ do not depend on the fast timescale τ_0, i.e., $\tau_0 = \tau$. The validity of this assumption will be checked during the multiple scale analysis or via searching an asymptotic state when $\tau_0 \to \infty$ [Ture Savadkoohi et al., 2016b]. Applying Eq. (2.19) in system (2.18), yields:

$$\begin{cases} \dfrac{\dot{\varphi}_1}{2} + \dfrac{i\vartheta\varphi_1}{2} + \dfrac{1}{(1+\varepsilon)}\dfrac{\varphi_1}{2i\vartheta} + \dfrac{\varepsilon}{(1+\varepsilon)}\dfrac{\varphi_2}{2i\vartheta} + \dfrac{\varepsilon}{(1+\varepsilon)}\zeta_1\left(\dfrac{\varphi_1}{2} + \varepsilon\dfrac{\varphi_2}{2}\right) - \dfrac{\varepsilon\gamma}{2i} = 0 \\ \dfrac{\dot{\varphi}_2}{2} + \dfrac{i\vartheta\varphi_2}{2} + \dfrac{1}{(1+\varepsilon)}\dfrac{\varphi_1}{2i\vartheta} + \dfrac{\varepsilon}{(1+\varepsilon)}\dfrac{\varphi_2}{2i\vartheta} + \dfrac{\varepsilon}{(1+\varepsilon)}\zeta_1\left(\dfrac{\varphi_1}{2} + \varepsilon\dfrac{\varphi_2}{2}\right) + \\ \mathcal{F}(\varphi_2, \varphi_2^*)(\varepsilon+1) + \zeta_2\dfrac{\varphi_2}{2}(\varepsilon+1) - \dfrac{\varepsilon\gamma}{2i} = 0 \end{cases} \tag{2.20}$$

Where $\mathcal{F}(\varphi_2, \varphi_2^*)$ is:

$$\mathcal{F}(\varphi_2, \varphi_2^*) = \frac{\vartheta}{2\pi} \int_0^{\frac{2\pi}{\vartheta}} f\left(\frac{\varphi_2 e^{i\vartheta\tau} - \varphi_2^* e^{-i\vartheta\tau}}{2i\vartheta}\right) e^{-i\vartheta\tau} d\tau \tag{2.21}$$

It can be shown that

$$\mathcal{F}(\varphi_2, \varphi_2^*) = -\frac{i\varphi_2}{2\vartheta} G(|\varphi_2|^2), \tag{2.22}$$

where $G(|\varphi_2|^2)$, obtained through a time averaging detailed in Annex A, can be written as follows:

$$G(|\varphi_2|^2) = \begin{cases} \dfrac{3K_{NL}|\varphi_2|^2}{4\vartheta^2} & \text{if } \dfrac{|\varphi_2|}{\vartheta} < \delta \\ \dfrac{3K_{NL}|\varphi_2|^2}{4\vartheta^2} + \dfrac{1}{4\pi\vartheta^2|\varphi_2|}\left[\left(-8\delta K_L\vartheta^3\sqrt{1-\dfrac{\delta^2\vartheta^2}{|\varphi_2|^2}}\right)\right. & \\ +K_{NL}\left(-6\delta|\varphi_2|^2\vartheta\sqrt{1-\dfrac{\delta^2\vartheta^2}{|\varphi_2|^2}} + 12\delta^3\vartheta^3\sqrt{1-\dfrac{\delta^2\vartheta^2}{|\varphi_2|^2}}\right) & \\ \left.+(8K_L|\varphi_2|\vartheta^2 - 6K_{NL}|\varphi_2|^3)\arccos\left(\dfrac{\delta\vartheta}{|\varphi_2|}\right)\right] & \text{if } \dfrac{|\varphi_2|}{\vartheta} \geq \delta \end{cases} \tag{2.23}$$

So one can write:

$$G(|\varphi_2|^2) = g(|\varphi_2|^2) + \mathcal{O}(\varepsilon^1) \tag{2.24}$$

where

$$g(|\varphi_2|^2) = \begin{cases} \dfrac{3K_{NL}|\varphi_2|^2}{4} & \text{if } |\varphi_2| < \delta \\ \dfrac{3K_{NL}|\varphi_2|^2}{4} + \dfrac{1}{4\pi|\varphi_2|}\left[\left(-8\delta K_L\sqrt{1-\dfrac{\delta^2}{|\varphi_2|^2}}\right)\right. & \\ +K_{NL}\left(-6\delta|\varphi_2|^2\sqrt{1-\dfrac{\delta^2}{|\varphi_2|^2}} + 12\delta^3\sqrt{1-\dfrac{\delta^2}{|\varphi_2|^2}}\right) & \\ \left.+(8K_L|\varphi_2| - 6K_{NL}|\varphi_2|^3)\arccos\left(\dfrac{\delta}{|\varphi_2|}\right)\right] & \text{if } |\varphi_2| \geq \delta \end{cases} \tag{2.25}$$

In the next section, Eq. (2.20) is treated by the method of multiple scales [Nayfeh and Mook, 1995] via looking at equations of different orders of ε. This will lead to the determination of different system dynamics, i.e., fast and slow ones [Charlemagne et al., 2016].

2.3 Detection of different dynamics of the system

We consider the system behavior in the vicinity of 1:1 resonance, where the frequency of the main system is close to that of the external force. From that, we set $\vartheta = 1 + \sigma\varepsilon$, where σ is the frequency detuning parameter.

2.3.1 Fast dynamics: ε^0 order of system equations

The system behavior at the fast time scale is described by the system of equations (2.20) at ε^0 order:

$$\begin{cases} \dfrac{\partial\varphi_1}{\partial\tau_0} = 0 \\ \dfrac{\partial\varphi_2}{\partial\tau_0} + i\varphi_2 - i\varphi_1 - i\varphi_2 g(|\varphi_2|^2) + \zeta_2\varphi_2 = 0 \end{cases} \tag{2.26}$$

The first equation implies that $\varphi_1 = \varphi_1(\tau_1, \tau_2, ...)$, validating for this variable the hypothesis made for use of Galerkin's method (Eq. (2.19)). For the second equation of (2.26), we seek the fixed point φ_2 verifying $\lim\limits_{\tau_0\to\infty}\dfrac{\partial\varphi_2}{\partial\tau_0} = 0$. From that, we obtain the slow invariant manifold (SIM):

$$\mathscr{H} = -i\varphi_2 + i\varphi_1 + i\varphi_2 g(|\varphi_2|^2) - \zeta_2\varphi_2 = 0 \tag{2.27}$$

ζ_1	ζ_2	γ
0.1	0.1	0

Table 2.1: Parameters of the system.

K_{NL}	K_L	δ
0.1	0.1	5

Table 2.2: Parameters of the nonlinear restoring force function.

From this equation, we notice that the SIM does not depend on the external solicitation of the main system. Furthermore, each combination of φ_1 and φ_2 solution of Eq. (2.27) corresponds to an admissible state of the system at slow time scales. Finally, we can say that the SIM is a geometrical representation of all possible asymptotic states of the system, since its validity begins when $\tau_0 \to \infty$. Thus, the behavior of a system is attracted by its SIM and evolves around it.
Let us express the complex variables of Manevitch in the polar domain as functions of amplitudes N_j and phases δ_j:

$$\varphi_j = N_j e^{i\delta_j} \tag{2.28}$$

where $N_j \in \mathbb{R}_+$ and $\delta_j \in \mathbb{R}$, $j = 1, 2$. From that, Eq. 2.27 reads:

$$N_2 - N_2 g(N_2^2) - i\zeta_2 N_2 = N_1 e^{i(\delta_1 - \delta_2)} \tag{2.29}$$

Separating the imaginary and real part of Eq. (2.29), it leads to:

$$\begin{cases} \text{Imaginary part:} & A = N_1 \sin(\delta_1 - \delta_2) \\ \text{Real part:} & B = N_1 \cos(\delta_1 - \delta_2) \end{cases} \tag{2.30}$$

with

$$\begin{cases} A = -N_2\zeta_2 \\ B = N_2 - N_2 g(N_2) \end{cases} \tag{2.31}$$

One can write

$$A^2 + B^2 = N_1^2 \tag{2.32}$$

which leads to the final equation of the SIM:

$$N_1 = N_2\sqrt{(1 - g(N_2^2))^2 + \zeta_2^2} \tag{2.33}$$

2.3.1.1 An example of SIM

Let us consider the parameters of Tables 2.1 and 2.2. The SIM of the system, obtained from Eq. (2.33), is presented in Fig. 2.4. It is seen that, for the nonlinearity studied in this manuscript (see Eq. (2.2) and Fig. 2.2), the geometry of the SIM differs from corresponding ones of systems with pure cubic and piecewise-linear nonlinearities [Gendelman et al., 2007, Gendelman, 2008], which present two local extrema. In comparison, here, the SIM exhibits four local extrema.

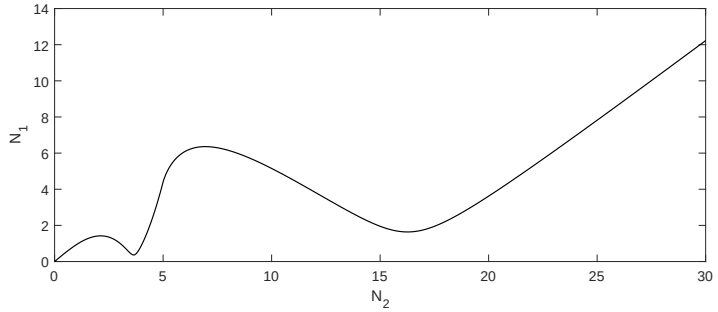

Figure 2.4: SIM obtained from Eq. (2.33). Parameters of the system are reported in Tables 2.1 and 2.2.

2.3.2 Stability analysis of the SIM

In order to detect the stable areas of the SIM, the second equation of system (2.26) is linearized after linear perturbation of φ_2, as follows:

$$\begin{cases} \varphi_2 \rightarrow \varphi_2 + \Delta\varphi_2 \\ \varphi_2^* \rightarrow \varphi_2^* + \Delta\varphi_2^* \end{cases} \tag{2.34}$$

where $|\Delta\varphi_2| << |\varphi_2|$.
Since φ_1 is independent of τ_0 (see the first equation of system (2.26)), we do not perturb φ_1 for this analysis. Applying the perturbed complex variables of Eq. (2.34) in Eq. (2.26), the following system can be obtained:

$$\begin{bmatrix} \dfrac{\partial\varphi_2}{\partial\tau_0} \\ \\ \dfrac{\partial\varphi_2^*}{\partial\tau_0} \end{bmatrix} = \mathbf{M} \begin{bmatrix} \Delta\varphi_2 \\ \Delta\varphi_2^* \end{bmatrix} \tag{2.35}$$

with

$$\mathbf{M} = \begin{bmatrix} M_{11} & M_{12} \\ M_{21} & M_{22} \end{bmatrix} \tag{2.36}$$

The components of $\mathbf{M}$ are:

$$\begin{aligned} M_{11} &= i[g'(|\varphi_2|^2)|\varphi_2|^2 + g(|\varphi_2|^2) - 1] - \zeta_2 \\ M_{12} &= i\varphi_2^2 g'(|\varphi_2|^2) \\ M_{21} &= -i\varphi_2^{*2} g'(|\varphi_2|^2) \\ M_{22} &= -i[g'(|\varphi_2|^2)|\varphi_2|^2 + g(|\varphi_2|^2) - 1] - \zeta_2 \end{aligned}$$

where $g'(|\varphi_2|^2)$ is the derivative of Eq. (2.25) with respect to $|\varphi_2|^2$.
The stability of the fixed points defining the SIM are deduced from the eigenvalues of matrix $\mathbf{M}$, which are obtained from the characteristic equation:

$$\det(\mathbf{M} - \lambda\mathbf{Id}_{2\times 2}) = \lambda^2 - (M_{11} + M_{22})\lambda + M_{11}M_{22} - M_{12}M_{21} = 0 \tag{2.37}$$

where $\mathbf{Id}_{2\times 2}$ is an identity matrix and λ_j, $j = 1, 2$, are eigenvalues of the system. The following relations can be defined from Eq. (2.37):

$$\begin{aligned} \lambda_1 + \lambda_2 &= M_{11} + M_{22} = -2\zeta_2 < 0 \\ \lambda_1\lambda_2 &= M_{11}M_{22} - M_{12}M_{21} \end{aligned} \tag{2.38}$$

We distinguish two cases:

- If $M_{11}M_{22} - M_{12}M_{21} > 0$:

  If λ_1 and λ_2 are real, then they both are certainly negative ($\lambda_1 + \lambda_2 < 0$), so the zone is stable;

  If λ_1 and λ_2 are complex, then their real parts should be $-\zeta_2$, so the zone is stable.

- If $M_{11}M_{22} - M_{12}M_{21} < 0$, then the real part of one of eigenvalues is positive, so the zone is unstable.

As a summary, the borders between stable and unstable zones of the SIM can be written as:

$$M_{11}M_{22} - M_{12}M_{21} = 0 \tag{2.39}$$

which leads to:

$$\begin{aligned} &1 - 2g(|\varphi_2|^2) + g^2(|\varphi_2|^2) - 2g'(|\varphi_2|^2)|\varphi_2|^2 + 2g(|\varphi_2|^2)g'(|\varphi_2|^2)|\varphi_2|^2 \\ &+g'^2(|\varphi_2|^2)|\varphi_2|^4 - g'^2(|\varphi_2|^2)\varphi_2^2\varphi_2^{*2} + \zeta_2^2 = 0 \end{aligned} \tag{2.40}$$

Figure 2.5 collects the stability borders obtained by Eq. (2.40).

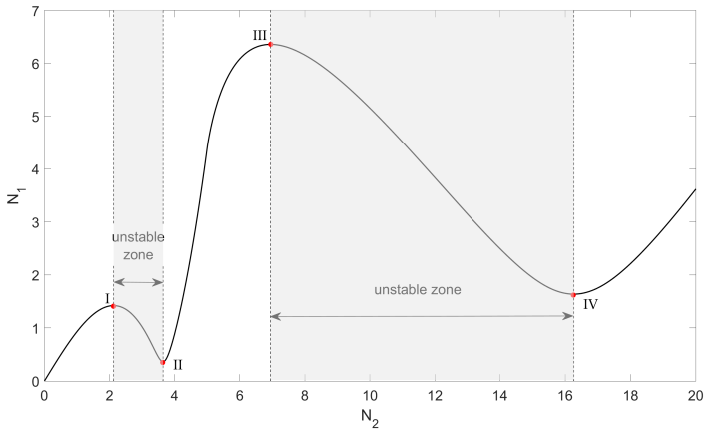

Figure 2.5: The SIM and its stability borders (- - -). Parameters of the system are reported in Tables 2.1 and 2.2.

There are many types of stability analysis of periodic solutions, such as asymptotic or uniform stabilities, whose definitions can be found in [Willems and Pandit, 1971]. Here, the local study of the linear stability of the reduced system is sufficient to explain the periodic and quasi-periodic behaviors of the system, as it will be shown later in this chapter.
Finally, the detection of the SIM and of its unstable zones makes it possible to identify the asymptotic behaviors of the studied system for any solicitation of the main structure. In order to obtain the complete system behavior, which includes the amplitudes of its responses at its equilibrium points for a given solicitation, the slow dynamics of the system are studied in the next section.

2.3.3 Slow dynamics: ε^1 order of system equations

The study of the slow dynamics of the system aims to define the asymptotic behaviors at slow time scale. To this end, the first equation of the system (2.20), corresponding to the primary structure, is studied at ε^1 order:

$$\frac{\partial \varphi_1}{\partial \tau_1} = E_1(\varphi_1, \varphi_2, \varphi_1^*, \varphi_2^*) \tag{2.41}$$

where

$$E_1(\varphi_1, \varphi_2, \varphi_1^*, \varphi_2^*) = -2\sigma\varphi_1 + i\zeta_1\varphi_1 + \varphi_2 - \varphi_1 - \gamma = 0 \tag{2.42}$$

To ensure that $E_1(\varphi_1, \varphi_2, \varphi_1^*, \varphi_2^*) = 0$ corresponds to the equilibrium point for the entire system, the next step consists in expressing the derivatives of φ_2 with respect to τ_1. For that, we look at the evolution of the SIM (see Eq. (2.27)) in τ_1 time scale, which leads to:

$$\begin{cases} \dfrac{\mathrm{d}\mathscr{H}}{\mathrm{d}\tau_1} = \dfrac{\partial\mathscr{H}}{\partial\varphi_1}\dfrac{\partial\varphi_1}{\partial\tau_1} + \dfrac{\partial\mathscr{H}}{\partial\varphi_1^*}\dfrac{\partial\varphi_1^*}{\partial\tau_1} + \dfrac{\partial\mathscr{H}}{\partial\varphi_2}\dfrac{\partial\varphi_2}{\partial\tau_1} + \dfrac{\partial\mathscr{H}}{\partial\varphi_2^*}\dfrac{\partial\varphi_2^*}{\partial\tau_1} = 0 \\ \dfrac{\mathrm{d}\mathscr{H}^*}{\mathrm{d}\tau_1} = \dfrac{\partial\mathscr{H}^*}{\partial\varphi_1}\dfrac{\partial\varphi_1}{\partial\tau_1} + \dfrac{\partial\mathscr{H}^*}{\partial\varphi_1^*}\dfrac{\partial\varphi_1^*}{\partial\tau_1} + \dfrac{\partial\mathscr{H}^*}{\partial\varphi_2}\dfrac{\partial\varphi_2}{\partial\tau_1} + \dfrac{\partial\mathscr{H}^*}{\partial\varphi_2^*}\dfrac{\partial\varphi_2^*}{\partial\tau_1} = 0 \end{cases} \tag{2.43}$$

Equation (2.43) can also be written in matrix form as:

$$\underbrace{\begin{bmatrix} \dfrac{\partial\mathscr{H}}{\partial\varphi_2} & \dfrac{\partial\mathscr{H}}{\partial\varphi_2^*} \\ \dfrac{\partial\mathscr{H}^*}{\partial\varphi_2} & \dfrac{\partial\mathscr{H}^*}{\partial\varphi_2^*} \end{bmatrix}}_{\mathbf{S}_1} \begin{bmatrix} \dfrac{\partial\varphi_2}{\partial\tau_1} \\ \dfrac{\partial\varphi_2^*}{\partial\tau_1} \end{bmatrix} = -\underbrace{\begin{bmatrix} \dfrac{\partial\mathscr{H}}{\partial\varphi_1} & \dfrac{\partial\mathscr{H}}{\partial\varphi_1^*} \\ \dfrac{\partial\mathscr{H}^*}{\partial\varphi_1} & \dfrac{\partial\mathscr{H}^*}{\partial\varphi_1^*} \end{bmatrix}}_{\mathbf{S}_2} \begin{bmatrix} E_1 \\ E_1^* \end{bmatrix} \tag{2.44}$$

Multiplying by $\mathbf{S}_1^{-1} = \mathrm{adj}(\mathbf{S}_1)/\det(\mathbf{S}_1)$, the following system is obtained:

$$\det(\mathbf{S}_1)\mathbf{Id}_{2\times 2} \begin{bmatrix} \dfrac{\partial\varphi_2}{\partial\tau_1} \\ \dfrac{\partial\varphi_2^*}{\partial\tau_1} \end{bmatrix} = -\mathrm{adj}(\mathbf{S}_1)\mathbf{S}_2 \begin{bmatrix} E_1 \\ E_1^* \end{bmatrix} \tag{2.45}$$

where $\mathrm{adj}(\mathbf{S}_1)$ is the adjugate matrix of $\mathbf{S}_1$ defined by $\mathrm{adj}(\mathbf{S}_1) = \mathrm{cof}(\mathbf{S}_1)^T$, and $\mathrm{cof}(\mathbf{S}_1)$ is the cofactor matrix of $\mathbf{S}_1$.
The study of the relation (2.45) allows the detection of equilibrium and singular points of the system. The mathematical distinction between them relates to the invertibility of the matrix $\mathbf{S}_1$. Analyzing the system (2.45), we notice that when $\mathbf{S}_1$ is not invertible, the derivatives at slow time scale are no longer defined. As explained in [Starosvetsky and Gendelman, 2008], this singularity could be due to the existence of saddle-node bifurcations that give rise to relaxation oscillations between stable branches of the SIM.
Let us seek singular and equilibrium points, which mainly correspond to non-periodic and periodic regimes, respectively:

Singular points The following conditions are set:

$$\begin{cases} E_1(\varphi_1, \varphi_2, \varphi_1^*, \varphi_2^*) = 0 \\ \mathscr{H}(\varphi_1, \varphi_2, \varphi_1^*, \varphi_2^*) = 0 \\ \det(\mathbf{S}_1) = 0 \end{cases} \tag{2.46}$$

Equilibrium points The following conditions are set:

$$\begin{cases} E_1(\varphi_1, \varphi_2, \varphi_1^*, \varphi_2^*) = 0 \\ \mathscr{H}(\varphi_1, \varphi_2, \varphi_1^*, \varphi_2^*) = 0 \\ \det(\mathbf{S}_1) \neq 0 \end{cases} \tag{2.47}$$

Thus, from $\det(\mathbf{S}_1) = 0$, the amplitudes of all possible singular points are determined as:

$$1 - 2g(N_2^2) + g^2(N_2^2) - 2N_2^2 g'(N_2^2) + 2N_2^2 g(N_2^2)g'(N_2^2) + \zeta_2^2 = 0 \tag{2.48}$$

Furthermore, when we solve $\dfrac{\partial N_1^2}{\partial N_2} = 0$ from Eq. (2.33) in order to find the local extrema of the SIM, we arrive at Eq. (2.48). This means that the positions of the singular points amplitudes, namely singular lines, coincide with those of local extrema of the SIM which are housed by stability borders as well. These extrema are marked as I, II, III and IV in Fig. 2.5.
Solving Eq. (2.42), the equilibrium points are obtained. Considering Eq. (2.27) that links the variables φ_1 and φ_2, Eq. (2.42) leads to:

$$(-2\sigma + i\zeta_1 - 1)(\varphi_2 - g(N_2^2) - i\zeta_2\varphi_2) + \varphi_2 - \gamma = 0 \tag{2.49}$$

After writing Eq. (2.49) in the polar domain, the separation of its real and imaginary parts leads to the following system:

$$\begin{cases} \text{Imaginary part:} & A = -\gamma \sin(\delta_2) \\ \\ \text{Real part:} & B = \gamma \cos(\delta_2) \end{cases} \tag{2.50}$$

with

$$\begin{cases} A = 2\sigma N_2\zeta_2 + \zeta_1 N_2 - \zeta_1 N_2 g(N_2) + \zeta_2 N_2 \\ \\ B = -2\sigma N_2 + 2\sigma N_2 g(N_2) + N_2 g(N_2) + \zeta_1\zeta_2 N_2 \end{cases} \tag{2.51}$$

One can write

$$A^2 + B^2 = \gamma^2 \tag{2.52}$$

From that, the equilibrium points are computed as:

$$\begin{aligned} &N_2^2 g^2(N_2^2)(1 + \zeta_1^2 + 4\sigma + 4\sigma^2) + N_2^2 g(N_2^2)(-8\sigma^2 - 4\sigma - 2\zeta_1^2) \\ &+N_2^2(4\sigma^2 + 4\zeta_2^2\sigma^2 + 4\sigma^2\zeta_2^2 + 4\zeta_2^2\sigma + \zeta_1^2\zeta_2^2 + \zeta_1^2 + 2\zeta_1\zeta_2 + \zeta_2^2) - \gamma^2 = 0 \end{aligned} \tag{2.53}$$

Detection of N_2 as roots of Eq. (2.53) in a direct manner is a challenging task due to the nature of the equation. If we reorganize this equation with respect to σ, it becomes a polynomial of degree two (Eq. (2.54)) which is easy to be solved.

$$\begin{aligned} &\left(4N_2^2 - 8N_2^2 g(N_2^2) + 4N_2^2 g^2(N_2^2) + 4N_2^2\zeta_2^2\right)\sigma^2 \\ &+\left(-4N_2^2 g(N_2^2) + 4N_2^2 g^2(N_2^2) + 4N_2^2\zeta_2^2\right)\sigma \\ &+N_2^2\left(\zeta_1^2\zeta_2^2 + g^2(N_2^2) + \zeta_1^2 - 2\zeta_1^2 g(N_2^2) + 2\zeta_1\zeta_2 + \zeta_1^2 g^2(N_2^2) + \zeta_2^2\right) - \gamma^2 = 0 \end{aligned} \tag{2.54}$$

For a given N_2, Eq. (2.54) can be solved with respect to σ, then one can obtain the frequency response curve in term of N_2 for a given forcing amplitude γ. Subsequently, the frequency response curve in term of N_1 can be obtained by the equation of the SIM (see Eq. (2.33)).

2.3.4 Backbone curves of the system

The backbone curves define the nonlinear modal characteristics of conservative systems, showing an amplitude dependency of the frequency, a classical phenomenon in nonlinear dynamic systems [Nayfeh and Mook, 1995]. Thus, after detecting all equilibrium points of the system, which are clarified in Eq. (2.54), we can obtain the backbone curves by setting the system's excitation and damping terms equal to zero. Thus, Eq. (2.54) reads:

$$\left(4 - 8g(N_2^2) + 4g^2(N_2^2)\right)\sigma^2 + \left(-4g(N_2^2) + 4g^2(N_2^2)\right)\sigma + g^2(N_2^2) = 0 \tag{2.55}$$

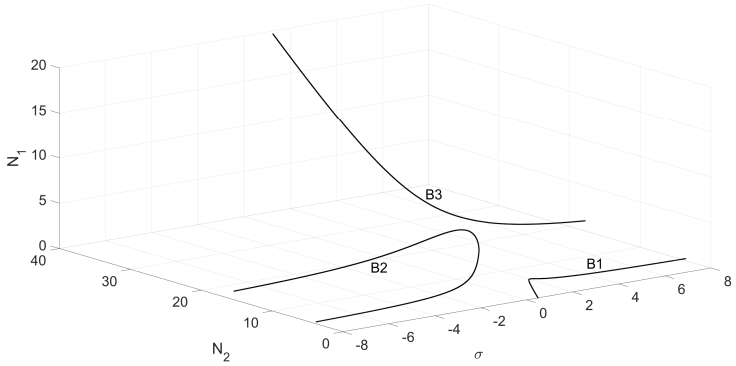

Figure 2.6: Backbone curves of the system.

Backbone curves of the system as a function of the detuning parameter σ or of the frequency ($\vartheta = 1 + \sigma\varepsilon$) are obtained from Eq. (2.55) and then from Eq. (2.33). The three-dimensional view of the backbone curves, composed of three branches, B1, B2, and B3, is illustrated in Fig. 2.6.
The projection of Fig. 2.6 on the N_1-N_2 plane is plotted in Fig. 2.7, which represents the SIM of the system when damping terms are zero. These figures show the emergence of complicated and possibly non-continuous frequency responses, indicating the possible existence and positions of isola in the system. Classical systems, such as those with Duffing-type nonlinearity, have a single backbone curve. However, the present study presents three segments of backbone curves: $B1$, $B2$, and $B3$. This is because a different type of nonlinearity was utilized rather than cubic. The frequency response curves of the meta-cell are presented in Sect. 2.4.2, followed by more discussions on backbone curves in Sect. 2.4.3.

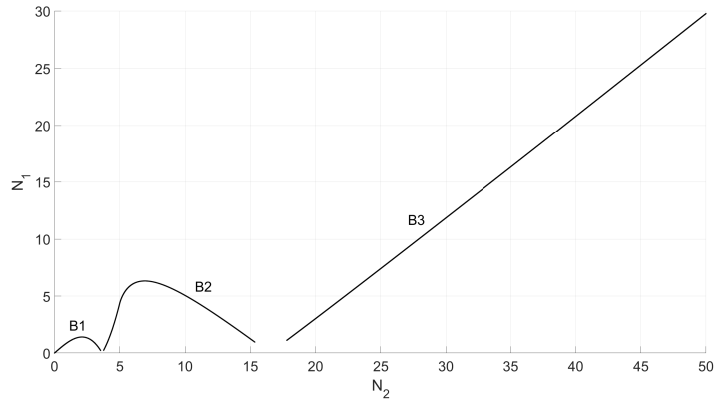

Figure 2.7: Projection of the backbone curves of Fig. 2.6 in the N1-N2 plane.

2.3.5 Parametric study of singular points

This section presents a study on the influence of different parameters on the position of the singular lines of the SIM, which depend on the parameters of the nonlinear restoring force function (Table 2.2) as we can see in Eq. (2.48). Thus, the positions of the singular lines were studied by varying each parameter of the restoring force function, i.e., K_L, K_{NL}, and δ, one at a time. In all figures

presented here, the position of singular lines I and III (local maxima of the SIM) are in blue and pink color, respectively, while the positions of II and IV (local minima of the SIM) are in red and green, respectively.
As an example, the three-dimensional view of the amplitudes of the singular points, in terms of N_1 and N_2, for sweeping K_L and the other parameters fixed (see Table 2.2) is illustrated in Fig. 2.8a. For clarity, a SIM is plotted in the same figure for $K_L = 0.5$. Two-dimensional views of this figure are presented in Figs. 2.8b and 2.8c. From these figures, it is noticed that K_L affects only the position of the singular lines III and IV of Fig. 2.4: if the value of K_L increases, their amplitudes in terms of N_1 and N_2 increase too. However, there is a value of K_L beyond which the singular lines III and IV do not exist. As an example, the corresponding SIM for $K_L = 1$ is presented in Fig. 2.9, attesting to the local extrema III and IV disappearance.

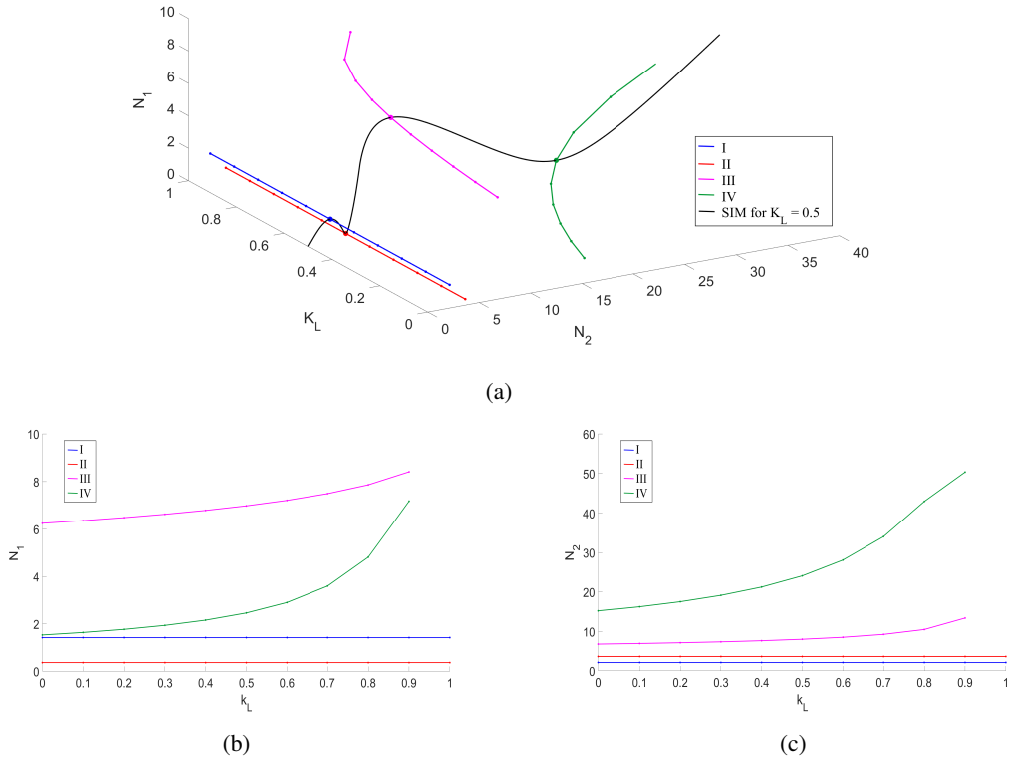

(a)

(b)

(c)

Figure 2.8: (a) Amplitudes of singular points with respect to the parameter K_L of the restoring force function. The black solid line represents the SIM of the system for $K_L = 0.5$; (b) N_1 versus K_L; (c) N_2 versus K_L.

For sweeping K_{NL}, the three-dimensional view of singular points amplitudes is illustrated in Fig. 2.10a, and a SIM is plotted on the same figure for $K_{NL} = 0.5$. Two-dimensional views of Fig. 2.10a are presented in Figs. 2.10b and 2.10c. These figures show that K_{NL} influences the position of all singular lines, but its effects are more significant over the last two, namely on N_1 of the singular line III and on N_2 of IV.
For sweeping parameter δ, parameter that marks the boundary between the cubic and linear behavior in the restoring force, the three-dimensional view of the singular points amplitudes is illustrated in Fig. 2.11a. A SIM is plotted in the same figure for $\delta = 5$ for clarity. Figures 2.11b and 2.11c

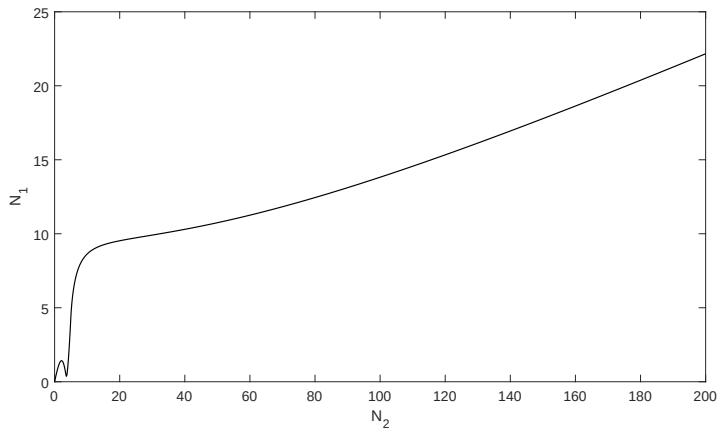

Figure 2.9: SIM for $K_L = 1$ and other fixed parameters of Table 2.2.

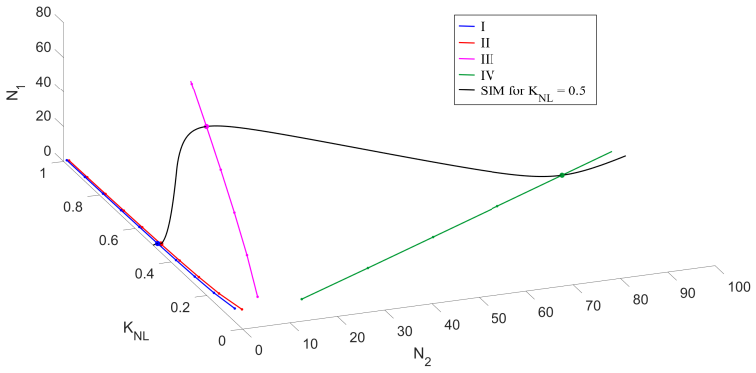

(a)

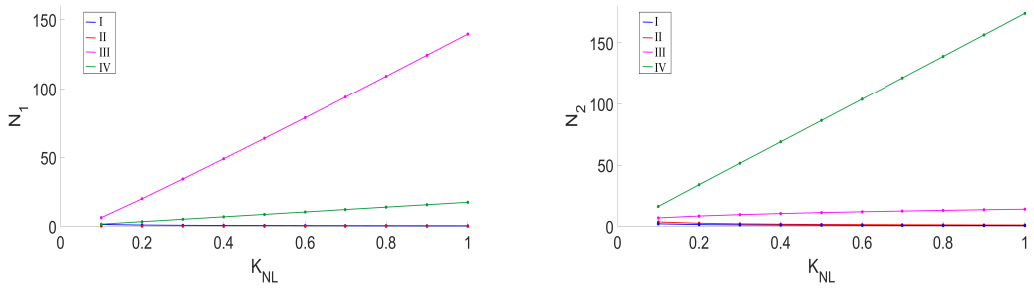

(b) (c)

Figure 2.10: (a) Amplitudes of singular points with respect to the parameter K_{NL} of the restoring force function. The black solid line represents the SIM of the system for $K_{NL} = 0.5$; (b) N_1 versus K_{NL}; (c) N_2 versus K_{NL}.

present two-dimensional views of Fig. 2.11a. From this, the emergence of the singular lines III and IV from a minimum value of δ is observed. Increasing this value, the amplitudes of these points increase significantly, mainly in terms of N_1 for III and in terms of N_2 for IV.

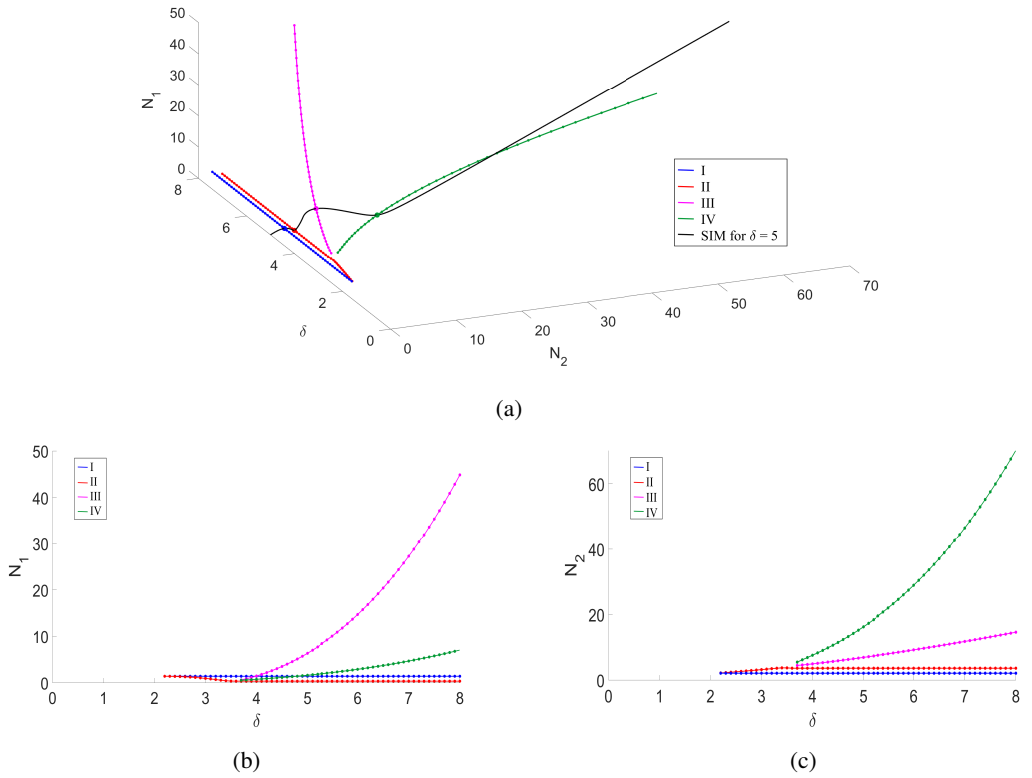

(a)

(b) (c)

Figure 2.11: (a) Amplitudes of singular points with respect to the parameter δ of the restoring force function. The black solid line represents the SIM of the system for $\delta = 5$; (b) N_1 versus δ; (c) N_2 versus δ.

Let us summarize the observations from mentioned parametric studies here:

- The SIM can be tuned via modifying parameters of the restoring force function;
- These parameters affect mainly the singular lines III (second local maxima) and IV (second local minima) of the SIM;
- K_L affects mainly the singular line IV. Meanwhile, there is a value of K_L beyond which the singular lines III and IV disappear;
- K_{NL} influences the singular lines III and IV in a linear manner;
- δ influences the singular lines III and IV in a non-linear manner.

Furthermore, since this first parametric study showed us that the SIM could be tuned, it became a motivation to pursue the work on optimizing the nonlinear restoring function, which is the subject of Chapter 4 of this manuscript.

2.4 Numerical results versus analytical predictions

In this section, analytical predictions of previous sections are compared with results obtained by numerical time integration of Eq. (2.13).

2.4.1 Free response

To analyze a free response, let us consider the following conditions at $\tau = 0$: $(w, v, \dot{w}, \dot{v}) = (7, 7, 0, 0)$, illustrated by $\times$ symbol in Fig. 2.12a. Numerical results are added to the SIM of the system in Fig. 2.12a, while Figs. 2.12b and 2.12c summarize the time histories of system amplitudes.

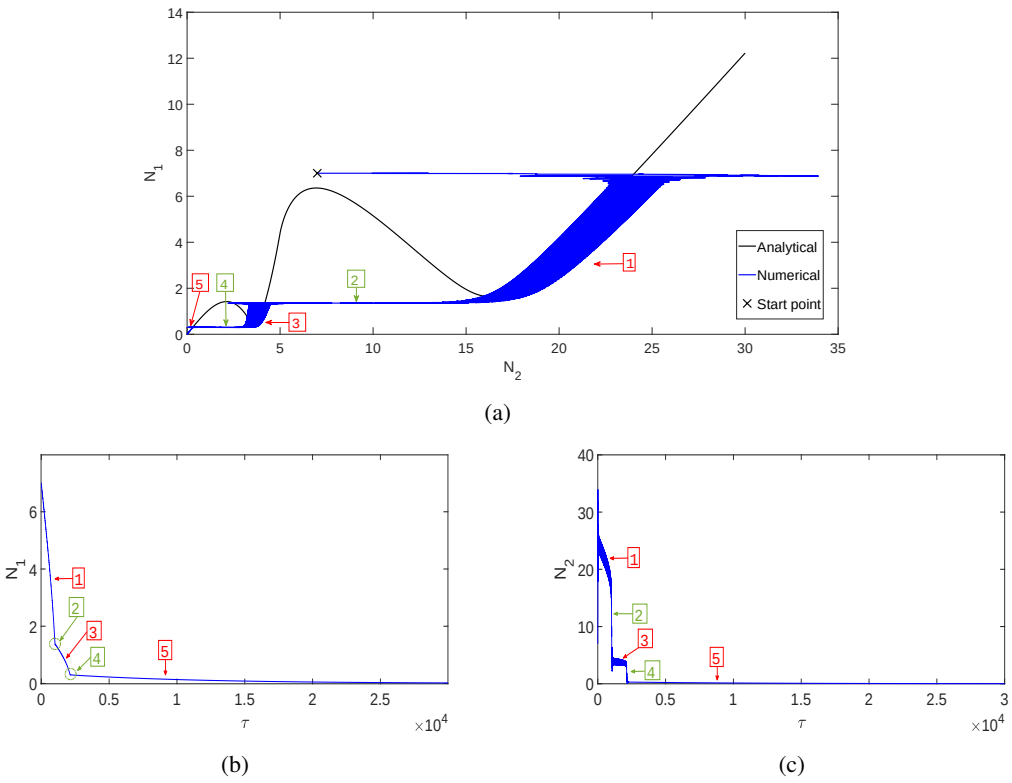

(a)

(b) (c)

Figure 2.12: (a) The SIM of the system and corresponding numerical results obtained by numerical time integration of Eq. (2.13) with $\gamma = 0$ (free response). (b) N_1 versus τ; (c) N_2 versus τ. The initial conditions are $(w, v, \dot{w}, \dot{v}) = (7, 7, 0, 0)$.

The energy reduction process can be observed in Fig. 2.12, which comprises five distinctive phases. The system's response starts from the initial condition represented by $\times$ and is attracted by the SIM during phase 1. Upon reaching the stability border at point IV of Fig. 2.5, the system undergoes its first bifurcation (phase 2), moving to another branch of the SIM and leading to phase 3. Subsequently, the system reaches another stability border at point II of Fig. 2.5, bifurcating to another branch during phase 4. Finally, in phase 5, the system reduces its energy until it reaches the rest position. The different geometry of the SIM, i.e., the possession of two unstable zones, compared to the one of systems with pure cubic nonlinearity, can permit more efficient energy exchanges in the meta-cell due to possible double bifurcations (depending on initial conditions). Furthermore, as it can be seen in Figs. 2.12b and 2.12c, the vibratory energy reduction can be faster or slower depending on which branch of the SIM it occurs, i.e., depending on the energy levels. By examining Fig. 2.12c more closely, it becomes clear that the two significant energy reductions, i.e., phases 2 and 4, take a similar time, while the amount of reduced energy is larger in the first stage.
The system can present two, one, or no bifurcations for free responses depending on initial conditions. Let us consider the initial conditions $(w, v, \dot{w}, \dot{v}) = (2, 2, 0, 0)$ and $(w, v, \dot{w}, \dot{v}) = (1, 1, 0, 0)$, represented by $\times$ symbol in Figs. 2.13a and 2.13b, respectively. Numerical results of Fig. 2.13a present a simple bifurcation. In contrast, the results of Fig. 2.13b do not show any bifurcation due to the position of initial conditions below the threshold of any bifurcation.

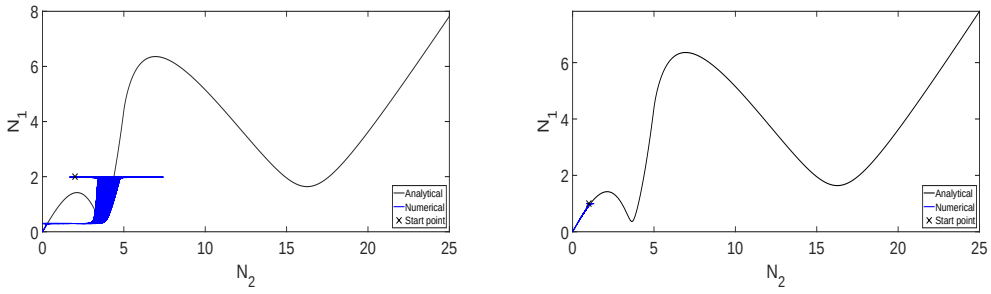

(a) (b)

Figure 2.13: The SIM of the system and corresponding responses obtained by numerical time integration of Eq. (2.13) with $\gamma = 0$. The initial conditions are: (a) $(w, v, \dot{w}, \dot{v}) = (2, 2, 0, 0)$; (b) $(w, v, \dot{w}, \dot{v}) = (1, 1, 0, 0)$.

2.4.2 Forced responses

Frequency response curves, obtained from analytical developments (see Eq. (2.54)), are presented in this section. Depending on the excitation amplitude γ, different frequency responses are observed, including the emergence of an isola. In addition, numerical time responses for some excitation frequencies in the vicinity of the resonance, obtained by setting σ to a specific value, are provided and compared with analytical predictions, representing different possible dynamic regimes.

2.4.2.1 External forcing amplitude $\gamma = 1$

A forced system with $\gamma = 1$ is studied. Equilibrium points of the system for sweeping detuning parameter σ or sweeping deriving frequency ($\vartheta = 1 + \sigma\varepsilon$) are obtained from Eq. (2.54) and, then,

from Eq. (2.33). The three-dimensional view of corresponding frequency responses is illustrated in Fig. 2.14, as well as its orthogonal projections on each plane. In this figure, the equilibrium points situated in the unstable zones of the SIM are highlighted in green color. Two-dimensional

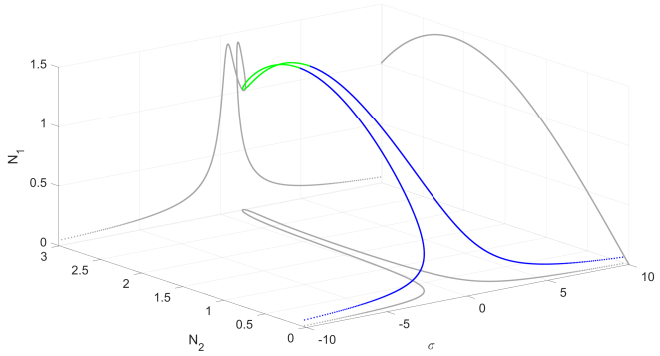

Figure 2.14: Branch of detected equilibrium points of the system with respect to the detuning parameter σ or deriving frequency ($\vartheta = 1 + \sigma\varepsilon$) for the system with $\gamma = 1$. Projections of this three-dimensional curve on different plans are presented in grey. The equilibrium points in the unstable zones of the SIM are represented in green color. Results are obtained from Eqs. (2.54) and (2.33).

views of Fig. 2.14 are presented in Figs. 2.15a and 2.15b. These figures show that the system can present more than one equilibrium point depending on the value of σ. The two-dimensional view of Fig. 2.14 in terms of N_1 and N_2 is depicted in Fig. 2.15c. This figure is a part of the SIM of the system, and it provides necessary information about the positions of equilibrium points on the SIM for the given forcing amplitude and for an interval of deriving frequency. In other words, Fig. 2.15c shows the geometrical positions of all possible equilibrium points on the SIM for $\gamma = 1$ and a given interval of σ. For clarity, the covered equilibrium points on the SIM for $\gamma = 1$ are framed in Fig. 2.15d.
In summary, analytical developments permit to:

- Identify the SIM and the three-dimensional frequency response curves;
- Detect the position of equilibrium points on the SIM for a given forcing amplitude and a sweeping frequency;
- Identify equilibrium points situated in the unstable zones of the SIM. If the system possesses only one equilibrium point and it is in the unstable zone, it will present modulated response [Starosvetsky and Gendelman, 2008, Hurel et al., 2019];
- Identify all possible branches of frequency response curves, even the isola, which can correspond to high amplitude levels of the cell. This should be avoided if the objective is system control, but it can be advantageous if the goal is energy harvesting.

Let us consider some detuning parameters for the case of $\gamma = 1$ and compare analytical predictions with numerical results.

Meta-cell behavior for $\sigma = 0$ For $\sigma = 0$, there is only one equilibrium point that is stable (Figs. 2.15a and 2.15b). A periodic response is thus expected whatever the initial conditions. The SIM is plotted in Fig. 2.16a, as well as the corresponding numerical results for $\gamma = 1$, $\sigma = 0$ and the

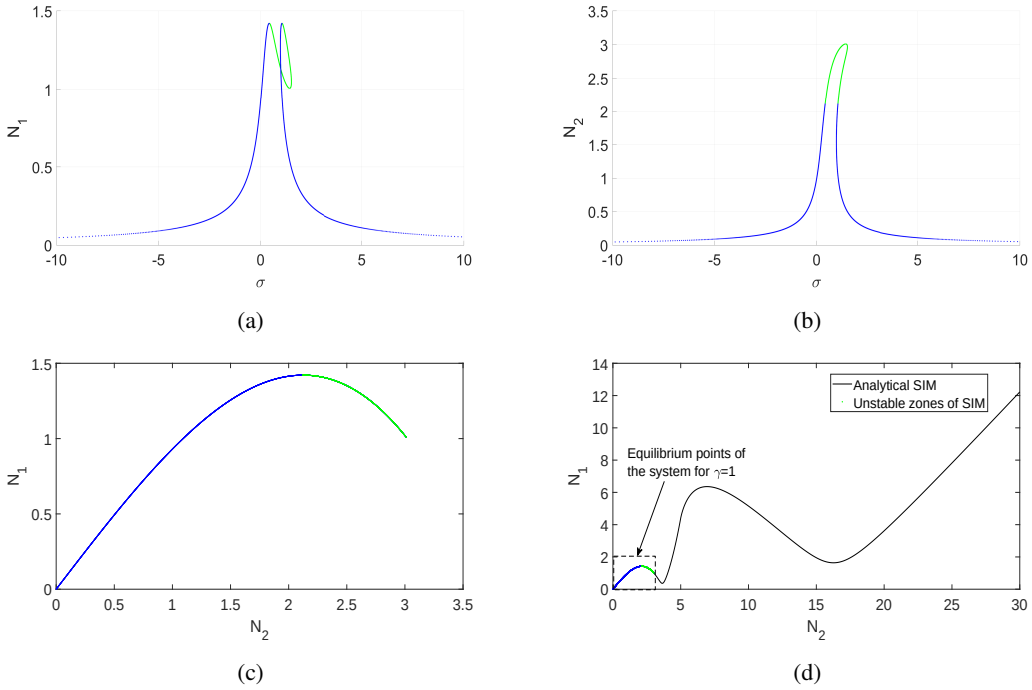

Figure 2.15: Two-dimensional views of Fig. 2.14. (a) N_1 with respect to the detuning parameter σ; (b) N_2 with respect to σ; (c) N_1 versus N_2; (d) Superposition of Fig. 2.15c on the SIM of Fig. 2.4.

initial conditions $(w, v, \dot{w}, \dot{v}) = (0, 0, 0, 0)$. The behavior of N_1 and N_2 over time can be visualized in Figs. 2.16b and 2.16c respectively, from which it is noticed that N_1 and N_2 present a periodic response, converging to the values of Figs. 2.15a and 2.15b, respectively, for $\sigma = 0$.

Meta-cell behavior for $\sigma = 0.8$ From Figs. 2.15a and 2.15b, it is noticed that the only equilibrium point for $\sigma = 0.8$ is situated in an unstable zone of the SIM. Thus, a SMR is expected, whatever the initial conditions. It should be mentioned that this modulated response will be around the first pair of local extrema of the SIM (I and II in Fig. 2.4) because of the predictions depicted in Figs. 2.15c and 2.15d.
The SIM accompanied by numerical results for $\gamma = 1$, $\sigma = 0.8$ and the initial conditions $(w, v, \dot{w}, \dot{v}) = (0, 0, 0, 0)$ are presented in Fig. 2.17a. The behavior of N_1 and N_2 over time can be visualized in Figs. 2.17b and 2.17c respectively, from which it is noticed that N_1 and N_2 present SMR, as predicted. These results show that the SMR is around local extrema I and II, as already predicted by analytical developments.

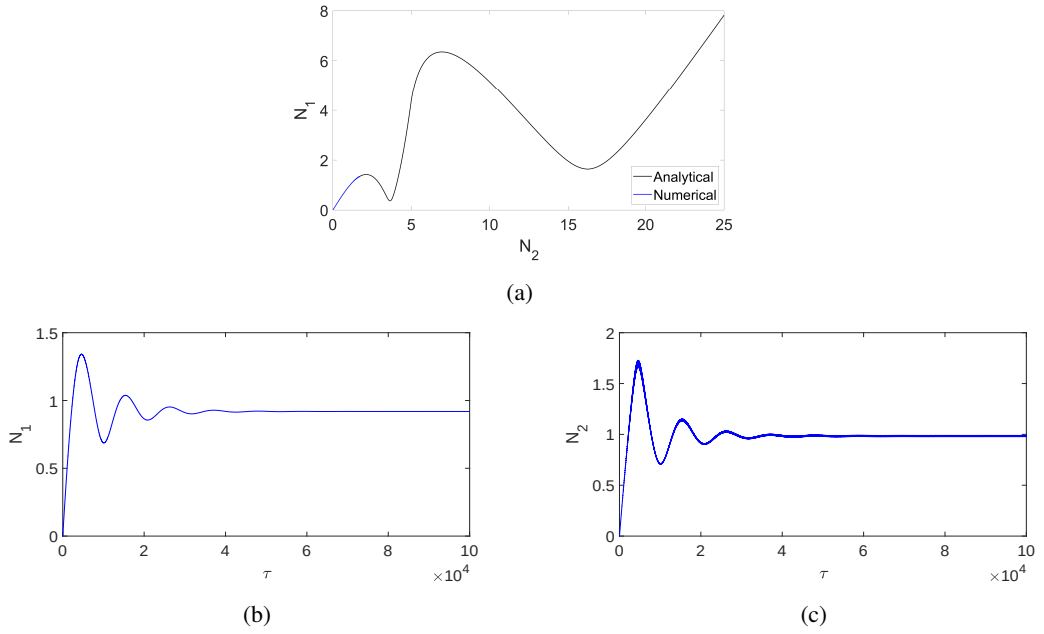

(a) (b) (c)

Figure 2.16: (a) SIM of the system and corresponding numerical results obtained by numerical time integration of Eq. (2.13); (b) N_1 versus τ; (c) N_2 versus τ. The system is under external excitation with $\gamma = 1$, $\sigma = 0$ and $(w, v, \dot{w}, \dot{v}) = (0, 0, 0, 0)$ at $\tau = 0$.

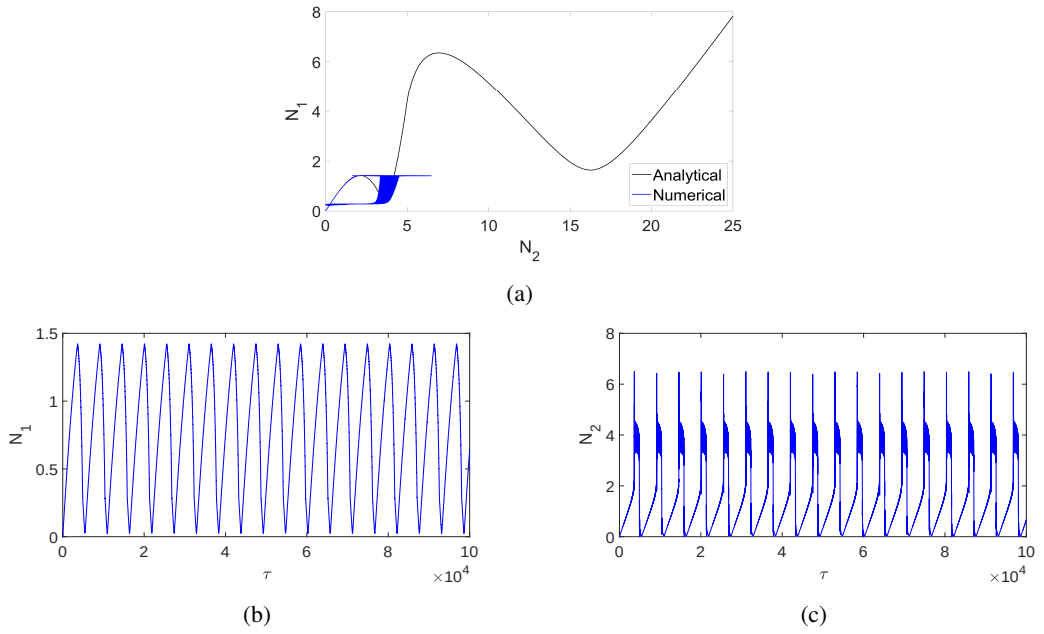

(a) (b) (c)

Figure 2.17: (a) The SIM of the system and corresponding numerical results obtained by numerical time integration of Eq. (2.13); (b) N_1 versus τ; (c) N_2 versus τ. The system is under external excitation with $\gamma = 1$, $\sigma = 0.8$ and $(w, v, \dot{w}, \dot{v}) = (0, 0, 0, 0)$ at $\tau = 0$.

2.4.2.2 External forcing amplitude $\gamma = 2$

For a forcing amplitude γ larger than a certain value, the emergence of an isola is observed. This isola is represented in red in Fig. 2.18 for $\gamma = 2$. Two-dimensional views of Fig. 2.18 are presented in Figs. 2.19a and 2.19b. The isola could present high energy levels for the outer cell and be unsafe if the goal is system control. However, for energy harvesting aspects, the isola could be interesting. The two-dimensional view of Fig. 2.18 in terms of N_1 and N_2 is depicted in Fig. 2.19c, and is accompanied by the SIM in Fig. 2.19d, highlighting the position of the isola on the SIM for $\gamma = 2$. It is seen that the second main part of the SIM, corresponding to the second local maximum (i.e., point III in Fig. 2.4), is activated for this set of characteristics of external excitation.

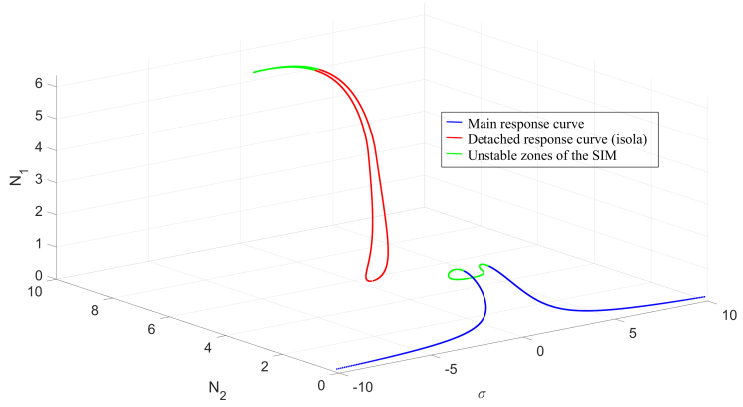

Figure 2.18: Detected equilibrium points of the system with respect to the detuning parameter σ or deriving frequency $(\vartheta = 1 + \sigma\varepsilon)$ for the system with $\gamma = 2$. The unstable zone of the SIM is represented in green color. Results are obtained from Eqs. (2.54) and (2.33).

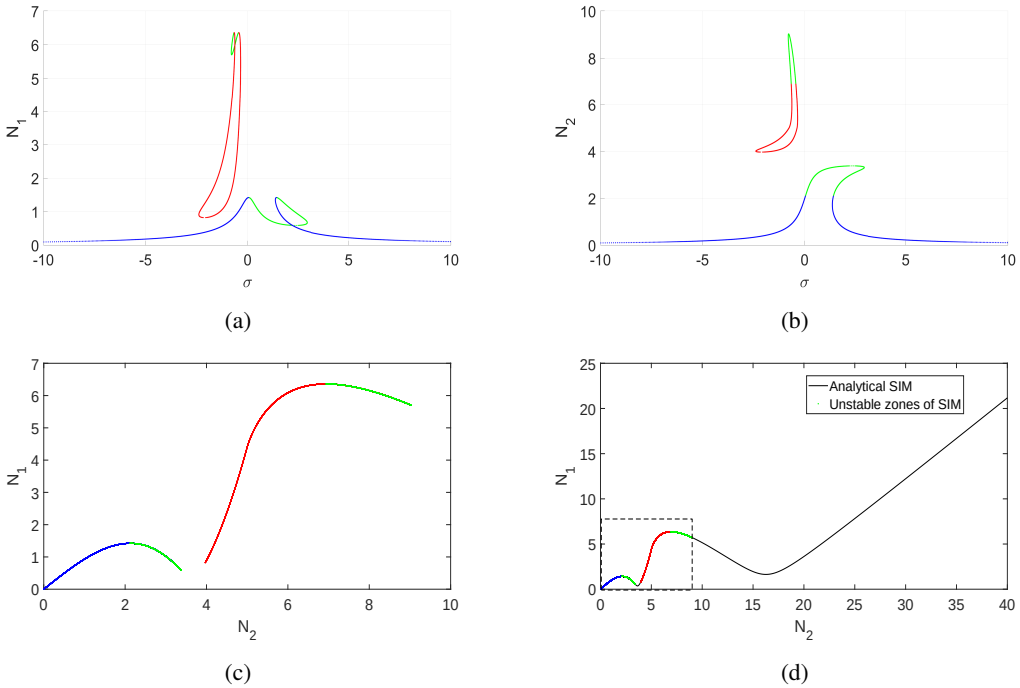

Figure 2.19: Two-dimensional views of Fig. 2.18. (a) N_1 with respect to the detuning parameter σ; (b) N_2 with respect to σ; (c) N_1 versus N_2; (d) Superposition of Fig. 2.19c on the SIM of Fig. 2.4.

Let us now consider some detuning parameters for the case of $\gamma = 2$ and compare analytical predictions with numerical results.

Meta-cell behavior for $\sigma = -1.8$ Figure 2.20a collects the SIM of the system and corresponding numerical results for $\gamma = 2$, $\sigma = -1.8$ and the initial conditions $(w, v, \dot{w}, \dot{v}) = (4, 4, 0, 0)$. The time histories of N_1 and N_2 can be visualized in Figs. 2.20b and 2.20c respectively. Comparing Figs. 2.19a and Fig. 2.20b, one can see that the system is attracted by the lowest branch of frequency response curves for $\sigma = -1.8$. Besides that, in Fig. 2.20, we spot three distinct phases of energy reduction: Phase 1, which is quick; Phase 2, which is slightly slower; and Phase 3, which is the slowest. The classification is based on the energy reduction rate. This allows an absorber to act in different phases, which can be adjusted with the proper design of the SIM.

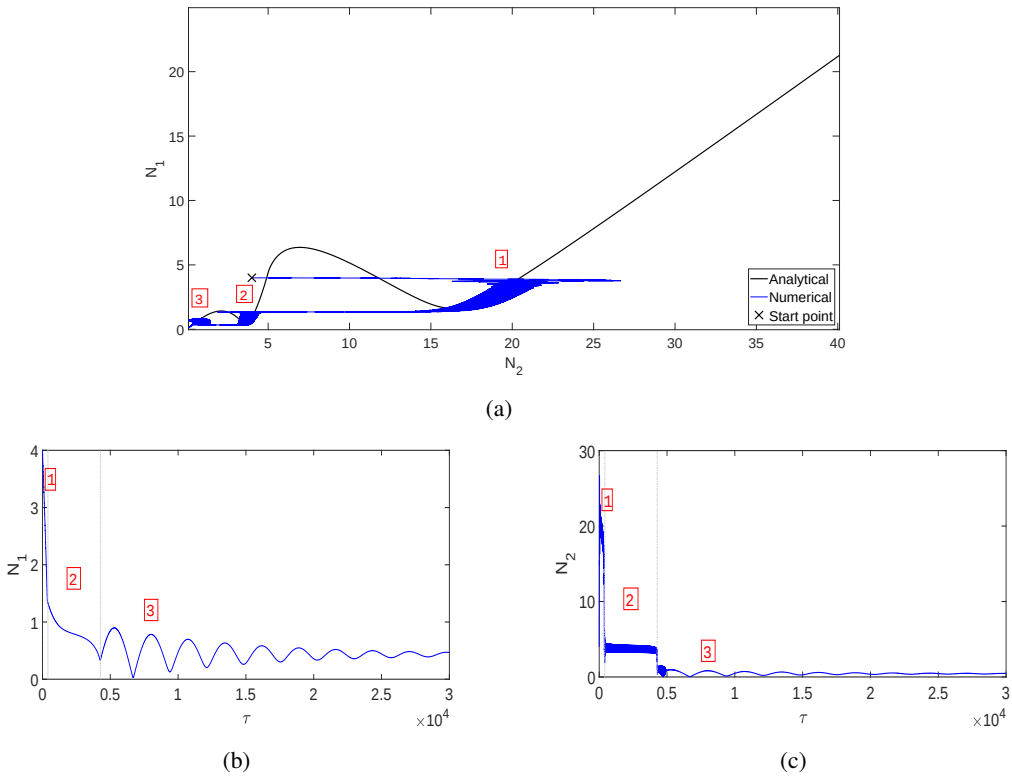

(a)

(b) (c)

Figure 2.20: (a) The SIM of the system and corresponding numerical results obtained by numerical time integration of Eq. (2.13); (b) N_1 versus τ; (c) N_2 versus τ. Three phases of vibratory energy reduction are depicted in these figures. The system is under external excitation with $\gamma = 2$, $\sigma = -1.8$ and $(w, v, \dot{w}, \dot{v}) = (4, 4, 0, 0)$ at $\tau = 0$.

Depending on the initial conditions, the system may reach a higher equilibrium point in the isola. This behavior can be observed for the initial conditions $(w, v, \dot{w}, \dot{v}) = (14, 7, 0, 0)$ in Fig. 2.21a. This can be spotted by comparing the results of numerical integration (Figs. 2.21b and 2.21c) and the values of N_1 and N_2 in Figs. 2.19a and 2.19b, respectively, for $\sigma = -1.8$.

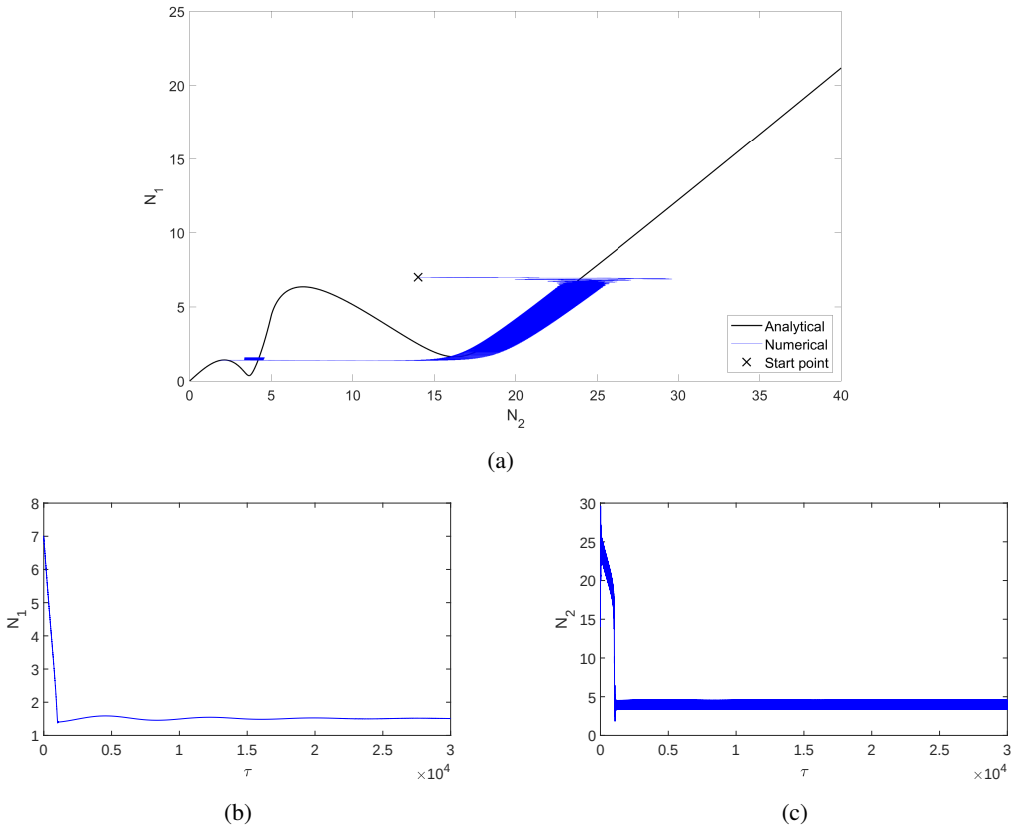

Figure 2.21: (a) The SIM of the system and corresponding numerical results obtained by numerical time integration of Eq. (2.13); (b) N_1 versus τ; (c) N_2 versus τ. The system is under external excitation with $\gamma = 2$, $\sigma = -1.8$ and $(w, v, \dot{w}, \dot{v}) = (14, 7, 0, 0)$ at $\tau = 0$.

Meta-cell behavior for $\sigma = -0.66$ The SIM is plotted in Fig. 2.22a, accompanied by numerical results for $\gamma = 2$, $\sigma = -0.66$ with initial conditions $(w, v, \dot{w}, \dot{v}) = (6, 9, 0, 0)$. The behavior of N_1 and N_2 over time can be visualized in Figs. 2.22b and 2.22c respectively. In this case, it is observed a peculiar transient response with two cycles of double bifurcation and subsequent attraction to the equilibrium point in the lowest branch of the frequency response curves.

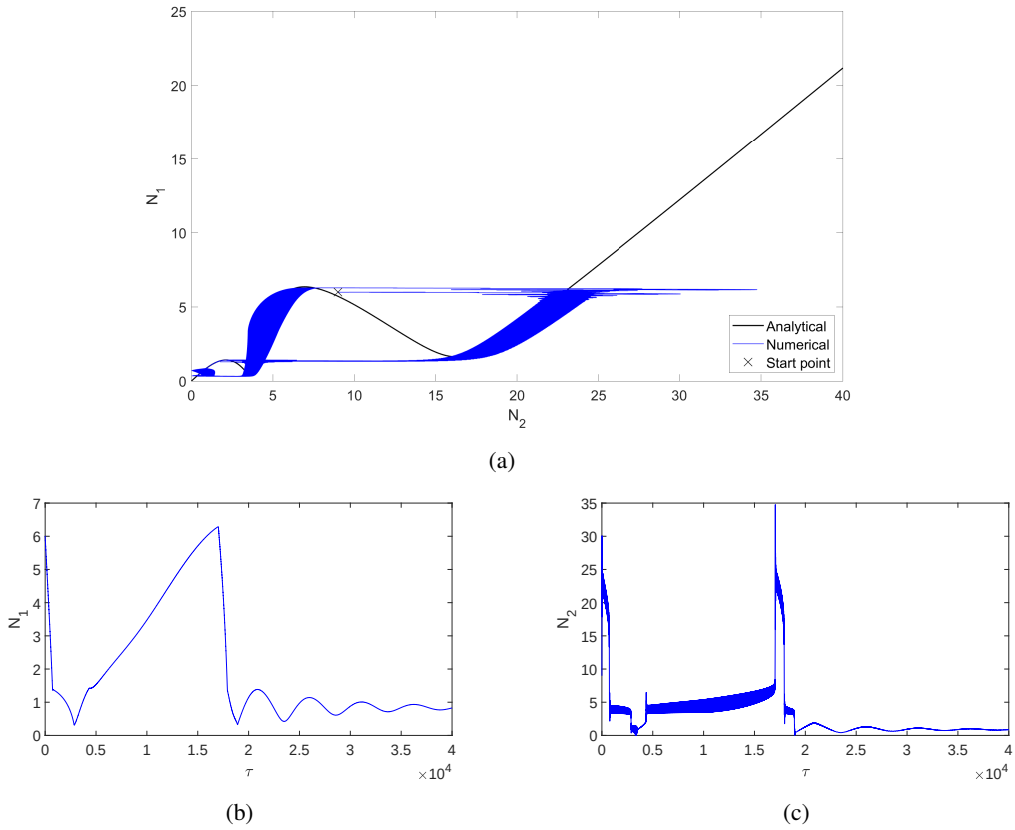

Figure 2.22: (a) The SIM of the system and corresponding numerical results obtained by numerical time integration of Eq. (2.13); (b) N_1 versus τ; (c) N_2 versus τ. The system is under external excitation with $\gamma = 2$, $\sigma = -0.66$ and $(w, v, \dot{w}, \dot{v}) = (6, 9, 0, 0)$ at $\tau = 0$.

Meta-cell behavior for $\sigma = 1$ For $\sigma = 1$ in Figs. 2.19a and 2.19b, it is seen that the equilibrium point is situated in an unstable zone of the SIM. The SIM is plotted in Fig. 2.23a, as well as the numerical results for the initial conditions $(w, v, \dot{w}, \dot{v}) = (0, 0, 0, 0)$. Time histories of N_1 and N_2 are presented in Figs. 2.23b and 2.23c respectively. These figures show that the system reaches a SMR as predicted by analytical developments.

2.4.2.3 External forcing amplitude $\gamma = 3.5$

Let's look at the systems behavior when the forcing amplitude is $\gamma = 3.5$. The corresponding frequency response curves and their two-dimensional views are in Figs. 2.24, 2.25a, and 2.25b, respectively. Figure 2.25c shows a two-dimensional view of Figure 2.24 in terms of N_1 and N_2 and is accompanied by the SIM in Figure 2.25d.

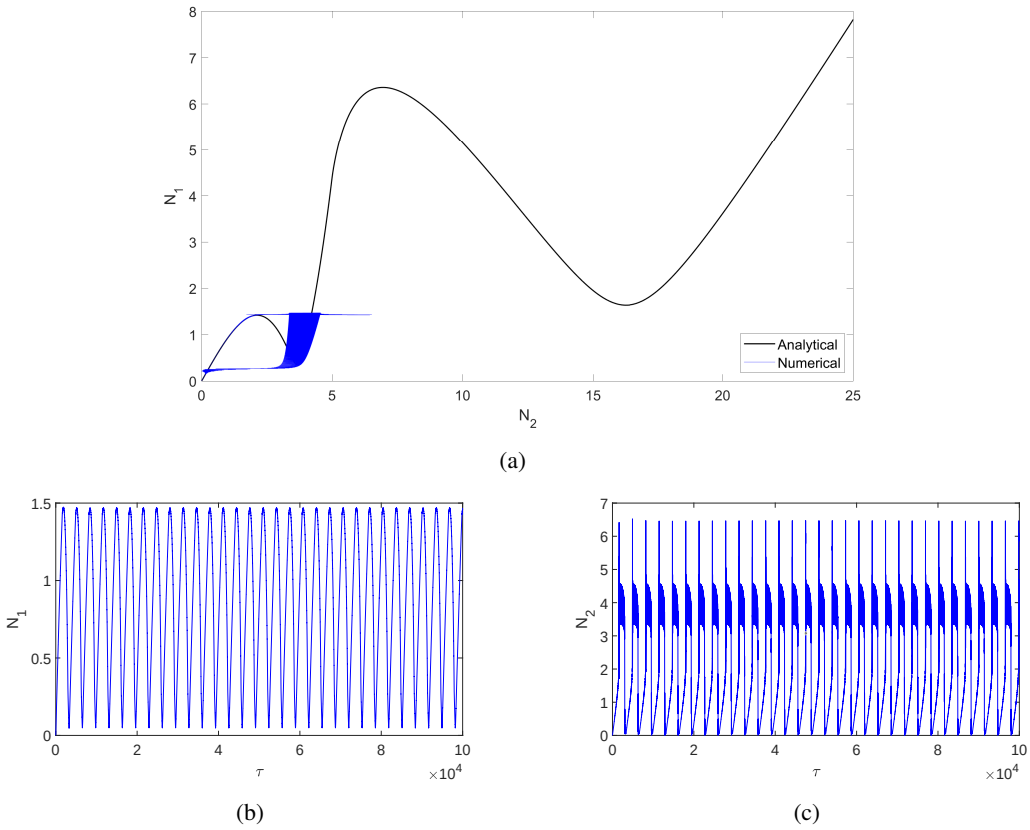

Figure 2.23: (a) The SIM of the system and corresponding numerical results obtained by numerical time integration of Eq. 2.13; (b) N_1 versus τ; (c) N_2 versus τ. The system is under external excitation with $\gamma = 2$, $\sigma = 1$ and $(w, v, \dot{w}, \dot{v}) = (0, 0, 0, 0)$ at $\tau = 0$.

Let us now compare analytical predictions with numerical results considering the detuning parameters $\sigma = -0.4$.

Meta-cell behavior for $\sigma = -0.4$ Based on Figs. 2.25a and 2.25b, it can be observed that when $\sigma = -0.4$, all equilibrium points are either located in the unstable regions (highlighted in green) or in the lowest branch of the isola, also known as an unstable region [Guillot et al., 2022]. Therefore, one can expect only modulated responses for this particular value of σ.
Figure 2.26a shows the SIM of the system and the corresponding numerical results for $\gamma = 3.5$, $\sigma = -0.4$, and initial conditions of $(w, v, \dot{w}, \dot{v}) = (10, 10, 0, 0)$. The time histories of N_1 and N_2 are presented in Figs. 2.26b and 2.26c, respectively. We notice here a new behavior, that is, a SMR concentrated in the highest part of the SIM, where the response bifurcates between the local extrema III and IV.

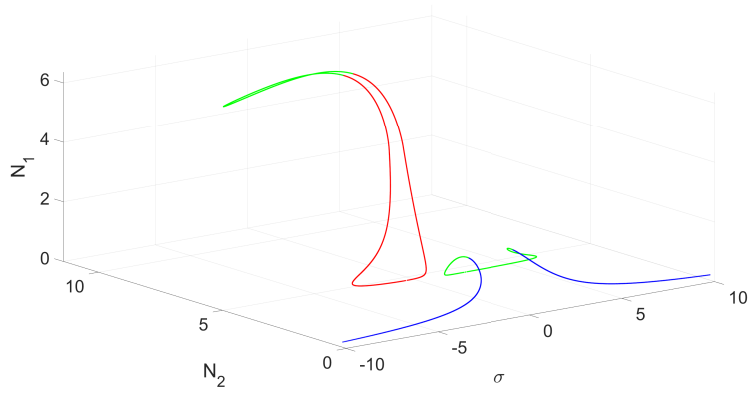

Figure 2.24: Detected equilibrium points of the system with respect to the detuning parameter σ or deriving frequency $(\vartheta = 1 + \sigma\varepsilon)$ for the system with $\gamma = 3.5$. The unstable zone of the SIM is represented in green color. Results are obtained from Eqs. (2.54) and (2.33).

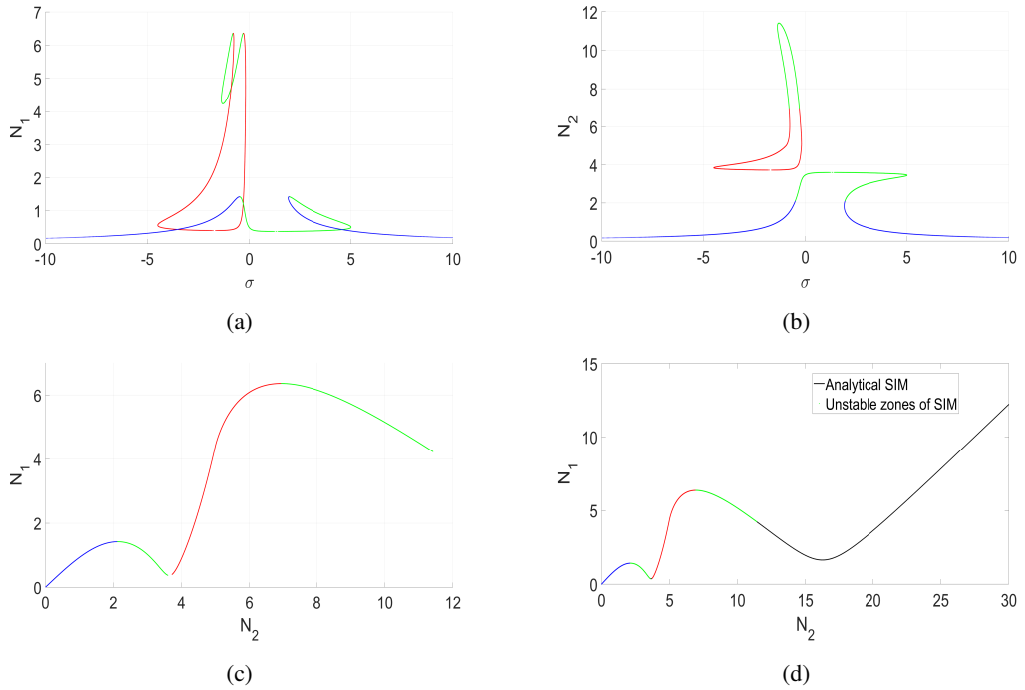

Figure 2.25: Two-dimensional views of Fig. 2.24. (a) N_1 with respect to the detuning parameter σ; (b) N_2 with respect to σ; (c) N_1 versus N_2; (d) Superposition of Fig. 2.19c on the SIM of Fig. 2.4.

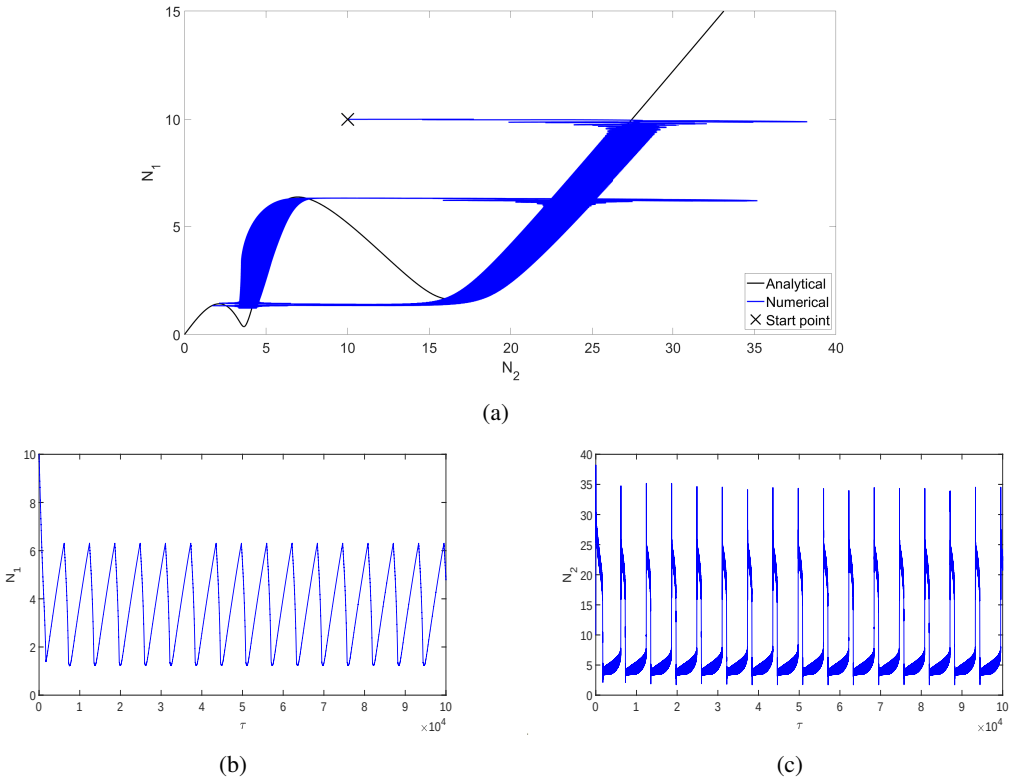

(a) (b) (c)

Figure 2.26: (a) The SIM of the system and corresponding numerical results obtained by numerical time integration of Eq. (2.13); (b) N_1 versus τ; (c) N_2 versus τ. The system is under external excitation with $\gamma = 3.5$, $\sigma = -0.4$ and $(w, v, \dot{w}, \dot{v}) = (10, 10, 0, 0)$- at $\tau = 0$.

2.4.2.4 External forcing amplitude $\gamma = 10$

The equilibrium points of the system concerning the sweeping detuning parameter σ are depicted in Fig. 2.27 for $\gamma = 10$. For this level of excitation, it can be observed that the previous isola merged with the main response curve and that a new isola appeared at higher amplitudes. Figs. 2.28 and 2.29 present different two-dimensional views derived from Fig. 2.27. Figures 2.28a and 2.28b show the possible multiplicity of equilibrium points in terms of N_1 and N_2, respectively, for a specific σ. Meanwhile, Figs. 2.29a and 2.29b reveal that the forcing amplitude $\gamma = 10$ activates both zones of local extrema of the SIM.

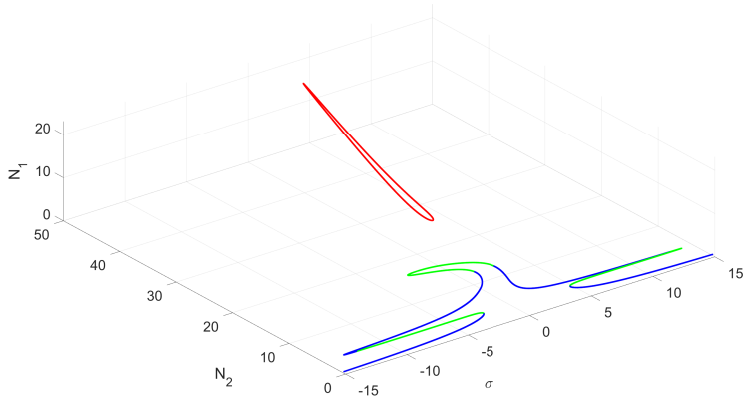

Figure 2.27: Detected equilibrium points of the system with respect to the detuning parameter σ or deriving frequency $(\vartheta = 1 + \sigma\varepsilon)$ for $\gamma = 10$. The unstable zone of the SIM is represented in green color. Results are obtained from Eqs. (2.54) and (2.33).

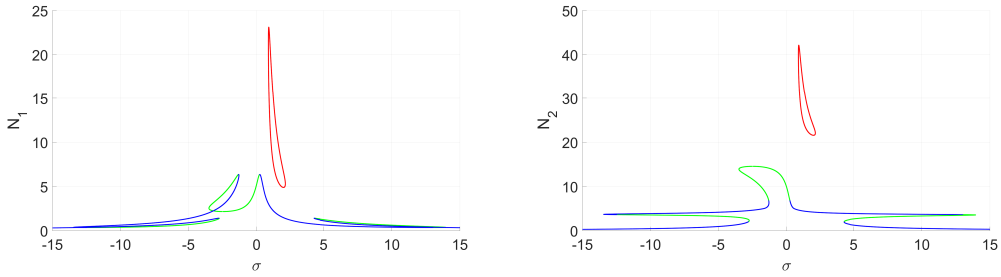

(a) (b)

Figure 2.28: Two-dimensional views of Fig. 2.27. (a) N_1 with respect to the detuning parameter σ; (b) N_2 with respect to σ.

2.4.3 Backbone curves

The backbone curves provide an overall vision of all possible dynamic behaviors of the system, as we can see in Fig. 2.30, where the frequency response curves corresponding to different values of γ treated in Sect. 2.4.2 are added to Fig. 2.6. Fig. 2.30 shows the emergence of possible non-continuous frequency responses of the system with an isola placed in the B2 or B3 branches. Moreover, it is seen that the backbone curves pass (almost) through local extrema of frequency responses under different external forcing amplitudes.
This study provides valuable tools to estimate possible system amplitude levels for a range of external excitation characteristics, including amplitudes and frequencies.

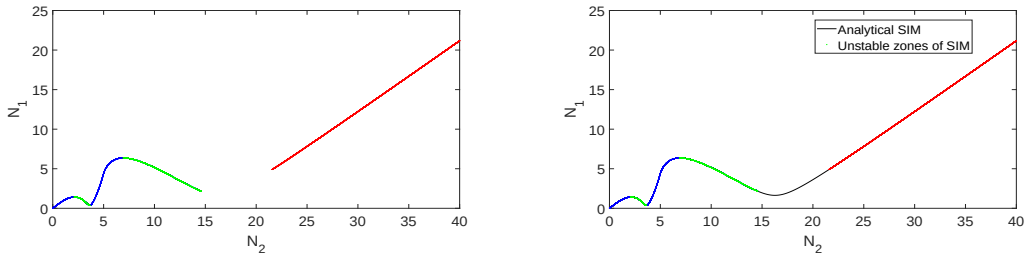

(a) (b)

Figure 2.29: Two-dimensional views of Fig. 2.27. (a) N_1 versus N_2; (b) Superposition of Fig. 2.29a on the SIM of Fig. 2.4.

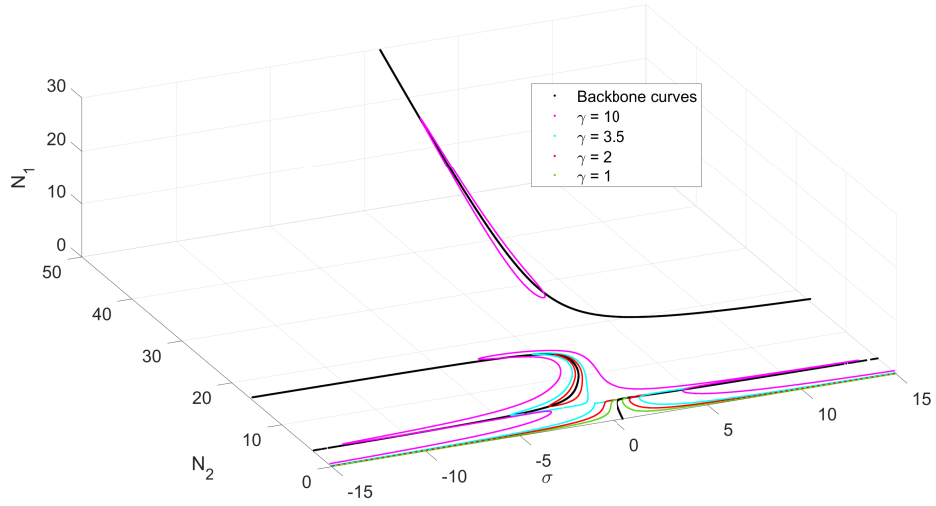

Figure 2.30: Backbone and frequency response curves for different values of γ.

2.5 Conclusions of the chapter

Vibratory energy exchanges between particles of a two-degree-of-freedom meta-cell are studied. The system is composed of an outer mass that houses an inner mass with a piecewise nonlinearity. Fast and slow dynamics of the system are investigated, leading to detection of the slow invariant manifold and of dynamic characteristic points. The piecewise nonlinearity of the inner mass results in a slow invariant manifold with four local extrema, differing from corresponding ones of systems with pure cubic and piecewise-linear nonlinearities. The frequency response curves, along with a three-dimensional view of detected equilibrium points, permit the identification of possible isolas and the position of equilibrium points on the slow invariant manifold, especially in its unstable zones. Depending on the nature of the equilibrium points and the existence of singularities, the system can present one, two, or several bifurcations, leading to final periodic or non-periodic regimes. Furthermore, the vibratory energy reduction can be faster or slower depending on which branch of the slow invariant manifold it occurs, i.e., depending on the energy level. This allows an absorber to act in different phases, which can be adjusted with the proper design of the slow invariant manifold. Special attention must be paid to systems that present isola. If the objective is the system control,

these isola should not present high energy levels for the cell. However, isola can be interesting for energy harvesting aspects.
The analytical developments in this chapter offer design tools for adjusting the piecewise nonlinearity of the inner mass. This tuning enables the system to exhibit periodic or non-periodic responses based on given external forcing characteristics or to fulfill specific objectives, such as control or energy harvesting.
The system presented in this chapter serves several objectives: the inner mass, with its proposed piecewise nonlinearity, can be utilized for multi-phase vibration control, serving as a nonlinear energy sink and/or for harvesting the vibratory energy of the outer mass. Additionally, it can be considered as a single meta-cell with spatial characteristics in a chain of nonlinear mass-in-mass cells. This aspect is further explored in Chapter 3 of this manuscript.

CHAPTER 3

Chain of nonlinear meta-cells

In this chapter, we delve into the study of a chain of coupled meta-cells introduced in Chapter 2. Firstly, the discrete model of the system is presented, followed by the transition to the continuous domain. The modal characteristics of the continuous model are evaluated and the system is studied in the vicinity of one of its arbitrary modes. Then, employing the multiple time scale method, we analyze the complexified system equations to reveal both fast and slow dynamics. To conclude, we compare the dynamic responses of the original model with those obtained from analytical predictions of the projected model.

3.1 Model of the discrete chain

A periodic chain of mass-in-mass cells is illustrated in Fig. 3.1. It consists of outer masses denoted as M that house inner masses labeled as m, with corresponding generalized displacements $u_j(t)$ and $v_j(t)$, respectively. The outer masses are spaced with a distance of ΔX at their rest positions and are interconnected by linear springs with a constant stiffness of K_1 and linear dampers with a constant coefficient of C_1. The inner and outer masses are linked via a constant damping coefficient, C_2 and a nonlinear restoring force, $F(\alpha)$, which is a function of the relative displacement between the two masses of a same cell, as defined in Eq. (2.2). Additionally, the outer masses are subject to external sinusoidal excitation $S_j(t) = P_j \sin(\Omega t)$. The L-periodicity of the chain establishes a relationship between cells numbered 1 and L, treating them as neighbors. This periodic arrangement is employed to approximate the concept of a metamaterial.
The equations governing the jth cell, $j = 1, ..., L$, are expressed as follows:

$$\begin{cases} M\dfrac{\mathrm{d}^2u_j}{\mathrm{d}t^2} + K_1(2u_j - u_{j-1} - u_{j+1}) + F(u_j - v_j) \\ +C_1\left(2\dfrac{\mathrm{d}u_j}{\mathrm{d}t} - \dfrac{\mathrm{d}u_{j-1}}{\mathrm{d}t} - \dfrac{\mathrm{d}u_{j+1}}{\mathrm{d}t}\right) + C_2\left(\dfrac{\mathrm{d}u_j}{\mathrm{d}t} - \dfrac{\mathrm{d}v_j}{\mathrm{d}t}\right) = P_j \sin(\Omega t) \\ \\ m\dfrac{\mathrm{d}^2v_j}{\mathrm{d}t^2} + F(v_j - u_j) + C_2\left(\dfrac{\mathrm{d}v_j}{\mathrm{d}t} - \dfrac{\mathrm{d}u_j}{\mathrm{d}t}\right) = 0 \end{cases} \tag{3.1}$$

Let us introduce the dimensionless time τ as:

$$\tau = \omega t \tag{3.2}$$

where ω represents an arbitrary frequency. Therefore, Eq. (3.1) can be expressed as:

$$\begin{cases} M\omega^2\dfrac{\mathrm{d}^2u_j}{\mathrm{d}\tau^2} + K_1(2u_j - u_{j-1} - u_{j+1}) + F(u_j - v_j) \\ +C_1\omega\left(2\dfrac{\mathrm{d}u_j}{\mathrm{d}\tau} - \dfrac{\mathrm{d}u_{j-1}}{\mathrm{d}\tau} - \dfrac{\mathrm{d}u_{j+1}}{\mathrm{d}\tau}\right) + C_2\omega\left(\dfrac{\mathrm{d}u_j}{\mathrm{d}\tau} - \dfrac{\mathrm{d}v_j}{\mathrm{d}\tau}\right) = P_j \sin(\lambda\tau) \\ \\ m\omega^2\dfrac{\mathrm{d}^2v_j}{\mathrm{d}\tau^2} + F(v_j - u_j) + C_2\omega\left(\dfrac{\mathrm{d}v_j}{\mathrm{d}\tau} - \dfrac{\mathrm{d}u_j}{\mathrm{d}\tau}\right) = 0 \end{cases} \tag{3.3}$$

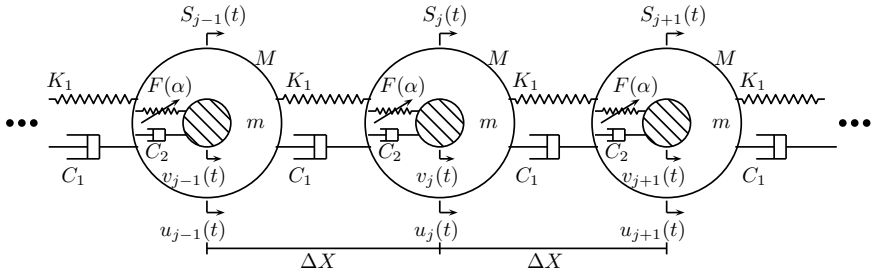

Figure 3.1: Representation of the periodic mass-in-mass chain. The outer masses denoted as M, with displacements $u_j(t)$, enclose inner masses labeled as m, with associated displacements $v_j(t)$. The nonlinear function $F(\alpha)$ governs the restoring force acting on the inner masses.

where $\lambda = \dfrac{\Omega}{\omega}$. Dividing Eq. (3.3) by $M\omega^2$, it reads:

$$\begin{cases} \dfrac{\mathrm{d}^2 u_j}{\mathrm{d}\tau^2} + \dfrac{K_1}{M\omega^2}(2u_j - u_{j-1} - u_{j+1}) + \dfrac{F(u_j - v_j)}{M\omega^2} \\ + \dfrac{C_1}{M\omega}\left(2\dfrac{\mathrm{d}u_i}{\mathrm{d}\tau} - \dfrac{\mathrm{d}u_{j-1}}{\mathrm{d}\tau} - \dfrac{\mathrm{d}u_{j+1}}{\mathrm{d}\tau}\right) + \dfrac{C_2}{M\omega}\left(\dfrac{\mathrm{d}u_i}{\mathrm{d}\tau} - \dfrac{\mathrm{d}v_j}{\mathrm{d}\tau}\right) = \dfrac{P_j}{M\omega^2}\sin(\lambda\tau) \\ \\ \dfrac{m}{M}\dfrac{\mathrm{d}^2 v_j}{\mathrm{d}\tau^2} + \dfrac{F(v_j - u_j)}{M\omega^2} + \dfrac{C_2}{M\omega}\left(\dfrac{\mathrm{d}v_j}{\mathrm{d}\tau} - \dfrac{\mathrm{d}u_j}{\mathrm{d}\tau}\right) = 0 \end{cases} \tag{3.4}$$

Assuming $0 < \varepsilon = \dfrac{m}{M} \ll 1$, then the following parameters are introduced:

$$\begin{aligned} \frac{1}{\mu^2} = \frac{K_1}{M\omega^2} \quad , \quad \varepsilon\zeta_1 = \frac{C_1}{M\omega} \quad , \quad \varepsilon\zeta_2 = \frac{C_2}{M\omega} \quad , \quad \varepsilon p_j = \frac{P_j}{M\omega^2} \\ \varepsilon f(u_i - v_i) = \frac{F(u_i - v_i)}{M\omega^2} \quad , \quad \varepsilon K_{NL} = \frac{k_{NL}}{M\omega^2} \quad , \quad \varepsilon K_L = \frac{k_L}{M\omega^2} \end{aligned} \tag{3.5}$$

Consequently, Eq. (3.4) adopts the following dimensionless expression:

$$\begin{cases} \dfrac{\mathrm{d}^2 u_{j,D}}{\mathrm{d}\tau^2} + \dfrac{1}{\mu^2}(2u_{j,D} - u_{j-1,D} - u_{j+1,D}) + \varepsilon f(u_{j,D} - v_{j,D}) \\ + \varepsilon\zeta_1\left(2\dfrac{\mathrm{d}u_{j,D}}{\mathrm{d}\tau} - \dfrac{\mathrm{d}u_{j-1,D}}{\mathrm{d}\tau} - \dfrac{\mathrm{d}u_{j+1,D}}{\mathrm{d}\tau}\right) + \varepsilon\zeta_2\left(\dfrac{\mathrm{d}u_{j,D}}{\mathrm{d}\tau} - \dfrac{\mathrm{d}v_{j,D}}{\mathrm{d}\tau}\right) = \varepsilon p_{j,D}\sin(\lambda\tau) \\ \\ \varepsilon\dfrac{\mathrm{d}^2 v_{j,D}}{\mathrm{d}\tau^2} + \varepsilon f(v_{j,D} - u_{j,D}) + \varepsilon\zeta_2\left(\dfrac{\mathrm{d}v_{j,D}}{\mathrm{d}\tau} - \dfrac{\mathrm{d}u_{j,D}}{\mathrm{d}\tau}\right) = 0 \end{cases} \tag{3.6}$$

where the subscript D is introduced to indicate the discrete domain of the variables.

3.2 Passage from discrete to continuous domain

To analyze the system in the continuous domain, we establish:

$$X = (j-1)\Delta X \tag{3.7}$$

and we define:

$$x = \frac{X}{\Delta X} \tag{3.8}$$

Assuming that the considered chain possesses a large number of cells, i.e., $L \gg 1$, it is established:

$$u_{j,D}(\tau) = u_C(x = j-1, \tau) \qquad v_{j,D}(\tau) = v_C(x = j-1, \tau) \tag{3.9}$$

where the subscript C indicates the variables in the continuous domain, $x \in [0, L-1]$ and $(L-1)$ is the length of the chain in the continuous domain.
Applying Taylor series, one can write

$$u_{j\pm1,D}(\tau) = u_C\left(j-1,\tau\right) \pm \frac{\partial u_C\left(j-1,\tau\right)}{\partial x} + \frac{1}{2!}\frac{\partial u_C^2\left(j-1,\tau\right)}{\partial x^2} + ... + \frac{(\pm1)^n}{n!}\frac{\partial u_C^n\left(j-1,\tau\right)}{\partial x^n} \tag{3.10}$$

$$v_{j\pm1,D}(\tau) = v_C\left(j-1,\tau\right) \pm \frac{\partial v_C\left(j-1,\tau\right)}{\partial x} + \frac{1}{2!}\frac{\partial v_C^2\left(j-1,\tau\right)}{\partial x^2} + ... + \frac{(\pm1)^n}{n!}\frac{\partial v_C^n\left(j-1,\tau\right)}{\partial x^n} \tag{3.11}$$

From that, the term $(2u_{j,D} - u_{j-1,D} - u_{j+1,D})$ found in Eq. (3.6) can be written as follows:

$$\begin{aligned}
&2u_{j,D} - u_{j-1,D} - u_{j+1,D} = 2u_C\left(j-1,\tau\right) - \left[u_C\left(j-2,\tau\right) + u_C\left(j,\tau\right)\right] \\
&= 2u_C\left(j-1,\tau\right) - \Bigg[u_C\left(j-1,\tau\right) - \frac{\partial u_C\left(j-1,\tau\right)}{\partial x} + \frac{1}{2}\frac{\partial u_C^2\left(j-1,\tau\right)}{\partial x^2} + \mathcal{O}(u^3) \\
&+u_C\left(j-1,\tau\right) + \frac{\partial u_C\left(j-1,\tau\right)}{\partial x} + \frac{1}{2}\frac{\partial u_C^2\left(j-1,\tau\right)}{\partial x^2} + \mathcal{O}(u^3)\Bigg] \\
&= -\frac{\partial u_C^2\left(x,\tau\right)}{\partial x^2}
\end{aligned} \tag{3.12}$$

From this approximation and from Eq. (3.6), the dimensionless governing equations of the mass-in-mass system in the continuous domain are written as follows:

$$\begin{cases}
\dfrac{\partial^2 u_C(x,\tau)}{\partial \tau^2} - \dfrac{1}{\mu^2}\dfrac{\partial^2 u_C(x,\tau)}{\partial x^2} + \varepsilon f(w_C(x,\tau)) - \varepsilon\zeta_1\dfrac{\partial}{\partial\tau}\left(\dfrac{\partial^2 u_C(x,\tau)}{\partial x^2}\right) \\
+\varepsilon\zeta_2\dfrac{\partial w_C(x,\tau)}{\partial\tau} = \varepsilon p(x)\sin(\lambda\tau) \\
\\
\varepsilon\dfrac{\partial^2(u_C(x,\tau) - w_C(x,\tau))}{\partial\tau^2} - \varepsilon f(w_C(x,\tau)) - \varepsilon\zeta_2\dfrac{\partial w_C(x,\tau)}{\partial\tau} = 0
\end{cases} \tag{3.13}$$

where $w_C(x,\tau) = u_C(x,\tau) - v_C(x,\tau)$, i.e., the relative displacement of the two masses of each cell.

3.3 Evaluation of modal characteristics

In order to obtain the linear modes of the system defined in Eq. (3.13), we consider only the linear and conservative terms of this equation. Thus, we have:

$$\begin{cases}
\dfrac{\partial^2 u_C(x,\tau)}{\partial \tau^2} - \dfrac{1}{\mu^2}\dfrac{\partial^2 u_C(x,\tau)}{\partial x^2} = 0 \\
\\
\varepsilon\dfrac{\partial^2(u_C(x,\tau) - w_C(x,\tau))}{\partial\tau^2} = 0
\end{cases} \tag{3.14}$$

Let us suppose that

$$u_C(x,\tau) = A(x)e^{i\beta\tau} \qquad w_C(x,\tau) = C(x)e^{i\beta\tau} \tag{3.15}$$

where $\beta = 1$. Thus, system (3.14) takes the following solutions:

$$A(x) = B_1\cos(\mu x) + B_2\sin(\mu x) \tag{3.16}$$

$$C(x) = A(x) \tag{3.17}$$

Considering the conditions of periodicity defined as:

$$\begin{cases} u_C(x,\tau) = u_C(x+L,\tau) \\ \dfrac{\partial u_C(x,\tau)}{\partial x}\Big|_{x,\forall\tau} = \dfrac{\partial u_C(x,\tau)}{\partial x}\Big|_{x+L,\forall\tau} \end{cases} \tag{3.18}$$

where L is the period of the chain. It leads to:

$$\begin{cases} A(0) = A(L) \\ \dfrac{\partial A(x)}{\partial x}\Big|_{x=0,\forall\tau} = \dfrac{\partial A(x)}{\partial x}\Big|_{x=L,\forall\tau} \end{cases} \tag{3.19}$$

After injection of conditions from Eq. (3.19) into Eq. (3.16), we obtain:

$$\underbrace{\begin{bmatrix} 1-\cos(\mu L) & -\sin(\mu L) \\ \sin(\mu L) & 1-\cos(\mu L) \end{bmatrix}}_{M} \begin{bmatrix} B_1 \\ B_2 \end{bmatrix} = \begin{bmatrix} 0 \\ 0 \end{bmatrix} \tag{3.20}$$

Non-trivial solutions of system (3.20) demands $\det(M) = 0$. From that, we obtain μ_k as

$$\mu_k = \frac{2k\pi}{L} \tag{3.21}$$

where k is the number of mode, that is, $k \in \mathbb{N}$.
From the first equation of the system (3.20), we obtain B_2 in function of B_1 as follows:

$$B_2 = \frac{1-\cos(\mu L)}{\sin(\mu L)}B_1 \tag{3.22}$$

Replacing B_2 in Eq. (3.16), we obtain the following mathematical expression for the mode shape:

$$A(x) = B_1\left(\cos(\mu x) + \frac{1-\cos(\mu L)}{\sin(\mu L)}\sin(\mu x)\right) \tag{3.23}$$

When $\lim\limits_{\mu\to\mu_k} \dfrac{1-\cos(\mu L)}{\sin(\mu L)} = 0$. Then, the final mathematical expression of the mode shape reads:

$$A_k(x) = B_1\cos(\mu_k x) \tag{3.24}$$

If one considers the second equation of the system (3.20), then following mode shape can be found as well:

$$A_k(x) = B_2\sin(\mu_k x) \tag{3.25}$$

Both Eqs. 3.24 and 3.25 define the mode shapes of the considered periodic chain. Due to the periodicity of the considered system, the functions $A_k(x) = B\sin(\mu_k x+\theta)$ or $A_k(x) = B\cos(\mu_k x+\theta)$ can be defined as the mode shape as well. For the rest of the paper we consider Eq. 3.24 as the mode shape of the system.
The coefficient B_1 in Eq. 3.24 can be obtained via normalization of $A_k(x)$ as:

$$\int_0^L A_k^2(x)\,dx = 1 \tag{3.26}$$

Leading to:

$$B_1 = \sqrt{\frac{2}{L}} \tag{3.27}$$

For further studies, we are interested in the system behaviors in the vicinity of one of its modes. To achieve this, we will project the system (3.13) on an arbitrary k^{th} mode, as shown in the next section.

3.4 Study of the system in the vicinity of one of its arbitrary modes

Projecting the system on the kth mode, the equations from (3.13) read:

$$\begin{cases} \displaystyle\int_0^L \left(\frac{\partial^2 u_C(x,\tau)}{\partial\tau^2} - \frac{1}{\mu_k^2}\frac{\partial^2 u_C(x,\tau)}{\partial x^2} + \varepsilon f(w_C(x,\tau)) - \varepsilon\zeta_1\frac{\partial}{\partial\tau}\left(\frac{\partial^2 u_C(x,\tau)}{\partial x^2}\right)\right. \\ \left. +\varepsilon\zeta_2\dfrac{\partial w_C(x,\tau)}{\partial\tau}\right)A_k(x)\,dx = \displaystyle\int_0^L \varepsilon p(x)\sin(\lambda\tau)A_k(x)\,dx \\ \\ \displaystyle\int_0^L \left(\varepsilon\frac{\partial^2(u_C(x,\tau)-w_C(x,\tau))}{\partial\tau^2} - \varepsilon f(w_C(x,\tau)) - \varepsilon\zeta_2\frac{\partial w_C(x,\tau)}{\partial t}\right)A_k(x)\,dx = 0 \end{cases} \tag{3.28}$$

We can express the overall responses of the system in terms of $u_C(x,\tau)$ and $w_C(x,\tau)$ as follows:

$$u_C(x,\tau) = \sum_{k=1}^{\infty} A_k(x)g_k(\tau) \qquad w_C(x,\tau) = \sum_{k=1}^{\infty} A_k(x)q_k(\tau) \tag{3.29}$$

where $g_k(\tau)$ and $q_k(\tau)$ represent the kth modal coordinates of the system.
Considering that the response of the system is dominated by its kth mode, we set:

$$u_C(x,\tau) = A_k(x)g_k(\tau) \qquad w_C(x,\tau) = A_k(x)q_k(\tau) \tag{3.30}$$

In further developments, we will remove the index k for $g_k(\tau)$ and $q_k(\tau)$.
Supposing that the external excitation distribution takes the form of kth mode via setting $p(x) = \gamma A(x)$, the system (3.28) yields the following reduced model:

$$\begin{cases} \dfrac{d^2 g_{MC}(\tau)}{d\tau^2} + g_{MC}(\tau) + \varepsilon\mathscr{F}(\tau) + \varepsilon\zeta_1\mu_k^2\dfrac{dg_{MC}(\tau)}{d\tau} + \varepsilon\zeta_2\dfrac{dq_{MC}(\tau)}{d\tau} = \varepsilon\gamma\sin(\lambda\tau) \\ \\ \varepsilon\left(\dfrac{d^2 g_{MC}(\tau)}{d\tau^2} - \dfrac{d^2 q_{MC}(\tau)}{d\tau^2}\right) - \varepsilon\mathscr{F}(\tau) - \varepsilon\zeta_2\dfrac{dq_{MC}(\tau)}{d\tau} = 0 \end{cases} \tag{3.31}$$

where the subscript MC indicates the variables in the modal domain obtained from the continuous one through projection. $\mathscr{F}(\tau)$ can be expressed as:

$$\mathscr{F}(\tau) = \begin{cases} \dfrac{3Lq_{MC}(\tau)^3 B_1^4 K_{NL}}{8} & \text{if} \quad |q_{MC}(\tau)| \leq \dfrac{\delta}{B_1} \\ \dfrac{LB_1}{16k\pi}\Bigg(16\delta q_{MC}(\tau)^2\sqrt{1-\dfrac{\delta^2}{q_{MC}(\tau)^2 {B_1}^2}}{B_1}^2 K_{NL} \\ +3(-1+2k)\pi q_{MC}(\tau)^3 {B_1}^3 K_{NL} \\ -16\delta\sqrt{1-\dfrac{\delta^2}{q_{MC}(\tau)^2 {B_1}^2}}K_L + 4\pi q(\tau) B_1 K_L\Bigg) & \text{if} \quad |q_{MC}(\tau)| > \dfrac{\delta}{B_1} \end{cases} \tag{3.32}$$

The calculation of $\mathscr{F}(\tau)$ was achieved by performing a space averaging process, as explained in Annex B.

3.5 Detection of different dynamics of the projected system

The complex variables introduced by Manevitch [Manevitch, 2001], which were previously detailed in this thesis, are employed according to the following relationship:

$$\begin{cases} \varphi_1 e^{i\lambda\tau} = \dot{g}_{MC}(\tau) + i\lambda g_{MC}(\tau) \\ \varphi_2 e^{i\lambda\tau} = \dot{q}_{MC}(\tau) + i\lambda q_{MC}(\tau) \end{cases} \tag{3.33}$$

with $i^2 = -1$.
Then, the Galerkin method, which was explained and applied in Chapter 2, is also employed in the system (3.31), leading to:

$$\begin{cases} \dfrac{\dot{\varphi}_1}{2} + \dfrac{i\lambda\varphi_1}{2} - \dfrac{i\varphi_1}{2\lambda} + \varepsilon\mathbb{F}(\varphi_2,\varphi_2^*) + \dfrac{\varepsilon\zeta_1\mu_k^2\varphi_1}{2} + \dfrac{\varepsilon\zeta_2\varphi_2}{2} = -\dfrac{i\varepsilon\gamma}{2} \\ \varepsilon\left(\dfrac{\dot{\varphi}_1}{2} + \dfrac{i\lambda\varphi_1}{2} - \dfrac{\dot{\varphi}_2}{2} - \dfrac{i\lambda\varphi_2}{2}\right) - \varepsilon\mathbb{F}(\varphi_2,\varphi_2^*) - \dfrac{\varepsilon\zeta_2\varphi_2}{2} = 0 \end{cases} \tag{3.34}$$

Where $\mathbb{F}(\varphi_2,\varphi_2^*)$ is:

$$\mathbb{F}(\varphi_2,\varphi_2^*) = \frac{\lambda}{2\pi}\int_0^{\frac{2\pi}{\lambda}} \mathscr{F}\left(\frac{\varphi_2 e^{i\lambda\tau} - \varphi_2^* e^{-i\lambda\tau}}{2i\lambda}\right) e^{-i\lambda\tau} d\tau \tag{3.35}$$

It can be shown that

$$\mathbb{F}(\varphi_2,\varphi_2^*) = -\frac{i\varphi_2}{2\lambda}\mathcal{G}(|\varphi_2|), \tag{3.36}$$

where $\mathcal{G}(|\varphi_2|)$ is obtained through a time averaging detailed in Annex C, where $\mathcal{G}(|\varphi_2|) = \mathbb{G}(|\varphi_2|) + \mathcal{O}(\varepsilon^1)$.

3.5.1 Fast dynamics: ε^0 order of system equations

Considering the system behaviors around a 1:1 resonance, i.e., setting $\lambda = 1 + \sigma\varepsilon$, where σ is a detuning parameter, the Eq. (3.34) for ε^0 order yields:

$$\begin{cases} \dot{\varphi}_1 + i\varphi_1 - i\varphi_1 = 0 \\ i\varphi_1 - \dot{\varphi}_2 - i\varphi_2 + i\varphi_2\mathbb{G}(|\varphi_2|) - \zeta_2\varphi_2 = 0 \end{cases} \tag{3.37}$$

As demonstrated in Chapter 2, we can derive $\dfrac{\partial\varphi_1}{\partial\tau_0}=0$ from the first equation of (3.37), and from the second equation, we can determine the asymptotic state of the system, which is:

$$\mathscr{H}=i\varphi_1-i\varphi_2+i\varphi_2\mathbb{G}(|\varphi_2|)-\zeta_2\varphi_2=0 \tag{3.38}$$

where $\mathscr{H}$ is the SIM of the system.
After expressing Manevitch's complex variables in the polar domain and applying them to Eq. (3.38), we arrive at the equation of the SIM in the real domain as follows:

$$N_1=N_2\sqrt{(1-\mathbb{G}(N_2))^2+\zeta_2^2} \tag{3.39}$$

3.5.2 Slow dynamics: ε^1 order of system equations

The first equation of system (3.34) at $\mathcal{O}(\varepsilon^1)$ reads:

$$\frac{\mathrm{d}\varphi_1}{\mathrm{d}\tau_1}=E_1(\varphi_1,\varphi_2,\varphi_1^*,\varphi_2^*) \tag{3.40}$$

where

$$E_1(\varphi_1,\varphi_2,\varphi_1^*,\varphi_2^*)=-2i\sigma\varphi_1+i\varphi_2\mathbb{G}(|\varphi_2|)-\zeta_1\mu_k^2\varphi_1-\zeta_2\varphi_2-i\gamma=0 \tag{3.41}$$

We will now search for singular and equilibrium points based on Eqs. (2.46) and (2.47), respectively. From $\det(\mathbf{S}_1)=0$, the amplitudes of all possible singular points are determined as:

$$1+\mathbb{G}^2(N_2)-2\mathbb{G}(N_2)-2N_2^2\mathbb{G}'(N_2)+2N_2^2\mathbb{G}(N_2)\mathbb{G}'(N_2)+\zeta_2^2=0 \tag{3.42}$$

From Eq. (2.47), the equilibrium points are defined by $E_1(\varphi_1,\varphi_2,\varphi_1^*,\varphi_2^*)=0$. After introducing the equation of the SIM (Eq. (3.38)) in Eq. (3.41), and the separation of real and imaginary parts, we have:

$$\begin{cases}\text{Imaginary part:} & \mathbb{A}=-\gamma\sin(\delta_2)\\ \\ \text{Real part:} & \mathbb{B}=\gamma\cos(\delta_2)\end{cases} \tag{3.43}$$

with

$$\begin{cases}\mathbb{A}=2\sigma N_2\zeta_2+\zeta_1\mu_k^2N_2-\zeta_1\mu_k^2N_2\mathbb{G}(N_2)+\zeta_2N_2\\ \\ \mathbb{B}=-2\sigma N_2+2\sigma N_2\mathbb{G}(N_2)+N_2\mathbb{G}(N_2)+\zeta_1\zeta_2\mu_k^2N_2\end{cases} \tag{3.44}$$

One can write

$$\mathbb{A}^2+\mathbb{B}^2=\gamma^2 \tag{3.45}$$

From that, the equilibrium points are determined by the following mathematical expression:

$$\mathbb{W}\sigma^2+\mathbb{X}\sigma+\mathbb{Y}=0 \tag{3.46}$$

with

$$\begin{cases}\mathbb{W}= & N_2^2(4+4\zeta_2^2-4\mathbb{G}(N_2)+4\mathbb{G}^2(N_2))\\ \\ \mathbb{X}= & N_2(4\zeta_2\zeta_1\mu_k^2-2\zeta_2\zeta_1\mu_k^2\mathbb{G}(N_2)+4\zeta_2^2-4\mathbb{G}(N2)-4\zeta_1\mu_k^2\zeta_2+4g^2(N_2)\\ & +4\mathbb{G}(N_2)\mu_k^2\zeta_2)\\ \\ \mathbb{Y}= & N_2^2(\zeta_1^2\mu_k^4-2\zeta_1^2\mu_k^4\mathbb{G}(N_2)+2\zeta_1\zeta_2\mu_k^2+\zeta_1^2\mu_k^4\mathbb{G}^2(N_2)-2\zeta_1\zeta_2\mu_k\mathbb{G}(N_2)\\ & +\zeta_2^2+\mathbb{G}^2(N_2)+2\mathbb{G}(N_2)\zeta_1\mu_k^2\zeta_2+\zeta_1^2\zeta_2^2\mu_k^4)-\gamma^2\end{cases} \tag{3.47}$$

3.6 Numerical results versus analytical predictions

In this section, analytical predictions derived from the model of the continuous system projected on one of its arbitrary modes are confronted with numerical results. In order to compare the discrete and continuous models, the data is post-treated, as detailed in the following subsection.

3.6.1 Post-treatment of data

Table 3.1 displays all the models discussed in this chapter, including originating and final domains, models' abbreviations and respective variables. Thus far, only three models were introduced: the discrete model (represented by "D"), the continuous model ("C"), and the modal model obtained from the continuous one ("MC"). In the following text of this subsection, we will present the derivation of the other models.

Originating domain	Final domain	Abbreviation	Variables
Discrete	-	D	$u_{j,D}(\tau)$, $w_{j,D}(\tau)$
Discrete	Modal (projected)	MD	$g_{MD}(\tau)$, $q_{MD}(\tau)$
Continuous	-	C	$u_C(x,\tau)$, $w_C(x,\tau)$
Continuous	Modal (projected)	MC	$g_{MC}(\tau)$, $q_{MC}(\tau)$
Modal obtained from continuous	Discrete	DMC	$u_{j,DMC}(\tau)$, $w_{j,DMC}(\tau)$

Table 3.1: Summary of the models discussed in this chapter: originating and final domains, models' abbreviations and corresponding variables.

Discrete model "D" can be projected on the kth mode to obtain $g_{MD}(\tau)$ and $q_{MD}(\tau)$, corresponding to the variables of "MD". Considering Eqs. (3.9) and (3.30), one can write:

$$\boldsymbol{u_D} = \boldsymbol{A_j}(x = j-1).g_{MD}(\tau) \qquad \boldsymbol{w_D} = \boldsymbol{A_j}(x = j-1).q_{MD}(\tau) \tag{3.48}$$

where $\mathbf{A_j}$ is the mode shape vector obtained from Eq. 3.24, with $j = 1, 2, ..., L$. $\mathbf{u_D}$ and $\mathbf{w_D}$ stand for the displacement vectors obtained from the numerical integration of Eq. (3.6):

$$\boldsymbol{A_j} = \begin{bmatrix} B_1\cos(0) \\ B_1\cos(\mu_k) \\ \vdots \\ B_1\cos(\mu_k(j-1)) \\ \vdots \\ B_1\cos(\mu_k(L-1)) \end{bmatrix}, \quad \mathbf{u_D} = \begin{bmatrix} u_{1,D} \\ u_{2,D} \\ \vdots \\ u_{j,D} \\ \vdots \\ u_{L,D} \end{bmatrix}, \quad \mathbf{w_D} = \begin{bmatrix} w_{1,D} \\ w_{2,D} \\ \vdots \\ w_{j,D} \\ \vdots \\ w_{L,D} \end{bmatrix} \tag{3.49}$$

Finally, $g_{MD}(\tau)$ and $q_{MD}(\tau)$ can be obtained for the discrete model through the following relation:

$$g_{MD}(\tau) = \boldsymbol{A_j^T}.\mathbf{u_D} \qquad \mathbf{q_{MD}}(\tau) = \mathbf{A_j^T}.\mathbf{w_D} \tag{3.50}$$

Thus, dynamic responses from "MD" and "MC" (Eqs. (3.6) and (3.31), respectively) can be compared.

The complex variables of Manevitch can be computed by applying Eq. (3.33) for the "MD" variables:

$$\begin{cases} \varphi_1 e^{i\lambda\tau} = \dot{g}_{MD}(\tau) + i\lambda g_{MD}(\tau) \\ \varphi_2 e^{i\lambda\tau} = \dot{q}_{MD}(\tau) + i\lambda q_{MD}(\tau) \end{cases} \tag{3.51}$$

From Eq. 3.51, the Manevitch variables can be obtained for "D" and, thus, for each cell as follows:

$$\begin{cases} \varphi_1 e^{i\lambda\tau} A_j(x = j-1) = (\dot{g}_{MD}(\tau) + i\lambda g_{MD}(\tau)) A_j(x = j-1) \\ \varphi_2 e^{i\lambda\tau} A_j(x = j-1) = (\dot{q}_{MD}(\tau) + i\lambda q_{MD}(\tau)) A_j(x = j-1) \end{cases} \tag{3.52}$$

which reads:

$$\begin{cases} |\varphi_1 e^{i\lambda\tau} A_j(x = j-1)| = |\dot{u}_{j,D}(\tau) + i\lambda u_{j,D}(\tau)| \\ |\varphi_2 e^{i\lambda\tau} A_j(x = j-1)| = |\dot{w}_{j,D}(\tau) + i\lambda w_{j,D}(\tau)| \end{cases} \tag{3.53}$$

Considering $|A_j(x = j-1)| = B_1$, we finally obtain N_1 and N_2 for each cell:

$$\begin{cases} N_{1,j,D} = \dfrac{|\dot{u}_{j,D}(\tau) + i\lambda u_{j,D}(\tau)|}{B_1} \\ N_{2,j,D} = \dfrac{|\dot{w}_{j,D}(\tau) + i\lambda w_{j,D}(\tau)|}{B_1} \end{cases} \tag{3.54}$$

Continuous model From Eq. (3.31) of the "MC" model, we can directly obtain $g_{MC}(\tau)$ and $q_{MC}(\tau)$ through numerical integration. We can derive a discrete model from the continuous one in the modal domain ("DMC") using a relation similar to the one presented in Eq. (3.48), with $u_{j,DMC}(\tau)$ and $w_{j,DMC}(\tau)$ as follows:

$$u_{j,DMC}(\tau) = A_j(x = j-1) g_{MC}(\tau) \qquad w_{j,DMC}(\tau) = A_j(x = j-1) q_{MC}(\tau) \tag{3.55}$$

Thus, results of "DMC" model can be compared with those obtained from numerical time integration of Eq. (3.6) of "D" model.
The complex variables of Manevitch can be computed for the "MC" model using the results from Eq. (3.31) and by applying Eq. (3.33). For the "DMC" model, N_1 and N_2 can be obtained for each cell in a similar manner as shown for Eq. (3.54):

$$\begin{cases} N_{1,j,DMC} = \dfrac{|\dot{u}_{j,DMC}(\tau) + i\lambda u_{j,DMC}(\tau)|}{B_1} \\ N_{2,j,DMC} = \dfrac{|\dot{w}_{j,DMC}(\tau) + i\lambda w_{j,DMC}(\tau)|}{B_1} \end{cases} \tag{3.56}$$

In the upcoming section, we will compare the results obtained from analytical developments with those derived from numerical time integration of the system equations, following the required post-treatments.

3.6.2 Numerical examples

Let us consider the values in Table 3.2 for the system's parameters. The system is projected on its first mode, i.e., $k = 1$. Here, various scenarios are explored, corresponding to different levels of excitation, and leading to distinct dynamic regimes.

ζ_1	ζ_2	K_{NL}	K_L
0.1	0.1	0.1	0.1
k	L	ε	δ
1	100	10^{-2}	5

Table 3.2: Numerical values for parameters of considered system.

3.6.2.1 Free response - $\gamma = 0$

To analyze a free response of the system, the following conditions are considered at $\tau = 0$: $(g_{MC}, q_{MC}, \dot{g}_{MC}, \dot{q}_{MC}) = (g_{MD}, q_{MD}, \dot{g}_{MD}, \dot{q}_{MD}) = (40, 40, 0, 0)$. In Fig. 3.2, the responses obtained from numerical time integration of "MC" (for abbreviations, please refer to Table 3.1), defined in Eq. (3.31), are added to the SIM of the system, obtained from Eq. (3.39). In order to obtain a more precise behavior, a numerical integration is also carried out with $\varepsilon = 10^{-3}$ and the results are added to the SIM in Fig. 3.3. From that, it is seen that the system follows the SIM and, after three bifurcations, it reaches the rest position. Numerical integration provides results that conform to the SIM with greater precision as ε decreases. However, to minimize computational cost, we will use $\varepsilon = 10^{-2}$ for subsequent numerical integrations.

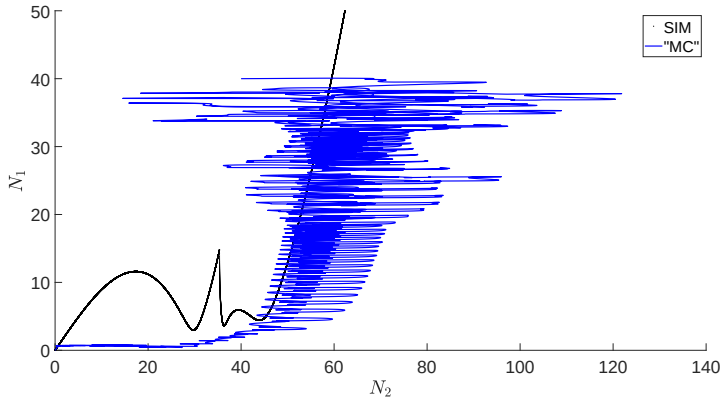

Figure 3.2: SIM of the system and corresponding numerical results obtained by numerical time integration of Eq. (3.31) with $\gamma = 0$ and $\varepsilon = 10^{-2}$. The initial conditions are $(g_{MC}, q_{MC}, \dot{g}_{MC}, \dot{q}_{MC}) = (40, 40, 0, 0)$. For abbreviations, please refer to Table 3.1.

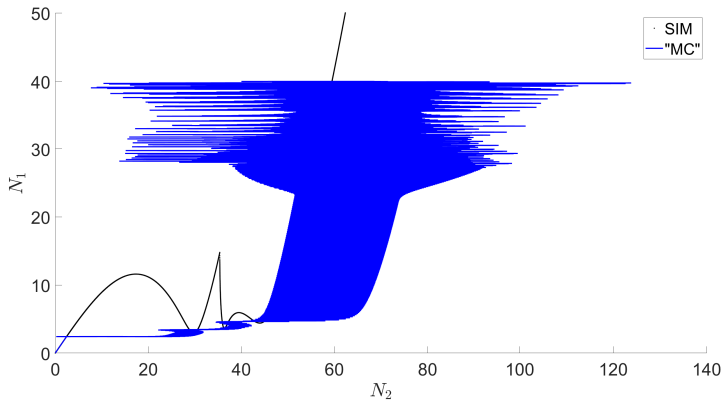

Figure 3.3: SIM of the system and corresponding numerical results obtained by numerical time integration of Eq. (3.31) with $\gamma = 0$ and $\varepsilon = 10^{-3}$. The initial conditions are $(g_{MC}, q_{MC}, \dot{g}_{MC}, \dot{q}_{MC}) = (40, 40, 0, 0)$. For abbreviations, please refer to Table 3.1.

To add responses from the "D" model to the SIM, it is necessary to obtain $g_{MD}(\tau)$ and $q_{MD}(\tau)$ by projection on the mode (as detailed in Section 3.6.1). This enables a comparison between $g(\tau)$ and $q(\tau)$ obtained from the "MD" and "MC" models, as shown in Fig. 3.4b.

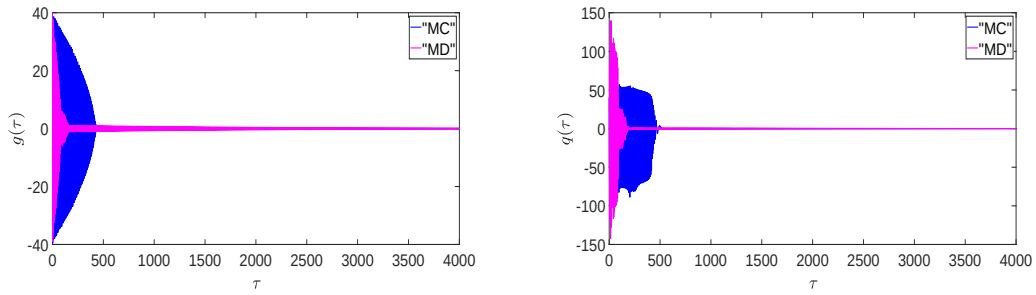

(a) (b)

Figure 3.4: Time histories of modal variables obtained from "MD" and "MC" for $\gamma = 0$: a) $g(\tau)$; b) $q(\tau)$. The initial conditions are $(g_{MC}, q_{MC}, \dot{g}_{MC}, \dot{q}_{MC}) = (g_{MD}, q_{MD}, \dot{g}_{MD}, \dot{q}_{MD}) = (40, 40, 0, 0)$. For abbreviations, please refer to Table 3.1.

To obtain more detailed information about the system's responses, we conducted a Fourier analysis considering the responses of both models: "MD" and "MC". The results of the Fourier transforms of $g(\tau)$ and $q(\tau)$ are presented in Figures 3.5 and 3.6, respectively. In Fig. 3.5, which accounts for the displacement of the external masses, only the first harmonic is observed. However, upon examining Fig. 3.6, corresponding to the relative displacement coordinate, it becomes evident that other harmonics than the first one contribute to the system responses.

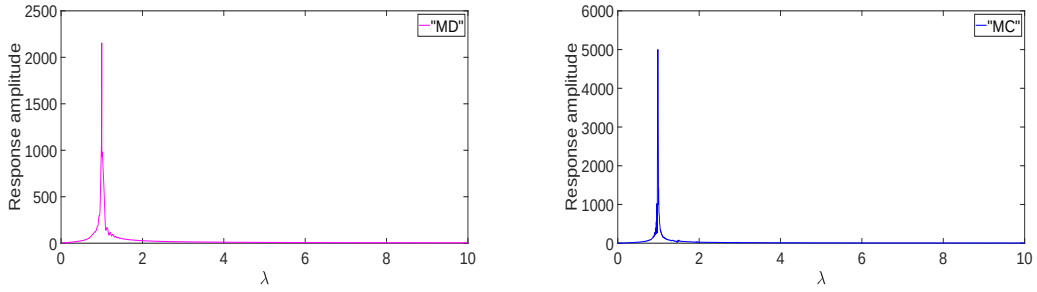

(a) (b)

Figure 3.5: Fourier transform of $g(\tau)$ (Fig. 3.4a) obtained from models: a) "MD"; b) "MC". For abbreviations, please refer to Table 3.1.

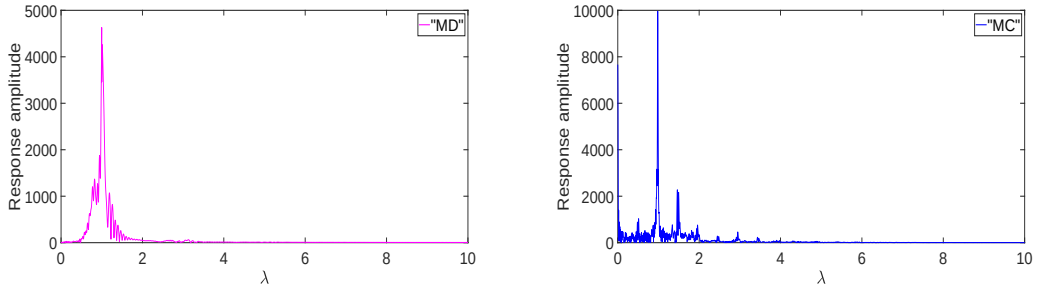

(a) (b)

Figure 3.6: Fourier transform of $q(\tau)$ (Fig. 3.4b) obtained from models: a) "MD"; b) "MC". For abbreviations, please refer to Table 3.1.

Since the system under consideration is excited in the vicinity of its first mode, the dominant effects of the first harmonic are evident in Figs. 3.5 and 3.6. However, due to the extreme nonlinear response of the inner mass and the presence of internal resonances (as seen in Eq. 3.21), other harmonics can also influence the system responses, particularly those of $q(\tau)$ (as shown in Fig. 3.6). In the development of the "MC" model, the chain is projected on the mode k, thus serving as an approximation of the discrete chain. To enhance the reliability of the "MC" model, projection on multiple modes should be taken into account. Nevertheless, this aspect is beyond the scope of the current study, and it explains the disparities between the outcomes obtained with discrete and reduced models.

Finally, the complex variables of Manevitch can be computed for "MD" model, and its results can be added to the SIM depicted in Fig. 3.7a, in addition to the responses of the "MC" model. Figures 3.7b and 3.7c provide the time histories of system amplitudes. The differences between the results of the two models is due to the effect of higher harmonics and modes, which are not taken into account in the "MC" model.

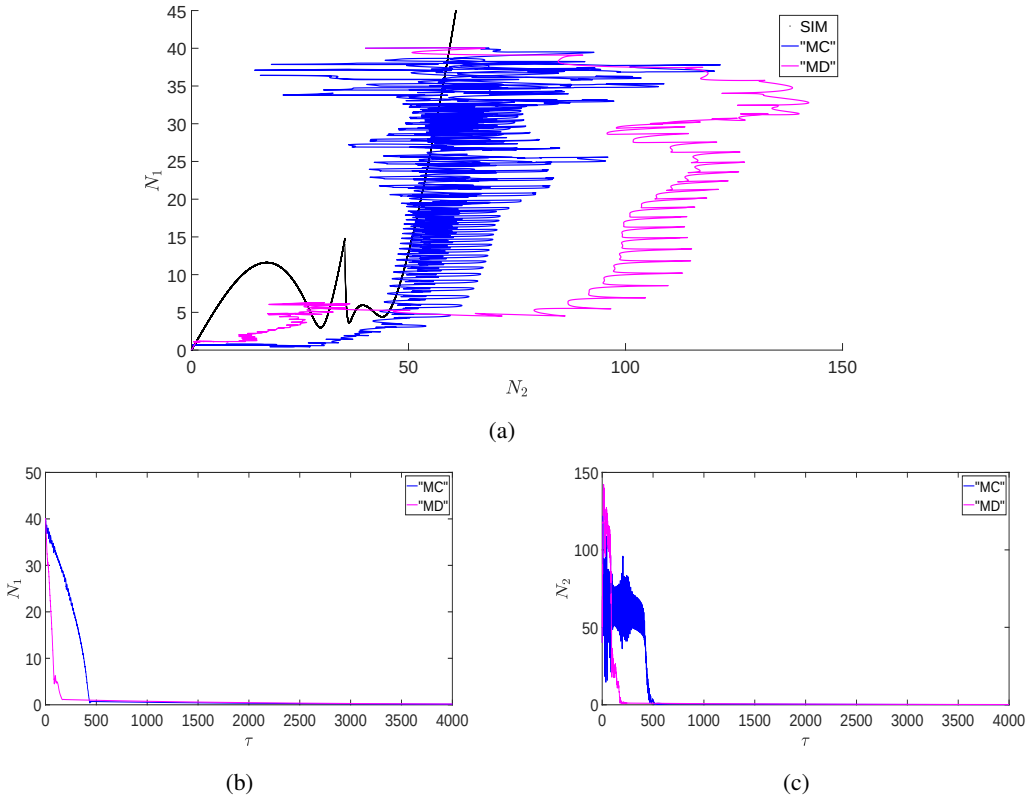

Figure 3.7: a) SIM of the system and corresponding numerical results of "MC" and "MD" with $\gamma = 0$ (free response). b) N_1 versus τ; c) N_2 versus τ. The initial conditions are $(g_{MC}, q_{MC}, \dot{g}_{MC}, \dot{q}_{MC}) = (g_{MD}, q_{MD}, \dot{g}_{MD}, \dot{q}_{MD}) = (40, 40, 0, 0)$. For abbreviations, please refer to Table 3.1.

The time histories of amplitudes for each cell of the chain in terms of N_1, obtained from "D" (see Eq. 3.54) and "DMC" (see Eq. 3.56), are illustrated in Figs. 3.8a and 3.8b, respectively. These figures demonstrate qualitatively good agreements with the results obtained from "MD" and "MC," as presented in Fig. 3.7.

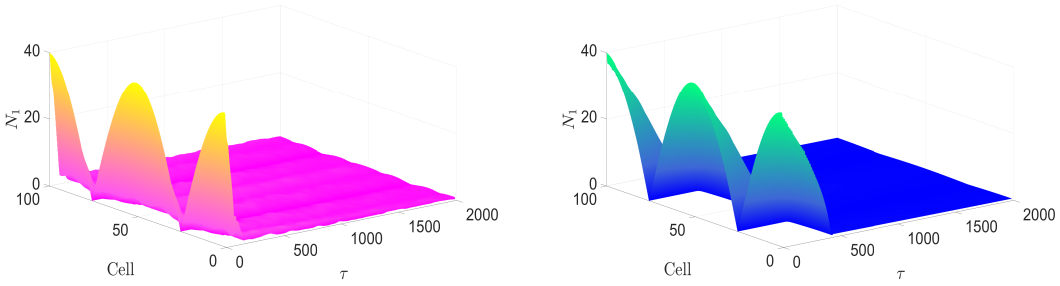

(a) (b)

Figure 3.8: Time histories of N_1 corresponding to each cell of the system with $\gamma = 0$ obtained from (a) "D" and (b) "DMC". For abbreviations, please refer to Table 3.1.

N_2 is plotted as a function of the cell number and time in Figs. 3.9a and 3.9b, illustrating the responses of "D" and "DMC", respectively. These figures demonstrate that the time histories of N_2 for each cell obtained from "D" and "DMC" do not exhibit good agreement. This lack of agreement can be explained by the Fourier transform of the results (see Fig. 3.6), and it can be attributed to the presence of other harmonics and modal interactions in the response of "D".

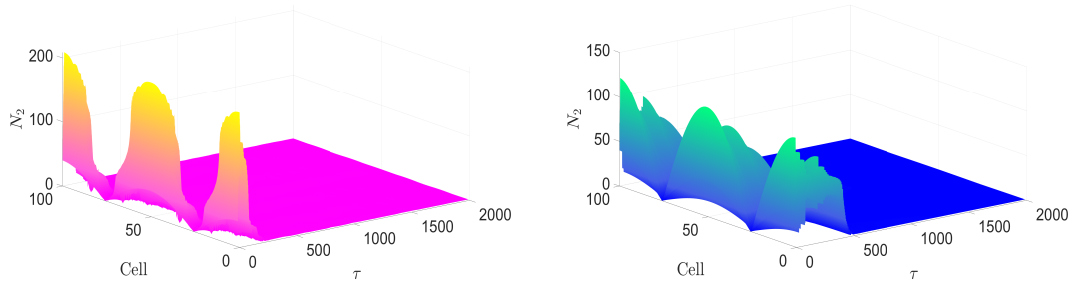

(a) (b)

Figure 3.9: Time histories of N_2 corresponding to each cell of the system with $\gamma = 0$ from (a) "D" and (b) "DMC". For abbreviations, please refer to Table 3.1.

The first harmonics of the results from Figs. 3.8 and 3.9 are depicted in Figs. 3.10 and 3.11, respectively. Notably, the magnitude of responses decreases when considering only the first harmonics of the system. However, the difference between the responses of "D" and "DMC" remains significant, indicating that the influence of other harmonics and modal interactions, which are not taken into account in this study, is important.

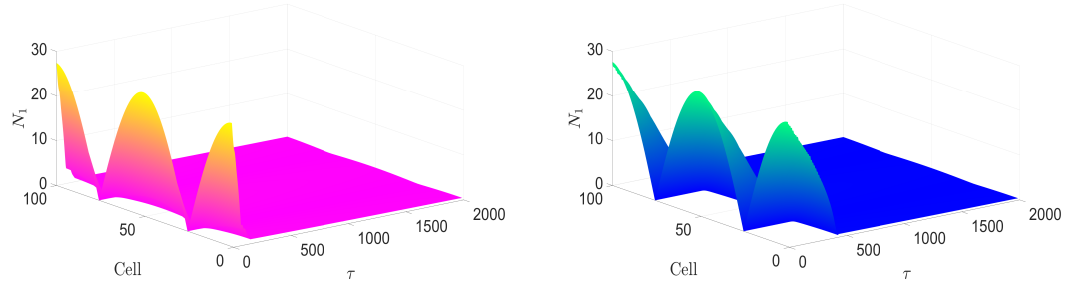

(a) (b)

Figure 3.10: First harmonics of time histories of N_1 corresponding to each cell of the system with $\gamma = 0$ obtained from (a) "D" and (b) "DMC". For abbreviations, please refer to Table 3.1.

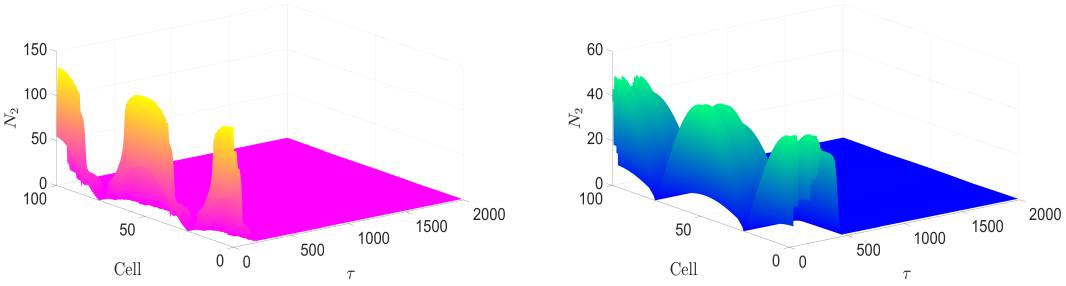

(a) (b)

Figure 3.11: First harmonics of time histories of N_2 corresponding to each cell of the system with $\gamma = 0$ obtained from (a) "D" and (b) "DMC". For abbreviations, please refer to Table 3.1.

We can further compare both models by examining the displacements of corresponding cells, as illustrated in Fig. 3.12. This figure depicts the displacements of the 15th cell in terms of u_{15} and v_{15}, representing the displacement of its external and internal masses, respectively.

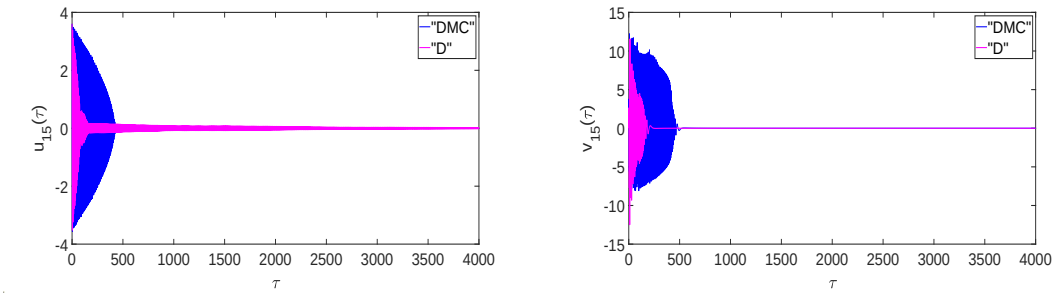

(a) (b)

Figure 3.12: Displacements of the 15th cell from "D" and "DMC" models (for abbreviations, please refer to Table 3.1) for $\gamma = 0$: a) u_{15} versus τ; b) v_{15} versus τ. The initial conditions are $(g, q, \dot{g}, \dot{q}) = (40, 40, 0, 0)$.

Fourier analyses of the displacements of the external and internal masses, namely u_{15} and v_{15} respectively, are depicted in Figs. 3.13 and 3.14. In Fig. 3.13a, the results obtained from "D" indicate the presence of higher harmonics, particularly the third one. This phenomenon can be attributed to the existence of a 1:3 internal resonance and the nonlinearity present in the system. In contrast, when observing Fig. 3.13b, only the first harmonic is excited, as expected since it is obtained from the "DMC" model, which had its equations projected on the first mode. Fourier analyses of v_{15} for both "D" and "DMC" models are represented in Fig. 3.14 and reveal the pronounced effects of higher harmonics and modes. This phenomenon can be attributed to the system's nonlinearity, primarily arising from the inner masses, which requires the involvement of higher harmonics.

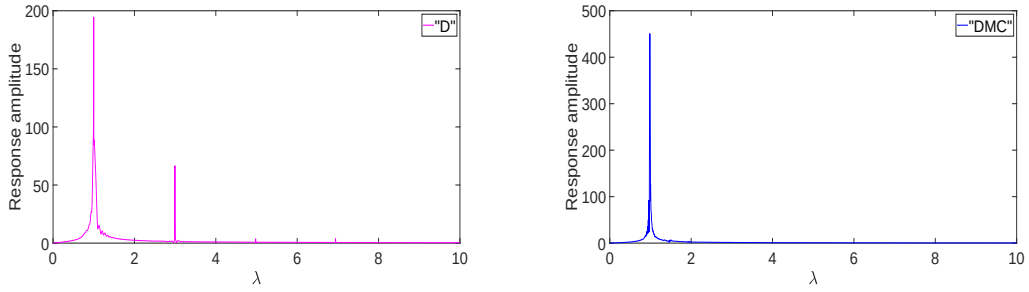

(a) (b)

Figure 3.13: Fourier transform of the displacement u_{15} (Fig. 3.12a) obtained from models: (a) "D"; (b) "DMC". For abbreviations, please refer to Table 3.1.

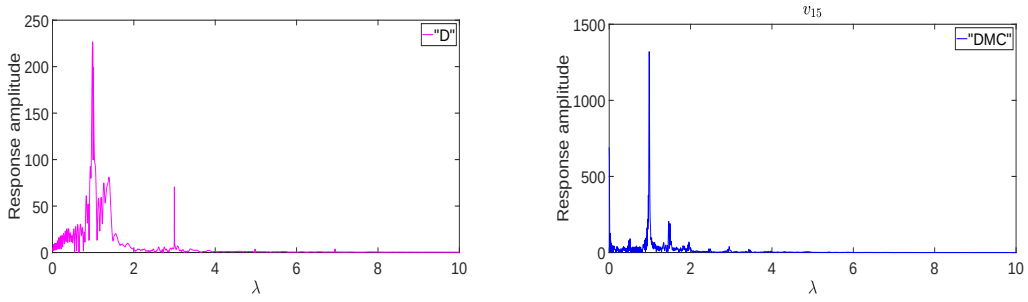

(a) (b)

Figure 3.14: Fourier transform of the displacement v_{15} (Fig. 3.12b) obtained from models: (a) "D"; (b) "DMC". For abbreviations, please refer to Table 3.1.

3.6.2.2 Forced responses - $\gamma = 6$

Here, a forced system with $\gamma = 6$ is under investigation. Equilibrium points of the system concerning the sweeping detuning parameter σ are computed first from Eq. (3.46) and then from Eq. (3.39). Analytically derived frequency response curves are presented in Fig. 3.15, including a three-dimensional view and corresponding orthogonal projections on each relevant plane. The unstable zone of the SIM is represented in green. Additionally, in the following text, we will compare numerical results collected from discrete and continuous models with analytical predictions for $\gamma = 6$ and specific excitation frequencies.

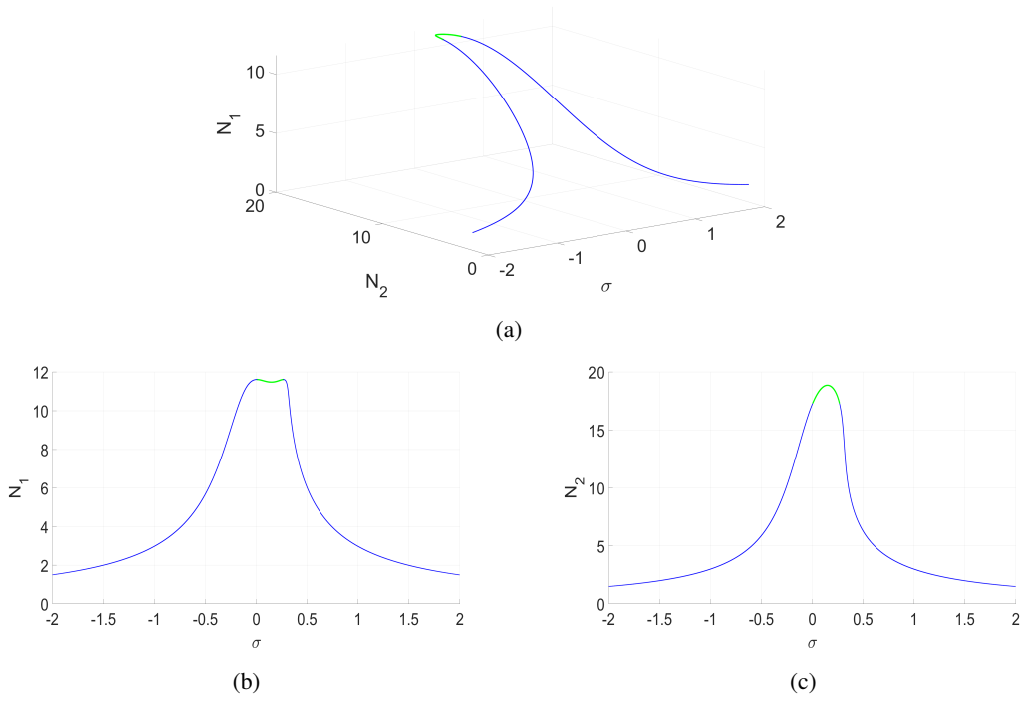

(a)

(b) (c)

Figure 3.15: a) Branch of detected equilibrium points with respect to the detuning parameter σ for the system with $\gamma = 6$. b) N_1 versus σ; c) N_2 versus σ. The unstable zone of the SIM is represented in green.

System behaviors for $\sigma = 0.1$ From Fig. 3.15, it is seen that for $\sigma = 0.1$, the only equilibrium point is located in the unstable zone of the SIM. Thus, a SMR is expected. The SIM is plotted in Fig. 3.16a, as well as the corresponding numerical results for $\gamma = 6$, $\sigma = 0.1$ and the initial conditions $(g_{MC}, q_{MC}, \dot{g}_{MC}, \dot{q}_{MC}) = (g_{MD}, q_{MD}, \dot{g}_{MD}, \dot{q}_{MD}) = (40, 40, 0, 0)$. The behavior of N_1 and N_2 over time can be visualized in Figs. 3.16b and 3.16c respectively, from which it is noticed that both "MD" and "MC" models exhibit SMR. The "MC", derived from the model of the continuous chain through projection on the first mode, accurately predicts the amplitude of the system qualitatively (see Fig. 3.16b). Globally, it also successfully captures bifurcations, as shown in Fig. 3.16c. The differences between the responses of the two models, particularly in Fig. 3.16c, can be attributed to the influence of other harmonics and the approximations of mono-modal behavior in the "MC" model, which diverge from the behavior of the real system. Moreover, due to these approximations, certain branches of the SIM can remain undetected.

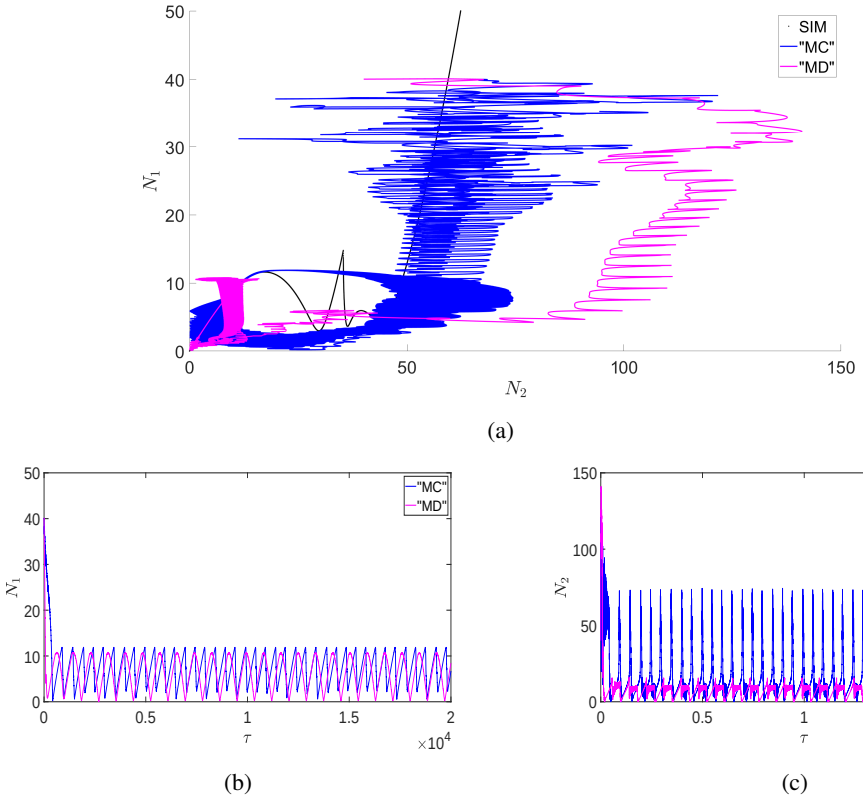

Figure 3.16: a) The SIM and corresponding numerical results of "MC" and "MD" with $\gamma = 6$ and $\sigma = 0.1$. b) N_1 versus τ; c) N_2 versus τ. The initial conditions are $(g_{MC}, q_{MC}, \dot{g}_{MC}, \dot{q}_{MC}) = (g_{MD}, q_{MD}, \dot{g}_{MD}, \dot{q}_{MD}) = (40, 40, 0, 0)$. For abbreviations, please refer to Table 3.1.

The SMR is also observable in the overall chain. Time histories of N_1 and N_2 obtained from "D" and "DMC" are depicted in Figs. 3.17 and 3.18, respectively. It is notable that the amplitudes of N_1 and N_2 depend on the position of the cell in the chain. This variation is due to the type of external excitation applied to the chain, which follows its first mode shape.

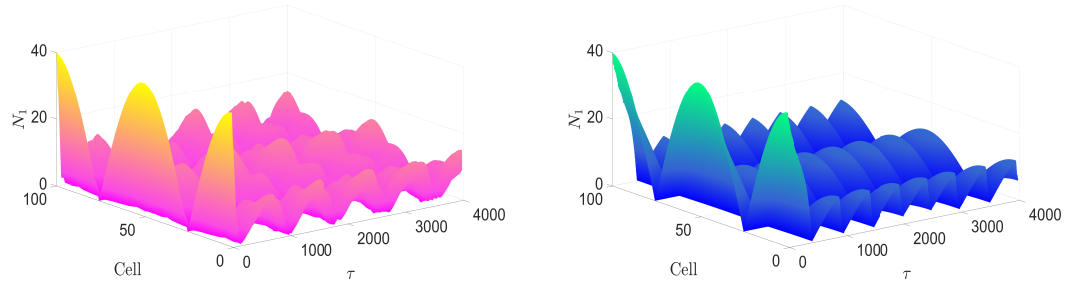

(a) (b)

Figure 3.17: Time histories of N_1 corresponding to each cell of the system with $\gamma = 6$ and $\sigma = 0.1$ from (a) "D" and (b) "DMC". For abbreviations, please refer to Table 3.1.

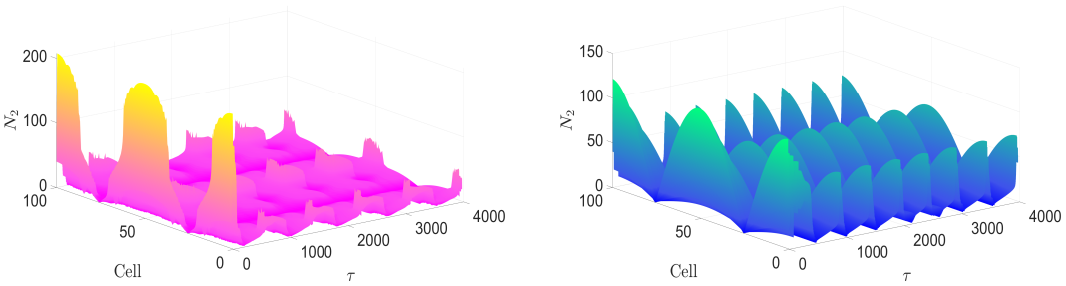

(a) (b)

Figure 3.18: Time histories of N_2 corresponding to each cell of the system with $\gamma = 6$ and $\sigma = 0.1$ from (a) "D" and (b) "DMC". For abbreviations, please refer to Table 3.1.

The Poincaré map corresponding to the "MC" model with specific parameter values ($\gamma = 6$ and $\sigma = 0.1$) is illustrated in Figs. 3.19a and 3.19b. The observed patterns in these figures are indicative of a non-periodic regime, SMR here, which corresponds to bifurcations between the stable branches of the SIM.

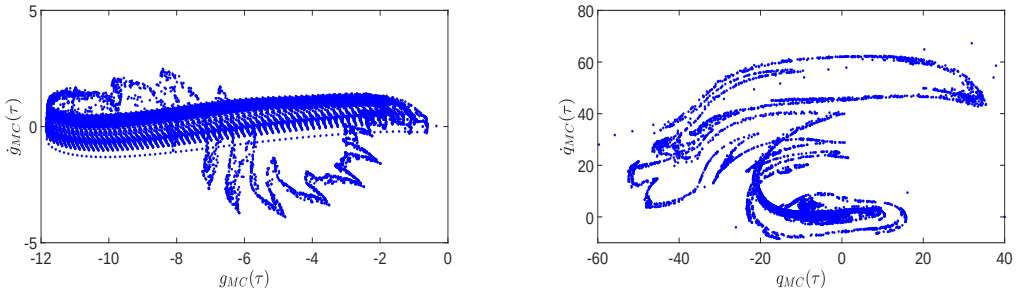

(a) (b)

Figure 3.19: Poincaré map of the "MC" model with $\gamma = 6$ and $\sigma = 0.1$ (for abbreviations, please refer to Table 3.1): (a) $g_{MC}(\tau)$ (b) $q_{MC}(\tau)$.

The Poincaré map for the "MD" model with $\gamma = 6$ and $\sigma = 0.1$ is presented in Figs. 3.20a and 3.20b, depicting variables g_{MD} and q_{MD}, respectively. These figures also illustrate a non-periodic response.

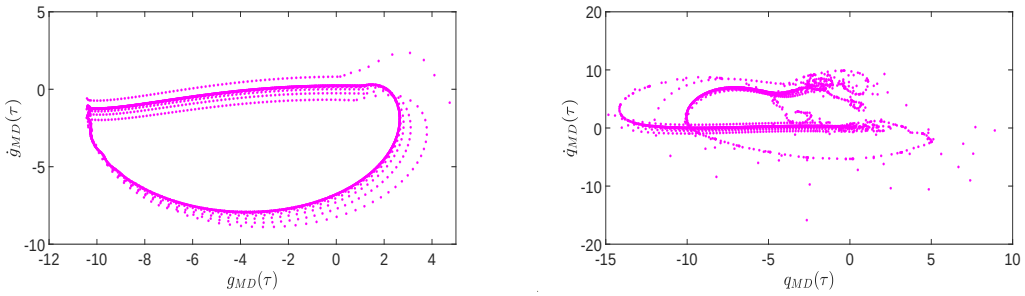

(a) (b)

Figure 3.20: Poincaré map of the "MD" model with $\gamma = 6$ and $\sigma = 0.1$ (for abbreviations, please refer to Table 3.1): (a) $g_{MD}(\tau)$ (b) $q_{MD}(\tau)$.

System behaviors for $\sigma = -0.3$ Figure 3.21 summarizes the obtained results for the system with excitation parameters $\gamma = 6$ and $\sigma = -0.3$. By examining Fig. 3.15, it can be observed that for $\sigma = -0.3$, there is a single equilibrium point situated in the stable region of the SIM, indicating a possible periodic response. The SIM is plotted in Fig. 3.21a, which also includes the corresponding numerical results with the initial conditions $(g_{MC}, q_{MC}, \dot{g}_{MC}, \dot{q}_{MC}) = (g_{MD}, q_{MD}, \dot{g}_{MD}, \dot{q}_{MD}) = (0, 0, 0, 0)$. The time evolutions of N_1 and N_2 are presented in Figs. 3.21b and 3.21c, respectively. From these figures, it is observed that after some bifurcations, the response from the "MC" model, obtained from the continuous chain, converges to a periodic regime, consistent with the equilibrium point predicted by the frequency response curves (Fig. 3.15). In contrast, the corresponding response generated by "MD" model exhibits SMR. The differences in responses between the models emphasize the impact of modal interactions and the involvement of higher harmonics, all of which are neglected in the analytical developments obtained from the reduced model. It is also observed that, despite the final regimes of "MD" and "MC" (SMR and periodic, respectively) being different, the mean behavior of the SMR of "MD" qualitatively follows the response of "MC".

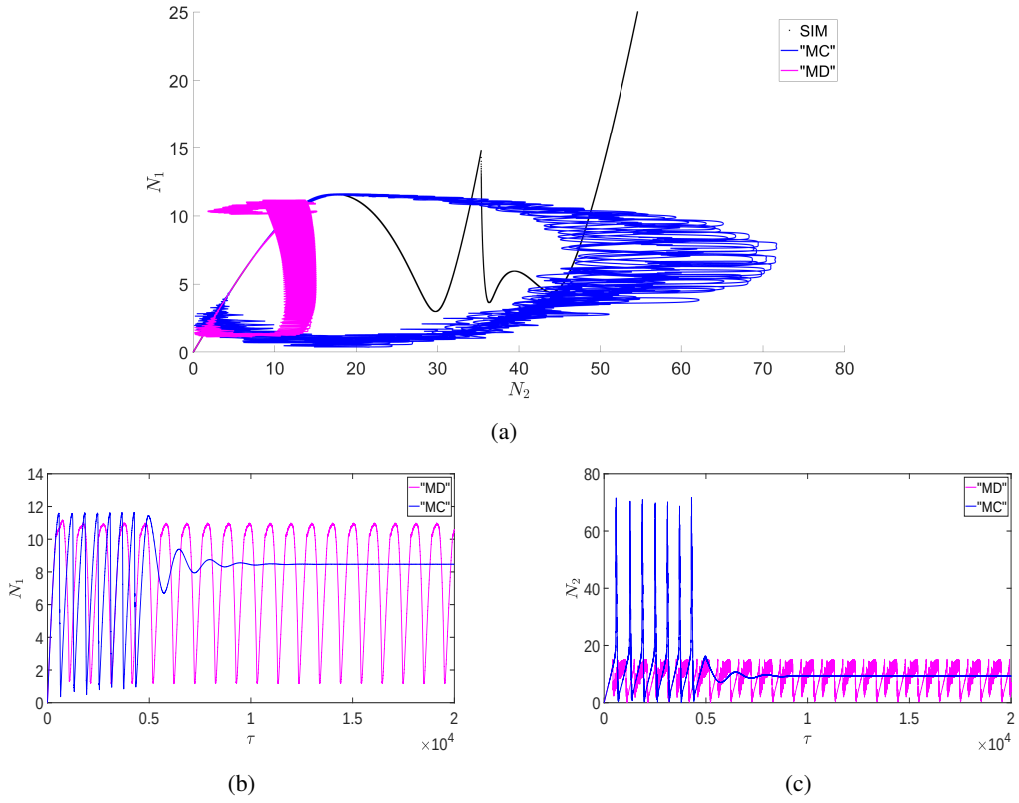

Figure 3.21: a) The SIM and corresponding numerical results of "MC" and "MD" with $\gamma = 6$ and $\sigma = -0.3$. b) N_1 versus τ; c) N_2 versus τ. The initial conditions are $(g_{MC}, q_{MC}, \dot{g}_{MC}, \dot{q}_{MC}) = (g_{MD}, q_{MD}, \dot{g}_{MD}, \dot{q}_{MD}) = (0, 0, 0, 0)$. For abbreviations, please refer to Table 3.1.

Time histories of N_1 and N_2 for different cells are presented in Figs. 3.22 and 3.23, respectively, for the models "D" and "DMC". It is observed that the "D" presents SMR, while the "DMC" converges to a periodic response after some SMR cycles, which is coherent with the results presented in Fig. 3.21.

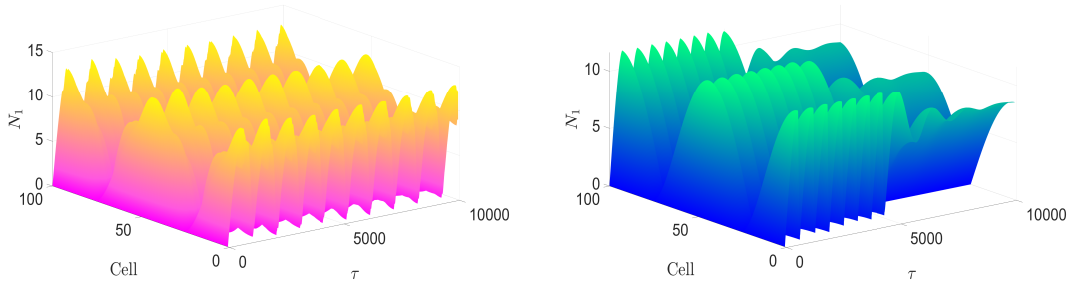

(a) (b)

Figure 3.22: Time histories of N_1 corresponding to each cell of the system with $\gamma = 6$ and $\sigma = -0.3$ from (a) "D" and (b) "DMC". For abbreviations, please refer to Table 3.1.

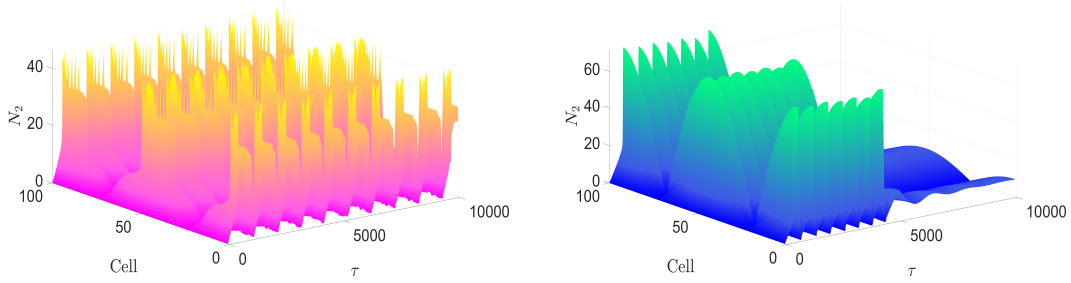

(a) (b)

Figure 3.23: Time histories of N_2 corresponding to each cell of the system with $\gamma = 6$ and $\sigma = -0.3$ from (a) "D" and (b) "DMC" models. For abbreviations, please refer to Table 3.1.

System behaviors for $\sigma = -0.5$ Figure 3.15 indicates that for $\sigma = -0.5$ the system will be probably attracted by a periodic regime. The numerical results are depicted in Fig. 3.24, where the periodic regime occurs as expected, given the equilibrium point's location in the stable zone of the SIM. The SIM is plotted in Fig. 3.24a accompanied by the numerical response for $\gamma = 6$, $\sigma = -0.5$ and the initial conditions $(g_{MC}, q_{MC}, \dot{g}_{MC}, \dot{q}_{MC}) = (g_{MD}, q_{MD}, \dot{g}_{MD}, \dot{q}_{MD}) = (0, 0, 0, 0)$. The temporal progression of N_1 and N_2 is presented in Figs. 3.24b and 3.24c, respectively. Both models' responses converge to a periodic regime, consistent with the predicted equilibrium point from the frequency response curves shown in Fig. 3.15.

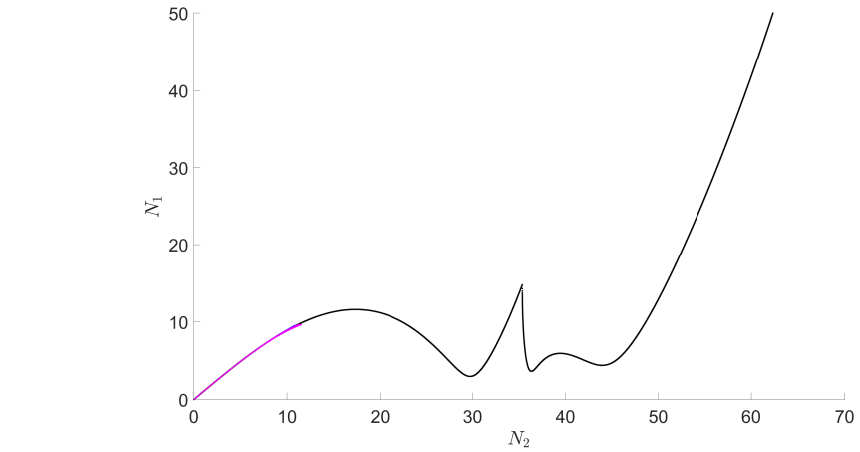

(a)

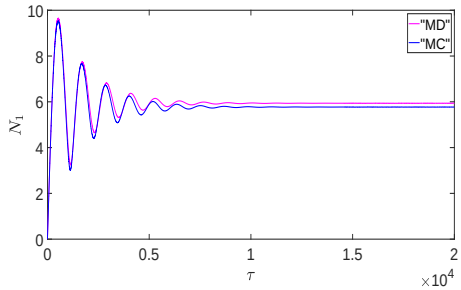

(b)

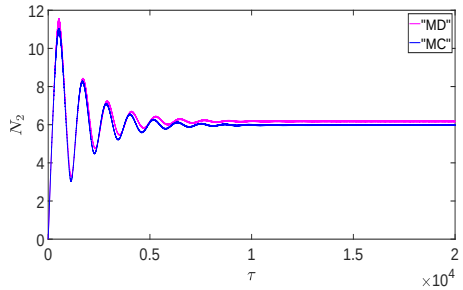

(c)

Figure 3.24: a) The SIM and corresponding numerical results of "MC" and "MD" with $\gamma = 6$ and $\sigma = -0.5$. b) N_1 versus τ; c) N_2 versus τ. The initial conditions are $(g_{MC}, q_{MC}, \dot{g}_{MC}, \dot{q}_{MC}) = (g_{MD}, q_{MD}, \dot{g}_{MD}, \dot{q}_{MD}) = (0, 0, 0, 0)$. For abbreviations, please refer to Table 3.1.

The behavior of N_1 and N_2 can be observed as a function of the time and the cell number in Figs. 3.25 and 3.26. These figures demonstrate that all cells converge to a periodic regime in both "D" and "DMC" models.

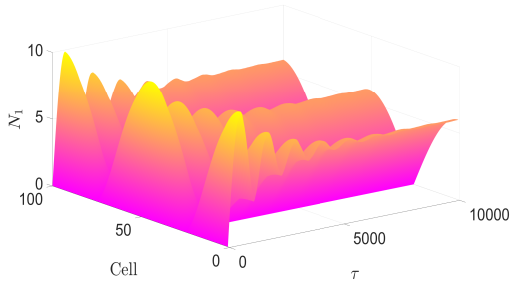

(a)

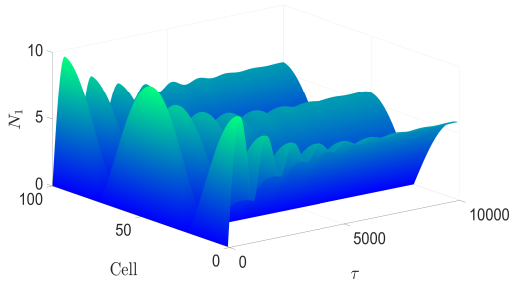

(b)

Figure 3.25: Time histories of N_1 corresponding to each cell of the system with $\gamma = 6$ and $\sigma = -0.5$ from (a) "D" and (b) "DMC". For abbreviations, please refer to Table 3.1.

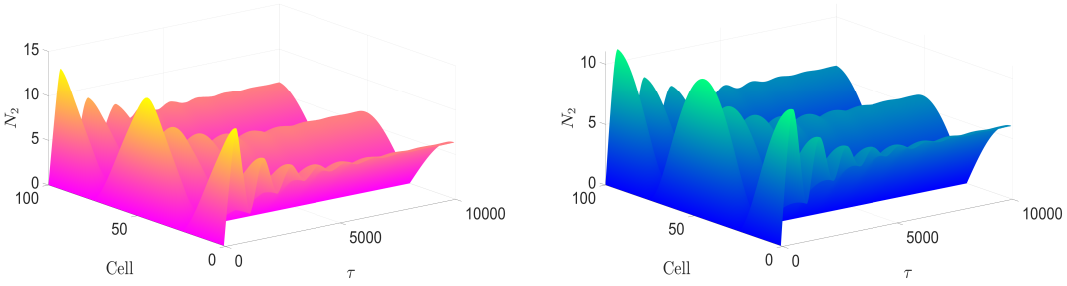

(a) (b)

Figure 3.26: Time histories of N_1 corresponding to each cell of the system with $\gamma = 6$ and $\sigma = -0.5$ from (a) "D" and (b) "DMC". For abbreviations, please refer to Table 3.1.

All of these figures demonstrate that, for $\sigma = -0.5$, the analytical predictions (obtained from the reduced model) align well with the numerical results from both models of the chain. Examining Fig. 3.15, it is seen that the region around $\sigma = -0.5$ does not exhibit extreme nonlinear behavior. Consequently, there are fewer modal interactions and reduced effects of higher harmonics in this zone, which is consistent with the main assumptions of the reduced model ("MC"). In contrast, extreme nonlinear zones on these curves may require greater involvement of harmonics in system responses and consideration of modal interactions [Guillot et al., 2022].
The Poincaré map for the "MC" model with parameters $\gamma = 6$ and $\sigma = -0.5$ is presented in Figs. 3.27a and 3.27b, corresponding to variables $g_{MC}(\tau)$ and $q_{MC}(\tau)$ respectively. These figures provide confirmation of the system's periodic regime.

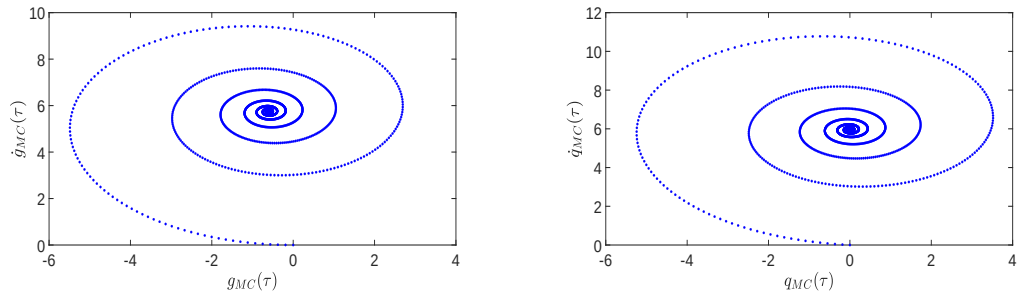

(a) (b)

Figure 3.27: Poincaré map of the "MC" model with $\gamma = 6$ and $\sigma = -0.5$ (for abbreviations, please refer to Table 3.1): (a) $g_{MC}(\tau)$ (b) $q_{MC}(\tau)$.

Figures 3.28a and 3.28b present the Poincaré map corresponding to the variables $g_{MD}(\tau)$ and $q_{MD}(\tau)$, respectively, obtained from the "MD" model with $\gamma = 6$ and $\sigma = -0.5$.

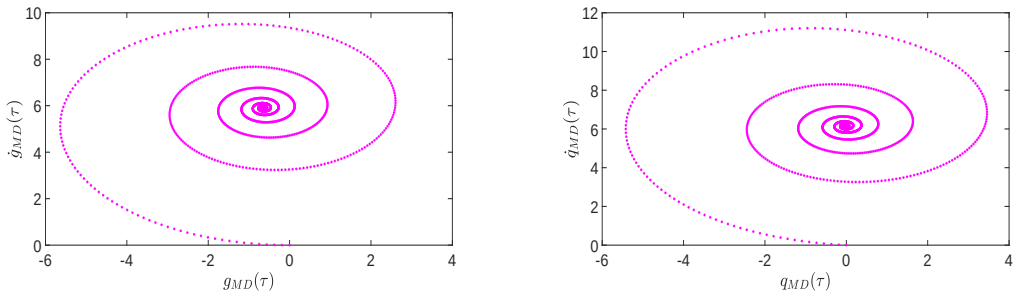

(a) (b)

Figure 3.28: Poincaré map of the "MD" model with $\gamma = 6$ and $\sigma = -0.5$ (for abbreviations, please refer to Table 3.1): (a) $g_{MD}(\tau)$ (b)$q_{MD}(\tau)$.

3.7 Conclusions of the chapter

The dynamics of a chain of coupled meta-cells, consisting of outer masses housing an inner mass with piecewise nonlinearity, are investigated. Initially, the discrete model is presented, followed by the transition to the continuous domain. The modal characteristics of the continuous model are evaluated, and the system is studied in the vicinity of one of its arbitrary modes. For that, two approximations are applied: the first involves using Taylor series expansion for transitioning to the continuous domain, while the second consists of projecting the equations of the continuous model onto an arbitrary single mode, applying a spatial averaging to the piecewise nonlinearity, and resulting in the development of a reduced model of the chain.

Subsequently, the investigation delves into the analysis of the system's fast and slow dynamics. Complex variables of Manevitch and the Galerkin method are employed to address the equations of the reduced (projected) model. To account for the piecewise nonlinearity, a time averaging approach is applied. The multiple time scale method is then used to identify the slow invariant manifold and dynamic characteristic points of the system.

Finally, comparisons between the dynamic responses of the original model and those of the projected one reveal discrepancies, attributed to the neglect of higher harmonics and intermodal interactions. Nevertheless, analytical results based on the single-mode approximation provide preliminary design tools for tuning the parameters of (piecewise) nonlinear inner masses to achieve qualitatively designed responses of the system.

CHAPTER 4

Stochastic optimization

This chapter presents the optimization of the nonlinear mass-in-mass meta-cell introduced in Chapter 2. It was shown that the considered system is sensitive to loading characteristics, initial conditions and design parameters. Consequently, this study addresses the optimization of the meta-cell while accounting for incertitudes, with the primary objective being the minimization of the expected efficiency metric. To achieve this, we begin by enhancing the understanding of the system's dynamic behavior, which includes recognizing potential discontinuities. Then, the optimization formulation and algorithm are introduced, along with essential tools such as Kriging and Support Vector Machines. Finally, optimization results are presented, considering two types of excitation and two different nonlinearities for the system.

4.1 Introduction to the optimization study

In Chapter 2, it was previously observed that the considered meta-cell can exhibit various types of responses depending on external forcing characteristics and initial conditions. Moreover, the equations governing a nonlinear mass-in-mass meta-cell are analogous to those of a primary system coupled to a NES. It is well-known that a NES is characterized by an activation threshold below which energy dissipation is ineffective [Vakakis et al., 2008, Boroson and Missoum, 2015]. Additionally, incertitudes have been shown to significantly affect the behavior and efficiency of NES devices [Boroson et al., 2014], prompting the use of various uncertainty quantification techniques, such as polynomial chaos expansions [Gourdon and Lamarque, 2006]. In fact, NES devices exhibit remarkable sensitivity to perturbations in design parameters or initial conditions, leading to discontinuous behavior, given that even slight alterations in these factors can trigger a transition from a state of "high" to "low" efficiency [Boroson et al., 2014].
This remarkably discontinuous nature of activation of NES devices has been observed in both experimental [Wierschem et al., 2014] and numerical studies [Vakakis et al., 2008]. It can be seen as an activation threshold requirement for the NES to effectively dissipate energy [Vakakis et al., 2008]. Given that NES devices must possess specific properties, and incertitudes can significantly affect their performance, the optimization of NES design becomes essential.
An algorithm for stochastic optimization of NES design was introduced in [Boroson et al., 2014]. This optimization approach employed sampling-based methods, including clustering, surrogate meta-models (e.g., Kriging), and classification techniques (e.g., Support Vector Machines (SVM)). The primary goal was to identify boundaries that separate regions with different efficiency levels and to perform reliability-based design optimization. Important algorithmic enhancements are implemented in [Boroson and Missoum, 2017], including the refinement of the SVM boundary between efficiency regions, the use of two Kriging meta-models for efficiency identification, and the use of predicted variance of Kriging approximations for sampling the space of aleatory variables. In summary, the introduced stochastic optimization algorithm addresses the problem through a sequence of steps: clustering and SVM to separate the regions of different efficiency levels, use of Kriging models within each region, local boundary updates of the failure domain, and the use of predicted Kriging variance for sampling. The last two steps account for the distribution of aleatory variables. In [Boroson et al., 2017], this stochastic optimization algorithm was applied to different

parallel NES configurations. This application focused on an unforced system with an initial velocity, leading to the development of more robust designs for the NES.
This study employs the algorithm presented in [Boroson and Missoum, 2017] and incorporates a joint probability density function to sample aleatory variables. Furthermore, in this study, we take into account effects of initial conditions and external excitation characteristics.

4.2 Potential discontinuous behavior of the system

In this section, we delve into the potential discontinuous behavior of the system, which is influenced by the sources of uncertainties. Therefore, in this study, we begin by introducing these sources of uncertainties, as well as the efficiency metric of the system under consideration.

4.2.1 Sources of incertitudes

One of the sources of incertitudes in the response of the studied system is related to its initial conditions, such as the initial velocity of the external mass $\dot{u}_1$. As seen in Chapter 2, the system exhibits the possibility of two, one, or no bifurcations for free responses depending on its initial conditions. Another source of incertitudes is the external force applied to the system. As also discussed in Chapter 2, varying the forcing amplitude γ activates different regions of the SIM. Depending on the frequency detuning parameter σ, the equilibrium point(s) can reside within either a stable or an unstable region of the SIM, which results in periodic or non-periodic responses with possible bifurcations around one or both unstable zones of the SIM.
It is important to note that design variables, as nonlinear stiffness properties, can be sources of incertitudes when the studied system is fabricated. In [Boroson et al., 2017, Boroson and Missoum, 2017], the nonlinear stiffness is considered as a stochastic design variable. However, in this study, only the external force and the initial velocity will be considered as stochastic variables.

4.2.2 Efficiency metric

To maximize the efficiency of the inner mass in improving the behavior of the outer mass, an optimization process should be carried out. To achieve this, an efficiency metric is introduced and defined as the ratio between the responses of the 2-dof, $\text{RMS}_{2dof}(\dot{u}_1)$, and the 1-dof (i.e., without inner mass), $\text{RMS}_{1dof}(\dot{u}_1)$, systems. This ratio is evaluated based on the root mean squares of $\dot{u}_1$, representing the velocity of the external mass. This metric is expressed as:

$$\text{RMS}^*_{\dot{u}_1} = \frac{\text{RMS}_{2dof}(\dot{u}_1)}{\text{RMS}_{1dof}(\dot{u}_1)} \tag{4.1}$$

This metric quantifies the efficiency of energy reduction in the 2-dof system compared to the 1-dof system. Consequently, smaller values of $\text{RMS}^*_{\dot{u}_1}$ indicate higher efficiency in vibratory energy reduction for the 2-dof system.

4.2.3 Potential discontinuous behavior

As we have seen in Chapter 2, the studied system can or not face bifurcations, which leads to a potential discontinuous behavior, which is evident when considering an unforced system. However, the behavior can become more complex in the case of a forced system, as we will see.
To facilitate the visualization of the distribution and patterns of the efficiency metric, histograms are generated by obtaining efficiency metric's values for given ranges of parameters. The values are

then divided into intervals (bins), and the number of data points in each bin is quantified. Finally, these quantifications are graphically represented as bars.
In Figure 4.1, histograms of the efficiency metric are presented considering responses of the unforced system. The only varying initial condition is the initial velocity of the outer mass ($\dot{u}_{1,0}$), with all other initial conditions set to zero. The values of other parameters remain fixed according to Tables 2.1 and 2.2.

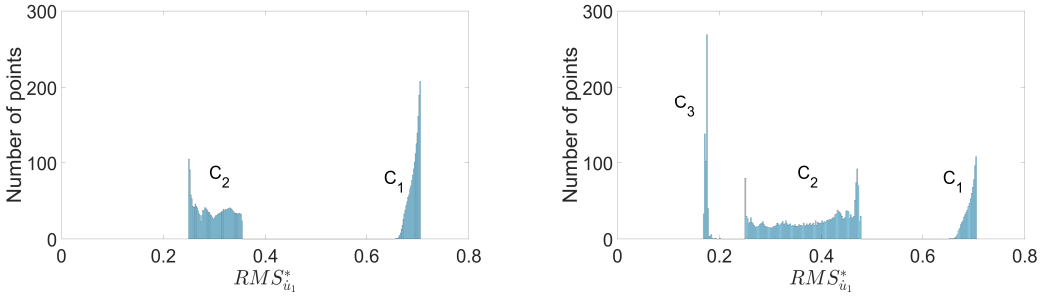

Figure 4.1: Histogram of the unforced system's responses: (a) $\dot{u}_{1,0} \in [0.5, 2.5]$; (b) $\dot{u}_{1,0} \in [0.5, 5]$. Different response clusters are denoted by C_1, C_2 and C_3.

In Fig. 4.1a, the range of $\dot{u}_{1,0}$ extends from 0.5 to 2.5 and two data clusters, namely C_1 and C_2, are distinguished: C_1 displays high values of the efficiency metric, indicating an absence of bifurcation in the system's response, and C_2 displays lower values, representative of the system's responses exhibiting one bifurcation. Upon further expansion of the range of $\dot{u}_{1,0}$ to include values from 0.5 to 5, the histogram in Fig. 4.1b illustrates the emergence of an additional response cluster C_3 featuring two bifurcations. One representative example of response for each cluster of Fig. 4.1b is depicted in Fig. 4.2.

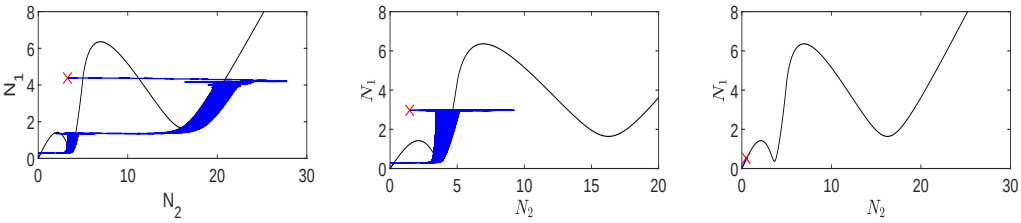

Figure 4.2: The SIM of the system (in black) and corresponding numerical responses of the unforced system (in blue) originating from the distinct clusters of Fig. 4.1b are depicted with different initial conditions represented by $\times$ symbol: (a) $(u_{1,0}, u_{2,0}, \dot{u}_{1,0}, \dot{u}_{2,0}) = (0, 0, 4.38, 0)$, within cluster C_3 of Fig. 4.1b; (b) $(u_{1,0}, u_{2,0}, \dot{u}_{1,0}, \dot{u}_{2,0}) = (0, 0, 2.98, 0)$, within cluster C_2 of Fig. 4.1b; (c) $(u_{1,0}, u_{2,0}, \dot{u}_{1,0}, \dot{u}_{2,0}) = (0, 0, 0.52, 0)$, within cluster C_1 of Fig. 4.1b. Numerical results are obtained from numerical time integration of Eq. (2.7).

In Fig. 4.2a, the response exhibits a double bifurcation and belongs to the cluster C_3, characterized by the highest efficiency of the studied system compared to the 1-dof system. Figure 4.2b depicts a response with a single bifurcation, corresponding to the cluster C_2. Finally, Fig. 4.2c presents a response from the cluster C_1, with no bifurcation, where the behavior of the studied system is closer to the behavior of the 1-dof system.

Figure 4.3 presents a histogram where, in addition to $\dot{u}_{1,0}$ ranging from 0.5 to 2.5, the parameter k_{NL} varies from 0 to 0.5 (see Eq. 2.2 for definition of the nonlinear restoring function). In such a configuration, the emergence of a third group of responses below the metric's value of 0.2, i.e., $\text{RMS}^*_{\dot{u}1} = 0.2$ (as seen in Fig. 4.1b), is observed due to the variation of k_{NL}.

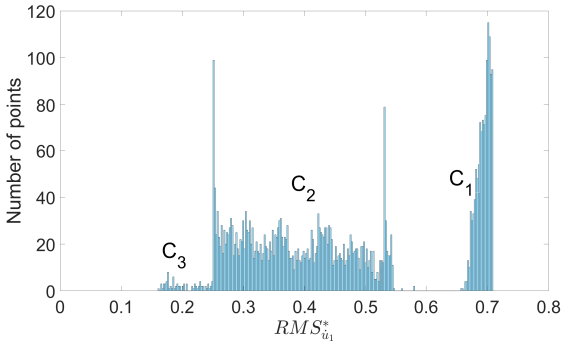

Figure 4.3: Histogram of the unforced system's responses: $\dot{u}_{1,0} \in [0.5, 2.5]$, $k_{NL} \in [0, 0.5]$. See Eq. 2.2 for definition of the nonlinear restoring function. Different response clusters are denoted by C_1, C_2 and C_3.

Figure 4.4 presents another histogram, where $\dot{u}_{1,0}$ ranges from 0.5 to 2.5 in conjunction with the parameter δ varying from 0 to 6 (see Eq. 2.2 for definition of the nonlinear restoring function). Some differences become apparent in the histogram of Fig. 4.4 when compared to that of Fig. 4.1a: the discontinuity is less evident, and we observe the emergence of the cluster C_3.

To explain the difference between the histograms of Figs. 4.4 and 4.1a and their discontinuities, let us consider a set of parameters around the metric's value of 0.58 in Fig. 4.4 (the same value where a discontinuity is present in Fig. 4.1a): $\delta = 2.72$ and the initial conditions as $(u_{1,0}, u_{2,0}, \dot{u}_{1,0}, \dot{u}_{2,0}) = (0, 0, 1.58, 0)$. The corresponding SIM and numerical responses are represented in Fig. 4.5a. Similarly, for the same initial conditions but with $\delta = 5$ (the constant value of δ in the histogram of Fig. 4.1a, where the discontinuity between clusters is clear), the SIM and the numerical response are plotted in Fig. 4.5b. The difference between the responses in both figures is evident: in Fig. 4.5b, the response presents a bifurcation with a larger amplitude than the one of Fig. 4.5a, and thus, it is more effective in terms of energy reduction of the primary mass. In other words, varying δ causes the amplitudes of bifurcations to vary, which explains the presence of responses between the identified clusters in the histogram of Fig. 4.4.

In Fig. 4.4, cluster C_3 exhibits responses with double bifurcations, whereas cluster C_2 displays a single bifurcation. To illustrate this, a set of parameters is selected from each cluster. Figure 4.6b presents the numerical response and the corresponding SIM obtained using a set of parameters around the metric's value of 0.17 (cluster C_3), resulting in a system's response with two bifurcations. Meanwhile, in Fig. 4.6a, a set of parameters around a metric's value of 0.3 (cluster C_2) is taken into account, revealing a single bifurcation. Figure 4.6c presents the numerical response and the SIM of the system obtained using a set of parameters from cluster C_1, around the metric's value of 0.7 and, as expected, this unforced response exhibits no bifurcations.

Figure 4.7 presents a histogram of the efficiency metric considering the responses of a forced system with all initial conditions set to zero (including $\dot{u}_{1,0} = 0$). Here, the amplitude of the external force γ varies from 0 to 2, and the detuning parameter σ from -1 to 1. In this case, it is difficult to distinguish different groups of efficiency metric. In fact, due to the initial conditions set to zero, it is more probable that the system is attracted to equilibrium points situated on the lower part of the main branch of the frequency response curves, one of which is illustrated for $\gamma = 2$ in Fig. 2.18. In other words, the system is less likely to face regimes positioned in the isola. However, if the initial

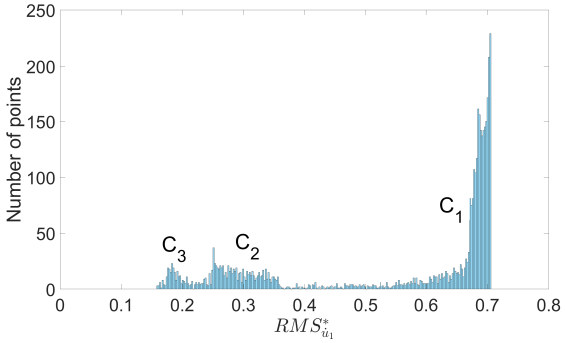

Figure 4.4: Histogram of the unforced system's responses: $\dot{u}_{1,0} \in [0.5, 2.5]$, $\delta \in [0, 6]$. See Eq. 2.2 for definition of the nonlinear restoring function. Different response clusters are denoted by C_1, C_2 and C_3.

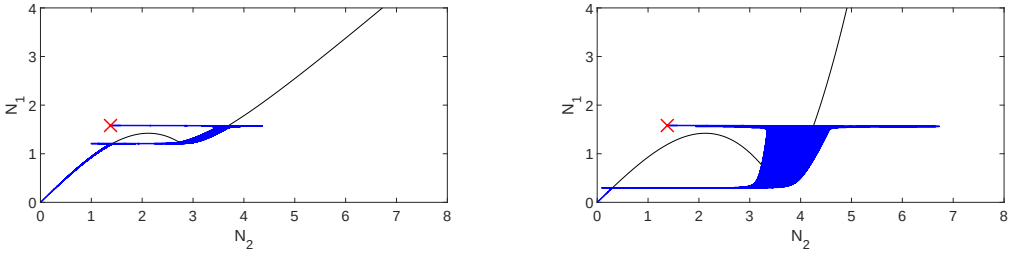

(a) (b)

Figure 4.5: The SIM of the system (in black) and corresponding free numerical responses (in blue) for the initial conditions $(u_{1,0}, u_{2,0}, \dot{u}_{1,0}, \dot{u}_{2,0}) = (0, 0, 1.58, 0)$, represented by $\times$ symbol, and (a) $\delta = 2.72$ (between the clusters C_1 and C_2 of Fig. 4.4); (b) $\delta = 5$ (constant value of δ in the histogram of Fig. 4.1a, where the discontinuity between clusters is clear). Numerical results are obtained from numerical time integration of Eq. (2.7).

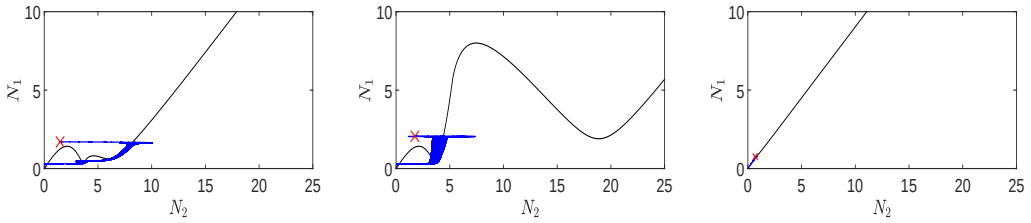

(a) (b) (c)

Figure 4.6: Numerical response of an unforced system and the SIM obtained using a set of parameters around the efficiency metric's value of (a) $\text{RMS}^*_{\dot{u}1} = 0.17$, within cluster C_3 of Fig. 4.4; (b) $\text{RMS}^*_{\dot{u}1} = 0.3$, within cluster C_2 of Fig. 4.4; (c) $\text{RMS}^*_{\dot{u}1} = 0.7$, within cluster C_1 of Fig. 4.4. The initial conditions are represented by $\times$ symbol. Numerical results are obtained from numerical time integration of Eq. (2.7).

velocity $\dot{u}_{1,0}$ is considered in addition to γ and σ, the system's response can reach the isola and, thus, present a discontinuous behavior. To exemplify this, Fig. 4.8 depicts a histogram of the efficiency metric, with $\dot{u}_{1,0}$ ranging from 0.5 to 2.5 and γ ranging from 0.01 to 2. After analyzing Fig.

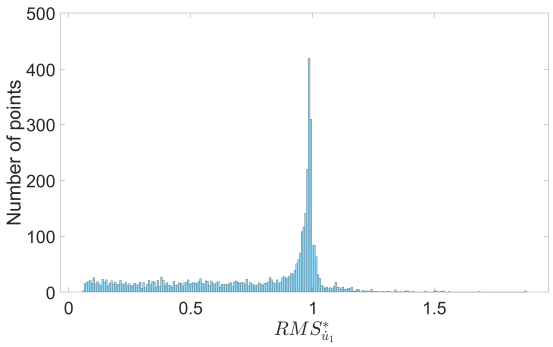

Figure 4.7: Histogram of the forced system's responses: $\gamma \in [0.01, 2], \sigma \in [-1, 1]$.

2.19a, the value of σ is fixed at -1.5 to enable the system to potentially reach responses positioned on the isola. Finally, Fig. 4.8 shows two groups of responses: C_2 with the equilibrium points of the 2-dof system in the main branch of the frequency response curves and C_1 in the isola. In other words, when the equilibrium point is situated in the isola, it corresponds to high energy levels of the outer mass, resulting in a high value of the efficiency metric, which is associated with cluster C_1.

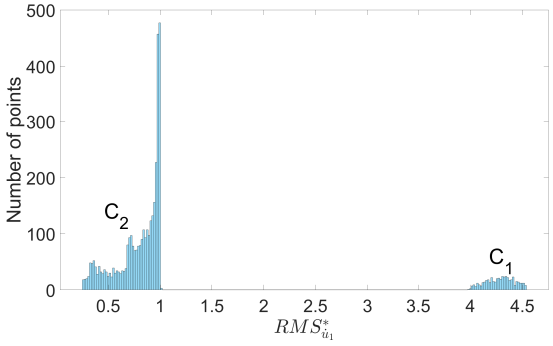

Figure 4.8: Histogram of the forced system's responses: $\dot{u}_{1,0} \in [0.5, 2.5], \gamma \in [0.01, 2], \sigma = -1.5$. Different response clusters are denoted by C_1 and C_2.

4.3 Formulation of the optimization problem

The optimization problem treated in this study is formulated as follows:

$$\begin{aligned} \min_{\mathbf{x}_\mathrm{d}} \quad & \mathbb{E}_{\mathbf{X}_a}(\mathrm{RMS}^*_{\dot{u}_1}(\mathbf{x}_\mathrm{d}, \mathbf{X}_a)) \\ \text{s.t.} \quad & \mathbf{x}_\mathrm{d}^{min} \leq \mathbf{x}_\mathrm{d} \leq \mathbf{x}_\mathrm{d}^{max} \end{aligned} \tag{4.2}$$

where $\mathbf{x}_d$ stands for design variables and $\mathbf{X}_a$ for aleatory variables. The design variables are parameters to be optimized, such as the stiffnesses of the nonlinear spring. The initial conditions imposed to the system, such as initial velocities or external forces, are examples of $\mathbf{X}_a$. The abbreviations "s.t." stands for "subject to". $\mathbb{E}_{\mathbf{X}_a}(\mathrm{RMS}^*_{\dot{u}_1})$ stands for the expected value of $\mathrm{RMS}^*_{\dot{u}_1}$, which is the average of its possible realizations, defined as follows:

$$\mathbb{E}_{\mathbf{X}_a}(\mathrm{RMS}^*_{\dot{u}_1}) = \frac{1}{N_{MC}} \sum_{i=1}^{N_{MC}} \mathrm{RMS}^*_{\dot{u}_1}(\mathbf{x}_d, \mathbf{X}_a) \tag{4.3}$$

where N_{MC} denotes N Monte Carlo samples. The calculation of the expected value is detailed in Sec. 4.4.5.
For the purpose of notation, capital letters represent random variables, and lowercase letters represent variables' realizations, i.e., values that a variable can take.

4.4 Optimization algorithm

Solving an optimization problem can demand a large number of function evaluations, making the problem computationally expensive. For this reason, the design optimization community often uses surrogates that replaces the functions by an approximation, which takes the form of a response surface or a meta-model. However, in cases where a discontinuous behavior is present, such as for the unforced system, using only one meta-model like Kriging [Cressie, 1990], based on an initial Design of Experiments (DOE) to approximate a function, may not produce accurate results. Therefore, the proposed method makes use of clustering techniques like K-means to identify discontinuities and employs an SVM classifier [Cristianini and Shawe-Taylor, 2000] to divide the design and aleatory space into two efficiency regions. The response in each region is assumed to be continuous and can thus be approximated using separate Kriging surrogates. These approximations, along with an SVM, are iteratively refined through a specific adaptive sampling scheme that takes into account the distributions of aleatory variables [Lacaze and Missoum, 2014].
Monte Carlo simulations over the Kriging surrogates are used to estimate the expected value of the efficiency metric. Additionally, the method makes use of predicted variance of Kriging approximations to sample the space of aleatory variables. It is important to note that solving this problem requires a global and zero-order optimizer, especially if the problem is non-smooth. In this work, Particle Swarm Optimization (PSO) is used [Kennedy and Eberhart, 1995]. In the following subsections, an overview of the main steps of the algorithm is provided.

4.4.1 Design of experiments

Meta-models predict an output based on a specific training set of samples, which is generated to be representative of the model using a DOE technique. Therefore, the DOE constitutes the initial step in this optimization algorithm. In this study, the DOE is obtained using the Optimal Latin Hypercube Sampling (OLHS) method.
In the Latin Hypercube Sampling (LHS) method [McKay et al., 1979], all the variables are divided into the same number n of subintervals, and each subinterval can only have one sample. For a $n \times n$ grid, for example, there can only be one sample on each row and column. Thus, the number of samples is equal to n and there is $n!^{(d-1)}$ possible LHS designs, where d is the number of variables. In Fig. 4.9, LHS was employed to generate a potential DOE with $n = 10$ and for the variables X_1 and X_2, i.e., $d = 2$, for example purposes.
However, the LHS is chosen at random and may present poor coverage of the space. In order to overcome this problem, OLHS searches among all possible LHS options to find an optimal configuration where the spatial distribution of samples is uniform. An example of criterion to build an OLHS is the maximization of the minimum distance between samples.

4.4.2 Clustering

The next step is to divide the space into two regions of the design and aleatory variables. This classification is possible due to the discontinuous behavior of the system. In this study, we employ the K-Means algorithm [Hartigan and Wong, 1979] to cluster the samples. This algorithm is used to quantify the information obtained by a given sample and to identify K groups with different

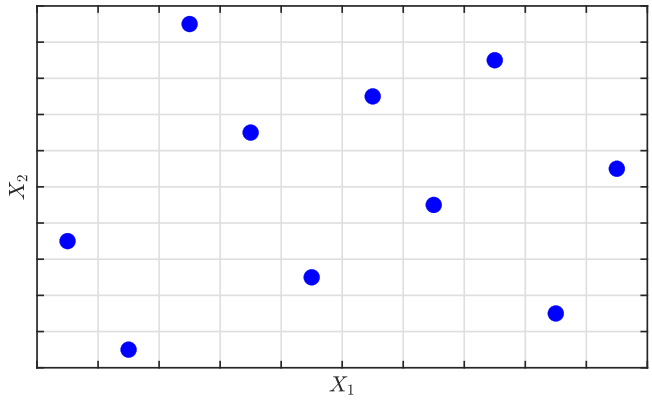

Figure 4.9: Representation of a possible LHS design for the variables X_1 and X_2.

responses, so that it minimizes the within-cluster sum of squares by moving the samples from one cluster to another. In Fig. 4.10, one can see an example of clustering using the K-means algorithm, with the two distinct groups represented by the blue and orange colored bullets.

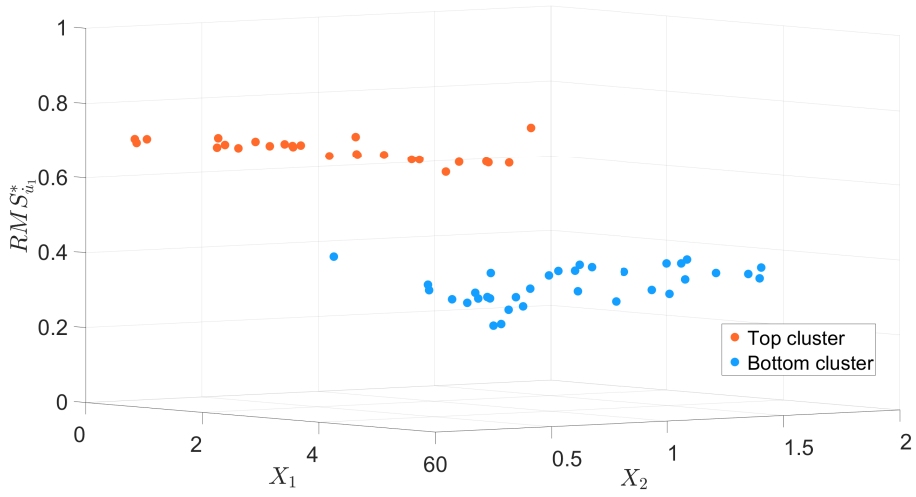

Figure 4.10: An example of clustering using K-means algorithm. $\text{RMS}^*_{\dot{u}_1}$ stands for the efficiency metric, while X_1 and X_2 represent the variables of the optimization problem.

4.4.3 Support vector machine

Based on the clustering results of the system's responses, the goal is to identify the region within the parameter space where the system's efficiency metric is lower. To achieve this, a technique known as Explicit Design Space Decomposition [Basudhar and Missoum, 2008] is employed. The fundamental concept behind this approach is to create a boundary that separates two classes of samples in terms of chosen parameters. This is accomplished using an SVM, which is a machine learning tool that provides an explicit expression of the boundary in terms of the parameters. The objective in SVM is to obtain an optimal classification boundary that maximizes the "margin".

Given a d-dimensional space sampled with N training points $\mathbf{x}_i$ and the corresponding class labels $y_i = \pm 1$, provided by the K-means clustering, the corresponding boundary that separates the two classes of data can be represented as [Basudhar and Missoum, 2008]:

$$s(\mathbf{x}) = b + \sum_{i=1}^{N} \lambda_i y_i K(\mathbf{x}_i, \mathbf{x}) = 0 \tag{4.4}$$

where b is a scalar referred to as the bias, λ_i are Lagrange multipliers obtained from the quadratic programming optimization problem used to construct the SVM, K is a kernel function that can take on various forms, such as polynomial or Gaussian radial basis kernels, as used in this study [Basudhar and Missoum, 2008]:

$$K(\mathbf{x}_i, \mathbf{x}_j) = \exp\left(-\frac{||\mathbf{x}_i - \mathbf{x}_j||^2}{2\kappa^2}\right) \tag{4.5}$$

where κ is the width parameter, and ||.|| stands for the Euclidean distance between two vectors.
The classification of any point $\mathbf{x}$ is given by the sign of $s(\mathbf{x})$. In Fig. 4.11 is shown an example of SVM.

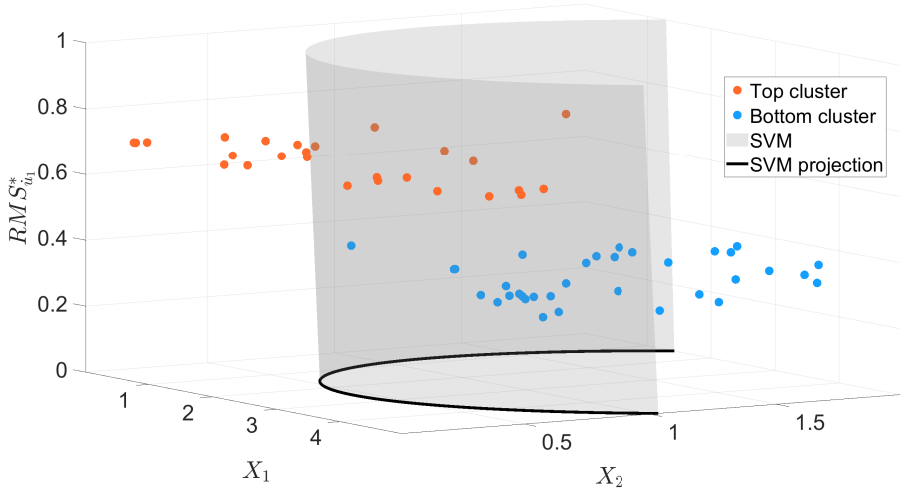

Figure 4.11: An example of SVM. $\text{RMS}^*_{\dot{u}_1}$ stands for the efficiency metric, while X_1 and X_2 represent the variables of the optimization problem.

The SVM boundary is first trained using a design of experiments that covers the entire space, then refined with additional samples, which is detailed in Sec. 4.4.6.

4.4.4 Kriging meta-model

Gaussian processes are random processes based on correlation between samples that can be read as

$$Y(\mathbf{x}) \sim \mathcal{N}(m_{\mathrm{x}}, \sigma^2_{\mathrm{x}}) \tag{4.6}$$

where m_{x} is a mean function and σ^2_{x} a covariance function.
Kriging meta-model is an approximation $(\tilde{f})$ of a function (f) constructed as a trend refined by a Gaussian process [Cressie, 1990]:

$$\tilde{f}(\mathbf{x}) = \mu + Z(\mathbf{x}) \tag{4.7}$$

where μ is a trend of the model and $Z(\mathbf{x})$ is a Gaussian process of mean 0, which accounts for uncertainty in prediction depending on the sparsity of data. In ordinary Kriging, μ is an unknown constant that depends on the correlation between $\mathbf{x}$ and the evaluated samples.
The covariance between any two samples a and b is defined as:

$$cov[Z(a), Z(b)] = {\sigma_Z}^2 R(a, b) \tag{4.8}$$

where ${\sigma_Z}^2$ is the variance of the process Z and R is the correlation function:

$$R(a, b) = e^{-\sum_{j=1}^{m} \theta_j |a_j - b_j|^{p_j}} \tag{4.9}$$

where θ_j is the scale parameter for the jth dimension and the parameter p_j determines the smoothness of the correlation function.
The unknowns of Kriging are solved using maximum likelihood constructed based on the known actual values and correlations for the evaluated samples. The main advantage of Kriging is that it gives the variance of the approximation, ${\sigma_Z}^2$, for any point in the design space. This variance is taken into account in the optimization technique referred to as Efficient Global Optimization (EGO)[Jones et al., 1998].
Figure 4.12 provides an illustrative example of two Kriging meta-models that have been constructed based on the two distinct clusters shown in Fig. 4.10.

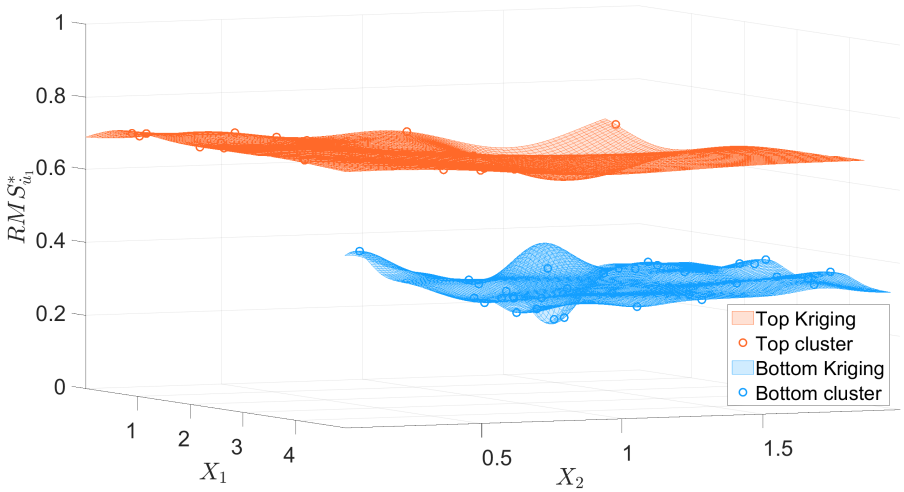

Figure 4.12: An example of two Kriging meta-models. $\text{RMS}^*_{\dot{u}_1}$ stands for the efficiency metric, while X_1 and X_2 represent the variables of the optimization problem.

4.4.5 Computation of the expected value using two Kriging

When the design space is divided into two regions, then two Kriging and one SVM meta-models are used to approximate the system's efficiency over the entire design and aleatory space. In this case, the expected value is computed as follows [Boroson and Missoum, 2017]:

$$\mathbb{E}_{\mathbf{X}_a}(\text{RMS}^*_{\dot{u}_1}) = \frac{1}{N_{MC}} \sum_{i=1}^{N_{MC}} Q(\mathbf{p}_i) \tag{4.10}$$

where Q is defined as:

$$Q(\mathbf{p}_i) = \begin{cases} \widetilde{\text{RMS}}^{*(1)}_{\dot{u}_1} & \text{if} \quad s(\mathbf{p}_i) \leq 0 \\ \widetilde{\text{RMS}}^{*(2)}_{\dot{u}_1} & \text{if} \quad s(\mathbf{p}_i) > 0 \end{cases} \tag{4.11}$$

$\mathbf{p}_i$ are the N_{MC} Monte Carlo samples around $\mathbf{x}_d$. $\widetilde{\text{RMS}}^{*(1)}_{\dot{u}_1}$ and $\widetilde{\text{RMS}}^{*(2)}_{\dot{u}_1}$ are the Kriging approximations which depend on the classification of the sample, determined by the sign of $s(\mathbf{x})$, i.e., the SVM approximation.

4.4.6 Adaptive sampling

Refinement of the SVM boundary In order to improve the precision of the SVM boundary, an adaptive sampling scheme referred as Generalized Max-Min (GMM) is used to refine the boundary of the failure domain. The sampling algorithm is described in detail in [Lacaze and Missoum, 2014]. The objective of this algorithm is to insert a new sample as far as possible from other samples and also in the region of highest probability of misclassification by the SVM, that is, where $s(\mathbf{x}) = 0$. GMM samples are found solving the following optimization problem:

$$\begin{aligned} \mathbf{x}_g^{(k)} = \underset{\mathbf{x}=\{\mathbf{x}_d,\mathbf{x}_a\}}{\arg\max} \quad & \mathbf{f}_{\mathbf{x}}(\mathbf{x}) \sqrt[N_d+N_a]{\min_i ||\mathbf{x} - \mathbf{x}_i||} \\ \text{s.t.} \quad & s(\mathbf{x}) = 0 \\ & \mathbf{x}_d^{\min} \leq \mathbf{x}_d \leq \mathbf{x}_d^{\max} \\ & \mathbf{x}_a^{\min} \leq \mathbf{x}_a \leq \mathbf{x}_a^{\max} \end{aligned} \tag{4.12}$$

where N_d and N_a are the number of design and aleatory variables, respectively. $\mathbf{f}_{\mathbf{x}}$ is a $(N_d + N_a)$-dimensional joint probability density function. Note that the distributions for the design variables, which are assumed deterministic, are uniform distributions. In addition, bounds on the aleatory variables were incorporated, as the considered distributions have finite support.
The process of SVM refinement is illustrated in Fig. 4.13. In the 1st iteration, a new sample (depicted in green in Fig. 4.13a) is added. Subsequently, in the 2nd iteration, the new sample is classified and the SVM is rebuilt as shown in Fig. 4.13b. Still in the 2nd iteration, a new sample is added in green and classified in the 3rd iteration (Fig. 4.13c). The refinement process continues, and in Fig. 4.13d, the state of the SVM in the 40th iteration is presented. Note that the SVM in these figures is projected for visualization purposes.

Update of the Kriging Another adaptive sampling scheme is used to update the Kriging surrogates. The optimization problem is centered only on finding the optimum in the design space without considering the availability of aleatory variables to update the approximations. Therefore, here we seek the values of aleatory variables that maximize the Kriging prediction variance at the optimum $\mathbf{x}_{\text{d}}^{(k)}$ at the kth iteration [Boroson and Missoum, 2017], while taking into account the joint probability distribution, representing the areas where the Kriging models are least accurate. This sub-problem can be presented as follows:

$$\begin{aligned} \mathbf{x}_a^{(k)} = \underset{\mathbf{X}_a}{\arg\max} \quad & \mathbf{f}_{\mathbf{X}_a}(\mathbf{x}_{\text{d}}^{(k)}, \mathbf{x}_a) \sqrt[N_a]{\hat{\sigma}^2(\mathbf{x}_{\text{d}}^{(k)}, \mathbf{x}_a)} \\ \text{s.t.} \quad & \mathbf{x}_a^{min} \leq \mathbf{x}_a \leq \mathbf{x}_a^{max} \end{aligned} \tag{4.13}$$

where $\hat{\sigma}^2$ is the predicted variance of the Kriging approximations at the kth iteration. The search is conducted over the two Kriging models employed in the algorithm.

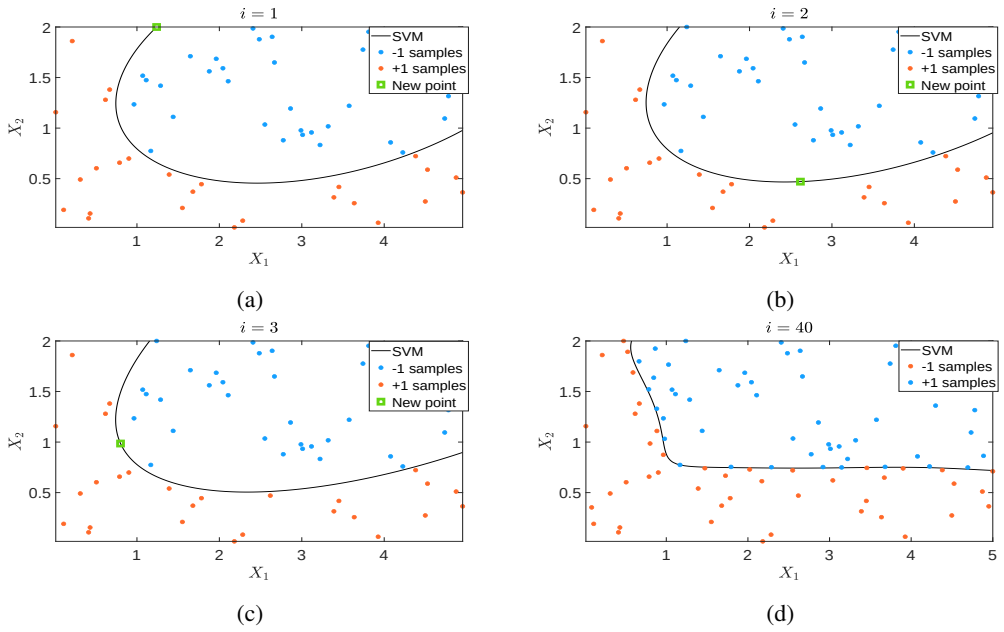

Figure 4.13: An example of adaptive sampling: a) 1st iteration; b) 2nd iteration; c) 3rd iteration; d) 40th iteration. X_1 and X_2 represent the variables of the optimization problem.

4.4.7 Algorithm

The procedure of the stochastic optimization algorithm is outlined in Algorithm 1. This algorithm is particularly employed in scenarios characterized by discontinuous behaviors, requiring the segregation of regions with distinct efficiency levels. An example of such a situation is when considering the unforced system.

After definition of an efficiency metric, $\text{RMS}^*_{\dot{u}_1}$, in *Step 1*, a DOE is generated (*Step 2*), and $\text{RMS}^*_{\dot{u}_1}$, is computed for each sample in *Step 3*. Subsequently, the K-means technique is applied to identify discontinuities (*Step 4*), and an SVM classifier is used to partition the design and aleatory space into two efficiency regions (*Step 5*). In *Step 6*, the response in each region is approximated as $\widetilde{\text{RMS}}^*_{\dot{u}_1}$ using separate Kriging surrogates. In *Step 7*, Monte Carlo simulations over the surrogates are employed to estimate the expected value of the efficiency metric, i.e., $\mathbb{E}_{\mathbf{X}_a}(\widetilde{\text{RMS}}^*_{\dot{u}_1})$, and an optimizer is then applied to find the design variables $\mathbf{x}_d$ that minimize $\mathbb{E}_{\mathbf{X}_a}(\widetilde{\text{RMS}}^*_{\dot{u}_1})$. The predicted variance of Kriging approximations is used in *Step 8* to determine the aleatory variables $\mathbf{x}_a$ that maximize the Kriging's variance at $\mathbf{x}_d$ obtained in *Step 7*. In *Step 9*, the SVM model is refined through a specific adaptive sampling scheme generating a new sample $\mathbf{x}_g$. Finally, $\text{RMS}^*_{\dot{u}_1}$ is computed for the new samples: the first one consists of the variables obtained in *Step 7* and *Step 8*, while the second sample is derived from *Step 9*. These new points are added to the database. This entire process is iterated from *Step 4* until convergence is achieved for both the expected value $\mathbb{E}_{\mathbf{X}_a}(\widetilde{\text{RMS}}^*_{\dot{u}_1})$ and the design variables $\mathbf{x}_d$.

4.5 Results

In this section, two distinct optimization problems related to the meta-cell introduced in Chapter 2 are presented. Firstly, the scenario takes into account the unforced system, where the outer mass is subject to an impulse represented by its initial velocity $\dot{u}_{1,0}$. Then, a forced system is considered,

Algorithm 1 Stochastic optimization

1. Define an efficiency metric: $\text{RMS}^*_{\dot{u}_1}$;
2. Generate a Design of Experiments (XDOE);
3. Compute the function $\text{RMS}^*_{\dot{u}_1}$(XDOE);
4. Divide the samples into two clusters;
5. Approximate the boundary between the clusters using an SVM;
6. Train two Kriging models, one for each cluster: $\widetilde{\text{RMS}}^*_{\dot{u}_1 1}$ and $\widetilde{\text{RMS}}^*_{\dot{u}_1 2}$;
7. Find the minimum $\mathbf{x}_d^{(k)}$ at the kth iteration:

$$\begin{aligned} \mathbf{x}_d^{(k)} = & \arg\min_{\mathbf{x}_d} \quad \mathbb{E}_{\mathbf{X}_a}(\widetilde{\text{RMS}}^*_{\dot{u}_1}(\mathbf{x}_d, \mathbf{X}_a)) \\ & \text{s.t.} \qquad \mathbf{x}_d^{\min} \leq \mathbf{x}_d \leq \mathbf{x}_d^{\max} \end{aligned}$$

8. Find $\mathbf{x}_a^{(k)}$ that maximizes the Kriging variance at $\mathbf{x}_{\text{d}}^{(k)}$ accounting for the joint distribution:

$$\begin{aligned} \mathbf{x}_a^{(k)} = & \arg\max_{\mathbf{X}_a} \quad \mathbf{f}_{\mathbf{X}_a}(\mathbf{x}_{\text{d}}^{(k)}, \mathbf{x}_a) \sqrt[\frac{1}{N_a}]{\hat{\sigma}^2(\mathbf{x}_{\text{d}}^{(k)}, \mathbf{x}_a)} \\ & \text{s.t.} \quad \mathbf{x}_a^{min} \leq \mathbf{x}_a \leq \mathbf{x}_a^{max} \end{aligned}$$

9. SVM refinement (generate a generalized max-min sample $\mathbf{x}_g^{(k)}$):

$$\begin{aligned} \mathbf{x}_g^{(k)} = & \arg\max_{\mathbf{x}=\{\mathbf{x}_d, \mathbf{x}_a\}} \quad \mathbf{f}_{\mathbf{x}}(\mathbf{x}) \sqrt[\frac{1}{N_d + N_a}]{\min_i ||\mathbf{x} - \mathbf{x}_i||} \\ & \text{s.t.} \qquad s(\mathbf{x}) = 0 \\ & \qquad\quad \mathbf{x}_d^{\min} \leq \mathbf{x}_d \leq \mathbf{x}_d^{\max} \\ & \qquad\quad \mathbf{x}_a^{\min} \leq \mathbf{x}_a \leq \mathbf{x}_a^{\max} \end{aligned}$$

10. Compute $\text{RMS}^*_{\dot{u}_1}$ at $\mathbf{x}_g^{(k)}$ and $(\mathbf{x}_d^{(k)}, \mathbf{x}_a^{(k)})$. Add to the database;
11. Repeat from *Step 4* until convergence.

with a forcing amplitude γ and a detuning parameter of the excitation frequency σ. Across all scenarios, the damping parameters ζ_1 and ζ_2 remain fixed at 0.1, and ε at 0.01 (see Eq. (2.7)). The parameters governing the restoring force are considered as design variables: k_{NL} and k_L span from 0 to 0.5, while δ varies from 0 to 6 (see Eq. 2.2 for definition of the nonlinear restoring function).
The optimization problems are conducted for the system featuring different restoring force functions: the piecewise nonlinearity studied in this thesis (see Eq. 2.2) and a pure cubic nonlinearity, represented as $f(\alpha) = k_{NL}\alpha^3$. This comparison is conducted to evaluate their respective efficiencies. The parameter k_{NL} of the pure cubic restoring force is considered as the design variable and varies in the range of 0 to 0.5.
Table 4.1 provides the ranges of all potential design or aleatory variables. Furthermore, in all the problems discussed here, the optimization problem is solved using truncated normal and uniform distributions [Devore and Berk, 2011] for aleatory variables and design variables, respectively.

k_{NL}	k_L	δ	$\dot{u}_{1,0}$	γ	σ
[0, 0.5]	[0, 0.5]	[0, 6]	[0.5, 2.5]	[0.01, 2]	[-1, 1]

Table 4.1: Ranges of design and aleatory variables.

4.5.1 Optimization problem considering unforced systems

The optimization problem considering an unforced system is formulated as follows:

$$\begin{aligned} \min_{\delta, k_{NL}, k_L} \quad & \mathbb{E}_{\dot{U}_{1,0}}(\text{RMS}^*_{\dot{u}_1}(\underbrace{\delta, k_{NL}, k_L}_{\mathbf{x}_d}, \underbrace{\dot{u}_{1,0}}_{\mathbf{X}_a})) \\ \text{s.t.} \quad & 0 \leq \delta \leq 6 \\ & 0 \leq k_{NL} \leq 0.5 \\ & 0 \leq k_L \leq 0.5 \end{aligned} \tag{4.14}$$

Here, $\dot{u}_{1,0}$ is the aleatory variable defined as $\dot{u}_{1,0} \sim \mathcal{N}_t(1.5, 0.0625)$, i.e., the variable $\dot{u}_{1,0}$ is distributed as a truncated normal distribution with mean of 1.5 and variance of 0.0625 (the standard deviation corresponds to 25% of the $\dot{u}_{1,0}$ ranges).
The optimization results of this problem, considering two different nonlinearities (pure cubic and the piecewise one), are detailed in Table 4.2. This table provides the optimal values of the design variables, along with the number of initial samples and total iterations used in the optimization process. To verify the validity of efficiency prediction at the optimum, the table includes a comparison between the surrogate-based expected value ($\mathbb{E}_{\Sigma,\Gamma}(\widetilde{\text{RMS}^*_{\dot{u}1}})$), i.e., determined through Kriging approximations, and the true expected values ($\mathbb{E}_{\Sigma,\Gamma}(\text{RMS}^*_{\dot{u}_1})$) derived from the actual metric using 2000 Monte Carlo samples. The table also provides the lower and upper bounds of the 95% confidence intervals (CI) of both expected values.

Parameters	Pure cubic nonlinearity	Piecewise nonlinearity
Number of Kriging surrogates	2	2
Initial DOE size	10	20
Iterations	16	17
k_{NL}	0.1605	0.2618
k_L		0.2520
δ		2.4043
$\mathbb{E}_{\Sigma,\Gamma}(\widetilde{\text{RMS}^*_{\dot{u}_1}})$ (%)	0.3182	0.1856
95% CI	[0.3164, 0.3199]	[0.1850, 0.1861]
$\mathbb{E}_{\Sigma,\Gamma}(\text{RMS}^*_{\dot{u}_1})$ (%)	0.3147	0.1844
95% CI	[0.3110, 0.3184]	[0.1828, 0.1859]

Table 4.2: Results of the optimization problem for the unforced system using pure cubic and the piecewise restoring forces.

The convergence behaviors of the objective function and the design variables are illustrated in Fig. 4.14 for the case involving pure cubic nonlinearity and in Fig. 4.15 for the system with the piecewise nonlinearity. Notably, few iterations are necessary to converge to the optimal solution. The approximations of the expected values exhibits a high level of accuracy, deviating by 2% from the actual values for each problem.

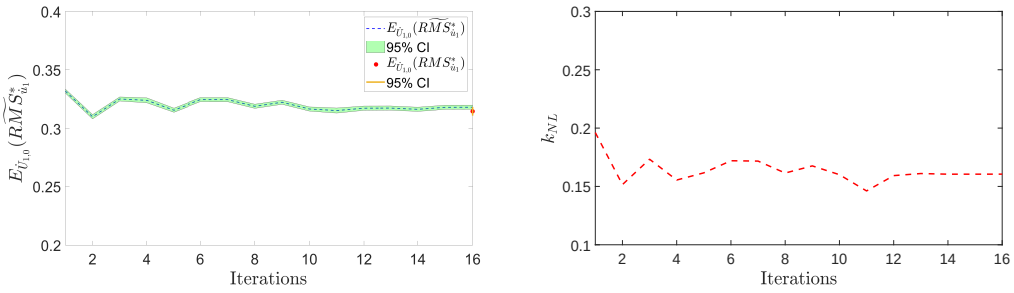

(a) (b)

Figure 4.14: Optimization of the unforced 2-dof system with pure cubic restoring force, i.e., $f(\alpha) = k_{NL}\alpha^3$. Convergences of: (a) Objective function and (b) k_{NL}.

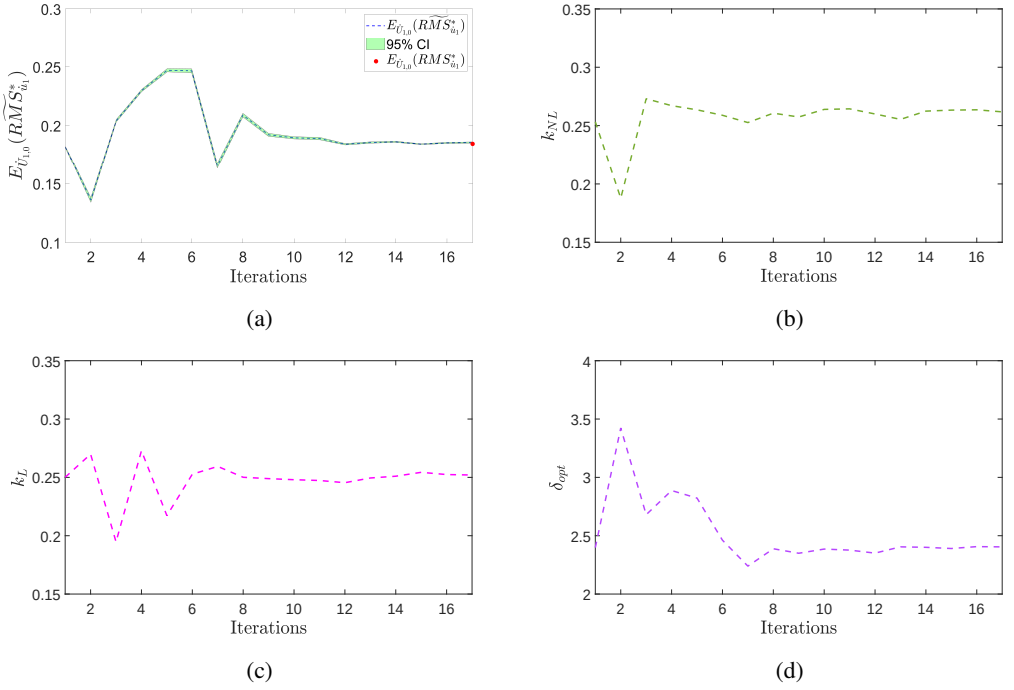

(a) (b)

(c) (d)

Figure 4.15: Optimization of the unforced 2-dof system with the piecewise restoring force (see Eq. 2.2). Convergences of: (a) Objective function; (b) k_{NL}; (c) k_L and (d) δ.

It is worth noting that the expected value for the system with the piecewise nonlinearity is significantly lower than the one of the system with pure cubic nonlinearity, showing a remarkable 41.8% reduction in the expected value. This highlights the superior efficiency of the piecewise nonlinearity in reducing energy for this specific problem set when compared to the use of pure cubic nonlinearity.

Figure 4.16 displays SIM of the system with pure cubic and piecewise nonlinear restoring forces, using optimal parameters reported in Table 4.2. Additionally, the free responses of both systems, with an initial velocity of $\dot{u}_{1,0} = 2.5$, are superimposed on the respective SIMs shown in Fig. 4.17. Analysing the results, we find that the system with piecewise nonlinearity presents two bifurcations, and a SIM with two minima at approximately the same values of N_1, resulting in an efficiency met-

ric of $\text{RMS}^*_{\dot{u}_1} = 0.2327$, while the system with pure cubic nonlinearity faces only one bifurcation leading to a $\text{RMS}^*_{\dot{u}_1} = 0.4257$.

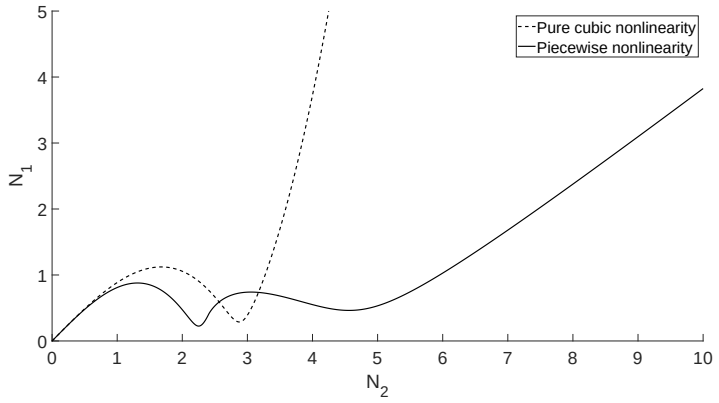

Figure 4.16: The SIM of the studied system with optimized restoring forces: pure cubic and piecewise nonlinearity. Numerical results are obtained from numerical time integration of Eq. (2.7). For optimized parameters, refer to Table 4.2.

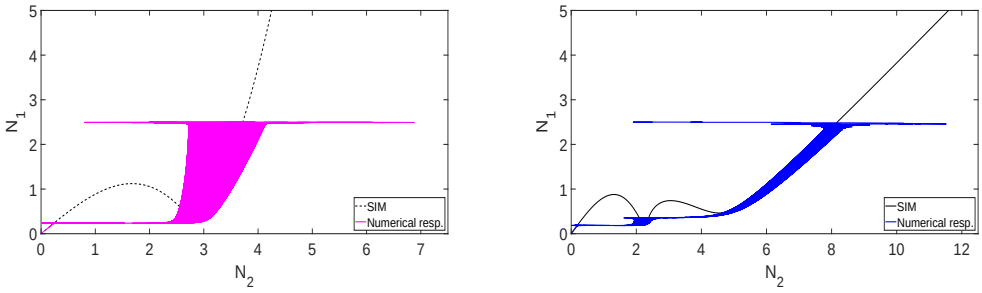

(a) (b)

Figure 4.17: The SIM and corresponding free numerical responses, with the initial conditions $(u_{1,0}, u_{2,0}, \dot{u}_{1,0}, \dot{u}_{2,0}) = (0, 0, 2.5, 0)$, of the system with optimized restoring forces: (a) Pure cubic and (b) Piecewise nonlinearity. Numerical results are obtained from numerical time integration of Eq. (2.7). For optimized parameters, refer to Table 4.2.

As N_1 represents mainly the vibratory amplitude of the outer mass, which is related to $\dot{u}_1$ (see Eqs. (2.8), (2.16) and (2.28)), it is a good representation of the efficiency metric used in this optimization study (see Eq. (4.1)). Time histories of N_1 for the meta-cell with optimized parameters for pure cubic and piecewise nonlinearities are illustrated in Fig. 4.18. It is evident from this figure that the system with optimized piecewise nonlinearity exhibits a faster reduction in N_1, i.e, a higher energy reduction efficiency when compared to the same system with optimized pure cubic nonlinearity.
Examples of SVM and Kriging models used in the optimization of the unforced 2-dof system with pure cubic restoring force, featuring just two variables and offering a 3D visualization, are illustrated in Fig. 4.19. Figure 4.19a presents the DOE and the SVM used to classify the samples, while Fig. 4.19b presents the two Kriging models built using the DOE to approximate the efficiency metric over the entire design space.

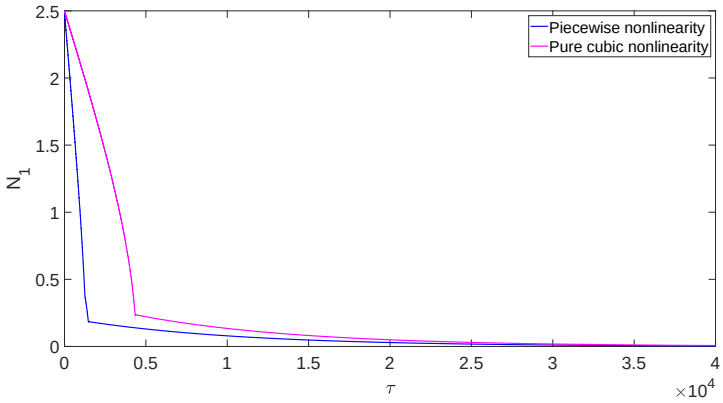

Figure 4.18: Time histories of N_1, with the initial conditions $(u_{1,0}, u_{2,0}, \dot{u}_{1,0}, \dot{u}_{2,0}) = (0, 0, 2.5, 0)$, of the system with optimized pure cubic and piecewise restoring forces (see Table 4.2). Numerical results are obtained from numerical time integration of Eq. (2.7).

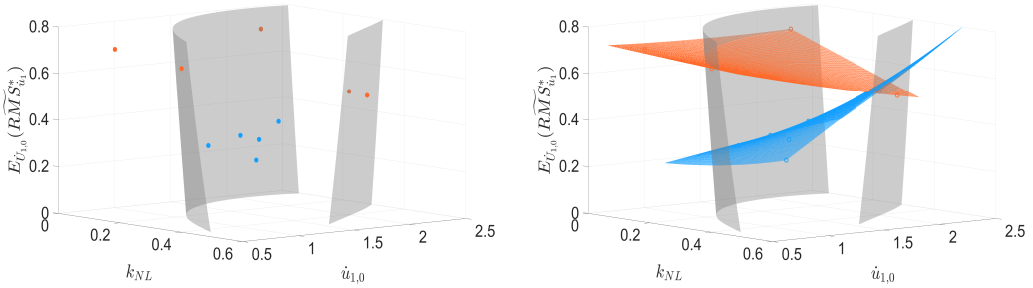

(a) (b)

Figure 4.19: Models used in the optimization of the unforced 2-dof system with pure cubic restoring force function: (a) Design of experiments and SVM model; (b) SVM and Kriging models.

Figure 4.20a displays the sample points and the SVM model at the final iteration of the optimization process. Meanwhile, Fig. 4.20b illustrates the two Kriging models constructed using the collected samples. Comparing Figs. 4.20b and 4.19b, we observe that the Kriging models in the last iteration (Fig. 4.20b) undergo a change in form due to refinement, resulting in more precise approximations of the efficiency metric's values.

4.5.2 Optimization problem considering forced systems

The optimization problem for the forced system is formulated as follows:

$$\begin{aligned} \min_{\delta, k_{NL}, k_L} \quad & \mathbb{E}_{\Gamma,\Sigma}(\mathrm{RMS}^*_{\ddot{u}_1}(\underbrace{\delta, k_{NL}, k_L}_{\mathbf{x}_d}, \underbrace{\gamma, \sigma}_{\mathbf{x}_a})) \\ \text{s.t.} \quad & 0 \leq \delta \leq 6 \\ & 0 \leq k_{NL} \leq 0.5 \\ & 0 \leq k_L \leq 0.5 \end{aligned} \tag{4.15}$$

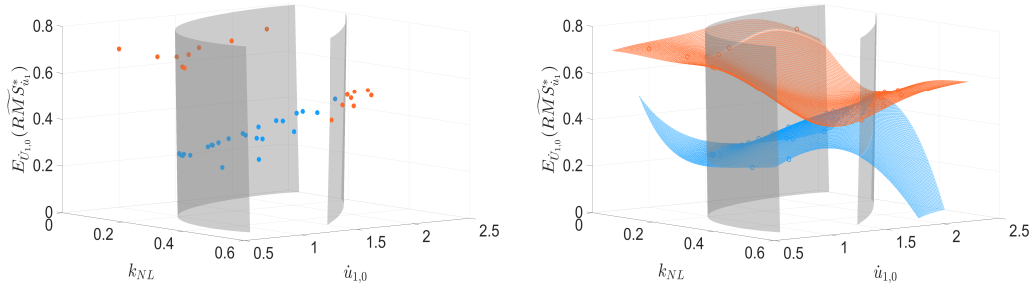

(a) (b)

Figure 4.20: Models used in the optimization of the unforced 2-dof system with pure cubic restoring force function: (a) Sample points and SVM model at the final iteration; (b) SVM and Kriging models at the final iteration.

Parameters	Pure cubic nonlinearity	Piecewise nonlinearity
Number of Kriging surrogates	1	1
Initial DOE size	15	25
Iterations	40	30
k_{NL}	0.3868	0.3574
k_L		0.3284
δ		2.0680
$\mathbb{E}_{\Sigma,\Gamma}(\widetilde{\text{RMS}^*_{\dot{u}_1}})$ (%)	0.2528	0.2080
95% CI	[0.2489, 0.2567]	[0.2048, 0.2112]
$\mathbb{E}_{\Sigma,\Gamma}(\text{RMS}^*_{\dot{u}_1})$ (%)	0.2577	0.2115
95% CI	[0.2459, 0.2695]	[0.2047, 0.2184]

Table 4.3: Results of the optimization problem for the forced system using pure cubic and piecewise restoring forces.

γ and σ are the aleatory variables of the problem and follow truncated normal distributions: $\gamma \sim \mathcal{N}_t(1, 0.0625)$ and $\sigma \sim \mathcal{N}_t(0, 0.0625)$. The standard deviations correspond to 25% of the range of aleatory variables. It is worth noting that in this problem, only one Kriging model is used to approximate the efficiency metric, given that distinguishing two groups of efficiency metric in a forced system with $\dot{u}_{1,0} = 0$ is challenging, as discussed in Sec. 4.2.3.

Table 4.3 presents the results and details of the optimizations of the forced systems. The convergence of the objective functions and design variables is shown in Fig. 4.21 for the problem with pure cubic nonlinearity and in Fig. 4.22 for the problem with the piecewise nonlinearity. In both cases, relatively few iterations are required to reach the converged optimum, and the approximations of the expected values are accurate, within 2% of the actual ones for each problem. When comparing the expected values for both types of nonlinearities, we observe a greater reduction for the system with the piecewise nonlinearity compared to the system with pure cubic nonlinearity, showing a 17.7% reduction in the expected value for this specific problem set.

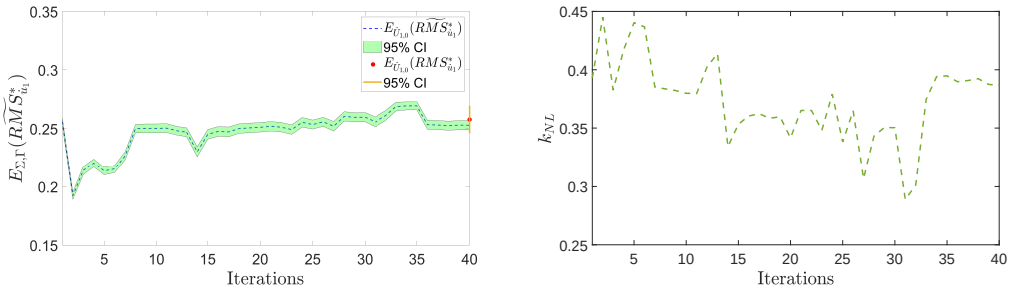

(a) (b)

Figure 4.21: Optimization of the forced 2-dof system with pure cubic restoring force, i.e., $f(\alpha) = k_{NL}\alpha^3$. Convergences of: (a) Objective function and (b) k_{NL}.

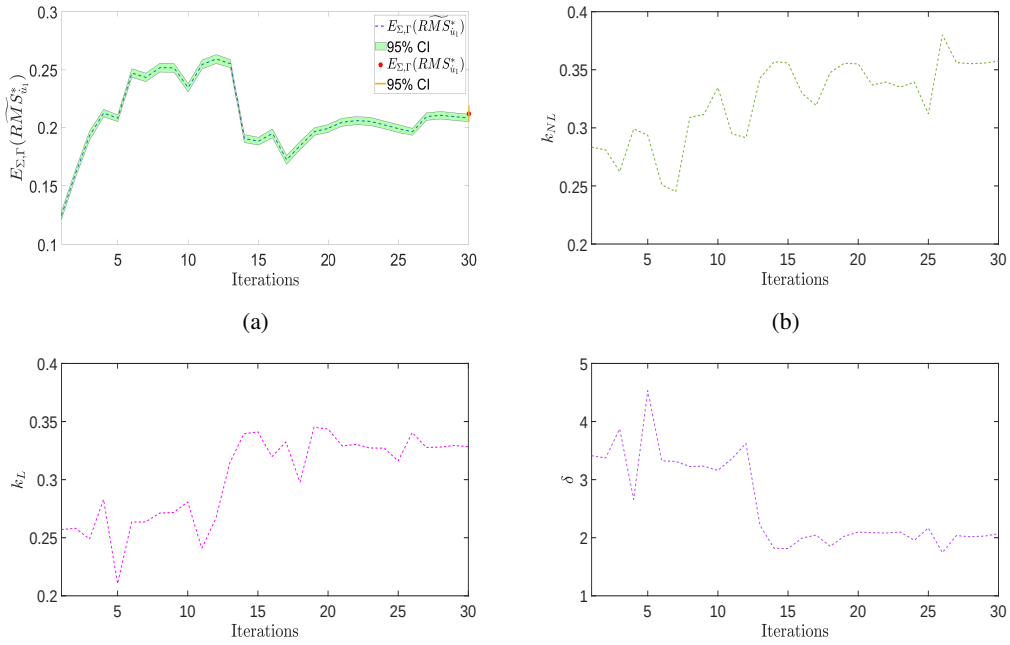

(a) (b)

(c) (d)

Figure 4.22: Optimization of the forced 2-dof system with the piecewise restoring force (see Eq. 2.2). Convergences of: (a) Objective function; (b) k_{NL}; (c) k_L and (d) δ.

Considering the 1-dof system, it is possible to trace its equilibrium points in terms of N_1 and σ. Figures 4.23, 4.24 and 4.25 present frequency response curves for different forcing amplitudes and systems: 1-dof, 2-dof with the optimized pure cubic nonlinearity and piecewise nonlinearity. From that, it is clear that the curve corresponding to the piecewise nonlinearity can intersect with the other two, but it predominantly stays beneath them. In detail, we notice that the curves representing the 2-dof systems are significantly lower than the 1-dof curve, indicating a notably higher efficiency in energy reduction of the outer mass (N_1) with the addition of the inner mass, as expected, given that this additional mass works as a NES for the outer mass. When comparing the curves of piecewise and pure cubic nonlinearity, we observe occasional overlap, but, in general, the piecewise nonlinearity curve is slightly lower than the pure cubic nonlinearity curve. Furthermore, an isola

emerges in the system with pure cubic nonlinearity under the considered excitation parameters in the optimization problem. In contrast, this isola does not manifest in the system with piecewise nonlinearity. These observations justify the observed 17.7% reduction in the expected value when employing the piecewise nonlinearity.

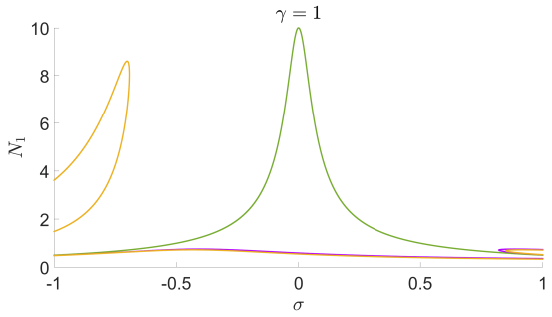

Figure 4.23: Frequency response curves for different systems: 1-dof system (green curve), 2-dof system with optimized pure cubic nonlinearity (yellow curve), and 2-dof system with the optimized piecewise nonlinearity (purple curve). The curves illustrate variations in N_1 and σ for $\gamma = 1$. For optimized parameters, refer to Table 4.3.

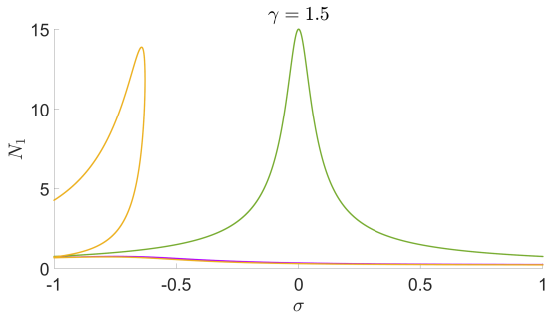

Figure 4.24: Frequency response curves for different systems: 1-dof system (green curve), 2-dof system with optimized pure cubic nonlinearity (yellow curve), and 2-dof system with the optimized piecewise nonlinearity (purple curve). The curves illustrate variations in N_1 and σ for $\gamma = 1.5$. For optimized parameters, refer to Table 4.3.

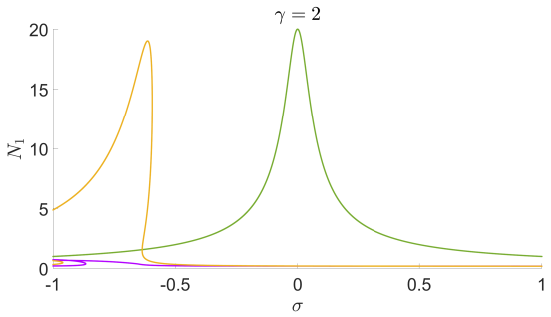

Figure 4.25: Frequency response curves for different systems: 1-dof system (green curve), 2-dof system with optimized pure cubic nonlinearity (yellow curve), and 2-dof system with the optimized piecewise nonlinearity (purple curve). The curves illustrate variations in N_1 and σ for $\gamma = 2$. For optimized parameters, refer to Table 4.3.

4.6 Conclusions of the chapter

A study on the optimization of the nonlinear mass-in-mass meta-cell presented in Chapter 2 is conducted. The comprehension of the system's dynamic behavior, including potential discontinuities, is enhanced through the analysis of histograms. After recognizing the system's high sensitivity to incertitudes, a stochastic optimization algorithm is employed to account for them.
The optimization of the meta-cells with piecewise and pure cubic nonlinearity are studied, considering not only initial velocities as excitation but also external forces. The results demonstrate that the system with optimized piecewise nonlinearity exhibits higher energy reduction efficiency when compared to the same system with optimized pure cubic nonlinearity.
The optimization process employed in this study can be applied to the design and fabrication of the considered meta-cells, aiming to enhance the efficiency of vibratory energy exchanges between two masses.

CHAPTER 5

Experiments using a programmable electroacoustic loudspeaker

Due to the difficulty of conceiving mechanically the nonlinearity explored in this thesis (see Eq. (2.2)), this chapter delves into the study of a programmable electroacoustic loudspeaker. A model-inversion technique for digitally programming the impedance of the loudspeaker to achieve a desired nonlinear behavior is presented. A Duffing-type nonlinearity is programmed and the electroacoustic loudspeaker is coupled to an acoustical mode of a closed tube. The experimental results demonstrate that the programmed nonlinearity can lead the system into both periodic and nonperiodic responses. Furthermore, this investigation reveals that the programmed nonlinearity of the electroacoustic loudspeaker, even in its non-optimized state, effectively manages nonlinear noise control in specific frequency ranges. This study demonstrates the feasibility of programming the behavior of an electroacoustic loudspeaker, despite the limited time to implement only a Duffing-type nonlinearity thus far. The outcomes of this chapter were already communicated in [da Silveira Zanin et al., 2023].

5.1 Introduction to the experimental study

Geometrical nonlinearities can be mechanically generated through various means, such as springs [Mojahed et al., 2018], magnets [Benacchio et al., 2016, Lo Feudo et al., 2019] and buckling beams [Iurasov and Mattei, 2020]. While customizing these nonlinear forces to meet specific requirements can be challenging, it can significantly enhance dynamic performances.

A general methodology for fabricating geometrical nonlinearities is presented in [Bigoni et al., 2012, Koutsogiannakis et al., 2023]. This involves a rod connected to a rotational linear spring at one end, and a roller constrained to move along a specific profile at the other end. The shape of the profile can be designed to achieve a desired load-displacement curve, enabling the realization of a complex restoring force upon the application of continuous displacement.

In [Dekemele et al., 2020], a NES was conceived using an axial spring following a precisely machined nonlinear track, ensuring a purely cubic stiffness characteristic. Another study by the same author, [Dekemele et al., 2022], proposed a force profile for a NES featuring periodically extended cubic stiffness.

In [Zou et al., 2021], a device capable of tailoring continuous but not necessarily smooth nonlinear forces was introduced. This device incorporates a pre-compressed spring, a rolling bearing, and a customized raceway, as shown in Figure 5.1a. The study included the customization of various nonlinear systems, including hardening, softening, bistable, tri-stable, and piece-wise nonlinear systems. The feasibility of these systems was demonstrated through simulations and experiments. Figure 5.1b offers an illustrative example of such a system.

The main idea in [Dekemele et al., 2020, Dekemele et al., 2022, Zou et al., 2021] involves achieving the desired stiffness characteristics through the use of 3D printing or CNC machining to create profiles that correspond to the elastic potential energy of the desired nonlinearity. These studies

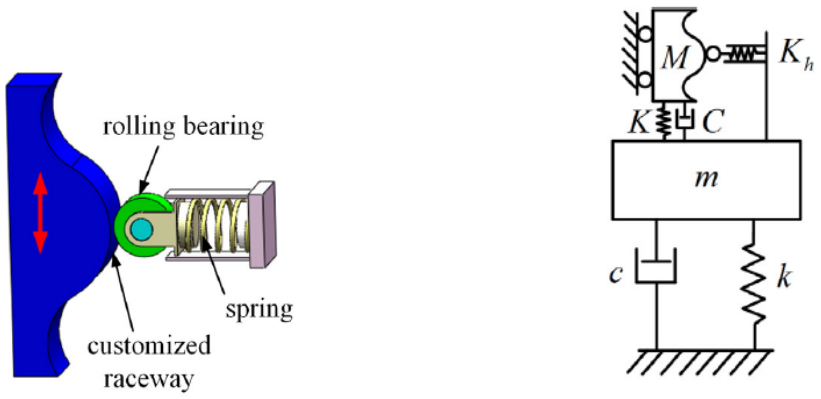

(a) (b)

Figure 5.1: Schematic diagram of: (a) Device capable of customizing nonlinear force; (b) Its application to a NES. [Zou et al., 2021]

point to mechanical approaches for implementing different nonlinear restoring forces, such as the one studied in this thesis. However, due to time constraints, this research direction was not further pursued. As part of this thesis, an existing experimental setup was used to demonstrate the feasibility of programming the behavior of an electroacoustic loudspeaker (EL) coupled to a tube.
In the field of acoustics, controlling the response of loudspeakers to external pressure excitations can lead to sound dissipation through electro-active means [Lissek, 2010], known as electroacoustic absorbers (EAs). A pressure-based current-driven architecture of digital control, along with a model-inversion technique, was implemented to adjust impedance by piloting the electrical current in the speaker coil and, consequently, tuning the resonance frequency [Rivet et al., 2017]. Furthermore, a nonlinear EA was explored in [Guo et al., 2020], where adjustable nonlinearity was achieved by defining an electrical current consisting of both linear and nonlinear components in an open field. A recent algorithm introduced in [De Bono, 2021, De Bono et al., 2024] targets nonlinear time-invariant dynamics, even in cases where information about diaphragm displacement is unavailable.
The study presented in this chapter makes use of the mentioned algorithm and focuses on presenting experimental results involving the digital programming of a Duffing-type nonlinearity using an EL. The objective is to demonstrate the feasibility of programming the behavior of an EL, potentially facilitating the implementation of the nonlinearity studied in this thesis.

5.2 Experimental setup

The sketch and physical model of the experimental setup are depicted in Figs. 5.2 and 5.3, respectively.
The experimental setup comprises several key components: a D-Space MicroLabBox DS1202 hardware responsible for the digital signal processing in controlling the EL, a plexiglass tube with a square cross-section measuring 50×50 mm^2, a calibrated sound source [Hussein, 2020], a Brüel & Kjaer microphone (two microphones are visible in Fig. 5.3, but only the left one is used), and the EL itself. The EL prototype, as depicted in Fig. 5.4, features a central speaker with four corner microphones and a back-case housing an analog electronic card interfacing with the D-Space. The sound source is a 5 cm loudspeaker (K 50 WP - 8 Ohm) from VISATON, featuring a frequency response of 180-17000 Hz and a resonance frequency of 300 Hz. The distance between the micro-

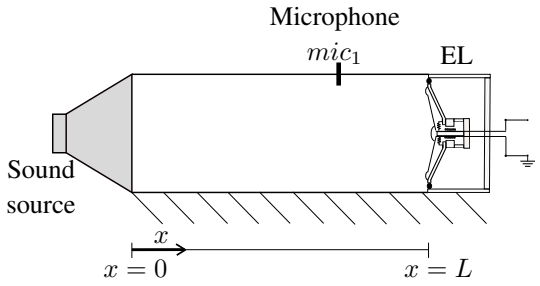

Figure 5.2: Sketch of the test bench where an EL is coupled to a tube at one end.

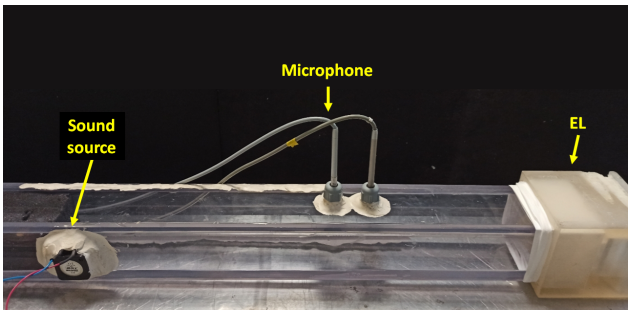

Figure 5.3: Photo of the experimental setup.

phone, referred to as "mic_1", and the EL is 27 cm. The experimental setup involves a closed-opened tube, where one end of the tube is sealed by a piece of plexiglass, and the EL is positioned at the other end. The programmable EL acts as a nonlinear damped oscillator, while the acoustical mode of the air inside the tube is treated as a damped linear oscillator [Cochelin et al., 2006b].



Figure 5.4: Photo of the EL prototype.

5.2.1 Acoustical mode of the tube

Let $u_a(x,t)$ be defined as the air displacement within the tube along the longitudinal direction x, as illustrated in Fig. 5.2. It is assumed that the length of the tube (L) is significantly larger than the dimensions of its cross-section (S_d). The considered system is subject to the following boundary conditions:

$$\begin{cases} u_a(0,t) = 0 \\ u_a(L,t) = u_m(t) \end{cases} \tag{5.1}$$

where $u_m(t)$ represents the displacement of the membrane of the EL. In our analysis, we apply the Rayleigh-Ritz method by establishing:

$$u_a(x,t) = q_a(t)\varphi_a(x) \tag{5.2}$$

where $q_a(t)$ denotes the modal coordinate, and $\varphi_a(x)$ represents the shape function, which must be continuous on the domain and must satisfy the kinematic boundary conditions described in Eq. (5.1). Therefore, we establish:

$$\varphi_a(x) = \sin\left(\frac{\pi x}{2L}\right) \tag{5.3}$$

The kinetic energy of the system, denoted as $\mathcal{T}$, is given by:

$$\mathcal{T} = \frac{\rho_a}{2}\int_0^L \left(\frac{\partial u_a(x,t)}{\partial t}\right)^2 S_d\, dx \tag{5.4}$$

Resulting in:

$$\mathcal{T} = \frac{\rho_a S_d \dot{q}_a^2(t) L}{4} \tag{5.5}$$

where $\dot{(\ )}$ denotes the derivative of a variable with respect to t, and ρ_a represents the density of air.

The total potential energy $\mathcal{U}$ is composed of two components: the strain energy in the fluid, $\mathcal{U}_{fl}$, and the work done on it by external forces, $\mathcal{U}_{ext}$. These components are defined as follows:

$$\begin{aligned} \mathcal{U}_{fl} &= \frac{1}{2}\rho_a c_0^2 \int_0^L \left(\frac{\partial u_a(x,t)}{\partial x}\right)^2 S_d\, dx \\ &= \frac{\rho_a c_0^2 S_d \pi^2}{16L} \end{aligned} \tag{5.6}$$

$$\begin{aligned} \mathcal{U}_{ext} &= -(p_1 S_d u_a(0,t) - p_2 S_d u_a(L,t)) \\ &= p_2 S_d u_m(t) \end{aligned}$$

where c_0 represents the speed of sound in air, p_1 and p_2 correspond to the pressure at the end of the tube on the sound source side and on the EL's membrane side, respectively. Consequently, p_2 is a function of the membrane's response, i.e., $u_m(t)$. By defining the Lagrangian of the system as $\mathcal{L} = \mathcal{T} - \mathcal{U}$, we obtain:

$$\mathcal{L} = \frac{\rho_a S_d L \ddot{q}_a^2(t)}{4} - \left(\frac{\rho_a c_0^2 S_d \pi^2}{16L} q_a(t) + p_2(u_m(t)) S_d u_m(t)\right) \tag{5.7}$$

From Eqs. (5.1), (5.2) and (5.3), we set $u_m(t) = q_a(t)$. and injecting Eq. (5.7) into the one-dimensional Euler-Lagrange equation, which is defined as:

$$\frac{\partial \mathcal{L}}{\partial q_a} - \frac{d}{dt}\left(\frac{\partial \mathcal{L}}{\partial(\dot{q}_a)}\right) = 0 \tag{5.8}$$

The following equation is obtained:

$$\left(\frac{\rho_a S_d L}{2}\right)\ddot{q}_a(t) + \left(\frac{\rho_a c_0^2 S_d \pi^2}{8L}\right) q_a(t) + p_2(u_m(t)) S_d = 0 \tag{5.9}$$

If one considers a viscous damping term for the system with a coefficient C_a, the resulting equation is as follows:

$$M_a \ddot{q}_a(t) + C_a \dot{q}_a(t) + K_a q_a(t) + p_2(u_m(t)) S_d = 0 \tag{5.10}$$

where $M_a = \dfrac{\rho_a S_d L}{2}$ and $K_a = \dfrac{\rho_a c_0^2 S_d \pi^2}{8L}$ are the modal mass and stiffness, respectively.

The analytical modeling of the coupled system follows the approach presented in [Cochelin et al., 2006b].

5.2.2 Loudspeaker and global system

An EL can be considered as a 1-dof oscillator within the frequency range around its linear mode [Beranek and Mellow, 2012]. It is mechanically driven by a voice coil with a length of l within a permanent magnetic field B. The EL's mechanical configuration is modeled as a mass-spring-damper, as depicted in Fig. 5.5, where M_{m_0}, K_{m_0} and C_{m_0} stand for the modal mass, stiffness and damping in open circuit conditions ($\iota = 0$), respectively. The effective area of the loudspeaker diaphragm is defined as S_e. The pressure near the membrane is denoted as $p(t)$, measured by the four corner microphones, and the force exerted by the moving-coil transducer is represented as $Bl\iota(t)$.

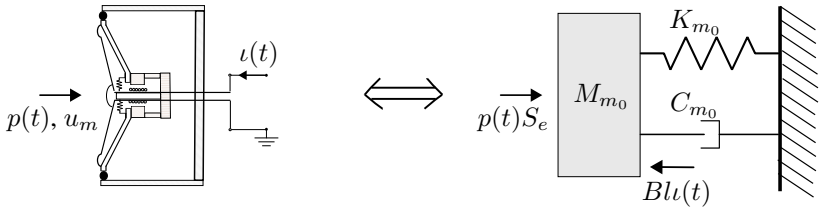

Figure 5.5: (a) Sketch of the EL employed in this study; (b) 1-dof piston-mode model.

The governing equation of the EL in the time domain t can be derived as follows:

$$M_{a_0}\ddot{u}_m(t) + C_{a_0}\dot{u}_m(t) + K_{a_0}u_m(t) = p(t) - \frac{Bl\iota(t)}{S_e} \tag{5.11}$$

where M_{a_0}, C_{a_0} and K_{a_0} are the acoustical mass, damping and stiffness of the EL in open circuit, respectively.
Finally, the governing equations of the coupled system, representing an acoustical mode of the tube and the EL, can be derived from Eqs. (5.10) and (5.11):

$$\begin{cases} M_{a_0}\ddot{u}_m(t) + C_{a_0}\dot{u}_m(t) + K_{a_0}u_m(t) = p(t) - \dfrac{Bl\iota(t)}{S_e} \\ \\ M_a\ddot{q}_a(t) + C_a\dot{q}_a(t) + K_aq_a(t) + p_2(u_m(t))S_d = 0 \end{cases} \tag{5.12}$$

The equations in (5.12) are coupled by $u_m(t)$, and with its appropriate adjustment, it becomes possible, for instance, to attenuate the acoustical mode $q_a(t)$. The next section outlines a method for digitally programming the response of the EL, i.e., $u_m(t)$, and clarifies its behavior.

5.3 Digital programming

In this section, we introduce the tools employed for digitally programming the EL. These include the use of a model-inversion technique [De Bono, 2021, De Bono et al., 2024] to obtain the desired behavior of the EL's membrane, the process for identifying the parameters of the EL, and the formulation of the targeted dynamics of the EL's membrane.

5.3.1 Model-inversion

We employ a model-inversion technique to obtain the desired output behavior of the EL's membrane based on both the input and the system model, as discussed in [Rivet et al., 2017]. The targeted dynamics of the membrane are further elaborated in Sec. 5.3.3, where we denote $u_{mt}(t)$ as the

targeted displacement of the membrane. It is important to emphasize that the EL operates within the linear domain, regardless of the targeted behavior.
Based on Eq. (5.11) and in alignment with the insights from [De Bono, 2021, De Bono et al., 2024], the equation governing the current in the EL is derived as follows:

$$\iota(t) = \frac{S_e}{Bl}\left[p(t) - (M_{a_0}\ddot{u}_{mt}(t) + C_{a_0}\dot{u}_{mt}(t) + K_{a_0}u_{mt}(t))\right] \tag{5.13}$$

Attaining the desired dynamic behavior of the EL relies on access to pressure measurements near the membrane, as these readings are crucial for determining the current to be injected into the system. To facilitate this, D-SPACE converts the analog pressure signal to a digital format, and time t is discretized: at each step n, time is denoted as t_n. Assuming no current circulates in the coil, the targeted behavior of the EL can be derived from Eq. (5.13) as:

$$\ddot{u}_{mt}(t_n) = \frac{p(t_n)}{M_t} - \frac{C_t}{M_t}\dot{u}_{mt}(t_n) - \frac{K_t}{M_t}u_{mt}(t_n) \tag{5.14}$$

Here, M_t, K_t, and C_t are adjustable parameters, and $\mathbf{u_{mt}}(t_n) = [\dot{u}_{mt}(t_n), u_{mt}(t_n)]$ is the state vector estimated at the previous time step.
Consequently, the digital control variable $i(t_n)$ is determined using Eq. (5.13), and an integration scheme is applied to Eq. (5.14) to estimate the targeted state vector $\mathbf{u_{mt}}(t_{n+1})$ for the subsequent step. In this investigation, we adopt the classical 4th-order Runge-Kutta integration scheme, chosen for its essential precision in handling nonlinearities. Although alternative numerical schemes like Euler can be used, the 4th order is generally preferred for its heightened accuracy, particularly in cases of hardening behavior with high nonlinear stiffness.
This iterative process is executed at each time step, where t_n is succeeded by t_{n+1}, i.e., $t_n \rightarrow t_{n+1}$, with the objective of achieving the targeted dynamics. The steps of this Real-Time Integration are summarized in Algorithm 2.

Algorithm 2 Real-Time Integration algorithm.

1. Evaluate $\ddot{u}_{mt}(t_n)$ using Eq. (5.14), where $p(t_n)$ is the measured pressure by the microphones of the EL, and $\mathbf{u_{mt}}(t_n)$ is the estimated vector from the previous time-step;
2. Calculate $\iota(t_n)$ using Eq. (5.13);
3. Estimate the vector $\mathbf{u_{mt}}(t_{n+1})$ by applying an integration scheme, such as 4th-order Runge-Kutta, to Eq. (5.14) with $p(t_{n+1}) = p(t_n)$;
4. Restart from *Step 1*, replacing t_n with t_{n+1}, i.e., $t_n \rightarrow t_{n+1}$.

We consider $\mathbf{u_{mt}}(t_0) = [0, 0]$ as the initial conditions of the system.

5.3.2 Parameters identification

To determine the parameters of the EL in the linear regime, Eq. (5.11) is analyzed in the Laplace domain, yielding:

$$Z_{a_0}(s)V(s) = P(s) - \frac{BlI(s)}{S_e} \tag{5.15}$$

Here, s stands for the Laplace variable, while $V(s)$, $P(s)$, and $I(s)$ represent the Laplace-transformed variables corresponding to membrane velocity, pressure near the membrane, and electric current, respectively. Z_{a_0} denotes the acoustical impedance and is expressed as:

$$Z_{a_0}(s) = M_{a_0}s + C_{a_0} + K_{a_0}\frac{1}{s} \tag{5.16}$$

A preliminary measurement is conducted in open circuit conditions to identify the parameters of the EL described in Eq. (5.16). For that, the EL's impedance is experimentally estimated using Eq. (5.15) with $I(s) = 0$, which results in:

$$Z_{a_0} = P(s)/V(s) \tag{5.17}$$

This estimation involves incorporating measurements of pressure and velocity on the loudspeaker diaphragm using a microphone and a Laser-Doppler-Velocimeter (LDV), respectively. Following this, the curve of the open circuit impedance is subjected to curve-fitting to obtain M_{a_0}, C_{a_0} and K_{a_0} from Eq. (5.16), as we can seen in Fig. 5.6. The curve-fitting is executed using the classical *lsqnonlin* Matlab function, designed for solving nonlinear least-squares curve fitting problems.

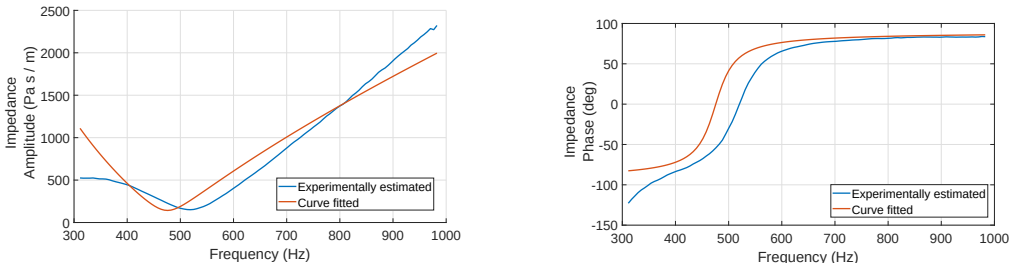

(a) (b)

Figure 5.6: Acoustical impedance in open circuit: (a) Amplitude; (b) Phase.

An additional measurement is required to estimate Bl/S_e. Considering a targeted acoustical impedance $Z_{at} = P(s)/V(s)$ (the behavior that the EL is programmed to present) and the loudspeaker model described in Eq. (5.15), it is possible to select the dynamic response of the loudspeaker diaphragm based on the pressure measured near the membrane. To achieve this, $I(S)$ is first isolated in Eq. (5.15) and expressed as follows:

$$I(s) = \frac{S_e}{Bl}\left(P(s) - Z_{a_0}(s)V(s)\right) \tag{5.18}$$

Considering $V(s) = P(s)/Z_{at}$ and replacing it in Eq. (5.18), we obtain the transfer function $H(s)$ from the sound pressure $P(s)$ to the electrical current $I(s)$ as follows:

$$H(s) = \frac{I(s)}{P(s)} = \frac{S_e}{Bl}\left(1 - \frac{Z_{a_0}(s)}{Z_{at}(s)}\right) \tag{5.19}$$

Introducing a proportional controller by setting $I(s) = dP(s)$, with d as a constant gain, allows us to express the targeted acoustical impedance of the EL as:

$$Z_{at}(s) = \frac{Z_{a_0}(s)}{1 - d\dfrac{Bl}{S_e}} \tag{5.20}$$

Consequently, a proportional controller is imposed to estimate Bl/S_e. Given the prior estimation of $Z_{a_0}(s)$ and the known value of d, another curve-fitting is performed to find Bl/S_e, as illustrated in Fig. 5.7. The identified parameters of the EL are presented in Table 5.1.

5.3.3 Nonlinear targeted dynamics

The control variable, the current, is defined as [Guo et al., 2020]:

$$\iota(t) = \iota_L(t) + \iota_{NL}(t) \tag{5.21}$$

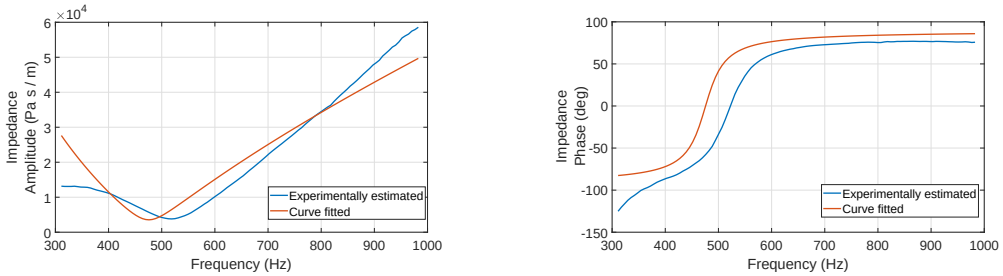

(a) (b)

Figure 5.7: Acoustical impedance with a proportional control: (a) Amplitude; (b) Phase.

M_{m_0}	C_{m_0}	K_{m_0}	Bl/S_e
4.203×10^{-4} kg	0.131 m.N^{-1}	3.486×10^{3} N.s.m^{-1}	238.372 N.A^{-1}.m^{-2}

Table 5.1: Parameters of the EL.

Here, ι_{NL} is a function of a nonlinear transformation of the pressure measured inside the EL's back-case, which is proportional to the displacement of the diaphragm. This current introduces a nonlinear component to the stiffness. Consequently, Eq. (5.14) can be expressed as:

$$\ddot{u}_{mt}(t_n) = \frac{p(t_n)}{M_t} - \frac{C_t}{M_t}\dot{u}_{mt}(t_n) - \frac{K_t}{M_t}(\beta_L u_{mt}(t_n) + \beta_{NL} u_{mt}^3(t_n)) \tag{5.22}$$

The parameters β_L and β_{NL} represent the tunable linear and nonlinear parameters, respectively. In other words, modifying β_L and β_{NL} allows us to alter the targeted dynamics of the EL. We chose the targeted dynamics to emulate a typical Duffing-type resonator, with $\beta_L = 1$ and $\beta_{NL} = 10^{13}\text{m}^{-2}$. β_{NL} value is determined experimentally to manifest the desired nonlinear phenomena, specifically by limiting the linear part of the stiffness and compensating for damping.
M_t, K_t, and C_t coefficients, i.e., the targeted impedance parameters used for adjusting the frequency response of the EL, are defined based on the previously identified parameters M_{m_0}, C_{m_0}, and K_{m_0}, respectively. The targeted mass and stiffness are expressed as $M_t = \mu_M M_{m_0}$ and $K_t = \mu_K K_{m_0}$, while the damping is formulated as a function of the characteristic impedance of air $\rho_0 c_0$ [Rivet et al., 2017]. The targeted resonance frequency can then be represented as $f_t = \sqrt{\frac{\mu_K}{\mu_M}} f_0$, where f_0 is the linear resonance frequency of the membrane, i.e., $f_0 = \sqrt{\frac{K_{m_0}}{M_{m_0}}} \frac{1}{2\pi} \approx 460$ Hz.
In order to activate a targeted energy transfer with the Duffing nonlinearity described in Eq. (5.22), and given that β_{NL} is positive, resulting in a hardening behavior, it is necessary that the nonlinear resonance of the membrane occurs above f_0. Consequently, the targeted resonance frequency is established to match one of the tube modes (for control purposes) beyond f_0. Hence, f_t is set to 700 Hz.
The applied control is subjected to certain limitations. Its effectiveness is restricted within the frequency range around the first mode of the loudspeaker, given the simplification of the EL as a 1-dof oscillator in the proximity of its linear mode. Moreover, the control relies on measurements at one time step to predict the displacement at the next time step and then inject the desired current accordingly. This process demands a system with a high sampling rate, specifically set to $50,000$ Hz in this study.

5.4 Experimental results

The tube is initially characterized by closing it with a piece of plexiglass at the position of the EL. This characterization involves a frequency sweep test with an amplitude of 0.1 Pa (all experimental measurements presented here are performed with this same amplitude), spanning from 300 Hz to 900 Hz. The amplitude of the Fourier transform of the pressure measured by microphone mic_1, denoted as "P_{mic_1}", is depicted in pink in Fig. 5.8. This figure reveals the presence of a mode of the tube at approximately 700 Hz, justifying the value of f_t.
The same frequency sweep tests have also been performed in the tube with coupled EL. In Fig. 5.8, the pressures resulting from back-and-forth frequency sweepings are depicted by the blue and green curves, respectively. Notably, the curves with the EL are below those of the closed tube between 540 Hz and 705 Hz, indicating a pressure attenuation introduced by the EL within this frequency range. Moreover, abrupt changes in the frequency responses at 736 Hz and 755 Hz indicate a nonlinear behavior, here hardening, of the system within this frequency range. These jumps correspond to different frequencies and signify the activation of the nonlinearity.

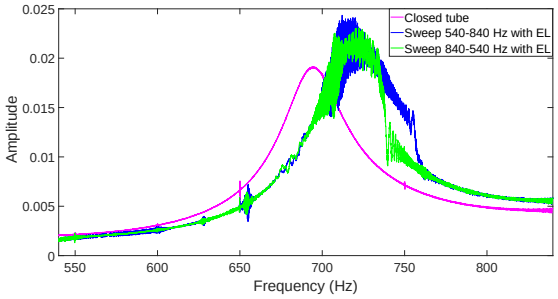

Figure 5.8: Amplitude of the Fourier transform of pressure measured by microphone mic_1 during a frequency sweep in the closed tube (without EL) and in the tube with EL.

Figure 5.9 illustrates the time history of the pressure measured by microphone mic_1 during the frequency sweep ranging from 500 to 850 Hz. Notably, a sudden decay in responses occurs at 22 seconds, aligning with the frequency of 755 Hz, as depicted in Fig. 5.8. In Fig. 5.10, the time history of measured pressures during the frequency sweep from 850 to 500 Hz are presented. Here, we observe a sudden increase in pressure at 9.8 seconds, corresponding to the jump at 736 Hz in Fig. 5.8.

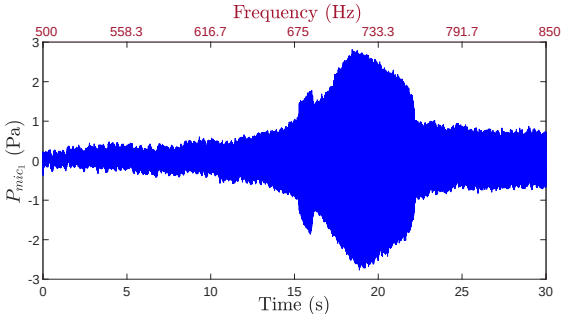

Figure 5.9: Time history of pressure measured by microphone mic_1 during a 500-850 Hz frequency sweep.

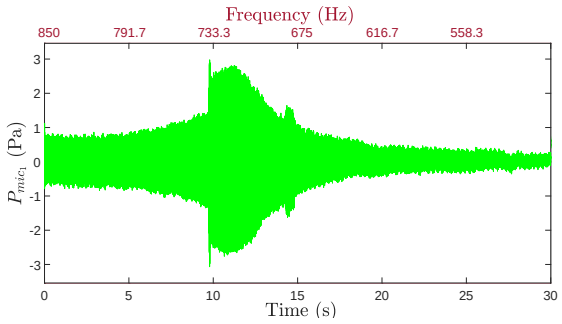

Figure 5.10: Time history of pressure measured by microphone mic_1 during a 850-500 Hz frequency sweep.

To validate the pressure behavior exhibited by the EL within the frequency range of 540 to 705 Hz (see Fig. 5.8), experimental measurements are conducted with forcing excitation in this frequency range. Figure 5.11 displays the measured pressures under periodic excitation at a frequency of 690 Hz. The pressure is recorded by microphone mic_1 in both the closed tube without EL (pink curve) and in the tube with EL (blue curve). As anticipated, we observe a pressure attenuation in the presence of the EL and a periodic response. An attenuation of approximately 6.4 dB is measured between the signals without and with the EL.

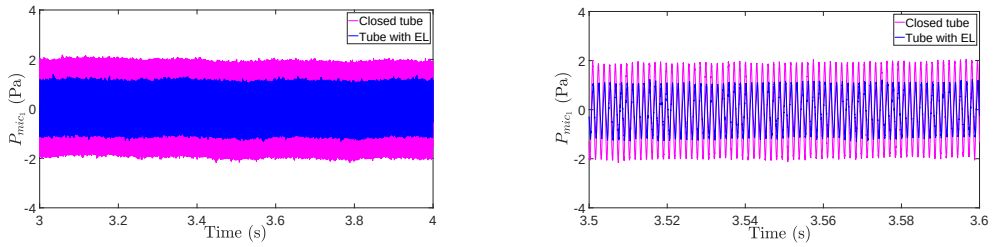

(a) (b)

Figure 5.11: Time history of pressures measured by microphone mic_1 during a 690 Hz source excitation: (a) 3-4 seconds; (b) 3.5-3.6 seconds.

Figure 5.12 presents the measured pressures under periodic excitation with a frequency of 680 Hz. As expected, we observe pressure attenuation due to coupling with the EL. Additionally, there is a change in the nature of system responses. The air pressure in the tube without EL exhibits a periodic response, which transforms into a non-periodic response when the EL is coupled to the tube. This nonlinear phenomenon occurs between 1 and 2 Pa, equivalent to 94 and 100 dB, respectively. This acoustic level is lower than values reported in the literature for passive nonlinear control in acoustics, such as 138 dB in [Gourdon et al., 2018].
To better understand the differences in the nature of the system's response, the Fourier transform of the time history of pressure during source excitations of 690 Hz and 680 Hz (Figs. 5.11 and 5.12, respectively) are plotted in Figs. 5.13a and 5.13b, respectively. The blue and pink curves represent the responses with and without the EL, respectively. For the periodic response (Fig. 5.13a), only one frequency, which is equal to the frequency of the tube, is activated. In contrast, for the non-periodic regime (Fig. 5.13b), several frequencies are excited, characteristic of non-periodic regimes.
These results show the interest of coupling the programmable EL to the tube, which can serve as a nonlinear resonator with potential applications in nonlinear semi-passive control (acoustically

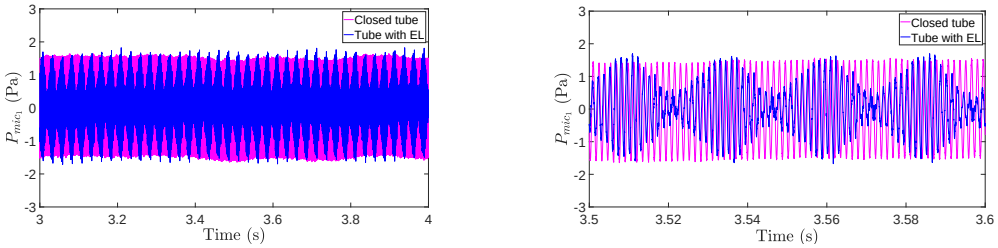

(a) (b)

Figure 5.12: Time history of pressures measured by microphone mic_1 during a 680 Hz source excitation: (a) 3-4 seconds; (b) 3.5-3.6 seconds.

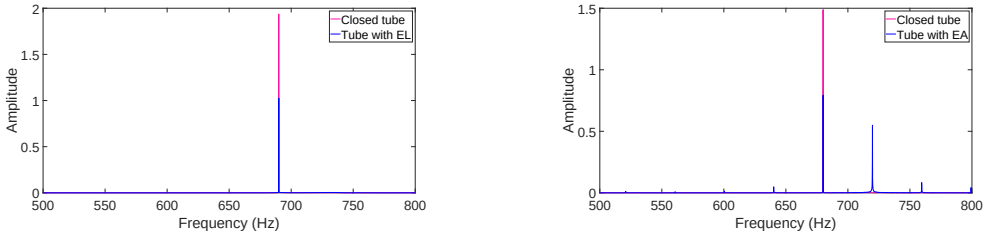

(a) (b)

Figure 5.13: Amplitude of the Fourier transform of pressures measured by microphone mic_1 during source excitations at: (a) 690 Hz; (b) 680 Hz.

passive but electrically active due to the loudspeaker) [Gourdon et al., 2020, De Bono et al., 2022, De Bono et al., 2024]. However, it is noteworthy, as seen in Fig. 5.8, that there are certain frequency zones, specifically between 710 Hz and 800 Hz, where the response of the system with the coupled EL exhibits higher amplitudes than the tube without EL, given that, we did not perform optimization of parameters for optimal sound attenuation via the EL.

5.5 Conclusions of the chapter

This study presents experimental results involving a programmable electroacoustic loudspeaker coupled to the acoustical mode of a tube. A model-inversion technique is applied for digitally programming the loudspeaker's impedance, aiming to achieve a Duffing-type targeted behavior. The experimental implementation demonstrates a reduction in the air pressure level within the tube, limited to a specific frequency range.

The programmed nonlinearity of the electroacoustic loudspeaker leads to two distinct types of responses observed in the experiments: periodic and non-periodic. The system, when decoupled from electroacoustic loudspeaker, exhibits a periodic response. However, upon coupling the electroacoustic loudspeaker, the nature of responses can change and present non-periodic characteristics.

The experimental findings highlight the potential for triggering acoustical energy, involving an irreversible transfer of vibrational energy, and demonstrate the feasibility of programming the behavior of an electroacoustic loudspeaker, paving the way for a semi-passive noise control process. Importantly, the observed non-periodic response occurs at an acoustic level lower than reported in the literature for passive nonlinear control in acoustics [Cochelin et al., 2006b, Bellet et al., 2010].

CHAPTER 6

Conclusion and perspectives

This PhD dissertation presents the investigations on exploiting nonlinear dynamics in a single mass-in-mass cell and in a chain of coupled cells with a specific nonlinearity. It marks an initial step towards the creation of new types of metamaterials with designed behaviors.

6.1 Results

Chapter 1 places the work in the context of the scientific literature through a comprehensive review of the bibliography, focusing particularly on technological solutions that enable the vibration control of structures. One of the systems under investigation is the nonlinear passive system known as NES, which has been extensively studied and found to be versatile in its applications. It is also explored the concept and various forms of metamaterials, which can be composed of unit cells or particles containing vibration absorbers, such as the ones discussed in the first part of the chapter. Additionally, it is provided an overview of the general methodology used in this manuscript to refine the behavior of systems or create new systems with designed behaviors.

Chapter 2 explores the dynamics of a single nonlinear mass-in-mass meta-cell, consisting of an outer mass that houses an inner mass with a piecewise restoring force term that is globally non-smooth. Fast and slow dynamics of the system are investigated, leading to detection of the slow invariant manifold and dynamic characteristic points. The piecewise nonlinearity of the inner mass results in a slow invariant manifold with four local extrema, distinct from those observed in systems with pure cubic and piecewise-linear nonlinearities. The frequency response curves, along with a three-dimensional view of detected equilibrium points, permit identifying possible isola and the position of equilibrium points on the slow invariant manifold. Depending on the nature of the equilibrium points and the existence of singularities, the system can present one, two, or multiple bifurcations, leading to final periodic or non-periodic regimes. Furthermore, the rate of vibratory energy reduction depends on the initial position of the system on different branches of the slow invariant manifold, enabling the absorber to function in different phases.
In summary, the analytical developments in this chapter offer design tools for adjusting the piecewise nonlinearity of the inner mass. This tuning enables the system to exhibit periodic or non-periodic responses based on given external forcing characteristics or to fulfill specific objectives, such as control or energy harvesting.

Chapter 3 introduces the study of a chain of coupled meta-cells discussed in Chapter 2. Initially, the discrete system is presented, followed by the transition to the continuous domain. The modal characteristics of the continuous system are evaluated, and the system is studied in the vicinity of one of its arbitrary modes. For that, two approximations are applied: the first involves using Taylor series expansion for transitioning to the continuous domain, while the second consists of projecting the equations of the continuous system on an arbitrary single mode. Subsequently, the investigation delves into the analysis of the system's fast and slow dynamics, and design tools for adjusting the piecewise nonlinearity are obtained. Comparisons between the dynamic responses of the original system and those of the projected one reveal discrepancies, which can be attributed

to the neglect of higher harmonics and intermodal interactions. Nevertheless, analytical results based on the single-mode approximation provide preliminary design tools for tuning the parameters of (piecewise) nonlinear inner masses to achieve qualitatively designed responses of the system.

Chapter 4 employs a stochastic optimization algorithm to design the mass-in-mass meta-cell studied in Chapter 2. The comprehension of the system's dynamic behavior, including potential discontinuities, is enhanced through the analysis of histograms. The optimization of the meta-cells with piecewise and pure cubic nonlinearity are carried out, considering not only initial velocities as excitation but also external forces. The efficiency of the meta-cell with piecewise nonlinearity after optimization is compared to that of a meta-cell with optimized pure cubic nonlinearity, as well as to that of a single dof system. The results demonstrate that the system with optimized piecewise nonlinearity exhibits higher energy reduction efficiency when compared to the other systems.

Chapter 5 provides at first a literature review for possibilities on the possibilities of mechanically fabricating the considered nonlinearity in this thesis. Then, an experimental study involving a programmable electroacoustic loudspeaker coupled to an acoustic mode of a tube is presented. A model-inversion technique is applied to digitally program the loudspeaker's impedance, aiming to achieve a Duffing-type targeted behavior. The experimental implementation demonstrates a reduction in the air pressure level within the tube, limited to a specific frequency range. The programmed nonlinearity of the electroacoustic loudspeaker leads to two distinct types of responses observed in the experiments: periodic and non-periodic. The experimental findings highlight the potential for triggering acoustical energy, involving an irreversible transfer of vibrational energy, and demonstrate the feasibility of programming the behavior of an electroacoustic loudspeaker.

This thesis leads to the following publications in peer-reviewed journal papers:

- da Silveira Zanin, C., Ture Savadkoohi, A., Baguet, S., Dufour, R., and Hurel, G. (2022). Nonlinear vibratory energy exchanges in a meta-cell. *International Journal of Non-Linear Mechanics*, 146:104148;

- Da Silveira Zanin, C. E., Labetoulle, A., De Bono, E., Gourdon, E., Collet, M., and Ture Savadkoohi, A. (2023). Experimental evidences of nonlinear programmable electroacoustic loudspeaker. *Building Acoustics*, 30(3):249263.

and the following communications in conferences:

- da Silveira Zanin, C., Ture Savadkoohi, A., Baguet, S., Dufour, R. Energy exchanges between particles of a nonlinear meta-cell, *16th International Conference: Dynamical Systems, Theory and Applications (DSTA 2021)*, December 6-9 2021 (online);

- da Silveira Zanin, C., Ture Savadkoohi, A., Baguet, S., Dufour, R. Canalisation d'énergie entre les particules des métacellules "mass-in-mass" nonlinéaires, *Le 16e Congrès Français d'Acoustique de la SFA*, 11-15 April 2022, Marseille, France;

- da Silveira Zanin, C., Ture Savadkoohi, A., Baguet, S., Dufour, R. Non-smooth nonlinearities as restoring forces in a mass-in-mass cell, *10th European Nonlinear Dynamics Conference (ENOC)*, July 17-22 2022, Lyon, France;

- da Silveira Zanin, C., Ture Savadkoohi, A., Baguet, S., Dufour, R. On the effects of different types of nonlinearities in fast/slow dynamics of a meta-cell, *15th World Congress on Computational Mechanics (WCCM-XV)*, 31 July-5 August 2022 (online);

- da Silveira Zanin, C., Missoum, S., Ture Savadkoohi, A., Baguet, S., Dufour, R. Towards the optimal design of metamaterials, *3rd Third International Nonlinear Dynamics Conference (NODYCON 2023)*, 18-22 June 2023, Rome, Italy.

6.2 Perspectives

This manuscript has unveiled potential avenues for future research, which are described in the following text.

6.2.1 Perspectives for analytical approaches

The chain presented in this manuscript is studied in the vicinity of one of its arbitrary modes. However, the considered chain can present internal resonances. To account for these internal resonances and minimize discrepancies between the dynamic responses of the original system and those of the projected one, the chain should be studied around at least two modes. Moreover, the consideration of 2D and 3D lattices is essential for the method to be extended to real materials.

6.2.2 Perspectives for optimization study

This manuscript focuses on the optimization of a single nonlinear meta-cell. A potential perspective involves extending the optimization to the entire chain by considering a field representation for the parameters. This representation would allow variations in parameters across different cells, contributing to a more comprehensive optimization of the entire chain.

6.2.3 Perspectives for experimental study

The experimental study detailed in this dissertation features a programmable electroacoustic loudspeaker coupled to an acoustic mode of a tube. Currently, only a Duffing-type nonlinearity has been implemented. Looking forward, the piecewise nonlinearity studied in this thesis could also be implemented. Moreover, this manuscript presents some possibilities for mechanically conceiving this nonlinearity that could also be explored in future works.

Bibliography

[Alderson et al., 2012] Alderson, K., Alderson, A., Anand, S., Simkins, V., Nazare, S., and Ravirala, N. (2012). Auxetic warp knit textile structures. *physica status solidi (b)*, 249(7):1322–1329. (Cited on page 17.)

[Alderson and Evans, 1992] Alderson, K. and Evans, K. (1992). The fabrication of microporous polyethylene having a negative Poisson's ratio. *Polymer*, 33(20):4435–4438. (Cited on page 17.)

[Ali et al., 2017] Ali, H., Forsberg, E., and Jun, H. (2017). Brain Imaging with Slotted Hybridized Magnetic Metamaterial Hat at 7-T MRI. *Applied Magnetic Resonance*, 48(1):67–83. (Cited on page 16.)

[Arnold, 1955] Arnold, F. R. (1955). Steady-State Behavior of Systems Provided With Nonlinear Dynamic Vibration Absorbers. *Journal of Applied Mechanics*, 22(4):487–492. (Cited on page 12.)

[Asami and Nishihara, 2003] Asami, T. and Nishihara, O. (2003). Closed-Form Exact Solution to H Optimization of Dynamic Vibration Absorbers (Application to Different Transfer Functions and Damping Systems). *Journal of Vibration and Acoustics*, 125(3):398–405. (Cited on page 12.)

[Aubry et al., 2001] Aubry, S., Kopidakis, G., Morgante, A., and Tsironis, G. (2001). Analytic conditions for targeted energy transfer between nonlinear oscillators or discrete breathers. *Physica B: Condensed Matter*, 296(1-3):222–236. (Cited on page 21.)

[Babaee et al., 2013] Babaee, S., Shim, J., Weaver, J. C., Chen, E. R., Patel, N., and Bertoldi, K. (2013). 3D Soft Metamaterials with Negative Poisson's Ratio. *Advanced Materials*, 25(36):5044–5049. (Cited on page 18.)

[Basudhar and Missoum, 2008] Basudhar, A. and Missoum, S. (2008). Adaptive explicit decision functions for probabilistic design and optimization using support vector machines. *Computers & Structures*, 86(19-20):1904–1917. (Cited on page 91.)

[Bellet et al., 2010] Bellet, R., Cochelin, B., Herzog, P., and Mattei, P.-O. (2010). Experimental study of targeted energy transfer from an acoustic system to a nonlinear membrane absorber. *Journal of Sound and Vibration*, 329(14):2768–2791. (Cited on pages 14 and 115.)

[Benacchio et al., 2016] Benacchio, S., Malher, A., Boisson, J., and Touzé, C. (2016). Design of a magnetic vibration absorber with tunable stiffnesses. *Nonlinear Dynamics*, 85(2):893–911. (Cited on page 105.)

[Beranek and Mellow, 2012] Beranek, L. L. and Mellow, T. (2012). *Acoustics: sound fields and transducers*. Academic Press. (Cited on page 109.)

[Bergeot and Berger, 2023] Bergeot, B. and Berger, S. (2023). Fast-Slow Analysis of Passive Mitigation of Self-Sustained Oscillations by Means of a Bistable Nonlinear Energy Sink. preprint, SSRN. (Cited on page 14.)

[Bertoldi et al., 2010] Bertoldi, K., Reis, P. M., Willshaw, S., and Mullin, T. (2010). Negative Poisson's Ratio Behavior Induced by an Elastic Instability. *Advanced Materials*, 22(3):361–366. (Cited on pages 18 and 19.)

[Bertoldi et al., 2017] Bertoldi, K., Vitelli, V., Christensen, J., and van Hecke, M. (2017). Flexible mechanical metamaterials. *Nature Reviews Materials*, 2(11):17066. (Cited on page 17.)

[Bigoni et al., 2012] Bigoni, D., Misseroni, D., Noselli, G., and Zaccaria, D. (2012). Effects of the constraint's curvature on structural instability: tensile buckling and multiple bifurcations. *Proceedings of the Royal Society A: Mathematical, Physical and Engineering Sciences*, 468(2144):2191–2209. (Cited on page 105.)

[Boroson and Missoum, 2015] Boroson, E. and Missoum, S. (2015). Reliability-based design optimization of nonlinear energy sinks. pages 750–757, Sydney. (Cited on page 83.)

[Boroson and Missoum, 2017] Boroson, E. and Missoum, S. (2017). Stochastic optimization of nonlinear energy sinks. *Structural and Multidisciplinary Optimization*, 55(2):633–646. (Cited on pages 83, 84 and 93.)

[Boroson et al., 2014] Boroson, E., Missoum, S., Mattei, P.-O., and Vergez, C. (2014). Optimization Under Uncertainty of Nonlinear Energy Sinks. In *Volume 8: 26th Conference on Mechanical Vibration and Noise*, page V008T11A084, Buffalo, New York, USA. American Society of Mechanical Engineers. (Cited on page 83.)

[Boroson et al., 2017] Boroson, E., Missoum, S., Mattei, P.-O., and Vergez, C. (2017). Optimization under uncertainty of parallel nonlinear energy sinks. *Journal of Sound and Vibration*, 394:451–464. (Cited on pages 83 and 84.)

[Bosia et al., 2022] Bosia, F., Dal Poggetto, V. F., Gliozzi, A. S., Greco, G., Lott, M., Miniaci, M., Ongaro, F., Onorato, M., Seyyedizadeh, S. F., Tortello, M., and Pugno, N. M. (2022). Optimized structures for vibration attenuation and sound control in nature: A review. *Matter*, 5(10):3311–3340. (Cited on page 17.)

[Boyvat and Hafner, 2012] Boyvat, M. and Hafner, C. V. (2012). Molding the Flow of Magnetic Field with Metamaterials: Magnetic Field Shielding. *Progress In Electromagnetics Research*, 126:303–316. (Cited on page 15.)

[Brillouin, 1946] Brillouin, L. (1946). *Wave propagation in periodic structures: Electric filters and crystal lattices*. Dover books on engineering and engineering physics. McGraw-Hill Book Company, Incorporated. tex.lccn: 46006703. (Cited on page 16.)

[Brock, 1946] Brock, J. E. (1946). A Note on the Damped Vibration Absorber. *Journal of Applied Mechanics*, 13(4):A284–A284. (Cited on page 12.)

[Buckmann et al., 2014] Buckmann, T., Thiel, M., Kadic, M., Schittny, R., and Wegener, M. (2014). An elasto-mechanical unfeelability cloak made of pentamode metamaterials. *Nature Communications*, 5(1):4130. (Cited on page 18.)

[Caddock and Evans, 1989] Caddock, B. D. and Evans, K. E. (1989). Microporous materials with negative Poisson's ratios. I. Microstructure and mechanical properties. *Journal of Physics D: Applied Physics*, 22(12):1877–1882. (Cited on page 17.)

[Charlemagne et al., 2016] Charlemagne, S., Ture Savadkoohi, A., and Lamarque, C.-H. (2016). Interactions Between Two Coupled Nonlinear Forced Systems: Fast/Slow Dynamics. *International Journal of Bifurcation and Chaos*, 26(09):1650155. (Cited on page 30.)

[Chen et al., 2016] Chen, Y. Y., Zhu, R., Barnhart, M. V., and Huang, G. L. (2016). Enhanced flexural wave sensing by adaptive gradient-index metamaterials. *Scientific Reports*, 6(1):35048. (Cited on page 18.)

[Chu et al., 2005] Chu, S. Y., Soong, T. T., and Reinhorn, A. M. (2005). *Active, hybrid, and semi-active structural control: a design and implementation handbook*. Wiley, Hoboken, NJ. (Cited on page 11.)

[Cochelin et al., 2006a] Cochelin, B., Herzog, P., and Mattei, P.-O. (2006a). Experimental evidence of energy pumping in acoustics. *Comptes Rendus Mécanique*, 334(11):639–644. (Cited on page 14.)

[Cochelin et al., 2006b] Cochelin, B., Herzog, P., and Mattei, P.-O. (2006b). Experimental evidence of energy pumping in acoustics. *Comptes Rendus Mécanique*, 334(11):639–644. (Cited on pages 107, 108 and 115.)

[Cressie, 1990] Cressie, N. (1990). The origins of kriging. *Mathematical Geology*, 22(3):239–252. (Cited on pages 89 and 92.)

[Cristianini and Shawe-Taylor, 2000] Cristianini, N. and Shawe-Taylor, J. (2000). *An Introduction to Support Vector Machines and Other Kernel-based Learning Methods*. Cambridge University Press, 1 edition. (Cited on page 89.)

[Cveticanin and Zukovic, 2017] Cveticanin, L. and Zukovic, M. (2017). Negative effective mass in acoustic metamaterial with nonlinear mass-in-mass subsystems. *Communications in Nonlinear Science and Numerical Simulation*, 51:89–104. (Cited on page 21.)

[da Silveira Zanin et al., 2022] da Silveira Zanin, C., Ture Savadkoohi, A., Baguet, S., Dufour, R., and Hurel, G. (2022). Nonlinear vibratory energy exchanges in a meta-cell. *International Journal of Non-Linear Mechanics*, 146:104148. (Cited on page 25.)

[da Silveira Zanin et al., 2023] da Silveira Zanin, C. E., Labetoulle, A., De Bono, E., Gourdon, E., Collet, M., and Ture Savadkoohi, A. (2023). Experimental evidences of nonlinear programmable electroacoustic loudspeaker. *Building Acoustics*, 30(3):249–263. (Cited on page 105.)

[De Bono, 2021] De Bono, E. (2021). *Electro-active boundary control for noise mitigation : local and advective strategies*. Theses, Université de Lyon, École Centrale de Lyon, École Doctorale ED162, Nř d'ordre NNT: 2021LYSEC24. Issue: 2021LYSEC24. (Cited on pages 106, 109 and 110.)

[De Bono et al., 2022] De Bono, E., Collet, M., Matten, G., Karkar, S., Lissek, H., Ouisse, M., Billon, K., Laurence, T., and Volery, M. (2022). Effect of time delay on the impedance control of a pressure-based, current-driven Electroacoustic Absorber. *Journal of Sound and Vibration*, 537:117201. Publisher: Elsevier. (Cited on page 115.)

[De Bono et al., 2024] De Bono, E., Morell, M., Collet, M., Gourdon, E., Ture Savadkoohi, A., Ouisse, M., and Lamarque, C. (2024). Model-inversion control to enforce tunable Duffing-like acoustical response on an Electroacoustic resonator at low excitation levels. *Journal of Sound and Vibration*, 570:118070. (Cited on pages 106, 109, 110 and 115.)

[Dekemele et al., 2022] Dekemele, K., Habib, G., and Loccufier, M. (2022). The periodically extended stiffness nonlinear energy sink. *Mechanical Systems and Signal Processing*, 169:108706. (Cited on page 105.)

[Dekemele et al., 2020] Dekemele, K., Van Torre, P., and Loccufier, M. (2020). Design, construction and experimental performance of a nonlinear energy sink in mitigating multi-modal vibrations. *Journal of Sound and Vibration*, 473:115243. (Cited on page 105.)

[Den Hartog, 1934] Den Hartog, J. P. (1934). *Mechanical Vibrations*. McGraw Hill, New York. (Cited on page 12.)

[Devore and Berk, 2011] Devore, J. and Berk, K. (2011). *Modern mathematical statistics with applications*. Springer texts in statistics. Springer New York. tex.lccn: 2011936004. (Cited on page 96.)

[Ebrahimi-Nejad and Kheybari, 2018] Ebrahimi-Nejad, S. and Kheybari, M. (2018). Honeycomb locally resonant absorbing acoustic metamaterials with stop band behavior. *Materials Research Express*, 5(10):105801. (Cited on page 17.)

[Ema and Marui, 1996] Ema, S. and Marui, E. (1996). Damping characteristics of an impact damper and its application. *International Journal of Machine Tools and Manufacture*, 36(3):293–306. (Cited on page 13.)

[Ema and Marui, 2000] Ema, S. and Marui, E. (2000). Suppression of chatter vibration of boring tools using impact dampers. *International Journal of Machine Tools and Manufacture*, 4:1141–1156. (Cited on page 13.)

[Fang et al., 2006a] Fang, N., Xi, D., Xu, J., Ambati, M., Srituravanich, W., Sun, C., and Zhang, X. (2006a). Ultrasonic metamaterials with negative modulus. *Nature Materials*, 5(6):452–456. (Cited on page 16.)

[Fang et al., 2006b] Fang, N., Xi, D., Xu, J., Ambati, M., Srituravanich, W., Sun, C., and Zhang, X. (2006b). Ultrasonic metamaterials with negative modulus. *Nature Materials*, 5(6):452–456. (Cited on page 17.)

[Faravelli et al., 2009] Faravelli, L., Fuggini, C., and Ubertini, F. (2009). Toward a hybrid control solution for cable dynamics: Theoretical prediction and experimental validation. *Structural Control and Health Monitoring*, pages n/a–n/a. (Cited on page 11.)

[Filipov et al., 2015] Filipov, E. T., Tachi, T., and Paulino, G. H. (2015). Origami tubes assembled into stiff, yet reconfigurable structures and metamaterials. *Proceedings of the National Academy of Sciences*, 112(40):12321–12326. (Cited on page 19.)

[Florijn et al., 2014] Florijn, B., Coulais, C., and van Hecke, M. (2014). Programmable Mechanical Metamaterials. *Physical Review Letters*, 113(17):175503. (Cited on page 18.)

[Frahm, 1909] Frahm, H. (1909). Device for damping vibrations of bodies. (Cited on page 12.)

[Gao et al., 2018] Gao, M., Wu, Z., and Wen, Z. (2018). Effective Negative Mass Nonlinear Acoustic Metamaterial with Pure Cubic Oscillator. *Advances in Civil Engineering*, 2018:1–15. (Cited on page 18.)

[Gardner et al., 2006] Gardner, J. P., Mather, J. C., Clampin, M., Doyon, R., Greenhouse, M. A., Hammel, H. B., Hutchings, J. B., Jakobsen, P., Lilly, S. J., Long, K. S., Lunine, J. I., Mccaughrean, M. J., Mountain, M., Nella, J., Rieke, G. H., Rieke, M. J., Rix, H.-W., Smith, E. P., Sonneborn, G., Stiavelli, M., Stockman, H. S., Windhorst, R. A., and Wright, G. S. (2006). The James Webb Space Telescope. *Space Science Reviews*, 123(4):485–606. (Cited on page 19.)

[Gendelman, 2012] Gendelman, O. (2012). Analytic treatment of a system with a vibro-impact nonlinear energy sink. *Journal of Sound and Vibration*, 331:4599–4608. (Cited on page 14.)

[Gendelman and Alloni, 2015] Gendelman, O. and Alloni, A. (2015). Dynamics of forced system with vibro-impact energy sink. *Journal of Sound and Vibration*, 358:301–314. (Cited on page 14.)

[Gendelman et al., 2005] Gendelman, O., Gorlov, D., Manevitch, L., and Musienko, A. (2005). Dynamics of coupled linear and essentially nonlinear oscillators with substantially different masses. *Journal of Sound and Vibration*, 286(1-2):1–19. (Cited on page 13.)

[Gendelman et al., 2006] Gendelman, O., Gourdon, E., and Lamarque, C. (2006). Quasiperiodic energy pumping in coupled oscillators under periodic forcing. *Journal of Sound and Vibration*, 294(4-5):651–662. (Cited on page 13.)

[Gendelman et al., 2001] Gendelman, O., Manevitch, L., Vakakis, A., and M'Closkey, R. (2001). Energy pumping in nonlinear mechanical oscillators: Part I-Dynamics of the underlying hamiltonian systems. *Journal of Applied Mechanics-transactions of The Asme*, 68:34–41. (Cited on page 13.)

[Gendelman, 2004] Gendelman, O. V. (2004). Bifurcations of Nonlinear Normal Modes of Linear Oscillator with Strongly Nonlinear Damped Attachment. *Nonlinear Dynamics*, 37(2):115–128. (Cited on page 14.)

[Gendelman, 2008] Gendelman, O. V. (2008). Targeted energy transfer in systems with non-polynomial nonlinearity. *Journal of Sound and Vibration*, 315(3):732–745. (Cited on pages 13, 14 and 31.)

[Gendelman et al., 2012] Gendelman, O. V., Sigalov, G., Manevitch, L. I., Mane, M., Vakakis, A. F., and Bergman, L. A. (2012). Dynamics of an Eccentric Rotational Nonlinear Energy Sink. *Journal of Applied Mechanics*, 79(1):011012. (Cited on page 14.)

[Gendelman and Starosvetsky, 2007] Gendelman, O. V. and Starosvetsky, Y. (2007). Quasi-Periodic Response Regimes of Linear Oscillator Coupled to Nonlinear Energy Sink Under Periodic Forcing. *Journal of Applied Mechanics*, 74(2):325–331. (Cited on page 13.)

[Gendelman et al., 2007] Gendelman, O. V., Starosvetsky, Y., and Feldman, M. (2007). Attractors of harmonically forced linear oscillator with attached nonlinear energy sink I: Description of response regimes. *Nonlinear Dynamics*, 51(1-2):31–46. (Cited on page 31.)

[Georgiades and Vakakis, 2009] Georgiades, F. and Vakakis, A. F. (2009). Passive targeted energy transfers and strong modal interactions in the dynamics of a thin plate with strongly nonlinear attachments. *International Journal of Solids and Structures*, 46(11-12):2330–2353. (Cited on page 13.)

[Georgiadis et al., 2005] Georgiadis, F., Vakakis, A. F., Mcfarland, D. M., and Bergman, L. (2005). Shock isolation through passive energy pumping caused by nonsmooth nonlinearities. *International Journal of Bifurcation and Chaos*, 15(06):1989–2001. (Cited on page 14.)

[Gourc et al., 2015] Gourc, E., Michon, G., Seguy, S., and Berlioz, A. (2015). Targeted energy transfer under harmonic forcing with a vibro-impact nonlinear energy sink: Analytical and experimental developments. *Journal of Vibration and Acoustics*, 137(3). (Cited on page 14.)

[Gourdon and Lamarque, 2006] Gourdon, E. and Lamarque, C. H. (2006). Nonlinear Energy Sink With Uncertain Parameters. *Journal of Computational and Nonlinear Dynamics*, 1(3):187–195. (Cited on page 83.)

[Gourdon et al., 2018] Gourdon, E., Ture Savadkoohi, A., and Alamo Vargas, V. (2018). Targeted Energy Transfer From One Acoustical Mode to an Helmholtz Resonator With Nonlinear Behavior. *Journal of Vibration and Acoustics*, (6):061005. (Cited on page 114.)

[Gourdon et al., 2020] Gourdon, E., Ture Savadkoohi, A., and Cauvin, B. (2020). Effects of shape of the neck of classical acoustical resonators on the sound absorption quality for large amplitudes: Experimental results. *Building Acoustics*, 27(2):169–181. Publisher: SAGE Publications Sage UK: London, England. (Cited on page 115.)

[Guillot et al., 2022] Guillot, V., Ture Savadkoohi, A., and Lamarque, C.-H. (2022). Tuning intermodal energy exchanges of a nonlinear electromechanical beam by a nonlinear circuit. *Archive of Applied Mechanics*, 92(8):2317–2349. (Cited on pages 50 and 80.)

[Guo et al., 2017] Guo, H., Sun, Z., and Zhou, C. (2017). Practical Design and Implementation of Metamaterial-Enhanced Magnetic Induction Communication. *IEEE Access*, 5:17213–17229. (Cited on page 16.)

[Guo et al., 2022] Guo, H., Yang, T., Chen, Y., and Chen, L.-Q. (2022). Singularity analysis on vibration reduction of a nonlinear energy sink system. *Mechanical Systems and Signal Processing*, 173:109074. (Cited on page 28.)

[Guo et al., 2020] Guo, X., Lissek, H., and Fleury, R. (2020). Improving Sound Absorption Through Nonlinear Active Electroacoustic Resonators. *Physical Review Applied*, 13(1):014018. (Cited on pages 106 and 111.)

[Guyomar and Badel, 2006] Guyomar, D. and Badel, A. (2006). Nonlinear semi-passive multimodal vibration damping: An efficient probabilistic approach. *Journal of Sound and Vibration*, 294(1-2):249–268. (Cited on page 12.)

[Guyomar et al., 2007] Guyomar, D., Richard, C., and Mohammadi, S. (2007). Semi-passive random vibration control based on statistics. *Journal of Sound and Vibration*, 307(3-5):818–833. (Cited on page 12.)

[Hartigan and Wong, 1979] Hartigan, J. A. and Wong, M. A. (1979). Algorithm AS 136: A K-Means Clustering Algorithm. *Applied Statistics*, 28(1):100. (Cited on page 90.)

[Haxton and A. D. S. Barr, 1972] Haxton, R. S. and A. D. S. Barr (1972). The autoparametric vibration absorber. *Journal of Engineering for Industry*, 94:119–125. (Cited on page 12.)

[Henry and Tobias, 1959] Henry, R. F. and Tobias, S. A. (1959). Instability and steady-state coupled motions in vibration isolating suspensions. *Journal of Mechanical Engineering Science*, 1:19–29. (Cited on page 12.)

[Henry and Tobias, 1961] Henry, R. F. and Tobias, S. A. (1961). Modes at rest and their stability in coupled non-linear systems. *Journal of Mechanical Engineering Science*, 3:163–173. (Cited on page 12.)

[Housner et al., 1997] Housner, G. W., Bergman, L. A., Caughey, T. K., Chassiakos, A. G., Claus, R. O., Masri, S. F., Skelton, R. E., Soong, T. T., Spencer, B. F., and Yao, J. T. P. (1997). Structural Control: Past, Present, and Future. *Journal of Engineering Mechanics*, 123(9):897–971. (Cited on page 11.)

[Hu et al., 2017] Hu, G., Tang, L., Das, R., Gao, S., and Liu, H. (2017). Acoustic metamaterials with coupled local resonators for broadband vibration suppression. *AIP Advances*, 7(2):025211. (Cited on page 16.)

[Huang and Sun, 2010] Huang, G. L. and Sun, C. T. (2010). Band Gaps in a Multiresonator Acoustic Metamaterial. *Journal of Vibration and Acoustics*, 132(3):031003. (Cited on page 20.)

[Huang et al., 2021] Huang, H., Cao, E., Zhao, M., Alamri, S., and Li, B. (2021). Spider Web-Inspired Lightweight Membrane-Type Acoustic Metamaterials for Broadband Low-Frequency Sound Isolation. *Polymers*, 13(7):1146. (Cited on page 17.)

[Huang and Sun, 2011] Huang, H. and Sun, C. (2011). Theoretical investigation of the behavior of an acoustic metamaterial with extreme Young's modulus. *Journal of the Mechanics and Physics of Solids*, 59(10):2070–2081. (Cited on page 16.)

[Huang et al., 2009] Huang, H., Sun, C., and Huang, G. (2009). On the negative effective mass density in acoustic metamaterials. *International Journal of Engineering Science*, 47(4):610–617. (Cited on page 20.)

[Huang and Sun, 2009] Huang, H. H. and Sun, C. T. (2009). Wave attenuation mechanism in an acoustic metamaterial with negative effective mass density. *New Journal of Physics*, 11(1):013003. (Cited on page 20.)

[Hunt and Nissen, 1982] Hunt, J. B. and Nissen, J.-C. (1982). The broadband dynamic vibration absorber. *Journal of Sound and Vibration*, 83(4):573–578. (Cited on page 13.)

[Hurel et al., 2019] Hurel, G., Ture Savadkoohi, A., and Lamarque, C.-H. (2019). Nonlinear Vibratory Energy Exchanges between a Two-Degree-of-Freedom Pendulum and a Nonlinear Absorber. *Journal of Engineering Mechanics*, 145(8):04019058. (Cited on page 42.)

[Hussein, 2020] Hussein, T. M. E.-B. (2020). Calibration and uncertainty estimation for the reference sound source in reverberation room. *Romanian Journal of Acoustics and Vibration*, 17(2):118–127. (Cited on page 107.)

[Iurasov and Mattei, 2020] Iurasov, V. and Mattei, P.-O. (2020). Bistable nonlinear damper based on a buckled beam configuration. *Nonlinear Dynamics*, 99(3):1801–1822. (Cited on page 105.)

[Jing et al., 2012] Jing, Y., Xu, J., and Fang, N. X. (2012). Numerical study of a near-zero-index acoustic metamaterial. *Physics Letters A*, 376(45):2834–2837. (Cited on page 16.)

[Jones et al., 1998] Jones, D. R., Schonlau, M., and Welch, W. J. (1998). Efficient Global Optimization of Expensive Black-Box Functions. *Journal of Global Optimization*, 13(4):455–492. (Cited on page 92.)

[Kadic et al., 2012] Kadic, M., Bückmann, T., Stenger, N., Thiel, M., and Wegener, M. (2012). On the practicability of pentamode mechanical metamaterials. *Applied Physics Letters*, 100(19):191901. (Cited on page 18.)

[Karkar et al., 2014] Karkar, S., Cochelin, B., and Vergez, C. (2014). A comparative study of the harmonic balance method and the orthogonal collocation method on stiff nonlinear systems. *Journal of Sound and Vibration*, 333(12):2554–2567. (Cited on page 28.)

[Kennedy and Eberhart, 1995] Kennedy, J. and Eberhart, R. (1995). Particle swarm optimization. In *Proceedings of ICNN'95 - International Conference on Neural Networks*, volume 4, pages 1942–1948, Perth, WA, Australia. IEEE. (Cited on page 89.)

[Khajehtourian and Hussein, 2014] Khajehtourian, R. and Hussein, M. I. (2014). Dispersion characteristics of a nonlinear elastic metamaterial. *AIP Advances*, 4(12):124308. (Cited on page 18.)

[Kojima and Saito, 1983] Kojima, H. and Saito, H. (1983). Forced vibration of a beam with a nonlinear dynamic absorber. *Journal of Sound and Vibration*, 88(4):559–568. (Cited on page 12.)

[Kopidakis et al., 2001] Kopidakis, G., Aubry, S., and Tsironis, G. P. (2001). Targeted Energy Transfer through Discrete Breathers in Nonlinear Systems. *Physical Review Letters*, 87(16):165501. (Cited on page 21.)

[Koutsogiannakis et al., 2023] Koutsogiannakis, P., Bigoni, D., and Dal Corso, F. (2023). Double restabilization and design of forcedisplacement response of the extensible elastica with movable constraints. *European Journal of Mechanics - A/Solids*, 100:104745. (Cited on page 105.)

[Lacaze and Missoum, 2013] Lacaze, S. and Missoum, S. (2013). Reliability-based design optimization using Kriging and support vector machines. (Not cited)

[Lacaze and Missoum, 2014] Lacaze, S. and Missoum, S. (2014). A generalized max-min sample for surrogate update. *Structural and Multidisciplinary Optimization*, 49(4):683–687. (Cited on pages 89 and 93.)

[Lakes, 1987] Lakes, R. (1987). Foam Structures with a Negative Poisson's Ratio. *Science*, 235(4792):1038–1040. (Cited on page 17.)

[Lamarque et al., 2011] Lamarque, C.-H., Gendelman, O., Ture Savadkoohi, A., and Etcheverria, E. (2011). Targeted energy transfer in mechanical systems by means of non-smooth nonlinear energy sink. *Acta mechanica*, 221(1):175–200. Publisher: Springer. (Cited on page 14.)

[Lamarque et al., 2012] Lamarque, C.-H., Savadkoohi, A. T., Etcheverria, E., and Dimitrijevic, Z. (2012). Multi-scale dynamics of two coupled nonsmooth systems. *International Journal of Bifurcation and Chaos*, 22(12):1250295. (Cited on page 13.)

[Lamarque et al., 2013] Lamarque, C.-H., Ture Savadkoohi, A., and Naudan, M. (2013). Multiscale energy exchanges between a nonlinear oscillator of Bouc-Wen type and another coupled nonlinear system. *The European Physical Journal Special Topics*, 222(7):1617–1636. (Cited on page 13.)

[Lang, 2009] Lang, R. J. (2009). Expandable Tubes with Negative Poissons Ratio and Their Application in Medicine. In *Origami 4*, pages 129–140. A K Peters/CRC Press, 0 edition. (Cited on page 19.)

[Lazarov and Jensen, 2007] Lazarov, B. and Jensen, J. (2007). Low-frequency band gaps in chains with attached non-linear oscillators. *International Journal of Non-Linear Mechanics*, 42(10):1186–1193. (Cited on page 21.)

[Lee et al., 2017] Lee, D., Nguyen, D. M., and Rho, J. (2017). Acoustic wave science realized by metamaterials. *Nano Convergence*, 4(1):3. (Cited on pages 14 and 15.)

[Lee et al., 2007] Lee, Y. S., Vakakis, A. F., Bergman, L. A., McFarland, D. M., and Kerschen, G. (2007). Suppression Aeroelastic Instability Using Broadband Passive Targeted Energy Transfers, Part 1: Theory. *AIAA Journal*, 45(3):693–711. (Cited on page 13.)

[Leroux et al., 2023] Leroux, M., Langlois, S., and Ture Savadkoohi, A. (2023). Investigation of nonlinear control of galloping with a linear beam with elastic boundary conditions. *International Journal of Non-Linear Mechanics*, page 104484. (Cited on page 13.)

[Lissek, 2010] Lissek, H. (2010). Les absorbeurs electroacoustiques: un concept unique pour différentes stratégies de contrôle actif d'Impédance acoustique. In *10ème Congrès Français d'Acoustique, 12-16 april 2010, lyon, france*. tex.hal_id: hal-00550904 tex.hal_version: v1. (Cited on page 106.)

[Liu et al., 2008] Liu, Y., Matsuhisa, H., and Utsuno, H. (2008). Semi-active vibration isolation system with variable stiffness and damping control. *Journal of Sound and Vibration*, 313(1-2):16–28. (Cited on page 11.)

[Liu et al., 2005a] Liu, Y., Waters, T., and Brennan, M. (2005a). A comparison of semi-active damping control strategies for vibration isolation of harmonic disturbances. *Journal of Sound and Vibration*, 280(1-2):21–39. (Cited on page 11.)

[Liu et al., 2005b] Liu, Z., Chan, C. T., and Sheng, P. (2005b). Analytic model of phononic crystals with local resonances. *Physical Review B*, 71(1):014103. (Cited on page 16.)

[Lo Feudo et al., 2019] Lo Feudo, S., Touzé, C., Boisson, J., and Cumunel, G. (2019). Nonlinear magnetic vibration absorber for passive control of a multistorey structure. *Journal of Sound and Vibration*, 438:33–53. (Cited on page 105.)

[Luongo and Zulli, 2014] Luongo, A. and Zulli, D. (2014). Aeroelastic instability analysis of NES-controlled systems via a mixed multiple scale/harmonic balance method. *Journal of Vibration and Control*, 20(13):1985–1998. Publisher: Sage Publications Sage UK: London, England. (Cited on page 13.)

[Luongo and Zulli, 2015] Luongo, A. and Zulli, D. (2015). Nonlinear energy sink to control elastic strings: the internal resonance case. *Nonlinear Dynamics*, 81(1-2):425–435. (Cited on page 13.)

[Ma et al., 2014] Ma, F., Wu, J. H., Huang, M., Fu, G., and Bai, C. (2014). Cochlear bionic acoustic metamaterials. *Applied Physics Letters*, 105(21):213702. (Cited on page 17.)

[Magnus et al., 2008] Magnus, F., Wood, B., Moore, J., Morrison, K., Perkins, G., Fyson, J., Wiltshire, M. C. K., Caplin, D., Cohen, L. F., and Pendry, J. B. (2008). A d.c. magnetic metamaterial. *Nature Materials*, 7(4):295–297. (Cited on page 15.)

[Manevitch, 2001] Manevitch, L. I. (2001). The Description of Localized Normal Modes in a Chain of Nonlinear Coupled Oscillators Using Complex Variables. *Nonlinear Dynamics*, 25(1):95–109. (Cited on pages 28 and 62.)

[Manevitch et al., 2003] Manevitch, L. I., Gendelman, O., Musienko, A. I., Vakakis, A. F., and Bergman, L. (2003). Dynamic interaction of a semi-infinite linear chain of coupled oscillators with a strongly nonlinear end attachment. *Physica D: Nonlinear Phenomena*, 178(1-2):1–18. (Cited on page 13.)

[Manevitch et al., 2014] Manevitch, L. I., Sigalov, G., Romeo, F., Bergman, L. A., and Vakakis, A. (2014). Dynamics of a Linear Oscillator Coupled to a Bistable Light Attachment: Analytical Study. *Journal of Applied Mechanics*, 81(4):041011. (Cited on page 14.)

[Manimala et al., 2014] Manimala, J. M., Huang, H. H., Sun, C., Snyder, R., and Bland, S. (2014). Dynamic load mitigation using negative effective mass structures. *Engineering Structures*, 80:458–468. (Cited on pages 20 and 21.)

[Mattei et al., 2016a] Mattei, P.-O., Ponçot, R., Pachebat, M., and Côte, R. (2016a). Nonlinear targeted energy transfer of two coupled cantilever beams coupled to a bistable light attachment. *Journal of Sound and Vibration*, 373:29–51. (Cited on page 14.)

[Mattei et al., 2016b] Mattei, P.-O., Ponçot, R., Pachebat, M., and Côte, R. (2016b). Nonlinear targeted energy transfer of two coupled cantilever beams coupled to a bistable light attachment. *Journal of Sound and Vibration*, 373:29–51. (Cited on page 14.)

[McKay et al., 1979] McKay, M. D., Beckman, R. J., and Conover, W. J. (1979). A Comparison of Three Methods for Selecting Values of Input Variables in the Analysis of Output from a Computer Code. *Technometrics*, 21(2):239. (Cited on page 89.)

[Mead, 1998] Mead, D. J. (1998). *Passive vibration control*. Wiley, Chichester ; New York. (Cited on page 11.)

[Medina et al., 2020] Medina, E., Farrell, P. E., Bertoldi, K., and Rycroft, C. H. (2020). Navigating the landscape of nonlinear mechanical metamaterials for advanced programmability. *Physical Review B*, 101(6):064101. (Cited on page 18.)

[Mikoshiba et al., 2013] Mikoshiba, K., Manimala, J. M., and Sun, C. (2013). Energy harvesting using an array of multifunctional resonators. *Journal of Intelligent Material Systems and Structures*, 24(2):168–179. (Cited on page 20.)

[Milton and Cherkaev, 1995] Milton, G. W. and Cherkaev, A. V. (1995). Which Elasticity Tensors are Realizable? *Journal of Engineering Materials and Technology*, 117(4):483–493. (Cited on page 18.)

[Miura, 1993] Miura, K. (1993). Concepts of Deployable Space Structures. *International Journal of Space Structures*, 8(1-2):3–16. (Cited on page 19.)

[Moheimani and Fleming, 2006] Moheimani, S. O. R. and Fleming, A. J. (2006). *Piezoelectric transducers for vibration control and damping*. Advances in industrial control. Springer, London. (Cited on page 12.)

[Mojahed et al., 2018] Mojahed, A., Moore, K., Bergman, L. A., and Vakakis, A. F. (2018). Strong geometric softeninghardening nonlinearities in an oscillator composed of linear stiffness and damping elements. *International Journal of Non-Linear Mechanics*, 107:94–111. (Cited on page 105.)

[Nayfeh and Mook, 1995] Nayfeh, A. H. and Mook, D. T. (1995). *Nonlinear oscillations*. Wiley classics library. Wiley, New York, wiley classics library ed edition. (Cited on pages 27, 30 and 35.)

[Nicolaou and Motter, 2012] Nicolaou, Z. G. and Motter, A. E. (2012). Mechanical metamaterials with negative compressibility transitions. *Nature Materials*, 11(7):608–613. (Cited on page 17.)

[Nissen et al., 1985] Nissen, J.-C., Popp, K., and Schmalhorst, B. (1985). Optimization of a nonlinear dynamic vibration absorber. *Journal of Sound and Vibration*, 99(1):149–154. (Cited on page 13.)

[Nucera et al., 2007] Nucera, F., Vakakis, A., McFarland, D., Bergman, L., and Kerschen, G. (2007). Targeted energy transfers in vibro-impact oscillators for seismic mitigation. *Nonlinear Dynamics*, 50(3):651–677. Publisher: Springer. (Cited on page 14.)

[Ormondroyd and Den Hartog, 1928] Ormondroyd, J. and Den Hartog, J. P. (1928). Theory of the Dynamic Vibration Absorber. *Trans. ASME*, 55:9–22. (Cited on page 12.)

[Pendry et al., 1999] Pendry, J., Holden, A., Robbins, D., and Stewart, W. (1999). Magnetism from conductors and enhanced nonlinear phenomena. *IEEE Transactions on Microwave Theory and Techniques*, 47(11):2075–2084. (Cited on page 15.)

[Pendry, 2000] Pendry, J. B. (2000). Negative Refraction Makes a Perfect Lens. *Physical Review Letters*, 85(18):3966–3969. (Cited on pages 15 and 16.)

[Pendry et al., 1996] Pendry, J. B., Holden, A. J., Stewart, W. J., and Youngs, I. (1996). Extremely Low Frequency Plasmons in Metallic Mesostructures. *Physical Review Letters*, 76(25):4773–4776. (Cited on page 15.)

[Pendry et al., 2006] Pendry, J. B., Schurig, D., and Smith, D. R. (2006). Controlling Electromagnetic Fields. *Science*, 312(5781):1780–1782. (Cited on page 15.)

[Pipes, 1953] Pipes, L. A. (1953). Analysis of a Nonlinear Dynamic Vibration Absorber. *Journal of Applied Mechanics*, 20(4):515–518. (Cited on page 12.)

[Pyskir et al., 2021] Pyskir, A., Collet, M., Dimitrijevic, Z., and Lamarque, C.-H. (2021). Enhanced Vibration Isolation with Prestressed Resonant Auxetic Metamaterial. *Materials*, 14(22):6743. (Cited on page 18.)

[Ren et al., 2018] Ren, X., Das, R., Tran, P., Ngo, T. D., and Xie, Y. M. (2018). Auxetic metamaterials and structures: a review. *Smart Materials and Structures*, 27(2):023001. (Cited on page 17.)

[Rice and McCraith, 1987] Rice, H. J. and McCraith, J. R. (1987). Practical non-linear vibration absorber design. *Journal of Sound and Vibration*, 116(3):545–559. (Cited on page 13.)

[Rivet et al., 2017] Rivet, E., Karkar, S., and Lissek, H. (2017). Broadband Low-Frequency Electroacoustic Absorbers Through Hybrid Sensor-/Shunt-Based Impedance Control. *IEEE Transactions on Control Systems Technology*, 25(1):63–72. (Cited on pages 106, 109 and 112.)

[Roberson, 1952] Roberson, R. E. (1952). Synthesis of a nonlinear dynamic vibration absorber. *Journal of Franklin Institute*, 254:205–220. (Cited on pages 12 and 13.)

[Romeo et al., 2015] Romeo, F., Sigalov, G., Bergman, L. A., and Vakakis, A. F. (2015). Dynamics of a Linear Oscillator Coupled to a Bistable Light Attachment: Numerical Study. *Journal of Computational and Nonlinear Dynamics*, 10(1):011007. (Cited on page 14.)

[Roncen et al., 2023] Roncen, T., Michon, G., and Manet, V. (2023). Design and experimental analysis of a pneumatic Nonlinear Energy Sink. *Mechanical Systems and Signal Processing*, 190:110088. (Cited on page 14.)

[Rothos and Vakakis, 2009] Rothos, V. and Vakakis, A. (2009). Dynamic interactions of traveling waves propagating in a linear chain with an local essentially nonlinear attachment. *Wave Motion*, 46(3):174–188. (Cited on page 13.)

[Schenk and Guest, 2013] Schenk, M. and Guest, S. D. (2013). Geometry of Miura-folded metamaterials. *Proceedings of the National Academy of Sciences*, 110(9):3276–3281. (Cited on page 19.)

[Sevin, 1961] Sevin, E. (1961). On the parametric excitation of pendulum-type vibration absorber. *Journal of Applied Mechanics*, 28:330–334. (Cited on page 12.)

[Shelby et al., 2001] Shelby, R. A., Smith, D. R., Nemat-Nasser, S. C., and Schultz, S. (2001). Microwave transmission through a two-dimensional, isotropic, left-handed metamaterial. *Applied Physics Letters*, 78(4):489–491. (Cited on page 15.)

[Silva et al., 2019] Silva, P. B., Leamy, M. J., Geers, M. G. D., and Kouznetsova, V. G. (2019). Emergent subharmonic band gaps in nonlinear locally resonant metamaterials induced by autoparametric resonance. *Physical Review E*, 99(6):063003. (Cited on page 21.)

[Smith et al., 2000] Smith, D. R., Padilla, W. J., Vier, D. C., Nemat-Nasser, S. C., and Schultz, S. (2000). Composite Medium with Simultaneously Negative Permeability and Permittivity. *Physical Review Letters*, 84(18):4184–4187. (Cited on page 15.)

[Starosvetsky and Gendelman, 2008] Starosvetsky, Y. and Gendelman, O. (2008). Strongly modulated response in forced 2DOF oscillatory system with essential mass and potential asymmetry. *Physica D: Nonlinear Phenomena*, 237(13):1719–1733. (Cited on pages 13, 34 and 42.)

[Struble and J. H. Heinbockel, 1963] Struble, R. A. and J. H. Heinbockel (1963). Resonant oscillations of a beam-pendulum system. *Journal of Applied Mechanics*, 30:181–188. (Cited on page 12.)

[Takenaka, 2012] Takenaka, K. (2012). Negative thermal expansion materials: technological key for control of thermal expansion. *Science and Technology of Advanced Materials*, 13(1):013001. (Cited on page 18.)

[Ture Savadkoohi et al., 2016a] Ture Savadkoohi, A., Lamarque, C.-H., and Contessa, M. (2016a). Trapping vibratory energy of main linear structures by coupling light systems with geometrical and material non-linearities. *International Journal of Non-Linear Mechanics*, 80:3–13. (Cited on page 14.)

[Ture Savadkoohi et al., 2016b] Ture Savadkoohi, A., Lamarque, C.-H., Weiss, M., Vaurigaud, B., and Charlemagne, S. (2016b). Analysis of the 1:1 resonant energy exchanges between coupled oscillators with rheologies. *Nonlinear Dynamics*, 86(4):2145–2159. (Cited on page 29.)

[Vakakis, 2001] Vakakis, A. (2001). Inducing passive nonlinear energy sinks in vibrating systems. *Journal of Vibration and Acoustics*, 123:42–48. (Cited on page 13.)

[Vakakis and Gendelman, 2001] Vakakis, A. and Gendelman, O. (2001). Energy pumping in nonlinear mechanical oscillators: Part II-Resonance capture. *Journal of Applied Mechanics-transactions of The Asme*, 68. (Cited on page 13.)

[Vakakis et al., 2003] Vakakis, A., Manevitch, L., Gendelman, O., and Bergman, L. (2003). Dynamics of linear discrete systems connected to local, essentially non-linear attachments. *Journal of Sound and Vibration*, 264(3):559–577. (Cited on page 13.)

[Vakakis et al., 2008] Vakakis, A. F., Gendelman, O., Bergman, L. A., McFarland, M., Kerschen, G., and Lee, Y. S., editors (2008). *Nonlinear targeted energy transfer in mechanical and structural systems*. Number v. 156 in Solid mechanics and its applications. Springer, Dordrecht ; London. (Cited on page 83.)

[Vakakis et al., 2004] Vakakis, A. F., McFarland, D. M., Bergman, L., Manevitch, L. I., and Gendelman, O. (2004). Isolated Resonance Captures and Resonance Capture Cascades Leading to Single- or Multi-Mode Passive Energy Pumping in Damped Coupled Oscillators. *Journal of Vibration and Acoustics*, 126(2):235–244. (Cited on page 13.)

[Veselago, 1968] Veselago, V. G. (1968). The electrodynamics of substances with simultaneously negative values of permittivity and permeability. *Soviet Physics Uspekhi*, 10(4):509–514. (Cited on page 15.)

[Wang et al., 2014] Wang, P., Casadei, F., Shan, S., Weaver, J. C., and Bertoldi, K. (2014). Harnessing Buckling to Design Tunable Locally Resonant Acoustic Metamaterials. *Physical Review Letters*, 113(1):014301. (Cited on page 19.)

[Wang et al., 2016] Wang, Q., Jackson, J. A., Ge, Q., Hopkins, J. B., Spadaccini, C. M., and Fang, N. X. (2016). Lightweight Mechanical Metamaterials with Tunable Negative Thermal Expansion. *Physical Review Letters*, 117(17):175901. (Cited on page 18.)

[Wierschem et al., 2014] Wierschem, N. E., Luo, J., AL-Shudeifat, M., Hubbard, S., Ott, R., Fahnestock, L. A., Quinn, D. D., McFarland, D. M., Spencer, B. F., Vakakis, A., and Bergman, L. A. (2014). Experimental Testing and Numerical Simulation of a Six-Story Structure Incorporating Two-Degree-of-Freedom Nonlinear Energy Sink. *Journal of Structural Engineering*, 140(6):04014027. (Cited on page 83.)

[Willems and Pandit, 1971] Willems, J. L. and Pandit, M. (1971). Stability Theory of Dynamical Systems. *IEEE Transactions on Systems, Man, and Cybernetics*, SMC-1(4):408–408. (Cited on page 33.)

[Xie et al., 2017] Xie, L., Baguet, S., Prabel, B., and Dufour, R. (2017). Bifurcation tracking by Harmonic Balance Method for performance tuning of nonlinear dynamical systems. *Mechanical Systems and Signal Processing*, 88:445–461. (Cited on page 28.)

[Yamakawa et al., 1977] Yamakawa, I., Takeda, S., and Kojima, H. (1977). Behavior of a new type dynamic vibration absorber. *Bulletin of JSME*, 20(146):947–954. (Cited on page 12.)

[Yao et al., 2008] Yao, S., Zhou, X., and Hu, G. (2008). Experimental study on negative effective mass in a 1D massspring system. *New Journal of Physics*, 10(4):043020. (Cited on pages 16 and 20.)

[Zega et al., 2020] Zega, V., Silva, P. B., Geers, M. G. D., and Kouznetsova, V. G. (2020). Experimental proof of emergent subharmonic attenuation zones in a nonlinear locally resonant metamaterial. *Scientific Reports*, 10(1):12041. (Cited on pages 21 and 22.)

[Zheng et al., 2014] Zheng, X., Lee, H., Weisgraber, T. H., Shusteff, M., DeOtte, J., Duoss, E. B., Kuntz, J. D., Biener, M. M., Ge, Q., Jackson, J. A., Kucheyev, S. O., Fang, N. X., and Spadaccini, C. M. (2014). Ultralight, ultrastiff mechanical metamaterials. *Science*, 344(6190):1373–1377. (Cited on page 17.)

[Zhong et al., 2018] Zhong, R., Pai, P. F., Zong, Z., Deng, H., and Ruan, X. (2018). Metamaterial I-Girder for Vibration Absorption of Composite Cable-Stayed Bridge. *Journal of Engineering Mechanics*, 144(7):04018045. (Cited on page 18.)

[Zhou et al., 2023] Zhou, W., Bi, K., Hao, H., Pham, T. M., and Chen, W. (2023). Development of locally resonant meta-basement for seismic induced vibration control of high-rise buildings. *Engineering Structures*, 275:115229. (Cited on pages 20 and 21.)

[Zhu et al., 2013] Zhu, J., Chen, Y., Zhu, X., Garcia-Vidal, F. J., Yin, X., Zhang, W., and Zhang, X. (2013). Acoustic rainbow trapping. *Scientific Reports*, 3(1):1728. (Cited on page 17.)

[Zou et al., 2021] Zou, D., Liu, G., Rao, Z., Tan, T., Zhang, W., and Liao, W.-H. (2021). A device capable of customizing nonlinear forces for vibration energy harvesting, vibration isolation, and nonlinear energy sink. *Mechanical Systems and Signal Processing*, 147:107101. (Cited on pages 105 and 106.)

APPENDIX A

Time averaging

This annex aims to demonstrate the numerical development used to obtain $G(|\varphi_2|^2)$ in Chapter 2. From the definition of φ_2 and φ_2^* in Eq. (2.16), one can write $v(\tau)$ as it follows:

$$v(\tau) = \frac{-i(\varphi_2 e^{i\vartheta\tau} - \varphi_2^* e^{-i\vartheta\tau})}{2\vartheta} \tag{A.1}$$

In the polar domain, $\varphi_2 = |\varphi_2|e^{i\theta}$ and $\varphi_2^* = |\varphi_2|e^{-i\theta}$. Thus, Eq. (A.1) reads:

$$v(\tau) = \frac{-i(|\varphi_2|e^{i(\theta+\vartheta\tau)} - |\varphi_2|e^{-i(\theta+\vartheta\tau)})}{2\vartheta} \tag{A.2}$$

Using the Euler's formula, we finally obtain:

$$v(\tau) = \frac{|\varphi_2|\text{sin}(\vartheta\tau + \theta)}{\vartheta} \tag{A.3}$$

We can rewrite $f(\tau)$ as it follows:

$$f(\tau) = \begin{cases} \text{I-} & K_{NL}v(\tau)^3 & \text{if} & -\delta \leq v(\tau) \leq \delta \\ \text{II-} & K_L(v(\tau) - \delta) + K_{NL}\delta^3 & \text{if} & v(\tau) > \delta \\ \text{III-} & K_L(v(\tau) + \delta) - K_{NL}\delta^3 & \text{if} & v(\tau) < -\delta \end{cases} \tag{A.4}$$

If $|v(\tau)| \leq \delta$, $\mathcal{F}$ is obtained through the integral defined in Eq. (2.21) with an uniform $f(\tau) = \text{I}$ and, then, $G(|\varphi_2|^2)$ can be obtained from Eq. (2.22). However, $f(\tau)$ assumes a non-uniform behavior when $|v(\tau)| > \delta$, which is illustrated in Fig. A.1. In this case, $G(|\varphi_2|^2)$ is obtained through a time averaging using Eqs. (2.21) and (2.22) as it follows:

$$G(|\varphi_2|) = \frac{\vartheta^2}{\pi\varphi_2}\left(\int_0^{T_1} \text{I}\, e^{-i\vartheta\tau}\, d\tau + \int_{T_1}^{T_2} \text{II}\, e^{-i\vartheta\tau}\, d\tau + \int_{T_2}^{T_3} \text{I}\, e^{-i\vartheta\tau}\, d\tau \int_{T_3}^{T_4} \text{III}\, e^{-i\vartheta\tau}\, d\tau \right.$$
$$\left. + \int_{T_4}^{\frac{2\pi}{\vartheta}} \text{I}\, e^{-i\vartheta\tau}\, d\tau\right) \tag{A.5}$$

Considering $q(\vartheta T_1 + \theta) = \delta$, from Eq. (A.3) we obtain T_1:

$$T_1 = \frac{1}{\vartheta}\,\text{asin}\left(\frac{\delta\vartheta}{|\varphi_2|}\right) \tag{A.6}$$

Using some trigonometric identities, we obtain T_2, T_3, and T_4 as it follows:

$$T_2 = \frac{\pi}{\vartheta} - \frac{2\theta}{\vartheta} - T_1 \tag{A.7}$$

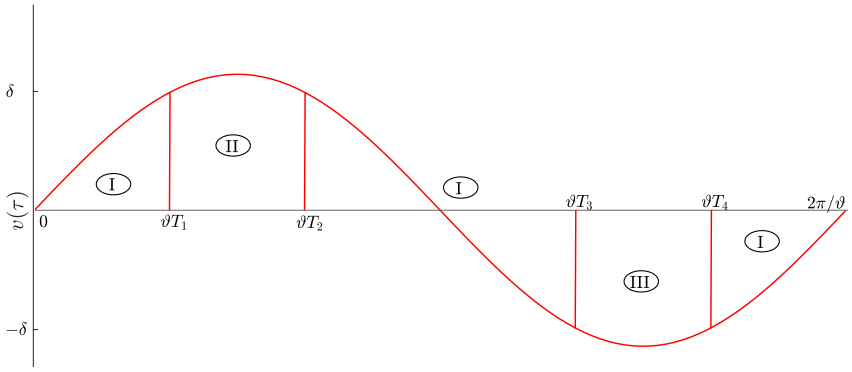

Figure A.1: Schematics of the behavior of $f(\tau)$ in a loop.

$$T_3 = \frac{3\pi}{2\vartheta} - \frac{\theta}{\vartheta} - \frac{1}{\vartheta}\text{acos}\left(\frac{\delta\vartheta}{|\varphi_2|}\right) \tag{A.8}$$

$$T_4 = \frac{3\pi}{\vartheta} - \frac{2\theta}{\vartheta} - T_3 \tag{A.9}$$

Finally, $G(|\varphi_2|^2)$ can be written as it follows:

$$G(|\varphi_2|^2) = \begin{cases} \dfrac{3K_{NL}|\varphi_2|^2}{4\vartheta^2} & \text{if } \dfrac{|\varphi_2|}{\vartheta} < \delta \\ \dfrac{3K_{NL}|\varphi_2|^2}{4\vartheta^2} + \dfrac{1}{4\pi\vartheta^2|\varphi_2|}\left[\left(-8\delta K_L\vartheta^3\sqrt{1-\dfrac{\delta^2\vartheta^2}{|\varphi_2|^2}}\right)\right. & \\ +K_{NL}\left(-6\delta|\varphi_2|^2\vartheta\sqrt{1-\dfrac{\delta^2\vartheta^2}{|\varphi_2|^2}} + 12\delta^3\vartheta^3\sqrt{1-\dfrac{\delta^2\vartheta^2}{|\varphi_2|^2}}\right) & \\ \left.+(8K_L|\varphi_2|\vartheta^2 - 6K_{NL}|\varphi_2|^3)\ \text{arccos}\left(\dfrac{\delta\vartheta}{|\varphi_2|}\right)\right] & \text{if } \dfrac{|\varphi_2|}{\vartheta} \geq \delta \end{cases} \tag{A.10}$$

So one can write:

$$G(|\varphi_2|^2) = g(|\varphi_2|^2) + \mathcal{O}(\varepsilon^1) \tag{A.11}$$

where

$$g(|\varphi_2|^2) = \begin{cases} \dfrac{3K_{NL}|\varphi_2|^2}{4} & \text{if } |\varphi_2| < \delta \\ \dfrac{3K_{NL}|\varphi_2|^2}{4} + \dfrac{1}{4\pi|\varphi_2|}\left[\left(-8\delta K_L\sqrt{1-\dfrac{\delta^2}{|\varphi_2|^2}}\right)\right. & \\ +K_{NL}\left(-6\delta|\varphi_2|^2\sqrt{1-\dfrac{\delta^2}{|\varphi_2|^2}} + 12\delta^3\sqrt{1-\dfrac{\delta^2}{|\varphi_2|^2}}\right) & \\ \left.+(8K_L|\varphi_2| - 6K_{NL}|\varphi_2|^3)\ \text{arccos}\left(\dfrac{\delta}{|\varphi_2|}\right)\right] & \text{if } |\varphi_2| \geq \delta \end{cases} \tag{A.12}$$

APPENDIX B

Space averaging

In this annex, the process of space averaging that led to the calculation of $\mathscr{F}(\tau)$ from Chapter 3 is explained in detail. Thus, let us inject Eq. (3.30) in Eq. (2.2) when dimensionless, it reads:

$$f(A_k(x)q(t)) = \begin{cases} \text{I-} & K_{NL}(A_k(x)q(t))^3 & \text{if} & -\dfrac{\delta}{q(\tau)} \leq A_k(x) \leq \dfrac{\delta}{q(\tau)} \\ \text{II-} & K_L(A_k(x)q(t)-\delta) + K_{NL}\delta^3 & \text{if} & A_k(x) > \dfrac{\delta}{q(\tau)} \\ \text{III-} & K_L(A_k(x)q(t)+\delta) - K_{NL}\delta^3 & \text{if} & A_k(x) < -\dfrac{\delta}{q(\tau)} \end{cases} \tag{B.1}$$

If $|w(x,\tau)| \leq \delta$, that is, $|A_k(x)q(\tau)| \leq \delta \;\; \Rightarrow \;\; |q(\tau)| \leq \dfrac{\delta}{B_1}$, the restoring force is purely cubic, otherwise it assumes the behavior illustrated in Fig. B.1 according to the mode shape. In the latter case, $\mathscr{F}(\tau)$ is obtained through space averaging as it follows:

$$\mathscr{F}(\tau) = \int_0^L d(w(x,\tau))A_k(x)\,dx = \int_0^{x_1} \text{I}\; A_k(x)\,dx + \int_{x_1}^{x_2} \text{II}\; A_k(x)\,dx + \int_{x_2}^{x_3} \text{I}\; A_k(x)\,dx$$
$$\int_{x_3}^{x_4} \text{III}\; A_k(x)\,dx + \int_{x_4}^{L} \text{I}\; A_k(x)\,dx \tag{B.2}$$

From Eq. (3.24), we can write x as a function of $A_k(x)$:

$$x = \frac{1}{\mu_k}\,\text{acos}\left(\frac{A_k(x)}{B_1}\right) \tag{B.3}$$

Considering $A_k(x_1) = \dfrac{\delta}{q(\tau)}$, we obtain x_1:

$$x_1 = \frac{1}{\mu_k}\,\text{acos}\left(\frac{\delta}{q(\tau)B_1}\right) \tag{B.4}$$

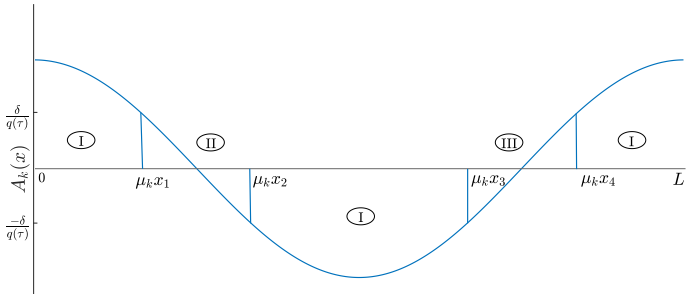

Figure B.1: Schematics of the behavior of the restoring force with respect to the space in a loop.

Using some trigonometric identities, we obtain x_2, x_3, and x_4 as it follows:

$$x_2 = \frac{\pi}{2\mu_k} + x_1 \tag{B.5}$$

$$x_3 = \frac{2\pi}{2\mu_k} - x_2 \tag{B.6}$$

$$x_4 = \frac{\pi}{2\mu_k} + x_3 \tag{B.7}$$

Thus, $\mathscr{F}(\tau)$ reads:

$$\mathscr{F}(\tau) = \begin{cases} \dfrac{3Lq_{MC}(\tau)^3 B_1^4 K_{NL}}{8} & \text{if} \quad |q_{MC}(\tau)| \leq \dfrac{\delta}{B_1} \\ \dfrac{LB_1}{16k\pi}\Bigg(16\delta q_{MC}(\tau)^2\sqrt{1-\dfrac{\delta^2}{q_{MC}(\tau)^2{B_1}^2}}{B_1}^2 K_{NL} & \\ +3(-1+2k)\pi q_{MC}(\tau)^3{B_1}^3 K_{NL} & \\ -16\delta\sqrt{1-\dfrac{\delta^2}{q_{MC}(\tau)^2{B_1}^2}}K_L + 4\pi q(\tau)B_1 K_L\Bigg) & \text{if} \quad |q_{MC}(\tau)| > \dfrac{\delta}{B_1} \end{cases} \tag{B.8}$$

APPENDIX C

Time averaging II

The following annex provides a detailed explanation of the time averaging process used to calculate $\mathcal{G}(|\varphi_2|)$ in Chapter 3.

From the definition of φ_2 in Eq. (3.33) and from its complex conjugate $\varphi_2^* = \frac{\dot{q}_{MC} - i\lambda q_{MC}}{e^{-i\lambda\tau}}$, one can write $q_{MC}(\tau)$ as it follows:

$$q_{MC}(\tau) = \frac{-i(\varphi_2 e^{i\lambda\tau} - \varphi_2^* e^{-i\lambda\tau})}{2\lambda} \tag{C.1}$$

In the polar domain, one can write $\varphi_2 = |\varphi_2|e^{i\theta}$ and $\varphi_2^* = |\varphi_2|e^{-i\theta}$. Replacing them in Eq. (C.1), we obtain

$$q_{MC}(\tau) = \frac{-i(|\varphi_2|e^{i(\theta+\lambda\tau)} - |\varphi_2|e^{-i(\theta+\lambda\tau)})}{2\lambda} \tag{C.2}$$

Using the Euler's formula, Eq. (C.2) reads to:

$$q_{MC}(\tau) = \frac{|\varphi_2|\sin(\lambda\tau + \theta)}{\lambda} \tag{C.3}$$

Furthermore, $\mathscr{F}(\tau)$ from Eq. (3.32) can be set in another way for the different conditions:

$$\mathscr{F}(\tau) = \begin{cases} \text{I-} \quad \dfrac{3Lq_{MC}(\tau)^3 B_1^4 K_{NL}}{8} & \text{if} \quad \dfrac{-\delta}{B_1} \leq q_{MC}(\tau) \leq \dfrac{\delta}{B_1} \\ \text{II-} \quad \dfrac{LB_1}{16k\pi}\left(16\delta q_{MC}(\tau)^2\sqrt{1-\dfrac{\delta^2}{q(\tau)^2 {B_1}^2}}{B_1}^2 K_{NL}\right. & \\ +3(-1+2k)\pi q_{MC}(\tau)^3 {B_1}^3 K_{NL} & \\ \left. -16\delta\sqrt{1-\dfrac{\delta^2}{q_{MC}(\tau)^2 {B_1}^2}}K_L + 4\pi q_{MC}(\tau)B_1 K_L\right) & \text{if} \quad q_{MC}(\tau) > \dfrac{\delta}{B_1} \\ \text{III-} \quad \dfrac{LB_1}{16k\pi}\left(-16\delta q_{MC}(\tau)^2\sqrt{1-\dfrac{\delta^2}{q_{MC}(\tau)^2 {B_1}^2}}{B_1}^2 K_{NL}\right. & \\ +3(-1+2k)\pi q_{MC}(\tau)^3 {B_1}^3 K_{NL} & \\ \left. +16\delta\sqrt{1-\dfrac{\delta^2}{q_{MC}(\tau)^2 {B_1}^2}}K_L + 4\pi q_{MC}(\tau)B_1 K_L\right) & \text{if} \quad q_{MC}(\tau) < \dfrac{-\delta}{B_1} \end{cases} \tag{C.4}$$

From that, if $|q_{MC}(\tau)| \leq \frac{\delta}{B_1}$, $\mathcal{F}(\varphi_2, \varphi_2^*)$ is obtained through the integral of Eq. (3.35) with an uniform $\mathscr{F}$ and, then, $\mathcal{G}(|\varphi_2|)$ is obtained from Eq. (3.36). However, $\mathscr{F}$ assumes a non-uniform behavior when $|q_{MC}(\tau)| > \frac{\delta}{B_1}$, which is illustrated in Fig. C.1. In this case, $\mathcal{G}(|\varphi_2|)$ is obtained through a time averaging using Eq. (3.35) and (3.36) as it follows:

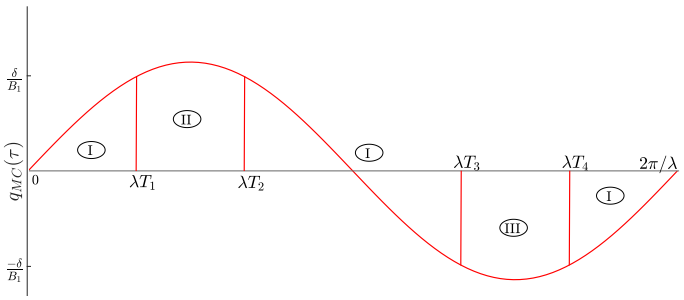

Figure C.1: Schematics of the behavior of $\mathscr{F}(\tau)$ in a loop.

$$\mathcal{G}(|\varphi_2|) = \frac{\lambda^2}{\pi\varphi_2}\left(\int_0^{T_1} \mathrm{I}\; e^{-i\lambda\tau}\, d\tau + \int_{T_1}^{T_2} \mathrm{II}\; e^{-i\lambda\tau}\, d\tau + \int_{T_2}^{T_3} \mathrm{I}\; e^{-i\lambda\tau}\, d\tau \right. \\ \left. \int_{T_3}^{T_4} \mathrm{III}\; e^{-i\lambda\tau}\, d\tau + \int_{T_4}^{\frac{2\pi}{\lambda}} \mathrm{I}\; e^{-i\lambda\tau}\, d\tau \right) \tag{C.5}$$

Considering $q(\lambda T_1 + \theta) = \dfrac{\delta}{B_1}$, from Eq. (C.3) we obtain T_1:

$$T_1 = \frac{1}{\lambda}\,\mathrm{asin}\left(\frac{\delta\lambda}{B_1|\varphi_2|}\right) \tag{C.6}$$

Using some trigonometric identities, we obtain T_2, T_3, and T_4 as it follows:

$$T_2 = \frac{\pi}{\lambda} - \frac{2\theta}{\lambda} - T_1 \tag{C.7}$$

$$T_3 = \frac{3\pi}{2\lambda} - \frac{\theta}{\lambda} - \frac{1}{\lambda}\mathrm{acos}\left(\frac{\delta\lambda}{B_1|\varphi_2|}\right) \tag{C.8}$$

$$T_4 = \frac{3\pi}{\lambda} - \frac{2\theta}{\lambda} - T_3 \tag{C.9}$$

Furthermore, one can say:

$$\mathcal{G}(|\varphi_2|) = \mathbb{G}(|\varphi_2|) + \mathcal{O}(\varepsilon^1) \tag{C.10}$$